Multi-scale simulations investigation of defects in semiconductor devices

Pierre-Louis Julliard

Université de Toulouse

THÈSE

En vue de l'obtention du

DOCTORAT DE L'UNIVERSITÉ DE TOULOUSE

Délivré par : *l'Université Toulouse 3 Paul Sabatier (UT3 Paul Sabatier)*

Présentée et soutenue le *19/06/2023* **par :**

Pierre-Louis JULLIARD

Simulations multi échelles des défauts dans les dispositifs semi-conducteurs

---

JURY

Lourdes PELAZ	Rapporteure
El Mehdi BAZIZI	Examinateur
Benoit SKLENARD	Examinateur
Filadelfo CRISTIANO	Directeur de thèse
Anne HEMERYCK	Co-directrice de thèse
Antonino LA MAGNA	Président

École doctorale et spécialité :
GEET : Micro et Nanosystèmes
Unité de Recherche :
LAAS - Laboratoire d'Analyse et d'Architecture des Systèmes
Directeur(s) de Thèse :
Anne HEMERYCK et *Filadelfo CRISTIANO*
Rapporteurs :
Lourdes PELAZ et *Antonino LA MAGNA*

I would like to thank the members of the jury, Prof. Lourdes Pelaz and Prof. Antonino La Magna for accepting to review the manuscript, Dr. El-Medhi Bazizi and Dr. Benoit Sklenard for being members of the jury.

Je remercie mon directeur et ma directrice de thèse au LAAS-CNRS Fuccio Cristiano et Anne Hémeryck. Anne je ne saurais combien te remercier pour toute ton aide pendant cette thèse. Ton écoute, ton expertise et ton travail sans relâche ont grandement contribué à la réalisation de ce travail de thèse. Tout n'a pas été facile au cours de ces 3 ans et j'ai toujours pu compter sur toi dans les moments compliqués. Fuccio, merci à toi de m'avoir accompagné avec bienveillance et rigueure pendant ma thèse. Nos discussions et tes conseils m'ont permis de progresser pendant ces trois ans et je te dois beaucoup.
Mes remerciements vont aussi à Denis Rideau qui a encadré mon travail au sein de STMicroelectronics. Tu as su me challenger dans mon travail et tu as toujours fais preuve d'une curiosité scientifique précieuse. Je tiens aussi à remercier Frédéric Monsieur qui m'a accueilli et a guidé mes premiers pas à ST. Merci d'avoir pris le temps de me former, d'avoir été à l'écoute et compréhensif au cours de cette thèse.
Je remercie toutes les personnes avec qui j'ai pu travailler pendant cette thèse. Merci Antoine qui a suivi de très près mon travail de thèse, particulièrement les calculs ab initio. Antoine, tu es un personnage. Ta générosité, ton aide et ta maîtrise de l'ab initio ont rythmé ma thèse au même titre que les parties d'échecs, tes théories farfelues sur la vie et les repas dans ta maison. Je remercie aussi les Richard du LAAS. Richard Monflier, pour ton aide sur la caractérisation des défauts et ses conseils de manière générale. Richard Daubriac, pour ton enthousiasme et ta disponibilité. Merci également à Rémi avec qui j'ai pu travailler à la caractérision des défauts. Je remercie les différentes personnes de l'équipe M3 avec qui j'ai passé du temps lors de mes deux ans et demi à Toulouse. Merci à Lionel pour ton accueil, merci Miha, Ruggero, Chloé, Abdul, Tingquiang pour les cafés, foot, échecs, coinche, ping-pong qui m'ont permis de me changer les idées. Merci aussi à tous les stagiaires, Alessandro, Jihan, Oussama, Juan qui ont permis d'apporter une ambiance encore plus chaleureuse. Merci aussi à George et à Marie qui viennent compléter avec brio l'équipe M3. Je remercie aussi toutes les personnes avec qui j'ai pu travailler à ST, notamment les différentes personnes travaillant en TCAD : Olivier, Pascal, Cristelle, Edgar, Guillaume, particulièrement Thomas et Nicolas, avec qui nous avons pu tomber dans les pièges de l'ab initio. Merci aussi à Julien, Paul, Fanny et Sylvain de l'équipe implantation avec qui j'ai pu échanger. Merci aux différents doctorants et stagiaires de ST avec qui j'ai partagé des discussion et des cafés. Merci à Richard, Yassine, merci à Antonin et Robin (que je recroise maintenant ma thèse terminée). Merci à Bruno malgré tes pièges aux échecs et merci à Rémi et Jeremy pour nos commérages sur la vie des doctorants et autres sujets. Merci à toutes les personnes avec qui j'ai pu travailler à travers des projets scientifiques, aux membres de MAMASMIAS pour les passionnantes discussions. Je remercie aussi les différents acteurs du projet MUNDFAB avec qui j'ai interagi.

Merci aussi à toutes les personnes qui m'ont accompagné en dehors de cette

thèse. Merci à mes amis d'enfance Lyonnais. Une description attentive de chaque personne nécéssiterait un travail de thèse tout entier. Je listerai donc plutôt des souvenirs que vous m'avez laissés durant ces 3 ans et je dresserai ensuite une liste très impersonnelle, en vous laissant le soin de relier votre nom à un ou plusieurs souvenirs. Merci donc pour ces fous rires, cette image de semi-conducteur, nos échanges Lidya, nos footing, les mariages, votre aptitude à être de mauvais joueurs pour n'importe quel jeux de société (même fictif), vos projets KO, vos expériences culinaires et capillaires, vos discussions trop sérieuses et trop longues à des heures trop tardives, nos "pestacles" qui m'ont permis de me motiver à m'inscrire aux théâtres, d'avoir élargi nos WE entre amis de deux cousins, de vos WE entre anciennes maîtrises (j'ai évidemment une préférence secrète pour une des deux). Merci donc à Puj, Adèle, Anaïs, Arthur(s),Baptiste, Antoine(s) (non je ne vous appellerai pas par vos surnoms), Bob, Camille, Claire, Clémence, Hélène, Cécile, Florence, Lucas, Mailys, Manon, Marion, Virgile, Pauline(s), Pierre, Pierric, Léa, Philippe, Solène, Tim, Théo, Ugo, Vianney.
Merci à mes amis d'école de Nancy. Thomas, je ne te remercie pas d'être un doctorant parfait, ça place la barre haut, mais je te remercie pour ton aide apportée en fin de thèse. Comme pour mes amis lyonnais, la description complète serait ardue, et je liste donc dans un premier temps des souvenirs auxquels certain et certaines pourront s'identifier. Merci donc pour ces WE et semaines à Paris, à Bayonne, en Corse, à Montpellier, pour être les plus mauvais gagnants que la Terre ait portée, merci pour ces victoires faciles au tchou Pilou (même sans Thomas Meyer), merci pour votre hospitalité, vos WE carte blanche, pour le surf, les foots, les brunchs, merci de répondre à mes questions sur chaque personne de la promo avec qui j'ai perdu contact, merci de me suivre dans des idées saugrenues, pour les rigolades, pour les bons repas, pour votre patience devant les trop fréquentes carbonaras, pour avoir subi le mercato départaimant, de vous lever tôt en lendemain de soirée, de votre gentillesse, de votre écoute. Merci à Anaïs, Alice, Alexandre, Antoine, Corentin, Capucine, Florin, Léo, Mathieu, Mathilde, Margot, Nicolas, Sami, Sahar, Sylvain, Titi et Thomas.
J'avais peur en arrivant à Toulouse de ne pas connaître grand monde mais connaître Sylvain c'est aussitôt être intégré dans un groupe d'amis des plus sympathiques ! Merci à Alban, Gabrielle, Laurent, Madec, Jolante, Vincent, Clémence, Mathilde et Paul-Louis pour ces moments partagés autour d'une pizza et d'un jeu de société.
Merci à toutes les personnes avec qui j'ai vécu en colocation durant ces trois années et demies, leur patience et leur bonne humeur et leurs rigolades ont aussi rythmé cette thèse. Merci à Victor, Anna, Pierre, Aloïs, Marine, Domitille, Célia, Valentin, Elodie, Hugo, Pomme, Aude, Thomas, Pierre-Yves.
Je remercie enfin ma famille à qui je dois beaucoup plus qu'une thèse. Merci à ma soeur (et à Pierre) de m'avoir écouté, de m'avoir supporté, d'avoir été là dans les bons moments comme dans les moins bons pendant beaucoup plus que 3 ans. Nos rigolades, nos discussions au Monot, nos jeux m'ont permi de grandir. Je rejoins ainsi Edgar et Mr.R au club des docteurs et tu seras toujours la bienvenue dans nos discussions philosophiques et scientifiques. Merci à mes parents pour leur soutien et leur amour de tous les instants. Merci de

m'avoir accompagné, consolé, félicité, grondé (quand c'était nécessaire), d'avoir été patients et doux pendant toute cette partie de ma vie.

Université Fédérale
Toulouse Midi-Pyrénées

THÈSE

En vue de l'obtention du
DOCTORAT DE L'UNIVERSITÉ DE TOULOUSE
Délivré par l'Université Toulouse 3 - Paul Sabatier

Présentée et soutenue par

Pierre-Louis JULLIARD

Le 19 juin 2023

Simulations multi échelles des défauts dans des les dispositifs semi-conducteurs

Ecole doctorale : **GEETS - Génie Electrique Electronique,Télécommunications et Santé : du système au nanosystème**

Spécialité : **MicroNano Systèmes**

Unité de recherche :
LAAS - Laboratoire d'Analyse et d'Architecture des Systèmes

Thèse dirigée par
Filadelfo CRISTIANO et Anne HEMERYCK

Jury

Mme Lourdes PELAZ, Rapporteure
M. El Mehdi BAZIZI, Examinateur
M. Benoit SKLENARD, Examinateur
M. Filadelfo CRISTIANO, Directeur de thèse
Mme Anne HEMERYCK, Co-directrice de thèse
M. Antonino LA MAGNA, Président

I would like to thank the members of the jury, Prof. Lourdes Pelaz and Prof. Antonino La Magna for accepting to review the manuscript, Dr. El-Medhi Bazizi and Dr. Benoit Sklenard for being members of the jury.

Je remercie mon directeur et ma directrice de thèse au LAAS-CNRS Fuccio Cristiano et Anne Hémeryck. Anne je ne saurais combien de remercier pour toute ton aide pendant cette thèse. Ton écoute, ton expertise et ton travail sans relache ont grandement contribué à la réalisation de ce travail de thèse. Tout n'a pas été facile au cours de ces 3 ans et j'ai toujours pu compter sur toi dans les moments compliqués. Fuccio, merci à toi de m'avoir accompagné avec bienveillance et rigueure pendant ma thèse. Nos discussions et tes conseils m'ont permis de progresser pendant ces trois ans et je te dois beaucoup.
Mes remerciements vont aussi à Denis Rideau qui a encadré mon travail au sein de STMicroelectronics. Tu as su me pousser à me dépasser dans mon travail et tu as toujours fais preuve d'une curiosité scientifique précieuse. Je tiens aussi à remercier Frédéric Monsieur qui m'a accueilli et a guidé mes premiers pas à ST. Merci d'avoir pris le temps de me former et d'avoir été à l'écoute et compréhensif au cours de cette thèse.
Je remercie toutes les personnes avec qui j'ai pu travailler pendant cette thèse. Merci Antoine qui a suivi de très près mon travail de thèse, particulièrement les calculs ab initio. Antoine, tu es un personnage. Ta générosité, ton aide et ta maîtrise de l'ab initio ont rythmé ma thèse au même titre que tes théories farfelues, les parties d'échecs et les repas dans ta maison. Je remercie aussi Richard Monflier pour ton aide sur la caractérisation des défauts et ses conseils de manière générale. Je remercie aussi Richard Daubriac, pour ton enthousiasme et ta disponibilité, et Rémi avec qui j'ai pu travailler à la caractérision des défauts. Je remercie les différentes personnes de l'équipe M3 avec qui j'ai passer du temps lors de mes deux ans et demi à Toulouse. Merci à Lionel pour ton accueil, merci Miha, Ruggero, Chloé, Abdul, Tingquiang pour les cafés, foot, échecs, coinche, ping-pong qui m'ont permis de me changer les idées. Merci aussi à tous les stagiaires, Alessandro, Jihan, Oussama, Juan qui ont permis d'apporter une ambiance encore plus chaleureuse. Merci aussi à George et à Marie qui viennent compléter avec brio l'équipe M3.
Je remercie aussi toutes les personnes avec qui j'ai pu travailler à ST. Merci aux différentes personnes travaillant en TCAD : Olivier, Pascal, Cristelle, Edgar, Guillaume et Thomas et Nicolas, avec qui nous avons pu tomber dans les pièges de l'ab initio. Merci aussi à Julien, Paul, Fanny et Sylvain de l'équipe implantation avec qui j'ai pu échanger. Merci aux différents doctorants et stagiaire de ST avec qui j'ai pu partager des discussion et des cafés. Merci à Richard, Yassine, merci à Antonin et Robin (que je recroise maintenant ma thèse terminée), merci à Bruno malgré tes pièges aux échecs et merci à Rémi et Jeremy pour nos comérages sur la vie des doctorants et autres sujets.
Merci à toutes les personnes avec qui j'ai pu travailler à travers des projets scientifiques. Merci aux membres de MAMASMIAS pour les passionnantes discussions. Je remercie aussi les différents acteurs du projet MUNDFAB avec qui j'ai pu interagir.

Merci aussi à toutes les personnes qui m'ont accompagné en dehors de cette thèse. Merci à mes amis d'enfance Lyonnais. Une description attentive de chaque personne nécéssiterait un travail de thèse tout entier. Je listerai donc plutôt des souvenirs que vous m'avez laissés durant ces 3 ans et je dresserai ensuite une liste très impersonnelle, en vous laissant le soin de relier votre nom à un ou plusieurs souvenirs. Merci donc pour ces fous rires, cette image de semi-conducteur, nos échanges Lidya, nos footing, les mariages, votre aptitude à être de mauvais joueurs pour n'importe quel jeux de société (même fictif), vos projets KO, vos expériences culinaires et capillaires, vos discussions trop sérieuses et trop longues à des heures trop tardives, nos "pestacles" qui m'ont permis de me motiver à m'inscrire aux théâtres, d'avoir élargi nos WE entre amis de deux cousins, de vos WE entre anciennes maîtrises (j'ai évidemment une préférence secrète pour une des deux). Merci donc à Puj, Anaïs, Arthur(s),Baptiste, Antoine(s) (non je ne vous appellerai pas vos surnoms), Bob, Camille, Claire, Clémence, Hélène, Cécile, Florence, Lucas, Mailys, Manon, Marion, Virgile, Paulines, Pierre, Pierric, Léa, Solène, Tim, Théo, Vianney.

Merci à mes amis d'école de Nancy. Thomas, je ne te remercie pas d'être un doctorant parfait, ça place la barre haut, mais je te remercie pour ton aide apportée en fin de thèse. Comme pour mes amis lyonnais, la description complète serait ardue, et je liste donc dans un premier temps des souvenirs auxquels certain et certaines pourront s'identifier. Merci donc pour ces WE/semaines à Paris, à Bayonne, en Corse, à Montpellier, pour être les plus mauvais gagnants que la Terre ait portée, merci pour ces victoires faciles au tchou Pilou (même sans Thomas Meyer), merci pour votre hospitalité, vos WE carte blanche, pour le surf, les foots, les brunchs, de répondre à mes questions sur chaque personne de la promo avec qui j'ai perdu contact, merci de me suivre dans des idées saugrenues, pour les rigolades, pour les bons repas, pour votre patience devant les trop fréquentes carbonara, pour avoir subi le mercato départaimant, de vous lever tôt en lendemain de soirée, de votre gentillesse, de votre écoute. Merci à Anaïs, Alice, Alexandre, Antoine, Corentin, Capucine, Florin, Léo, Mathieu, Mathilde, Margot, Nicolas, Sami, Sahar, Sylvain, Titi et Thomas.

J'avais peur en arrivant à Toulouse de ne pas connaître grand monde mais connaître Sylvain c'est aussitôt être intégré dans un groupe d'amis des plus sympathiques ! Merci à Alban, Gabrielle, Laurent, Madec, Jolante, Vincent, Clémence, Mathilde et Paul-Louis pour ces moments partagés autour d'une pizza et d'un jeu de société.

Merci à toutes les personnes avec qui j'ai vécu en colocation durant ces trois années et demies, leur patience et leur bonne humeur et leurs rigolades ont aussi rythmé cette thèse.

Je remercie enfin ma famille à qui je dois beaucoup plus qu'une thèse. Merci à ma soeur (et à Pierre) de m'avoir écouté, de m'avoir supporté, d'avoir été là dans les bons moments comme dans les moins bons pendant beaucoup plus que 3 ans. Merci à mes parents pour leur soutien et leur amour de tous les instants.

Multi-scale simulations investigation of defects in semiconductor devices

Pierre-Louis Julliard

Contents

Dark current center in imager devices

1

Contents

General introduction

Image sensors are an essential part of image acquisition. CMOS image sensors (CIS) have been commercialized since the early 2000s. Since their introduction on the market, the sector has been growing steadily until it reaches 21 billion dollars by 2021. The share of CIS in the semiconductor industry is also following a growing trend. CIS are used in many fields such as telephony, cameras, automotive, security, medical imaging ... Even though the cell phone market, the main area of use for CIS, is in slight decline, the diversity of use of CIS points to optimistic growth prospects. For example, CIS are increasingly used in the automotive industry to help driving. Three major players hold three quarters of the market share in 2021: Sony, Samsung and Omnivision (see Figure 1.1). STMicroelectronics plays also a role in the CIS market and has been the fourth major company for several years. These new uses of CIS require new specifications such as the reliability of the devices for which the driving and medical sectors have high requirements or the production cost so that the new devices must be financially attractive compared to the solutions offered by competing companies.

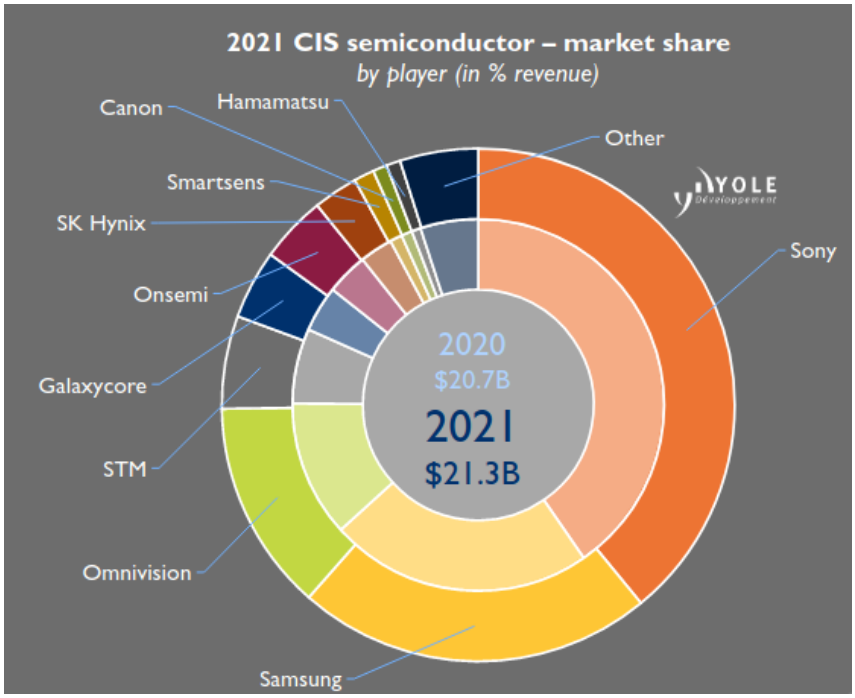

Figure 1.1: *CIS semiconductor market shared by players in 2022.*

1.1 Industrial context: dark current in image sensor

1.1.1 Image sensors working principle

The purpose of the image sensor is to convert a flow of light information into a flow of electrical information. This electrical information is then stored, processed, analyzed or reproduced in digital format depending on the application. An image sensor is composed of a matrix of several sub-sensors called pixels. The number of pixels present in the image sensor is directly related to the spatial resolution of the sensor, which then defines the quality of an image. The image acquisition process is described in Figure 1.2:

- First, the light is guided to the sensitive area of the pixel in a first step.

- The photons composing the light are then transformed into electric charge by the pixel.
- The created charges are collected towards the electrodes.
- The electrical signal is finally processed and analyzed.

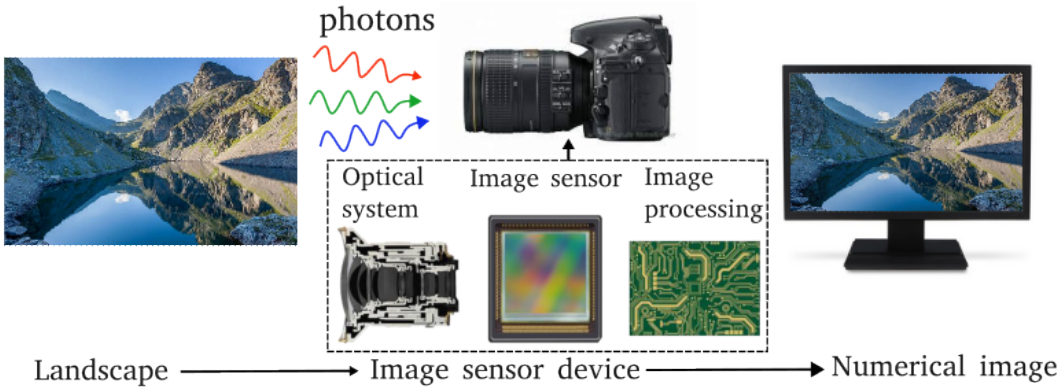

Figure 1.2: *Scheme of the functioning of an image sensor from the real image to the digital reconstitution.*

Among the various types of existing image sensors, it is interesting to mention the Single Photon Avalanche Photodiode (SPAD). This type of sensor can, as its name indicates it, convert a single photon arriving in the sensitive area into an electric signal.

SPADs are used for example to know the distance between two objects as can be seen in Figure 1.3. A light signal is sent to the outside toward an object and the signal reflected by the object whose distance to the source is to be known is detected by the photodiode. The time between the transmitted signal and the received signal allows to measure the distance between the source and the object, the speed of the signal being known. The detection of a single photon allows a faster acquisition of the image and is thus particularly adapted to a real-time image detection. This procedure is called TOF (Time of Flight). This type of sensor is very useful in facial recognition or autonomous driving applications where the distance between objects must be known with precision and is likely to vary rapidly over time.

1.1.2 Collection of charges

The routing of the light to the photosensitive areas is done with a system of lenses and mirrors. Before interacting with the pixel, the light passes through colored filters. This step allows the reconstruction of the image in color. Before reaching the photodiode, the light can also pass through the metal layers which are used to recover the electrical signal at the pixel output.
Upon reaching the photosensitive area made of silicon material, incident photons of sufficient energy are absorbed and converted into an electron-hole pair. Silicon is a semiconductor material with a bandgap of 1.12 eV at room temperature. When the energy is higher than this bandgap, an electron from the valence band can be excited to the conduction band, which is the origin of the electron-hole pair. The bandgap of silicon allows to convert photons whose wavelength is in the visible range into electron-hole pair. For other wavelengths such as infrared, the absorption is less efficient and other materials such as germanium are then used.
Once an electron-hole pair is created, it must be collected in a localized area of the pixel. A

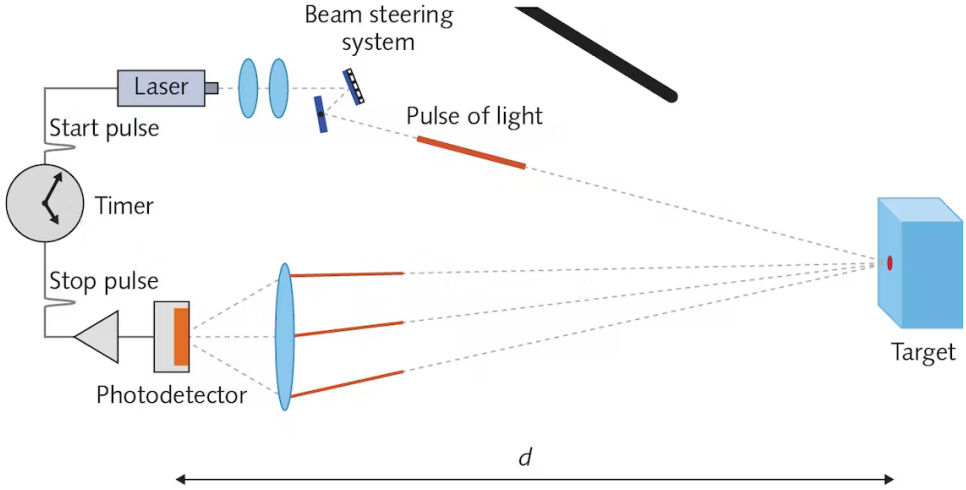

Figure 1.3: *Operating scheme of a SPAD for a TOF application.*

typical pixel is composed of a PN junction. One part of the silicon is doped with a p-type semiconductor (boron B) while the other is doped with n-type elements (phosphorus P, arsenic As). Unlike pure silicon where the chemical potential, also called Fermi level, is in the middle of the band gap, in the n-doped area the chemical potential is closer to the conduction band. This shift in chemical potential results in a greater concentration of electrons than holes. The opposite phenomenon occurs in the p-type region where the chemical potential is closer to the valence band and the concentration of holes is higher than that of electrons. At the interface between the n-doped zone and the p-doped zone, the chemical potential is balanced (see Figure 1.4. This equilibrium can also be considered as the diffusion of the majority electrons in the n-zone towards the p-zone and the diffusion of the holes from the p-zone towards the n-zone. The electrons of the n zone diffusing into the p-zone recombine with the majority holes in this zone and conversely for the holes diffusing from the p-zone to the n zone. These recombinations allow the alignment of the chemical potential and leave two zones where the charges of the dopants atoms are no more compensated by the presence of electrons and holes. The region near the interface of the n-doped area is thus positively charged whereas the p-type region at the interface is negatively charged. This charged region is called space charge region (SCR) and results in a potential barrier created by the negative area near the positive area. When electrons are created in the SCR as a result of the absorption of a photon, they are repelled into the n-doped zone of the junction by the voltage present in the SCR. This voltage has the opposite effect on the holes generated in the SCR: they are pushed back to the p side of the PN junction. The photo-generated electrons thus accumulate in the n-doped part of the junction.

In a SPAD, a voltage is applied to strongly increase the reverse voltage in the SCR. SPADs operate in a so-called Geiger mode where the reverse bias voltage is higher than the break-down voltage as show in Figure 1.5. During the the absorption of an incident photon, the charge carrier thus created will be strongly accelerated by this voltage. Their kinetic energy is then such as it can tear electrons to the silicon atoms on their trajectories. This phenomenon is known as impact ionization. These carriers, once pulled out, are also strongly accelerated by the voltage and can therefore also tear off electrons from other silicon atoms which, in turn, can generate other carriers. Through this charge carrier multiplication effect, a single electron-hole pair can generate enough current to be collected in the electrodes.

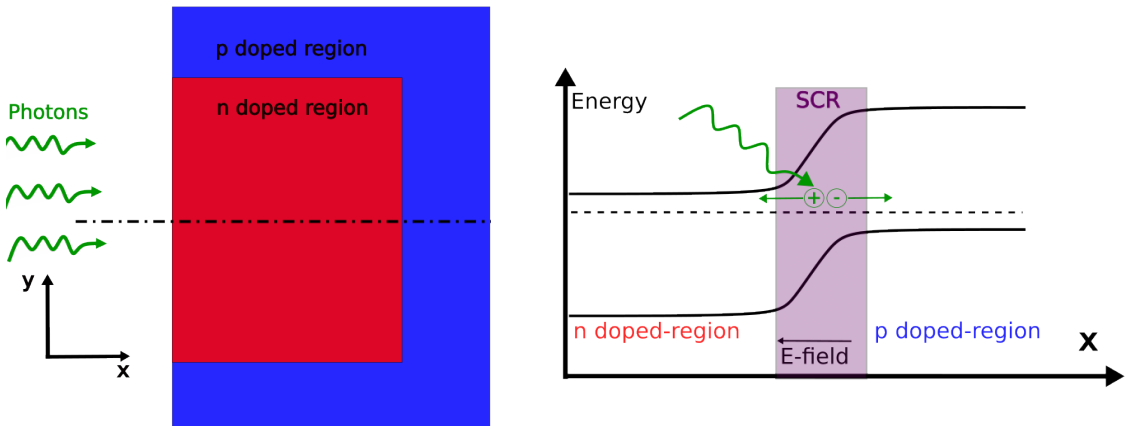

Figure 1.4: *Structure of a pixel and its Fermi level along dashed line.*

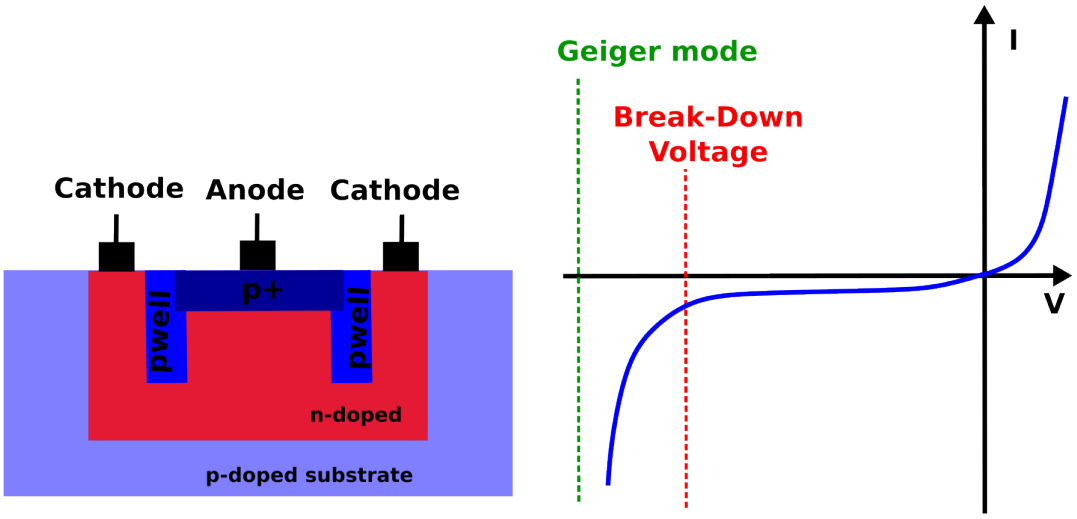

Figure 1.5: *(Left) Architecture of a SPAD pixel - (Right) Schematic of the functioning of a SPAD as a function of the applied voltage bias.*

1.1.3 Reading of charges

Once the charges are accumulated in a specific location, the device must be able to transfer them into electrical information. This transfer can be done in different ways. One way is to connect the n-zone of the junction to the gate of a readout transistor. The charges accumulated in the n-area due to photon absorption are converted into voltage. This voltage applied to the gate of the readout transistor will transfer the charges of the photodiode in an electric signal. Once the electric signal is generated, another transistor allows the reset of the photodiode and the evacuation of the charges.
Based on this method of charge reading, called 3T, the charge reading in the photodiode is done with a so-called 4T architecture in Figure 1.6. The 4T architecture introduces an additional transistor, called a transfer transistor, to separate where the charges are generated and where the charges are converted to voltage. In particular, this architecture avoids reset noise, also called kTC noise [1], following a reset of the read node. To avoid this noise, two measurements are made: one after the reset and the other after the transfer of the charges. The subtraction of these two measurements makes it possible to cancel the kTC noise [2].

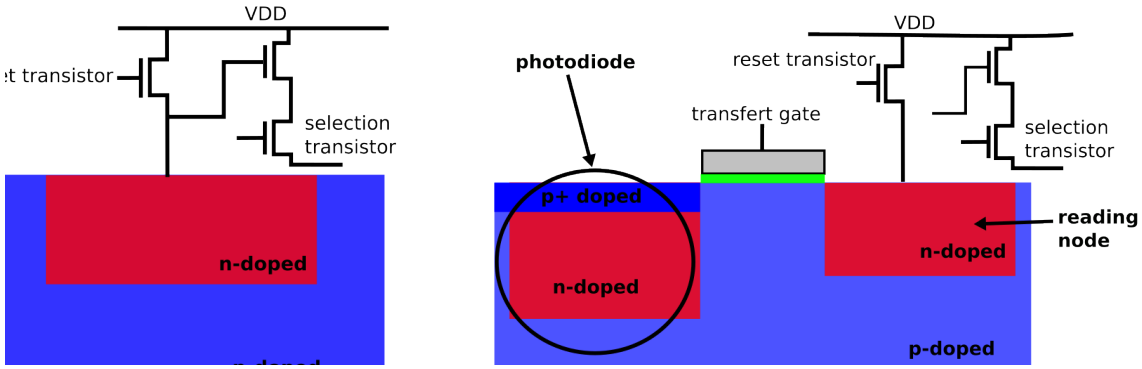

Figure 1.6: *(Left) Architecture of a pixel with a photodiode of type 3T - (Right) architecture of a pixel with a photodiode of type 4T.*

In SPADs, the charges reading is not done after a characteristic time but as soon as an avalanche is generated (Figure 1.7). Each avalanche generation gives access to information such as the source-object distance of Time of Fly (TOF) applications. It is also necessary to introduce a circuit allowing the quenching of the carrier avalanche. Indeed, if the avalanche is not stopped, it can damage the device.

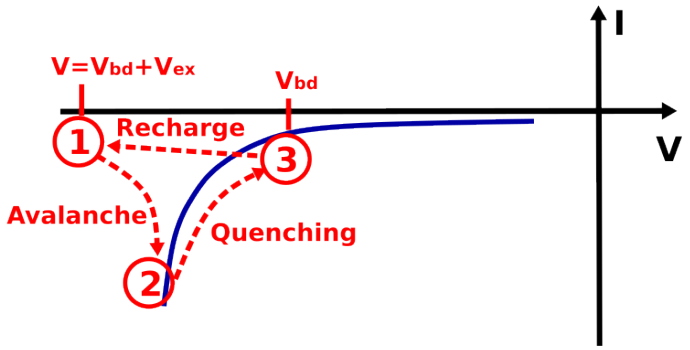

Figure 1.7: *Cycle of operation of a SPAD type pixel during the detection of a photon.*

1.1.4 Main figures of merit in imager devices

The quality and reliability of a pixel includes several aspects. One of the most important parameters to optimize is the quantum efficiency. This is the number of electrons generated per incident photon. This quantity is particularly important in SPADs where we want to get as close as possible to a quantum efficiency of 1. To be competitive, a pixel must also minimize certain negative effects. Among these effects, a pixel must for example avoid that an incident electron can excite a neighboring pixel. This effect, called cross-talk, is show in Figure 1.8 and is usually avoided by inserting trenches between the pixels.

One important aspects is the surface of the photosensitive area of the pixel in relation to its total surface. The pixel is integrated into the readout systems and separated by isolation trenches, as mentioned above. The larger the share of the photosensitive area compared to the other parts of the pixel, the better the charge collection. This aspect is summarized in the fill-factor.
The temporal dimension of image sensors is also important. One of the effects that can deteriorate the quality of a sensor over time is lag. Some collected charges may indeed be transferred

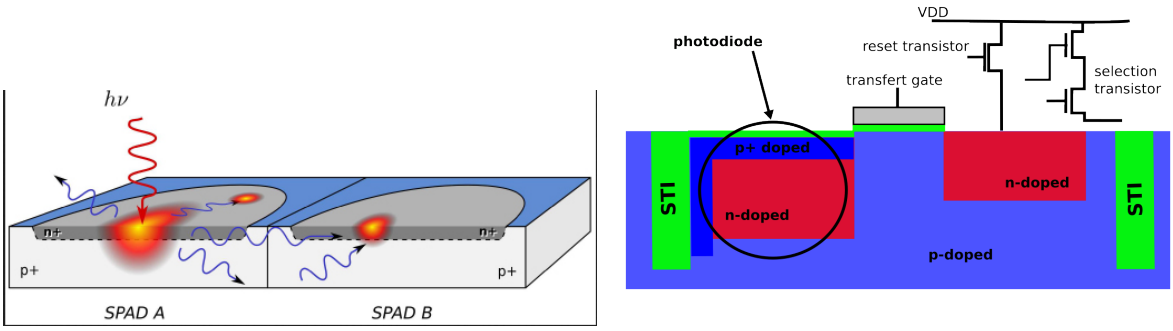

Figure 1.8: *(Left) Cross-talk between 2 pixels from [3] - (Right) Scheme of a 4T photodiode with STI to avoid cross-talk phenomena.*

in a time-shifted manner or never be transformed into a gate voltage for the readout transistor. This type of problem can be caused for example in pinched photodiodes in the presence of a pocket of potential in the doping profile which traps the charge. The potential pocket prevents electrons from passing to the readout node.
In the case of SPADs, an important parameter to maximize is the probability that an incident photon will lead to an avalanche. In applications where SPADs are used to measure distances, the time response is also very important. The time between two avalanche phenomena, so-called jitter, must thus be optimized.
Another parameter that can affect the quality of the pixel is the dark current. It corresponds to an electrical signal transmitted in the absence of light reaching the pixel. At low currents, the current increases the operating voltage thresholds of the pixel. At high currents, this phenomenon creates a white pixel which degrades the final quality of the image. The dark current is caused by the unintended creation of a charge carrier in the sensor. The appearance of these carriers is related to different types of defects that will be detailed in section 1.2. These defects introduce energy levels in the band gap that favor the appearance of these carriers. In a SPAD, the creation of a carrier can have other undesirable effects. During an avalanche, an electron or a hole can be trapped by a defect. If the carrier is then released by the defect, it can then cause an avalanche and thus a signal at a random time. The generation of these random signals is called afterpulsing. It should be noted that the location of defects that trap a charge carrier or release it in the sensor is of great importance. A charge carrier located in the SCR will be accelerated and will have a significant probability to form an avalanche while a carrier located in areas of lower potential is less likely to trigger an avalanche.

The problems addressed in this thesis concern mainly the figures of merit of the dark current and the trapping of carriers. The simulations and characterizations carried out in this thesis are indeed interested in the impact of the manufacturing process in the concentration of defects which can be at the origin of dark current. The following section aims to briefly explain the theory behind the dark current before detailing the defects associated to dark current in section 1.2.

1.1.5 Random Telegraph Noise and dark current in image sensors

Dark current is a primary figure of merit of image sensor devices, therefore it is essential to understand its origins. The dark current is mainly explained by the Stockley-Read-Hall (SRH) theory [4]. The dark current is caused by traps that capture electrons or holes and can then

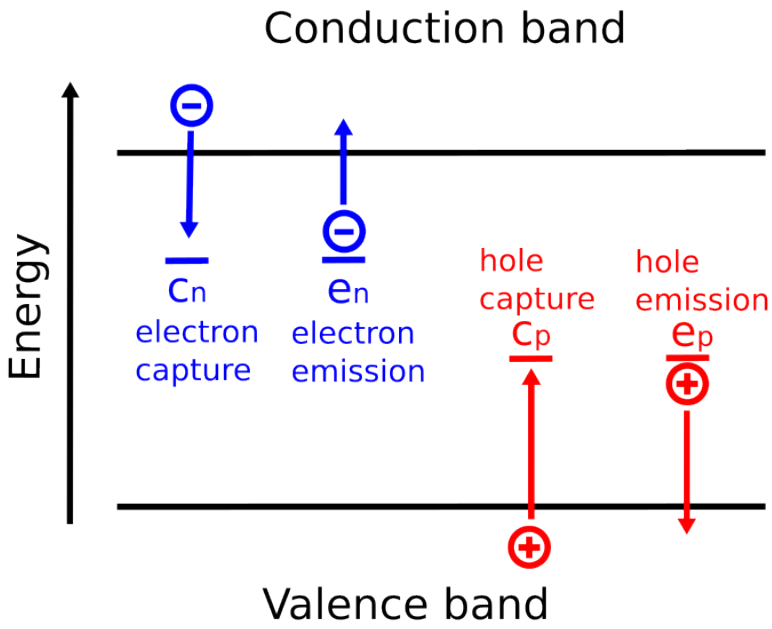

Figure 1.9: *Capture and emission of holes and electrons by a trap in the silicon gap.*

emit them. It is possible to model these traps by the knowledge of the energy levels in the bandgap of silicon. In the SRH theory, the emission of charge carriers from the traps is done through phonons. It is possible to estimate the unwanted current resulting from the emission of the charge carrier from these traps. The current per unit volume generated by a trap of energy level E_t is given by the following formula [5]:

$$U(E_t) = \sigma_n \sigma_p D_{defect}(E_t) v_{th} \frac{np - n_i^2}{\sigma_n (n + n_i e^{\frac{E_t - E_i}{kT}}) + \sigma_p (p + n_i e^{-\frac{E_t - E_i}{kT}})} \tag{1.1}$$

σ_n and σ_p are the electron and hole capture cross sections of energy E_t, D_{defect} is the defect density of energy E_t, n and p the electron and hole density, n_i the intrinsic density and E_i the Fermi level of silicon. The level E_i is not the same throughout the material and thus the impact of a trap of energy level E_t will have different effect depending on its position in a device.
In the n-doped regions the expression can be simplified to:

$$U = \frac{n_c(x) p_v(x) - n_i^2}{\tau_p^0 N_{dopants}} \tag{1.2}$$

In a similar way, in the p-doped regions the current can be written as:

$$U = \frac{n_c(x) p_v(x) - n_i^2}{\tau_n^0 N_{dopants}} \tag{1.3}$$

In the space charge zone, the term np can be neglected and the recombination rate per unit volume is then written:

$$U(E_t) = \frac{-n_i^2}{\sigma_n^0 e^{\frac{E_t - E_i}{kT}} + \sigma_p^0 e^{-\frac{E_t - E_i}{kT}}} \tag{1.4}$$

For an energy level located at the midgap this rate simplifies to:

$$U(E_t) = \frac{-n_i}{\sigma_n^0 e + \sigma_p^0} \tag{1.5}$$

Assuming that the electron capture cross-section is equal to that of the holes, the recombination rate is maximum for an energy level located at midgap.

1.2 Defects associated to dark current source

1.2.1 Point defects

The smallest defects that can be found in silicon are point defects. This name covers several different types of defects:

- The vacancies (V): they correspond to a missing silicon atom in the crystal lattice. The void created by the missing atom forces the neighboring silicon atoms to rearrange themselves in space. The neighboring atoms can relax into different structures. A vacancy can be charged and the most stable structure for each charge state depends on the charge. The different vacancy configurations are shown in Figure 1.10. The charged levels of vacancies in silicon were obtained by EPR (Electronic Paramagnetic Resonance) in [6]. The introduction of interstitials (introduced hereafter) and vacancies in the wafer will be detailed in section 1.3. It can be noted here that the generation of these defects is systematic during the manufacturing processes. They appear in particular during implantation and nitridation. In addition to their formation during the various steps of the process, the vacancies naturally have a non-zero concentration for a non-zero temperature. The concentration of vacancies at equilibrium follows the following law:

$$C(V) = \theta S_i \exp\left\{\frac{H_f}{kT}\right\} \tag{1.6}$$

  At room temperature, the resulting concentration of vacancies is negligible. Even though they introduce energy levels into the band gap, they are not the main candidates for the dark current. They are indeed very mobile in silicon and an excess vacancies concentration tends to diffuse before recombining at the interfaces.

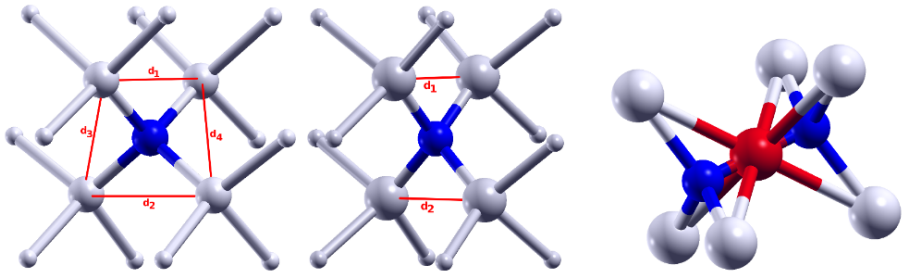

Figure 1.10: *Different vacancies configurations. Blue balls indicate a missing atom and red balls an additional atom. From left to right :* V_{Td}^{2+}, V_{D2d}^{0} *and* V_{Cs}^{-2} *vacancy configurations (pictures from M3 Team in LAAS-CNRS, not published)*

- Interstitials (I): they correspond to a silicon atom in excess in the crystal lattice. They can adopt several forms as shown by [7]. As in the case of vacancies, the interstitials can be charged and the stability of the different structures also depends on this charge state. As in the vacancy case, the the most stable interstitial structure of the interstitial depends on its charge state. The interstitials are introduced into the silicon after ion implantation or oxidation processes. Interstitials are also present at equilibrium in silicon for a non-zero temperature.

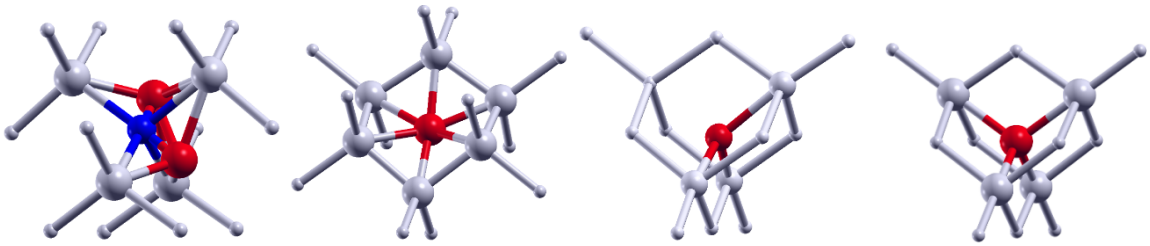

Figure 1.11: *Different interstitials configurations. Blue balls indicate a missing atom and red balls an additional atom. From left to right :* I^{0}_{dumbel}, I^{0}_{hex},I^{1}_{dhex} *and* I^{+2}_{tet} *interstitial configurations. (pictures from M3 Team in LAAS-CNRS, not published)*

- Doping atoms: they are voluntarily introduced in the material to form the n-doped and p-doped regions. If they have the right structure in the material, replacing a silicon atom in the lattice, the doping atoms are not a source of dark current. They contribute in an essential way to the good functioning of the device. Nevertheless, the dopant atoms can sometimes not be in a substitutional site or can be associates with another point defect. In this case, they do not contribute to the functioning of the sensor but they can be at the origin of the dark current. The E-center is a well-known example. It is an n-type dopant (arsenic, phosphorus, antimony Sb) associated with a vacancy. This defect causes the appearance of an acceptor energy level in the bandgap of silicon close to Ec-0.44 eV [8][9]. In the case of phosphorus, a donor level was also found at Ev+0.27 eV [10].

- Contaminants: Contrary to the doping atoms, they are not voluntarily introduced into the material and do not play a role in the operation of the device. These atoms come from defective processes. Their concentration must be as low as possible. Among the contaminants, the transition metals can be at the origin of energy levels in the bandgap. The experimental measurements concerning Fe and Ti have shown energy levels close to the midgap [11]. The energy levels induced by the contaminants depend again on the structure they take in the silicon. Ti is at the origin of levels in the bandgap when it is in interstitial site while Au creates a level in the bandgap in substitutional site. Several energy levels can be associated with the same contaminant. DLTS (Deep Level Transient Spectroscopy) measurements on Ti show a double donor level at 0.2 eV and a single donor level at 0.22 eV [12][13].

It is interesting to note that the role of certain impurities in silicon is sometimes ambiguous. This is the case of oxygen. The presence of oxygen allows for a better stress state in the material and is thus desired. However, oxygen can also form clusters with energy levels in the bandgap and be a possible cause of dark current.
The impact of point defects on dark current is not limited to being possible sites for charge trapping. They can also group together to form larger clusters, which can also act as traps for electrons and holes.

1.2.2 Vacancies, interstitial and impurity clusters

Point defects can agglomerate to form clusters during the different process steps. These clusters are also other candidates to explain the dark current in photodiodes. A cluster can contain several atoms of the same impurity, atoms of different impurities, a mixture of impurities and vacancies or interstitials or only vacancies and interstitials. The clusters discussed here are small (< 2 nm) and therefore cannot be directly observed in TEM (Transmission electron microscopy). In the following, small clusters composed only of interstitials will be called SMICs (for Small

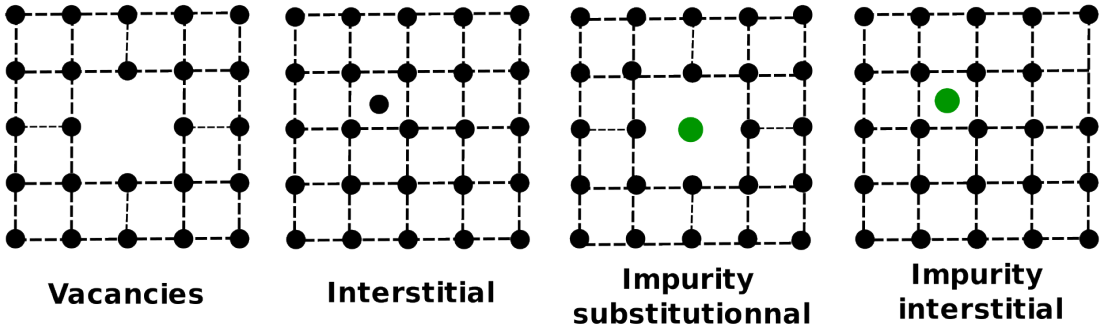

Figure 1.12: *Diagram of the different types of point defects in a silicon lattice.*

Interstitial Clusters). As in the case of point defects, the experimental evidence is often indirect: for clusters containing impurities, the stoichiometry of the cluster can be obtained experimentally by looking at the evolution of a signal as a function of the concentration of introduced impurity. For clusters containing only interstitials and vacancies, the characterization is more complicated. The evolution of the signals according to the process conditions used can help to estimate a certain size of the defect [14].

1.2.3 311 defects

Once interstitial clusters reach a larger size, their structure tends to be spatially organized. The defects {311} consist of chains of di-interstitials elongated along a direction <110>. These chains are organized into {311}-like planes in space. The {311} defects have been associated with leakage current degradation in PN junctions. DLTS studies have shown that these defects introduce energy levels into the bandgap. In [15], these defects were observed in experiments combining TEM and DLTS. Depending on the process used, {311} defects were observed or not on the TEM images. The presence of {311} defects was correlated with the appearance of a DLTS signal at 0.48 eV. A similar study was conducted in [16] and in this case the process conditions leading to the observation of {311} in TEM images is associated with a DLTS peak at 0.54 eV. These energy levels located near the midgap make it a potential source of dark current.

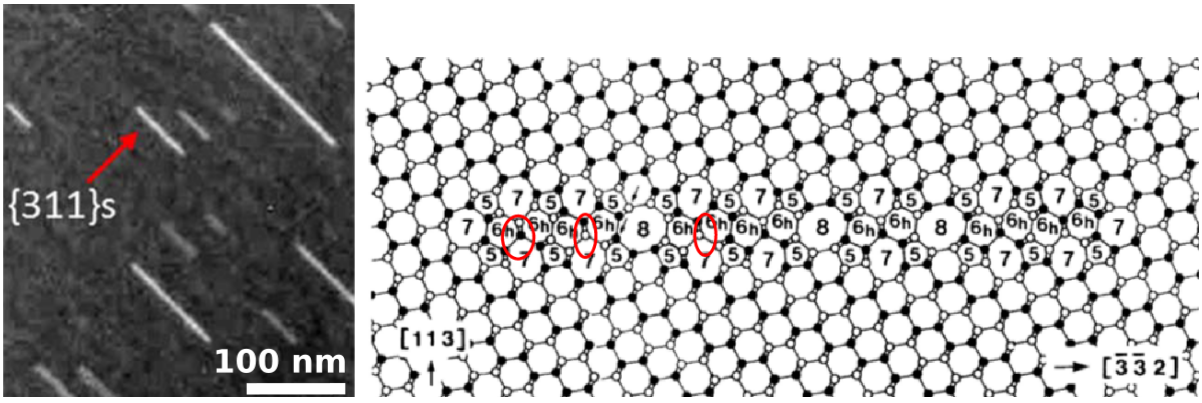

Figure 1.13: *(Left) TEM images of 311 defects from [17] (Right) Atomic structure of defects 311 from [18].*

1.2.4 Dislocation Loops

Dislocation loops (DLs) are an extended defect composed of interstitials. Dislocations are linear defects also studied in the mechanical behavior of materials, especially to understand the shear strength of a given material. The interstitials present in the loop fit between two planes of the crystal. There are two types of dislocation loops: faulted and perfect. Faulted dislocation loops have a circular shape while perfect dislocation loops have a more elongated shape [19]. These two types of loops are distinguished by their different Burgers vectors, which defines a dislocation. In the case of a perfect dislocation loop, the Burgers vector belongs to the plane of the dislocation, unlike the case of faulted dislocations.
Dislocation loops have also been linked to the degradation of the electronic properties of the devices. In the work of [20], the DLs were associated with an acceptor level and a donor level in the gap at Ev+0.25 eV and Ec-0.38 eV respectively. DLs were correlated with an increase in dark current [21]. DLs can also interact with impurities present in silicon. In the case where impurities are trapped in a dislocation loop, the DLs are said to be "decorated" [22]. The "decorated" DLs can have different electrical properties than those of DLs composed only of silicon atoms [23].
The size of a DL depends on the number of interstitials trapped in the DLs and can vary over several orders of magnitude. For a small number of interstitials, the dislocation loops are unstable but for thousands interstitials, the DLs configuration allows to reduce the energy. If there are enough excess interstitials or in the case of plastic deformations in the material, loops of about ten microns can be observed.

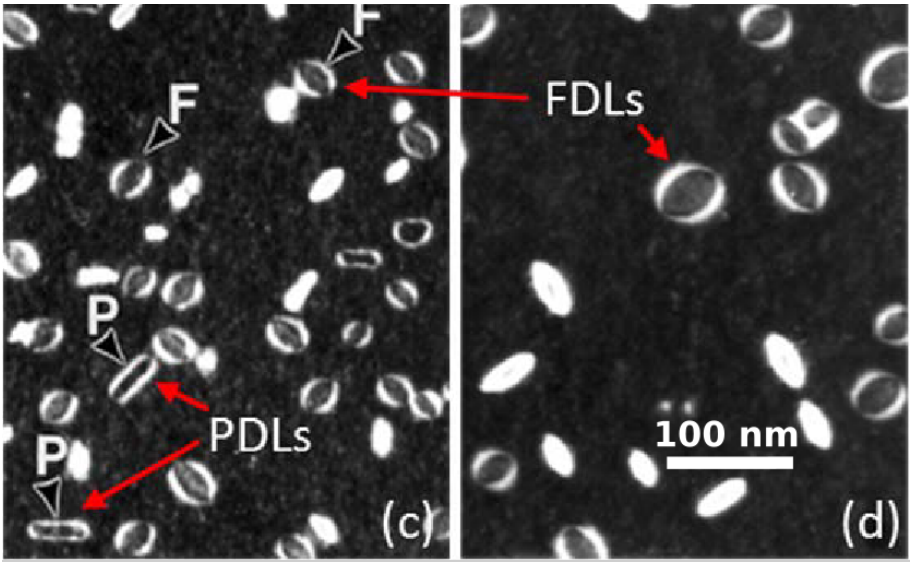

Figure 1.14: *TEM image of perfect and faulted dislocation loops in silicon [24].*

1.2.5 Interfaces

The interfaces of silicon with oxides also generate traps for charge carriers. The contribution of the interfaces to the dark current is higher than that of the defects in the bulk of the silicon. Several interfaces exist in crystalline silicon such as the surface-interface of a photodiode and the interfaces with the isolation trenches for instance. SiO_2 is generally in amorphous form. The differences between the crystalline structure of silicon and amorphous SiO_2 leads to the formation of dangling bonds of silicon atoms on the surface. The dangling bonds of silicon then generate energy levels in the bandgap. This interface is not studied in this thesis.

1.3 Formation of defects during manufacturing processes

1.3.1 Ion implantation process

As mentioned in the previous section, even if interstitials and vacancies are present at thermal equilibrium, their concentration at room temperature (RT) is too low to degrade the image sensor properties. The excess concentrations of interstitials or vacancies to form the defects mentioned above are therefore generated by the manufacturing processes of the materials, in particular during the ion implantation. Ion implantation steps are essential in the fabrication of image sensors to form the n and p regions in the device. The ions, which correspond to the dopant atoms, are accelerated with an electric field from a source to the surface of the silicon. They then penetrate the silicon where they are slowed down by collisions with the silicon atoms [25] and electronic interactions. Several parameters influence the profile of the implanted atoms such as the energy, the dose but also the mass of the implanted atom. For instance, high energy implantations produce more spread out doping profiles. The mass of the implanted ion also influences the doping profile: light ions produce a more extensive profile while heavy ions generate shallower profiles for the same implantation energy [26].
In order to obtain shallow dopant profiles, the beam is not always perpendicular to the wafer. Collisions between the ions and the crystal lattice are more numerous if the trajectory of the incident ion is perpendicular to a dense plane of the lattice. Indeed, the atomic plane (100) is not the densest plane of silicon. The collision number for a beam perpendicular to the (100) plane is not maximum and the ions are slowed down slightly, this is a called a channeling effect. An angle called tilt is therefore often applied in order to have denser planes and thus increase collisions with the crystal lattice leading to shallower profiles.

1.3.2 Ion implantation induced defects

During collisions of atoms with the lattice, if the energy of the incident ion exceeds a threshold, the Si atom is expelled from its crystalline site, thus generating an interstitial atom. Where the atom has been expelled, a vacancy is created. This interstitial and this vacancy form the so-called Frenkel pair. This interstitial can in turn produce a collision cascade [25] with other atoms of the crystal lattice: if the energy of the interstitial exceeds a threshold, it generates another interstitial atom which in turn can generate interstitials during these collisions. At the end of these cascades, clusters containing interstitials and vacancies are formed. This type of cluster is called in the rest of the thesis "amorphous pocket", noted AP.
An interstitial and a vacancy present in an amorphous pocket can recombine, thus decreasing the size of the amorphous pocket. This type of recombination occurs at several times during annealing. In the few ns that follow the collisions of the dopant atom with the silicon atoms, the wafer temperature is locally very high, which generates a large number of recombinations. The dopant atoms are generally implanted at a certain frequency, named the dose rate. Between two implantations of a dopant atom at the same place of the wafer, other I-V recombinations occur in the amorphous pockets.
The size and energy of the implanted ions are parameters that influence the size of the formed amorphous pockets: during a high energy implantation, the dopant atom displaces more crystalline silicon atoms, which lead to larger amorphous pockets. Heavier ions also tend to form larger amorphous pockets [27].

The amorphous pockets formed after an ion implantation also depend on the implanted dose. The higher the dose, the more likely the amorphous pockets formed by the successively implanted ions are to overlap and form even larger amorphous pockets.

When the damage created by the implantations exceeds a certain threshold, the interstitials and vacancies are so numerous that the silicon loses its crystalline properties and becomes amorphous. The mechanisms leading to the amorphization of the material are different depending on the implanted ion. For heavy ions having sufficient energy, the collisions of the dopants with the crystal lattice result in very large amorphous pockets which can be considered as amorphous zones in themselves. When these amorphous zones overlap, an amorphous layer is created. For light ions, the amorphization mechanism seems different. Small amorphous pockets are generated following the collisions generated by the implantation, but the silicon remains mainly in a crystalline state. These amorphous pockets accumulate without all overlapping, and above a certain threshold the material loses its crystalline properties.
The creation of an amorphous layer during the implantation process has an effect on the distribution of the as-implanted dopants. The amorphous region reduces the channelling effects and the dopants diffuse less deeply into the wafer. This difference in the as-implanted state of the material is likely to be observed after annealing processes.

1.3.3 Annealing process and thermal budget

Annealing processes are essential when manufacturing of electronic devices. In order to be able to control the charge carriers introduced by the dopant atoms, dopant atoms must be in substitutional sites. Indeed, after implantation, the dopant atoms are not necessarily found in substitutional sites, as expected. Many of them can be trapped in clusters or interstitial sites. In addition, as said, the ion implantation can produce amorphous zones or pockets, which would also degrade the electronic properties, that one needs to dissolve. These are the main reason for thermal annealing.
One of the difficulties of annealing lies in the fact that the temperature does not only place the dopants in a substitutional site but also makes them diffuse deep into the wafer. During an annealing step, the dopant atoms can associate with the point defects created during the implant to form dopant-defect pairs. The diffusion associated with a dopant atom in a substitutional site is very low, being associated with an atomic mechanism having a very high activation energy. In the case of an association with a point defect, the usual dopants generally diffuse much more easily. So-called "kick-out" mechanisms can explain this increase in diffusion [28]. Depending on the nature of the dopant, the part of the diffusion associated with the dopant-interstitial or dopant-vacancy pairs is different. Boron and phosphorus are associated with mechanisms involving interstitials [29][30] while antimony diffuses with dopant-vacancy pairs [31]. The diffusion of dopants is generally unwanted in the fabrication of smaller and smaller devices. In order to activate the dopants while limiting their diffusion, high temperature annealing (> 1000°C) and short duration annealing (from seconds to minutes) are used. In this context the temperature ramps are also important and must be taken into account.
Activation annealing is not the only process that can generate a temperature increase in the material, and therefore not the only mechanism that can thermally activate diffusion or defect formation mechanisms. Other process steps, such as oxide deposition or epitaxy, can heat up the wafer. The order of the different process steps is important and a complex issue. Many constraints must be taken into account to optimize the order of the various steps and it can happen that the activation annealing is performed after other steps heating the wafer.

1.3.4 Defects evolution during annealing process

The evolution of defects in the annealing stages following the ion implantation is different depending on whether an amorphous zone has been created or not.
For non-amorphizing implantations, the interstitials and vacancies in the amorphous pockets generally recombine at the beginning of the annealing. It is important to note that the number of interstitials is not necessarily equal to the number of vacancies in an amorphous pocket. Con-

sequently, these recombinations leave clusters of defects in the wafer which are composed solely of vacancies or interstitials in the wafer. The spatial distribution of interstitials and vacancies is generally not the same over the depth of the wafer. Since the interstitials are ejected from their crystalline site during implantation by atoms coming from the surface, the generation of an I-V pair creates a vacancy at the location of the ejected atom and an interstitial that is ejected deeper into the wafer. This mechanism leaves more vacancies close to the surface and more interstitials deep in the wafer.
The recombinations of the amorphous pockets during the beginning of the annealing can also generate mono-vacancies or mono-interstitials in the wafer (if there is one more or less interstitial than vacancies in an amorphous pocket). These interstitials and vacancies diffuse very easily into the wafer as mentioned earlier. They can recombine at the surface or interact with other defects (recombination of a point defect present in an amorphous pocket or agglomeration of a cluster of interstitial, vacancy).

The +1 model: In the case of a non-amorphizing implantation, a simple method to estimate the excess interstitial profile consists in considering the so-called +1 model [32] and is presented in Figure 1.15. Since a number n of interstitials have been introduced during the implantation and are placed on a substitutional site during the annealing, this means that the same number n of silicon atoms are displaced from their crystalline site and are placed in the interstitial position. To estimate the total density of excess interstitials during annealing, it is possible to integrate the dopant profile by depth:

$$\phi_{interstitials} = \int_{z=0}^{z=\infty} C_{dopant}(z)\, dz \tag{1.7}$$

This model has limitations and for heavy dopant atoms, a correction factor is needed. Heavy dopants generate more interstitials than the number of implanted atoms and are modeled by a +n model.
The distance to the surface of the formed defects is also of great importance for their evolution. In the case of a non-amorphous implantation, the maximum of excess interstitials, and therefore of defects, is located close to the depth where a maximum of dopant atoms has been implanted. This maximum corresponds to the mean project range and will be abbreviated Rp in the following. As can be seen in Figure 1.15, the resulting excess interstitial profile is therefore similar to the doping profile, slightly shifted in depth.

Model in the case an amorphizing implant: If a region of the silicon is amorphous, applying an annealing process can produce a solid phase epitaxial regrowth (SPER) in that region [33]. This effect is characterized by the disappearance of defects in the amorphous region once annealed, leaving a perfect crystalline silicon. The SPER occurs at annealing temperatures up to 600 °C and is commonly used in industry.

The wafers which comprise an amorphous layer before annealing are not totally free from defects after such annealing process. Near the crystalline-amorphous interface (A/C), part of the wafer is damaged, thus constituting a potential zone for growth of subsequent defects. There is a similar model to the +1 model for amorphizing implantations (see Figure). Unlike the non-amorphizing implantation, the excess interstitial profile differs from the dopant profile.

As shown in the bottom of Figure 1.15, after annealing, there is no more interstitials in the amorphized area (in grey on the figure). Deeper in the material where no amorphization occurred (and no SPER), the material is still damaged after the annealing. Recombinations can therefore take place between interstitials and vacancies. As shown in the bottom-left of Figure 1.15,

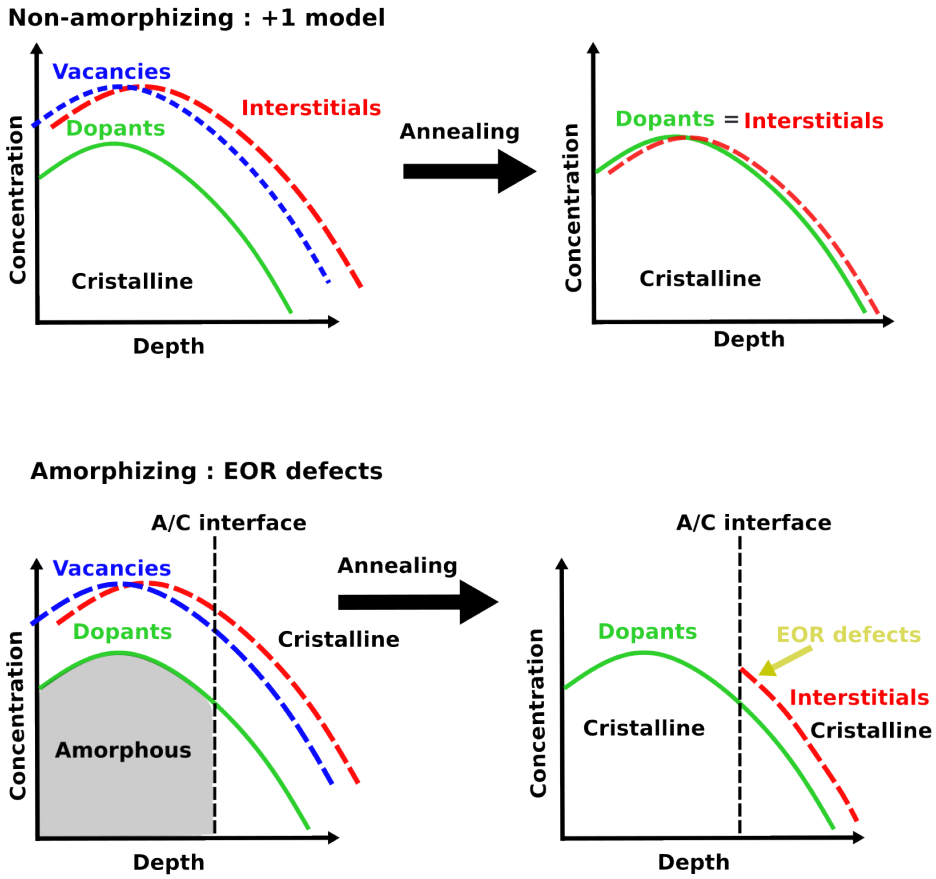

Figure 1.15: *Diagram of the different existing models to estimate the number of excess interstitials after amorphizing and non-amorphizing implantation.*

the vacancy and interstitial profiles are slightly shifted as-implanted. As already mentioned the interstitials are located deeper than the vacancies along the depth. After the I-V recombinations in the crystalline zone deeper than the amorphous layer, a significant number of interstitials remain which have not been able to recombine with vacancies (the amorphous layer being defect-free). The peak of this excess interstitial concentration is then located at the location of the A/C interface generated during the implantation process. The A/C interface is generally a place where the growth of extended defects is favored after annealing. The defects appearing at this interface are called End-of-Range (EOR) defects. In the case of a buried amorphous layer, there are two A/C interfaces and therefore two nucleation sites for EOR defects. An estimate of the density of excess interstitials is then given by the following formula:

$$\phi_{interstitials} = \int_{z=AC}^{z=\infty} C_{Interstitial} - C_{Vacancies}(z)\, dz \tag{1.8}$$

In both amorphizing or non-amorphizing implantations, the implantations generate excess interstitials during annealing, which can evolve into different kinds of defects. Interstitial or vacancy clusters have several possibilities of evolution during annealing. They can emit interstitials that will behave like free interstitials, recombining at the surface or interacting with clusters in the wafer. Interstitial clusters can also capture interstitials (from interstitials emitted by other clusters) and evolve towards more stable forms of defects, such as a {311} type defects. It can be observed in Figure 1.16 that the {311} defects have a formation energy per interstitial which decreases with the number of interstitials in the defect. The more interstitials there are in a

defect {311}, the more difficult it is to remove an interstitial.

The formation energy per interstitial of a {311} defect is generally lower than the formation energy of a small interstitial cluster [34]. However, there are some very stable sizes of interstitial clusters, which we will come back to in this thesis. An interstitial trapped in a {311} defect is therefore less likely to be emitted from this {311} than if it was trapped in a SMIC. When a {311} reaches a certain size, the structure becomes more favorable in the form of a loop of dislocation. The {311} can therefore evolve into DLs if it captures enough interstitial. The interstitial formation energy of DLs also decreases when their size increases as depicted in figure 1.16. As for the 311 defects, the more interstitial a DL contains, the more activation energy is needed to emit an interstitial from this loop.

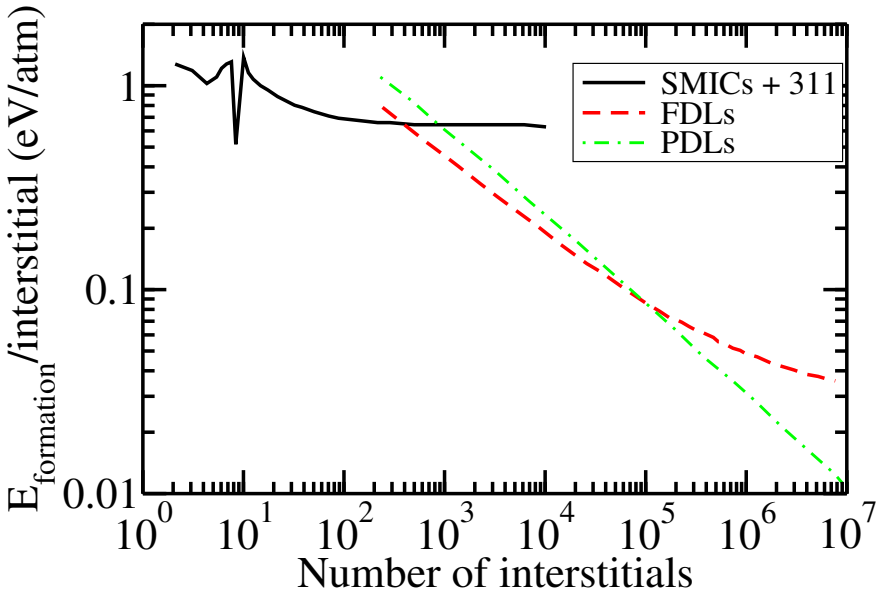

Figure 1.16: *Interstitial formation energies for different types of defects as a function of the number of interstitials in the defect [35][36][24]*

The increase in the stability of defect types as their size increases leads to a growth mechanism known as Ostwald ripening and is depicted in Figure 1.17. Since small interstitial defects emit more interstitial than larger ones, a gradient of interstitial is created between the smaller clusters and the nearest extended clusters. The interstitials emitted from the smaller clusters agglomerate around the larger defects, in which they are more stable. The size of an extended defect also increases its interstitial capture cross-section, which accentuates this phenomenon. The interstitials captured by a larger defect make the defect more stable, increasing the gradient between small and large clusters. More and more interstitials are captured by the larger defects and the small interstitial clusters disappear in favor of the larger and more stable defects. The interstitials are thus trapped in more and more extended defects and the distance between these defects increases as the smaller ones disappear. At some point, if the temperature and annealing time are high enough, the distance between the various extended defects is sufficiently large so that the interstitial capture site closest from a defect is the surface. The surface acts as a perfect sink, not re-emitting interstitials.

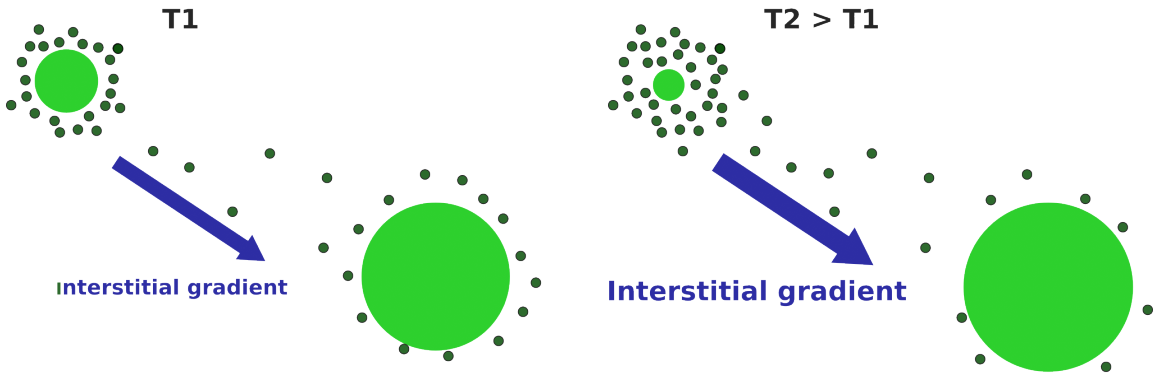

Figure 1.17: *Ostwald maturation model leading to the formation of more and more extended and fewer defects during annealing.*

1.4 Defects studied in this thesis work: the specific cases of BO_2 clusters and heated implantations simulations

1.4.1 Study 1 - BO_2 clusters in photovoltaic devices

Among all the cited candidates which could be at the origin of the dark current, this thesis will focus in part on an impurity cluster, namely the BO_2. In the photovoltaic industry, wafers containing both boron and oxygen have shown a degradation of performance when exposed to light [37]. During exposure to light, the quasi-steady-state photo-conductance (QSS-PC) experiments have shown that the concentration of minority carriers decreased over time (Figure 1.19). This phenomenon of decrease of minority charge carriers under illumination is called Light-Induced Degradation (LID) in the literature [38]. In order to study the stoichiometry of a possible defect involved in this phenomenon, QSS-PC experiments were performed by varying the boron and oxygen concentration in the wafers [39]. The results are presented in Figure 1.18 show that the LID phenomenon follows a linear behavior with the boron concentration and a quadratic behavior with the oxygen concentration. This leads to the conclusion that the defect responsible for the LID is composed of two oxygens and one boron.

The LID phenomenon produced by Boron-Oxygen clusters has several particularities. One of these features is that the lifetime of the minority carrier can be re-initialized by annealing in the dark at 200°C for a short time (5 minutes). Another particularity is that LID exhibits two regimes, one for short-term exposure and the other for long-term exposure [40]. A decrease in the LID phenomenon was observed by annealing the wafers at 600 °C for 0 hour before exposing them to light. The LID phenomenon has also been reported to depend not on the number of boron but on the number of p-type charge carriers. A large part of the experimental results on BO_2 clusters were obtained using QSCCP measurements. Several research teams have attempted to characterize the defect in more detail using DLTS measurements. The results of DLTS measurements are subject to discussion. In a previous work, energy levels in the bandgap have been found in DLTS at Ec-0.41 eV and Ev+0.37 eV [42]. These levels close to the mid-gap would make the BO_2 cluster a likely candidate for dark current phenomena. Other teams have tried to find these levels in the bandgap using DLTS but have not succeeded.
The fact that the characterization of this defect is difficult using DLTS has aroused an interest in the modeling of this defect and its properties. Several ab intio studies have been conducted to find out the atomic configuration of BO_2 but also how it was formed or what mechanism was at the origin of the LID effect [43][44][45]. Even if other structures have been considered like a

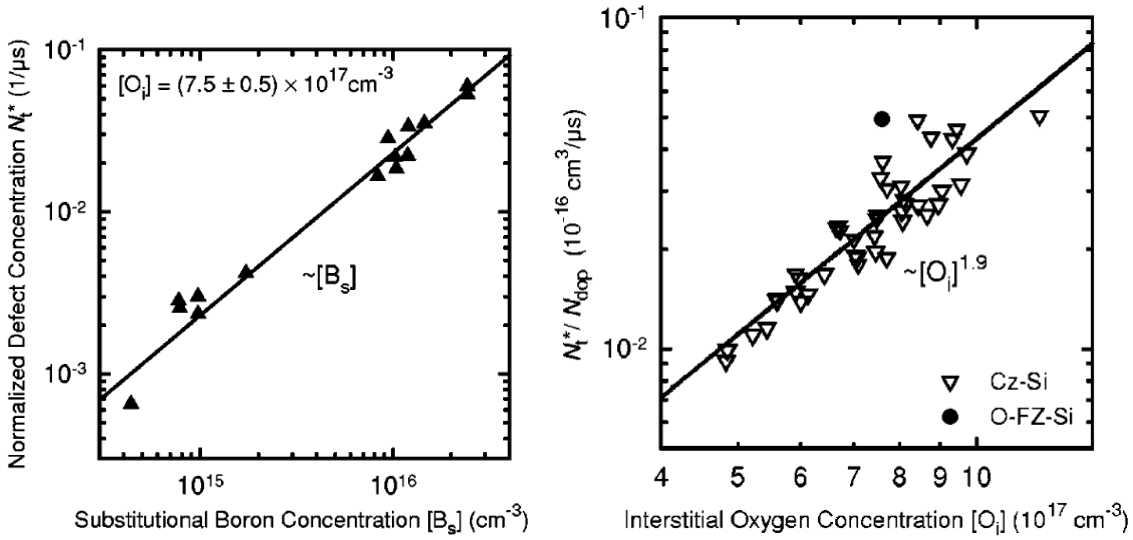

Figure 1.18: *Life-time minority carrier degradation as a function of the concentration of boron (left) and oxygen (right) in the wafer from [39].*

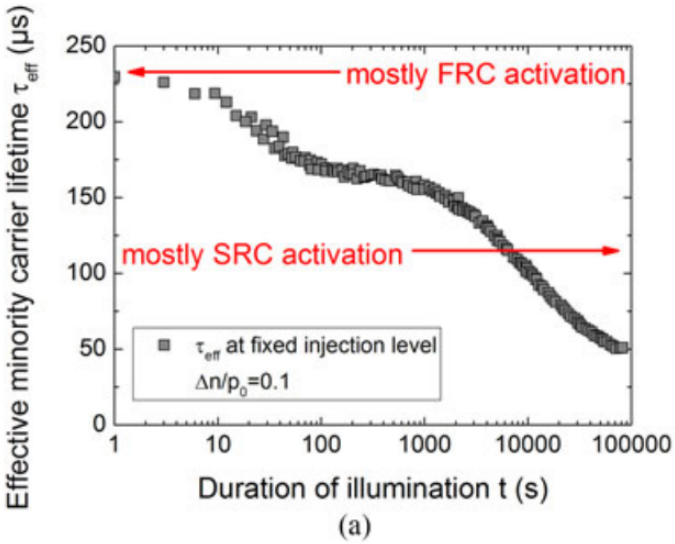

Figure 1.19: *Evolution of the minority carrier lifetime as a function of time under illumination [41]. Two regimes can be observed.*

B_iB_sO cluster [46], two main structures have been tested in ab initio. The first one is a structure where the Boron atom is in substitutional site and interacts with an interstitial oxygen dimer, B_sO_{2i}. The second structure tested is an interstitial Boron atom associated with an oxygen dimer, B_iO2i. The mechanisms of its formation remain to be elucidated and to model in a predictive way.

1.4.2 Study 2 - Heated implantations

The reduction of the concentration of defects capable of generating a dark current also requires the exploration of new processes. Heated implantations, even if they have been known for 40 years [47], are currently little used in silicon-based devices. However, through its use, performance gains have been reported in recent years. It has been shown that maintaining the chuck

at a temperature of 500°C reduces the number of defects in the final device leading to better electrical characteristics in the case of FinFET device fabrication [48]. Heated implantations therefore have an impact on the evolution of defects where applying targeted temperature on the few moments of implantation can have a significant impact on the final properties. However, the models used in the industry to simulate the evolution of defects have not been designed to take into account the implantation temperature. Moreover, the impact of heated implants does not seem to be limited to a simple reduction in the number of defects. In [49] work, the increase in the temperature of the implant does not result in a decrease in the number of extended defects. In figure 1.20, the defects resulting from heated implantations followed by annealing are observed using a photoluminescence technique. The density of defects formed in the case of the 500°C implantation seems here more important than in the case of the room temperature implantation.

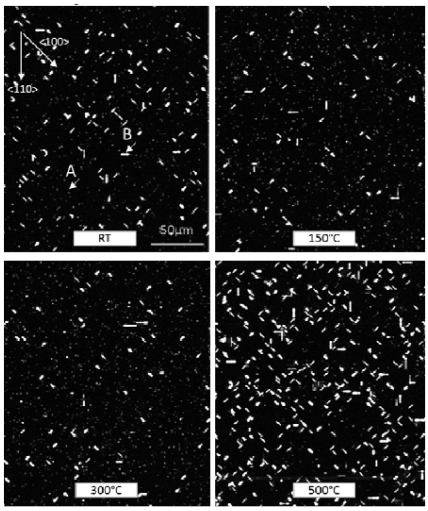

Figure 1.20: *Photoluminescence imaging of wafers implanted at different temperatures (RT, 150°C, 300°C and 500°C) then annealed at 950°C for 3 minutes from . Extended defects are visible in white on the images.*

1.5 Objectives of this thesis: modeling manufacturing processes to predict and mitigate the formation of harmful defects

1.5.1 Kinetic Monte Carlo simulation in an industrial context

In the industrial context, in order to optimize the manufacturing processes, simulation tools are used. Their primary goals are to reduce the manufacturing costs and reduce also the error and trials step. Such tools are called TCAD for Technology Computer Aided Design. The main objective of these simulation tools is to optimize the process parameters in order to obtain the best device performance. For instance, TCAD simulation softwares are also capable of simulating the effect of a manufacturing process on the type and concentration of defects in the device. Given as inputs a certain set of parameters, such as the dose and energy of the implanted species or the annealing temperatures and times, the TCAD software simulates the process and predicts activated dopant profiles. In a second step, these doping profiles are used to calculate the different electrical properties of a device.

Several software suites exist and this work is focused on the Sentaurus software [50]. The

software includes several methods for the simulation of manufacturing processes: a tool based on the resolution of differential equations to evaluate the concentrations of dopants and defects and a Kinetic Monte Carlo (KMC) tool using a stochastic approach. The calibration of each of the model requires different approaches and strategies. The operation of these two simulation methods will be detailed in the next chapter, some generalities are nevertheless exposed here in order to understand the objectives of this thesis.

- The continuous approach is the most used because it is generally faster than the KMC approach. The continuous model relies on the introduction of empirical parameters. These parameters are generally chosen to fit the experiments and do not necessarily have a physical meaning.
- The KMC is a method that introduces an atomistic granularity in the description of the evolution of the microstructure of a material. In the suite we use, it is possible to modify the equations that govern the diffusion of each species and even to enter new equations when it is necessary to implement new species. Also, a differential equation can be introduced for each type of cluster to be treated continuously slowing down the computation time even if this type of cluster is not present. Adding a different type of cluster in the KMC does not slow down the computation time. Another advantage is that some physical effects are taken into account in the KMC such as the dose rate during implantation. The calibration of the KMC also uses empirical parameters but is also based on the calibration of the activation energy of the physical mechanisms coming from more rigorous modeling approaches.

  The calibration of these physical parameters can be done using experimental results or using other simulation tools. For atomic mechanisms, ab initio simulations or molecular dynamics are used [51][52][53]. These simulation methods do not allow to simulate the processes of device simulation, being limited to much smaller system sizes. We can note that some TCAD software integrates its own ab initio solver but in this work the ab initio software used is external to the Sentaurus [50] simulation tools.

In this thesis, we are interested in the KMC method, which is used for process simulation in the industrial context. KMC is the only method able to make the link between the atomistic mechanisms simulated in ab initio and the larger scale properties simulated in TCAD as the concentration of DLs or the concentration of a cluster of impurities. We explore how the link between ab initio simulations and TCAD tools can be established.

1.5.2 Objectives of this thesis

In this thesis work, I was interested in two studies:

- The first study is motivated by the problem of the existence of BO_2 complexes, as described above. In order to be able to predict their formation, the implementation of a new species, the Oxygen species, has to be realized in the TCAD tools dedicated to process simulation. The calibration of oxygen will then be conducted by a DFT study.
- The study of the modelling of the heated implantation process using the TCAD tools and their ability to model this new technological process. A focus is made on the formation and dynamics of interstitial clusters as previously described.

Based on these two examples, the advantages and limitations of using a KMC in an industrial context are discussed. In particular, the possibility of improving the KMC, which remains the most used method in the industrial context to simulate processes, is looked at by calibration with data from DFT calculations, or by coupling with continuous methodologies. These methods are introduced in Chapter 2.

For each of the two studies, several issues need to be investigated.

In the case of BO_2 clusters, the following questions arise:

- What parameters should be implemented to be able to simulate the evolution of a species in the KMC?
- What parameters can be calibrated using ab initio calculations?
- What ab initio simulations should be performed in practice to calibrate them and is it possible to have a systematic approach in this calibration?
- Is the complexity of the atomic mechanisms found in the ab initio calculations implemented in the KMC used? And if not, what are the assumptions to be made?

These questions are addressed in Chapter 3.

In the case of heated implementations, it is not a matter of implementing a species or mechanism but of testing the validity of the implemented model and correcting it if necessary. The problems that arise in this case are the following:

- What are the effects of heated implementations on the evolution of extended defects at the end of the process?
- Do the continuous model and the KMC model in the software package "Sentaurus" [50] recover the experimental trends?
- Is it possible to link the KMC model to the continuous model?
- If the results of the simulations do not reproduce the experimental results, what parameters should be calibrated?
- How can ab initio approaches be used to calibrate these parameters?

These are the main concerns of Chapter 4.

References

[1] D. Buss, R. Kansy, and J. B. Barton, "Ktc noise on direct injection from ir diodes", IEEE Transactions on Electron Devices **27**, 998–1000 (1980).

[2] Y. Degerli, "Étude, modélisation des bruits et conception des circuits de lecture dans les capteurs d'images à pixels actifs cmos", PhD thesis (École nationale supérieure de l'aéronautique et de l'espace (Toulouse; 1972 ..., 2000).

[3] I. Rech, A. Ingargiola, R. Spinelli, I. Labanca, S. Marangoni, M. Ghioni, and S. Cova, "Optical crosstalk in single photon avalanche diode arrays: a new complete model", Optics express **16**, 8381–8394 (2008).

[4] W. Shockley and W. Read Jr, "Statistics of the recombinations of holes and electrons", Physical review **87**, 835 (1952).

[5] S. M. Sze, Y. Li, and K. K. Ng, *Physics of semiconductor devices* (John wiley & sons, 2021).

[6] G. Watkins, J. Troxell, and A. Chatterjee, "Vacancies and interstitials in silicon", in *Defects and radiation effects in semiconductors, 1978* (1979).

[7] R. Needs, "First-principles calculations of self-interstitial defect structures and diffusion paths in silicon", Journal of Physics: Condensed Matter **11**, 10437 (1999).

[8] G. Samara, "Breathing-mode lattice relaxation associated with the vacancy and phosphorus-vacancy-pair (e-center) defect in silicon", Physical Review B **37**, 8523 (1988).

[9] E. Sonder and L. Templeton, "Gamma irradiation of silicon. ii. levels in n-type float-zone material", Journal of Applied Physics **34**, 3295–3301 (1963).

[10] A. N. Larsen, A. Mesli, K. B. Nielsen, H. K. Nielsen, L. Dobaczewski, J. Adey, R. Jones, D. Palmer, P. Briddon, and S. Öberg, "E center in silicon has a donor level in the band gap", Physical review letters **97**, 106402 (2006).

[11] D. Macdonald and L. Geerligs, "Recombination activity of interstitial iron and other transition metal point defects in p-and n-type crystalline silicon", Applied Physics Letters **85**, 4061–4063 (2004).

[12] J.-W. Chen, A. Milnes, and A. Rohatgi, "Titanium in silicon as a deep level impurity", Solid-State Electronics **22**, 801–808 (1979).

[13] J. Morante, J. Carceller, P. Cartujo, and J. Barbolla, "Thermal emission rates and capture cross-section of majority carriers at titanium levels in silicon", Solid-State Electronics **26**, 1–6 (1983).

[14] P. Giri, "Photoluminescence signature of silicon interstitial cluster evolution from compact to extended structures in ion-implanted silicon", Semiconductor science and technology **20**, 638 (2005).

[15] J. Benton, S. Libertino, P. Kringho/j, D. Eaglesham, J. Poate, and S. Coffa, "Evolution from point to extended defects in ion implanted silicon", Journal of applied physics **82**, 120–125 (1997).

[16] C. Nyamhere, F. Cristiano, F. Olivie, E. Bedel-Pereira, J. Boucher, Z. Essa, D. Bolze, and Y. Yamamoto, "Electrical characterization of {311} defects and related junction leakage currents in n-type si after ion implantation", in Aip conference proceedings, Vol. 1496, 1 (American Institute of Physics, 2012), pp. 171–174.

[17] E. M. Bazizi, "Modélisation physique et simulation de défauts étendus et diffusion des dopants dans le si, soi, sige pour les mos avancés", PhD thesis (2010).

[18] S. Takeda, M. Kohyama, and K. Ibe, "Interstitial defects on { 113} in si and ge line defect configuration incorporated with a self-interstitial atom chain", Philosophical Magazine A **70**, 287–312 (1994).

[19] F. Cristiano, "Ion implantation-induced extended defects: structural investigations and impact on ultra-shallow junction properties", PhD thesis (Université Paul Sabatier-Toulouse III, 2013).

[20] C. Nyamhere, A. Scheinemann, A. Schenk, A. Scheit, F. Olivie, and F. Cristiano, "A comprehensive study of the impact of dislocation loops on leakage currents in si shallow junction devices", Journal of Applied Physics **118**, 184501 (2015).

[21] Y. Kang, H.-D. Liu, M. Morse, M. J. Paniccia, M. Zadka, S. Litski, G. Sarid, A. Pauchard, Y.-H. Kuo, H.-W. Chen, et al., "Monolithic germanium/silicon avalanche photodiodes with 340 ghz gain–bandwidth product", Nature photonics **3**, 59–63 (2009).

[22] S. Duguay, T. Philippe, F. Cristiano, and D. Blavette, "Direct imaging of boron segregation to extended defects in silicon", Applied Physics Letters **97**, 242104 (2010).

[23] M. Inoue, H. Sugimoto, M. Tajima, Y. Ohshita, and A. Ogura, "Microscopic and spectroscopic mapping of dislocation-related photoluminescence in multicrystalline silicon wafers", Journal of Materials Science: Materials in Electronics **19**, 132–134 (2008).

[24] F. Cristiano, J. Grisolia, B. Colombeau, M. Omri, B. De Mauduit, A. Claverie, L. Giles, and N. Cowern, "Formation energies and relative stability of perfect and faulted dislocation loops in silicon", Journal of Applied Physics **87**, 8420–8428 (2000).

[25] M. T. Robinson and I. M. Torrens, "Computer simulation of atomic-displacement cascades in solids in the binary-collision approximation", Physical Review B **9**, 5008 (1974).

[26] E. Dekempeneer, P. Zalm, G. Van Hoften, and J. Politiek, "Light-and heavy-ion channeling profiles in silicon", Nuclear Instruments and Methods in Physics Research Section B: Beam Interactions with Materials and Atoms **48**, 224–230 (1990).

[27] L. Pelaz, L. A. Marqués, and J. Barbolla, "Ion-beam-induced amorphization and recrystallization in silicon", Journal of applied physics **96**, 5947–5976 (2004).

[28] H. Bracht, N. Stolwijk, M. Laube, and G. Pensl, "Diffusion of boron in silicon carbide: evidence for the kick-out mechanism", Applied Physics Letters **77**, 3188–3190 (2000).

[29] N. Cowern, G. Van de Walle, D. Gravesteijn, and C. Vriezema, "Experiments on atomic-scale mechanisms of diffusion", Physical review letters **67**, 212 (1991).

[30] A. Ural, P. B. Griffin, and J. D. Plummer, "Fractional contributions of microscopic diffusion mechanisms for common dopants and self-diffusion in silicon", Journal of Applied Physics **85**, 6440–6446 (1999).

[31] T. S. T. Shimizu, T. T. T. Takagi, S. M. S. Matsumoto, Y. S. Y. Sato, E. A. E. Arai, and T. A. T. Abe, "Fraction of interstitialcy component of phosphorus and antimony diffusion in silicon", Japanese journal of applied physics **37**, 1184 (1998).

[32] D. Eaglesham, P. Stolk, H.-J. Gossmann, T. Haynes, and J. Poate, "Implant damage and transient enhanced diffusion in si", Nuclear Instruments and Methods in Physics Research Section B: Beam Interactions with Materials and Atoms **106**, 191–197 (1995).

[33] L. Csepregi, E. F. Kennedy, J. Mayer, and T. Sigmon, "Substrate-orientation dependence of the epitaxial regrowth rate from si-implanted amorphous si", Journal of Applied Physics **49**, 3906–3911 (1978).

[34] A. Claverie, B. Colombeau, F. Cristiano, A. Altibelli, and C. Bonafos, "Atomistic simulations of extrinsic defects evolution and transient enhanced diffusion in silicon", MRS Online Proceedings Library (OPL) **669** (2001).

[35] N. Cowern, G. Mannino, P. Stolk, F. Roozeboom, H. Huizing, J. Van Berkum, F. Cristiano, A. Claverie, and M. Jaraiz, "Energetics of self-interstitial clusters in si", Physical Review Letters **82**, 4460 (1999).

[36] B. Colombeau, F. Cristiano, A. Altibelli, C. Bonafos, G. B. Assayag, and A. Claverie, "Atomistic simulations of extrinsic defects evolution and transient enhanced diffusion in silicon", Applied Physics Letters **78**, 940–942 (2001).

[37] H. Fischer, "Investigation of photon and thermal changes in silicon solar cells", in Conference record of the 10ˆ¡ th¿ ieee photovoltaic specialists conference, 1973 (1973).

[38] J. Lindroos and H. Savin, "Review of light-induced degradation in crystalline silicon solar cells", Solar Energy Materials and Solar Cells **147**, 115–126 (2016).

[39] J. Schmidt and K. Bothe, "Structure and transformation of the metastable boron-and oxygen-related defect center in crystalline silicon", Physical review B **69**, 024107 (2004).

[40] H. Hashigami, Y. Itakura, and T. Saitoh, "Effect of illumination conditions on czochralski-grown silicon solar cell degradation", Journal of applied physics **93**, 4240–4245 (2003).

[41] T. Niewelt, J. Schön, W. Warta, S. W. Glunz, and M. C. Schubert, "Degradation of crystalline silicon due to boron–oxygen defects", IEEE Journal of Photovoltaics **7**, 383–398 (2016).

[42] T. Mchedlidze and J. Weber, "Direct detection of carrier traps in si solar cells after light-induced degradation", physica status solidi (RRL)–Rapid Research Letters **9**, 108–110 (2015).

[43] M.-H. Du, H. M. Branz, R. S. Crandall, and S. Zhang, "Bistability-mediated carrier recombination at light-induced boron-oxygen complexes in silicon", Physical review letters **97**, 256602 (2006).

[44] X. Chen, X. Yu, X. Zhu, P. Chen, and D. Yang, "First-principles study of interstitial boron and oxygen dimer complex in silicon", Applied Physics Express **6**, 041301 (2013).

[45] M. Vaqueiro-Contreras, V. P. Markevich, J. Coutinho, P. Santos, I. F. Crowe, M. P. Halsall, I. Hawkins, S. B. Lastovskii, L. I. Murin, and A. R. Peaker, "Identification of the mechanism responsible for the boron oxygen light induced degradation in silicon photovoltaic cells", Journal of Applied Physics **125**, 185704 (2019).

[46] V. V. Voronkov and R. Falster, "Light-induced boron-oxygen recombination centres in silicon: understanding their formation and elimination", in Solid state phenomena, Vol. 205 (Trans Tech Publ, 2014), pp. 3–14.

[47] P. D. Parry, "Target heating during ion implantation", Journal of Vacuum Science and Technology **13**, 622–629 (1976).

[48] T. Wen, C. Li, M. Hsieh, S. Tsai, P. Hsieh, S. Lin, H. Chiang, N. Yang, J. Wu, B. Guo, et al., "Finfet io device performance gain with heated implantation", in 2018 22nd international conference on ion implantation technology (iit) (IEEE, 2018), pp. 106–109.

[49] S. Joblot, R. Duru, N. Guitard, V. Lu, T. Nassiet, R. Beneyton, F. Cristiano, K. Dabertrand, J. Borrel, M. Juhel, et al., "Characterization of heated ion implantation for non amorphizing conditions and correlation with kinetic monte carlo simulations", in 2018 22nd international conference on ion implantation technology (iit) (IEEE, 2018), pp. 121–124.

[50] Sentaurus Process User Guide, R-2020.09, Synopsys Inc.

[51] I. Martin-Bragado, P. Castrillo, M. Jaraiz, R. Pinacho, J. Rubio, and J. Barbolla, "Physical atomistic kinetic monte carlo modeling of fermi-level effects of species diffusing in silicon", Physical Review B **72**, 035202 (2005).

[52] B. Sahli, K. Vollenweider, N. Zographos, and C. Zechner, "Ab initio calculations of phosphorus and arsenic clustering parameters for the improvement of process simulation models", Materials Science and Engineering: B **154**, 193–197 (2008).

[53] L. A. Marqués, L. Pelaz, J. Hernández, J. Barbolla, and G. H. Gilmer, "Stability of defects in crystalline silicon and their role in amorphization", Physical Review B **64**, 045214 (2001).

Simulation methods

2

Contents

Introduction

This chapter presents the different simulation tools used in this thesis to model the dynamics of atoms and more specifically of defects formed during technological manufacturing processes. As mentioned in the first chapter, this thesis focuses on the use of the Kinetic Monte Carlo (KMC) tool, which is one of the most widely used methodologies in the industry to link process parameters and the structure of the materials being elaborated. The first section of this chapter therefore describes the operation of this simulation method, and in particular the KMC integrated in the TCAD suite [1].

The other objective of this thesis is to propose solutions to improve this KMC methodology at several levels.

- We are particularly interested in the calibration of this method. Thus, one of the advantages of KMC is that it integrates atomistic events to simulate the dynamics of species. Its calibration can thus be carried out using fine parameters describing the mechanisms of atomic migrations, that can be obtained using ab initio calculations requiring few empirical parameters. The general principle of operation of these tools, and in the first place of the density functional theory (DFT), will be presented in a second section. This section will describe more specifically the use of these tools in the context of the simulation of the atomic mechanisms of defects. The impact of defects on the dark current can also be simulated in principle with these simulation tools and this issue will be briefly discussed. This method will be used in Chapters 3 and 4.

- One of the disadvantages of KMC is the time required for simulations. Simulations based on solving differential equations to predict defect concentration, called continuous methods in this work, are much faster. The principles of these simulation methods in the prediction of the doping profile, their main use, as well as their prediction of the defect concentration will be detailed in a third section. The formalism studied will be the one implemented in the software [1]. This method will be used in Chapter 4.

2.1 Kinetic Monte Carlo methodology

2.1.1 From the Metropolis to Kinetic Monte Carlo

Monte Carlo methods are based on a probabilistic approach and allow to approximate numerical values of integrals or physical quantities. One of the best known examples to introduce Monte Carlo methods is their use to calculate the numerical value of π. In this method a circle of radius a is inserted into a square of length a. Points are generated randomly in the square. After a certain number of generated points, it is possible to count the number of points inside, N_{in} and the total number of points N_{total}. The probability for a point to be inside the circle is equal to the ratio of the area, here equal to $\frac{\pi}{4}$. For a large number of generated points, the ratio of the number of points inside the circle to the total number of points, $\frac{N_{in}}{N_{total}}$ approximates the value $\frac{\pi}{4}$. It is a Monte Carlo method with direct sampling. Here there are only two different states (inside or outside the circle) but the random variables used can be much more complex. These methods are notably used to determine the probability of triggering an avalanche in a SPAD by simulating a large number of photons in a structure [2].

Another Monte Carlo method for estimating the number π, so-called indirect sampling, is the following:

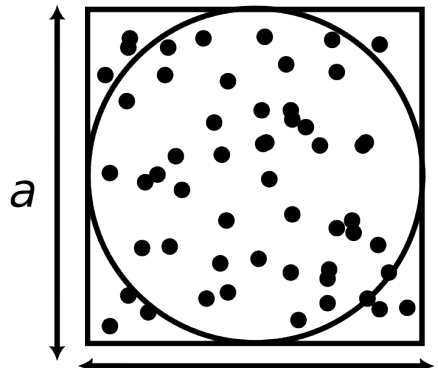

Figure 2.1: *Scheme of a Monte Carlo method to find the value of π.*

- The configuration is the same as above, a circle of diameter a in a square of length a
- A starting point is fixed in the square
- A new point is randomly generated at a distance dl from the starting point
- If the point is inside the square, it becomes the new starting point to choose a new point randomly
- If the point is outside the square, a new point is created at the actual starting point and new displacement dl is randomly chosen
- After a large number of moves it is possible to estimate the area of the circle by counting the number of points visited out of the total number of points generated (including those outside the circle)

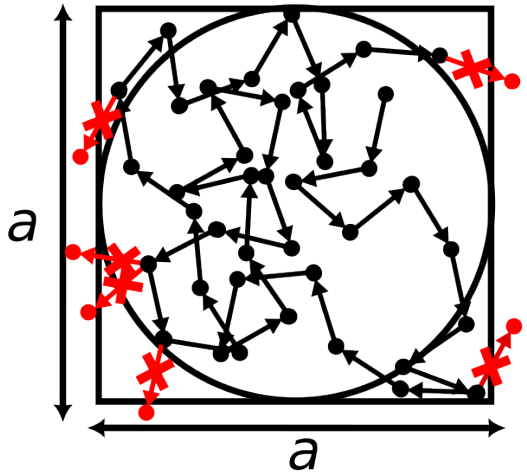

Figure 2.2: *Scheme of a Monte Carlo method to find the value of π.*

This Monte Carlo approach is based on Markov chains and also converges to the solution (a detailed demonstration can be found in [3]). The difference is that the position of the n-th point depends on the position of the n-1-th point. On the basis of this approach the Metropolis

algorithm [4] was developed to find the most stable configurations of a system. The Metropolis Monte Carlo algorithm is explained in the Figure 2.3. From a physical configuration a neighboring configuration is randomly chosen (by choosing for example an atom to change its position). The energy difference $E_{end} - E_{start}$ between the starting and the ending configuration is calculated and allows to compute a probability $p = min(exp((E_{end} - E_{start})/kT), 1)$. It is observed that if the arrival configuration has a lower energy the probability is equal to 1. A number r is then randomly chosen between 0 and 1 and if $r > p$ the arrival configuration is accepted and a new step is effected to explore the neighboring configurations from this new configuration. The algorithm will therefore gradually converge to the most stable configurations at a given temperature. A difference with the calculation of π is the complexity of the system, here the displacements are done in a space with 3N dimensions for a configuration comprising N particles in three dimensions. Another difference is that in the latter case the probability is 0 or 1 (inside or outside the square) whereas the Metropolis algorithm allows to explore higher energy configurations to cross the potential energy barriers leading to the most stable configuration.

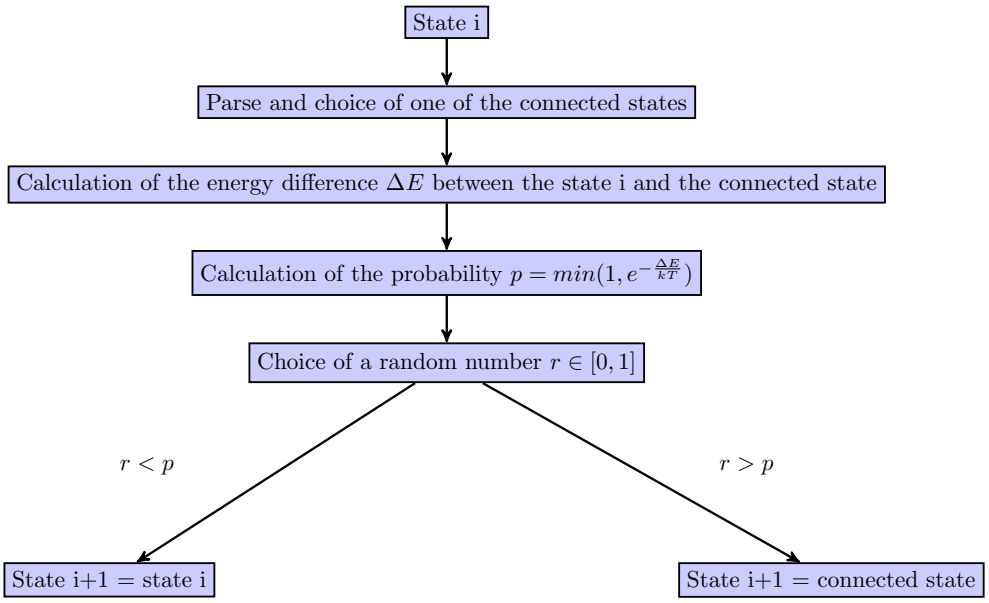

Figure 2.3: *Metropolis scheme from [5].*

The Metropolis approach is effective in finding the most stable structures in equilibrium but during the image sensor manufacturing processes the system is out of equilibrium. The duration and time of the annealing processes influence the final state of the material and it is essential to take into account kinetic parameters to reliably model the state of the system at the end of the process.

It is possible to follow the evolution of a configuration in time from an initial configuration using another Monte Carlo approach, namely the kinetic Monte Carlo (KMC). If two configurations are connected by a path having a physical meaning and without stable intermediate structures (migration of an atom towards the nearest neighboring atom), it is possible to associate a transition rate to this mechanism. The details of how this transition rate is calculated are explained in the next subsection. At each step of the KMC the different configurations connected physically to the current configuration are explored and their transition rate evaluated. According to their rate of transition a new structure is chosen and the time is incremented. The time step then depends on the transition rates of all configurations that were accessible at step i, the sum of these rates representing the average time for the configuration to change. The diagram of the

KMC algorithm is detailed in Figure 2.4.

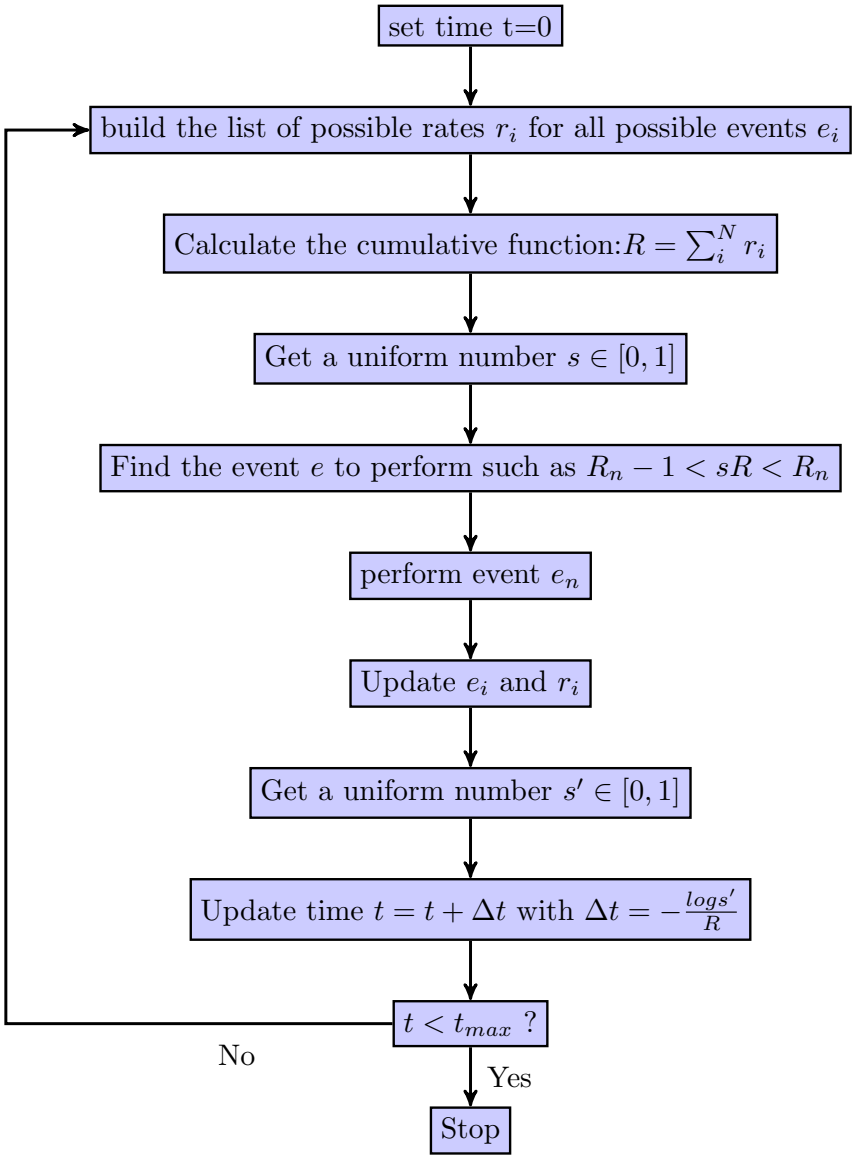

Figure 2.4: *KMC scheme from [5].*

2.1.2 Transition State Theory

As mentioned above, if two stable physical configurations A and B are connected by a physical path, it is possible to calculate a transition rate from A to B. The transition rate approach was formulated by Eyring in [6]. We will use here the approach developed in [7] to calculate them. The approach of [7] is based on the study of the potential energy surface (PES) of the considered material around the configurations A and B. The PES is the evolution of the energy landscape according to the coordinates of the atoms of a system. For a system containing N atoms the PES is represented by 3N coordinates (for the 3 directions of the space of the N atoms). Configurations A and B are physically connected if there is a single saddle point P in the PES allowing to go from A to B. It is possible to define an hyper-surface S of dimension 3N-1 that passes through P and is perpendicular to the contours of PES iso-surface everywhere else. It is then possible to define a hypersurface H of dimension 3N around A stopping at S. In

[7] it is shown that the transition rate Γ between A and B can be calculated using the following formula:

$$\Gamma = \sqrt{\frac{kT}{2\pi}} \frac{\int_S e^{-E(R_1,...,R_N)/kT}}{\int_H e^{-E(R_1,...,R_N)/kT}} \tag{2.1}$$

$E(R_1, .., R_N)$ is here the energy along the potential energy surface. It is possible to use the harmonic approximation to compute the two integrals and thus to approximate the functions E by a limited expansion of order 2 around A and P (for H and S respectively). A being a local minimum and S a saddle point the first derivative of the limited expansion is null and the energy of the two surfaces can be approximated around A by:

$$E(R_1, ..., R_N)_A \simeq E(A) + \sum_{i=1}^{3N} \frac{1}{2}(2\pi\omega_i^A)^2 q_i^2 \tag{2.2}$$

and close to S by:

$$E(R_1, ..., R_N)_S \simeq E(P) + \sum_{i=1}^{3N-1} \frac{1}{2}(2\pi\omega_i^S)^2 q_i^2 \tag{2.3}$$

where $(q_1, ..., q_{3N})$ are the normal co-ordinates and ω_i^A (ω_i^A) are the normal frequencies for vibrations about point A (point S). Using the formula 2.1 the calculation of the integrals allows to know the rate of transition from A to B :

$$\Gamma_{A-B} = De^{\frac{E_P - E_A}{kT}} \tag{2.4}$$

Where D is the entropic prefactor given by:

$$D = \frac{\prod_i^{3N} \omega_i^A}{\prod_j^{3N-1} \omega_j^S} \tag{2.5}$$

2.1.3 KMC TCAD object

The KMC implemented in the TCAD software suite [1] for the simulation of implantation and annealing processes is called Object KMC and what we will call a KMC on-lattice. It consists of a simulation domain where every atom, that is not a silicon atom in crystalline position, is represented. Crystalline silicon atoms are not represented in the KMC and cannot be involved in events. They form a periodic potential in which impurities, point defects (interstitial and vacancies) evolve. Impurities and defects can agglomerate between them and form different types of clusters that will have different events. As mentioned in Chapter 1, when interstitials agglomerate the nature of the defect formed depends on the number of interstitials in the defects. The KMC formalism takes it into account and depending on the number of interstitials in a defect, it can be simulated and organized in space as a SMICs, a {311} defect or a dislocation loop. Extended defects such as dislocations can generate stresses in the silicon. These stresses can change the activation energy of some events and are therefore taken into account in the KMC.

Each particle represented in the system is either on a substitutional site or on an interstitial site. In a physical system, there can be several metastable sites for an atom in an interstitial position but this variety of possible positions is not taken into account and there is therefore only one possible interstitial geometry. This assumption allows to restrict the number of events

in the catalog. Indeed, if several configurations were represented, the possible events could be different for each type of interstitial, a migration event on a neighboring site has indeed a different activation energy depending on whether it is an interstitial 1 or 2. It would then be necessary to take into account the events allowing to move from one interstitial configuration to another. Taking into account the different geometries would therefore significantly increase the number of possible events and consequently make the calibration even longer and more difficult.

The defects, potentially consisting of several atoms, are represented as objects. The list of available objects is as follows:

- point defect, which includes interstitials, vacancies, dopant atoms and point dopant-defect pairs.
- Icluster, for small interstitial clusters
- Void, for vacancy clusters
- {311} defect
- Loops
- Impurity clusters

The KMC also includes an internal mesh. The latter is not used to solve differential equations to obtain dopants profiles as in continuous methods but has several purposes:

- To be able to access a local Fermi level value in the simulation domain
- In case of partial amorphization of the structure to know which region is amorphous

Particles can be charged, including interstitials and vacancies. The kinetic properties of charged defects are generally different from the kinetic properties for a neutral charge state. This effect is also taken into account in the KMC. Each point defect is associated with a probability of being in a charged state according to the Fermi level in the simulation box. This Fermi level is calculated in each mesh element of the KMC according to the number of dopants in substitutional site in the mesh element and in the neighboring mesh elements. A hypothesis realized to model the effect of the Fermi level is to assume that the charge reactions are instantaneous because much faster than the atomic migration mechanisms. Substituted site dopants are also always considered charged. The Fermi level is regularly updated during the simulation with the calculation of the Fermi level for each mesh element. Indeed during the simulation the spatial distribution of the charged particles evolves (and consequently the Fermi level). Moreover, when a particle changes mesh element, its charge state is recalculated according to the Fermi level in its new environment.

2.1.4 TCAD KMC for ionic implantation

The above described KMC can be used to simulate the evolution of the distribution of dopants and interstitials or vacancy clusters during implantation processes. In the KMC solver used, the ions are implanted one by one. The TCAD solver using the KMC approach is separated into two algorithms used sequentially for each implanted ion:

- An algorithm chooses the trajectories of an implanted ion and calculates the interstitials and vacancies generated by the collision of the implanted ion with the crystalline lattice.
- Another algorithm, the KMC itself, simulates the evolution of interstitials, vacancies and dopant atoms during the time between two ion implantations in the simulation box.
- The first algorithm is then re-used to simulate a new ion implanted in the material.

The first algorithm uses the binary collision approximation (BCA) method [8]. In this method, the incident ion undergoes several collisions during which its trajectory changes and it loses energy. After each collision, the trajectory of the ion is recalculated and its energy updated. A new collision location is determined until the incident ion has no more energy. The starting energy of the incident ion is simply the energy at which the ion is accelerated into the material. The angle at which the incident ion enters the material is determined by the tilt, which is an input parameter of the implantation command line. The first atom with which the ion collides is estimated differently depending on whether the implanted material is crystalline or amorphous. The average path for an incident ion to collide with a silicon atom in an amorphous material is equal to $L = \frac{1}{N_{density}^{\frac{1}{3}}}$ where $N_{density}$ is the crystal density. Based on a probabilistic approach, a first collision distance b can be determined as equal to:

$$b = \sqrt{\frac{R_{rand}}{\pi N_{density}^{\frac{2}{3}}}} \tag{2.6}$$

With R_{rand} a random number between 0 and 1.

In a crystalline material, all atoms that are less than half the mesh parameter of the incident ion's trajectory are selected and projected onto the trajectory. The atom with the smallest distance to the trajectory is then chosen as collision partner. If other atoms are located at a distance of less than 2 nm from the collision partner, they are also considered as collision partners considering that the collision with these other atoms is instantaneous.

The second algorithm, the KMC, is then used to simulate the evolution of the defect cascades until a new ion is introduced in the simulation box. The KMC is mainly useful here to simulate the evolution of amorphous pockets which is the type of defect where interstitials and vacancies are agglomerated during implantation. During the implantation process, recombinations between interstitials and vacancies take place in these amorphous pockets. The implantation of a new ion in the material can generate defect cascades in the same area as a previously implanted ion. The interstitials and vacancies resulting from this new implanted ion can interact with the amorphous pockets formed by the previous ion and lead to the enlargement of amorphous pockets. The probability of interaction between a new defect cascade and an amorphous pocket is all the greater as the amorphous pocket is large (atoms outside their crystal site increase the probability of interactions with incident ions). The evolution of the size of amorphous pockets depends on the recombinations between interstitials and vacancies in an amorphous pocket before a new defect cascade is generated at the same place. The longer the time between two implanted ions, the smaller the size of the amorphous pocket due to recombination. The smaller the size of the amorphous pocket, the less likely it will interact with a new defect cascade and the less stable it will be. It is in this context that the KMC is useful: this method allows to take into account precisely the recombinations and thus the evolution of the size of the amorphous pockets.

Accumulation of amorphous pockets in the case of light ions or overlapping of large amorphous pockets in the case of heavier implantation can lead to amorphization of the material. To predict whether the enlargement of an amorphous pocket or their accumulation leads to amorphization of a region of the material the KMC uses its internal mesh. In the KMC formalism, an amorphous pocket is an agglomeration of interstitials and vacancies that can be counted. It is possible for each mesh element to calculate the concentration of point defects (interstitials or vacancies). If this concentration exceeds a threshold of 1.5×10^{22} cm^{-3} in a mesh element, then the latter is considered to be amorphous. When a mesh element is considered to be amorphous, the formalism applied to it changes. It is still possible to generate interstitials and vacancies in this element but recombinations in amorphous pockets are not taken into account. It is possible to form a layer of amorphous material by accumulating mesh elements that have become amorphous during amorphization. Taking into account the evolution dynamics of the amorphous pockets during the implantation process allows a good description of the creation of a potential amorphous layer during the implantation. The width of a potential amorphous layer is also reliably described by a good simulation of amorphous pockets. The KMC is therefore expected to be efficient in assessing amorphization following implantation.

Another advantage of the KMC is to reliably simulate the consequences of the appearance of an amorphous layer on the dopant distribution. Ion collisions in a crystalline or amorphous material are treated differently in the KMC. This method allows to reproduce faithfully the changes in the channeling phenomenon following the appearance of an amorphous layer. As mentioned in Chapter 1, in an amorphous material the incident ions are more likely to collide with silicon atoms if they do not form a periodic lattice. In the case of a periodic lattice, preferential directions exist for which an incident ion will be able to travel long distances before colliding with a lattice atom.

2.1.5 TCAD KMC for thermal annealing

After the implantation process, the dopants are usually activated in an annealing step that can be simulated in KMC. The amorphous pockets have different recombination energies depending on their sizes. The size of an AP (amorphous pocket) is defined by the number of interstitials and vacancies that compose it. The evolution of recombination energy in APs as a function of their size is linear. The recombination energy varies from 0.43 eV for an amorphous pocket containing one interstitial and one vacancy, to 2.7 eV for an AP containing 225 interstitials and vacancies. At temperatures above 600°C they disappear from the simulation box in a few minutes. As there is generally not the same number of interstitial as vacancies in an AP, following the recombinations the amorphous pocket leaves place to a cluster comprising interstitial only or vacancy only. These clusters are considered immobile in the KMC. However, they emit interstitials which can then migrate in the simulation and interact with other clusters. The KMC thus allows to model the Ostwald ripening phenomenon described in Chapter 1.

For the elements of mesh considered as amorphous there is also an activation energy for the element to become crystalline again. An amorphous mesh element that recrystallizes has no interstitial or vacancy once the event is performed.

During annealing, dopants can diffuse into the material. This diffusion is done via their interaction with interstitials and vacancies, the dopants in substitutional sites being considered immobile. These interstitials are those emitted from clusters or more extensive defects such as {311} defects or dislocation loops.

The simulation time for annealing is generally long. Indeed the time step following the realization of an event in the KMC depends on the inverse of the sum of the transition rates of all possible

events in the simulation domain. These transition rates depend exponentially on the temperature and increase as the temperature increases. For high temperatures, the realization of an event generates a very small time step and the number of time steps necessary to simulate the annealing time is thus very high.

2.1.6 Off-lattice and on-the fly KMC

The KMC presented before has the advantage to be fast and to be able to simulate complete simulation processes like ion implantation or annealing. It allows to fully simulate small devices. However, as mentioned before, it relies on several physical approximations.

The first one is that only one type of geometry is implemented for each defect. To be able to simulate this diversity in the different possible configurations, other types of KMC exist. These algorithms are called off-Lattice KMC in this work because they involve geometric configurations defined with other parameters than a lattice site. This type of KMC has already demonstrated its effectiveness in modeling non-equilibrium processes such as laser annealing [9]. A difference between KMC lattices and KMC off-lattices is in the catalog generation. For a KMC lattice it is sufficient to implement an energy and a prefactor and a migration direction for the point defect scattering or being emitted from a larger defect. For Off-Lattice KMC the local environment is no longer described by the crystal lattice but by all the atoms around the impurity or defect. To implement an event catalog it is necessary to implement the precise structure of the defect as well as its different possible mechanisms depending on its environment.

The TCAD software suite [1] includes an off-Lattice KMC that can be used for SPER simulations [10]. SPER simulations are not the focus of this thesis and we will not describe here the mechanism of this KMC.

In order to improve or test the calibration of the Lattice KMC of the software suite [1], an in-house off-Lattice KMC has been used during this thesis, developped during Miha Gunde's thesis [11]. In the rest of the manuscript, if not specified, the acronym KMC refers to the on-lattice KMC of the TCAD suite [1] and the term off-lattice KMC to the in-house solver.
In the off-lattice KMC used in this thesis, the description of the environment for each event is done using atomic coordinates. The atomic coordinates of the initial and final events are used as input for a shape matching algorithm, called IRA [12], which then generates an event catalog taking into account a restricted number of atoms. As input data of IRA, it is necessary to give the number of neighboring atoms included in an event from a central atom. The software then generates the different events taking into account the symmetries of the system.

When running the off-lattice KMC at each step, the different topologies of the system are studied. The off-lattice KMC must be able to recognize an event from the position of the atoms in the system. This implies that if the order of the atoms between the event and the catalog or if the configuration has undergone a rotation the KMC must be able to recognize it. This problem is not so easy to solve and is discussed in [11] work. The presented formalism generates a high number of events to be calibrated as soon as the system becomes more complex. To overcome this problem another type of KMC exists, the on-the-fly KMC [13]. This type of KMC does not have a catalog at the beginning of the simulation. At each step of the KMC, the local environment and its potential energy surface is analyzed using atomistic simulation tools (molecular dynamic or DFT). These explorations make it possible to find stable structures in the vicinity and the saddle points of the energetic pathway allowing access to them.

2.2 Density Functional Theory

As mentioned in the previous section, the KMC method relies on the knowledge of the transition rate associated with the different atomic mechanisms. These transition rates depend on the energies of the initial configuration and the saddle point between the initial and final configurations as well as on an entropic prefactor. This prefactor can be expressed as a function of the vibration frequencies around the initial position and the saddle point. All these parameters are accessible by the ab initio method.

In this section, we will explain how ab initio methods work and how they allow us to calculate the energies and modes of vibrations.

The ab initio methods such as the DFT and the algorithms using them are based on the calculation of the energy of a system according to the atomic coordinates and the elements constituting a system. The value of the energy of a system with M nuclei and N electrons is calculated from the Schrödinger equation:

$$\hat{H}_{tot}(\vec{r}_1, ..., \vec{r}_N, \vec{R}_1, ..., \vec{R}_M)\psi_{tot}(\vec{r}_1, ..., \vec{r}_N, \vec{R}_1, ..., \vec{R}_M) = E_{tot}\psi_{tot}(\vec{r}_1, ..., \vec{r}_N, \vec{R}_1, ..., \vec{R}_M) \quad (2.7)$$

where $\hat{H}_{tot}$ is the Hamiltonian of the entire system of N electrons and M nuclei, $\vec{r}_i$ are space coordinates of electron i, $\vec{R}_I$ are space coordinates of nuclei I, ψ_{tot} is the wavefunction of the entire system and E_{tot} is the total energy of the system [14].

The Hamiltonian of the system can be written as follows:

$$\begin{aligned}\hat{H}_{tot} = -\sum_i^N \frac{\hbar^2}{2m}\vec{\nabla}_i^2 - \sum_I^M \frac{\hbar^2}{2M}\vec{\nabla}_I^2 - \sum_i^N \sum_I^M \frac{Z_I e^2}{4\pi\epsilon_0|\vec{r}_i - \vec{R}_I|} + \\ \sum_i^N \sum_{j>i}^N \frac{e^2}{4\pi\epsilon_0|\vec{r}_i - \vec{r}_j|} + \sum_I^M \sum_{J>I}^M \frac{Z_I Z_J e^2}{4\pi\epsilon_0|\vec{R}_I - \vec{R}_J|}\end{aligned} \quad (2.8)$$

where m is the electron mass, M the nuclei mass, i indexes correspond to electrons, I indexes correspond to nuclei, e is the elementary charge, Z_I is the atomic number of nuclei I and $\vec{\nabla}^2 = \text{div}(\vec{\text{grad}})$ [14].

It is possible to give a physical interpretation to the different terms of the Hamiltonian. The kinetic energy of electrons is described by the first term, the kinetic energy of nuclei by the second term of the equation 2.8. The third, fourth and fifth terms of the equation describe respectively the electron-nuclei, electron-electron and nuclei-nuclei interactions.

2.2.1 From Hartree Fock to DFT

Except for the hydrogen atom, the resolution of the Schrödinger equation is in practice not possible from the point of view of computational resources. A first approach is to separate the motion of electrons and ions:

$$\psi_{tot}(\vec{r}_1, ..., \vec{r}_N, \vec{R}_1, ..., \vec{R}_M) = \phi_{nuclei}(\vec{R}_1, ..., \vec{R}_M) \times \psi_{elec}^{\mathbf{R}}(\vec{r}_1, ..., \vec{r}_N) \quad (2.9)$$

This approach developed by Born and Oppenheimer is justified by the difference in mass between the electrons and the nuclei. Even with this assumption, the equation is still very difficult to solve. Indeed, the interaction term between the electrons remains an important obstacle to the solution of the equation. One of the first approaches developed to simplify the equation,

is to consider that the wave functions are not very far from the case where the electrons are independent. In this case, the global wave function can be written as a Slater determinant :

$$\psi_{tot}(\vec{r}_1, ..., \vec{r}_N) = \frac{1}{N!}\begin{vmatrix} \phi_1(r_1) & \phi_2(r_1) & ... & \phi_N(r_1) \\ \phi_1(r_2) & \phi_2(r_2) & ... & \phi_N(r_2) \\ .. & .. & .. & .. \\ \phi_1(r_N) & \phi_2(r_N) & ... & \phi_N(r_N) \end{vmatrix} \tag{2.10}$$

With ϕ_n being single particles wave functions. Starting from this assumption it is possible to find the ϕ_n wave functions that allow to minimize the average energy.

This is the approach developed by Hartree and Fock (a description can be found in [15] or [16]). It consists in finding the ϕ_n wave functions minimizing the energy of the system $\langle\phi_n| H_{elec} |\phi_n\rangle$.The method to find these wave functions is based on a variational principle : the ϕ_n minimizing energy are those for which a $\phi_n + \delta\phi_n$ variation leads to a stationary energy ($\delta E = 0$). A rigorous resolution of the variational principle can be found in [15] and leads to the following formulation :

$$-\frac{\hbar}{2m}\Delta + V_1(r) + V_{dir}(r)]\phi_n(r) - \int d^3r' V_{ex}(r, r')\phi_n(r') = e_n\phi_n \tag{2.11}$$

With :

$$\begin{cases} V_{dir}(r) = \sum_{p=1}^{N} \int d^3r' |\phi_p(r')|^2 W_2(r, r') \\ V_{ex}(r, r') = \sum_{p=1}^{N} \phi_p^*(r')\phi_p(2)W_2(r, r') \\ W_2(r, r') = \frac{q_e^2}{4\pi\epsilon_0}\frac{1}{|r-r'|} \end{cases} \tag{2.12}$$

The term W corresponds to the electron-electron interaction energy and the term V to the interaction of nuclei on electrons. The electrons being identical particles, the terms V_{dir} and V_{ex} represent the direct term and the exchange term of the electron-electron interaction. In equations 2.11 and 2.12, we can see that the potentials themselves depend on the wave functions to be optimized. The resolution of this equation is therefore done through a self-consistent approach.

The Hartree-Fock method allows us to find the energy of a system from these coordinates with the approximation that the wave functions do not differ can be written in the form 2.10. Unfortunately, it is not possible to say that this is the case. It is also interesting to note that the energy found in 2.11 is not the real energy of the system.

Another method to access the total energy of a system without using this assumption was initiated in 1964 by the work of Hohenberg and Kohn. They showed that the total energy of the system is a functional of the electron density. This theory is based on three facts [17]:

- In the ground state the electron density determines uniquely the external potential of the nuclei, V_n.
- In any quantum state the external potential, V_n , determines uniquely the many-electron wavefunction, Φ.
- In any quantum state the total energy, E, is a functional of the many-body wavefunction.

This theory is accurate but has a significant drawback: the functional $F[n]$ is not known. To solve this problem, Kohn-Sham introduced a method in 1965 where the functional can be written

as follows:

$$E[n(r)] = T_{ni}[n(r)] + E_H[n(r)] + E_{ne}[n(r)] + E_{xc}[n(r)] \tag{2.13}$$

In 2.13, $T_{ni}[n(r]]$ is the kinetic energy of the non-interacting picture, E_{ne} takes into account the effect of the nucleus on the electrons, E_H is the Hartree energy and E_{xc} the exchange-correlation term. The Hartree energy corresponds to the classical density-density interaction energy [14].

To solve this problem a family of fictitious one-particle wave functions ϕ_n is introduced. The criterion imposed this time is that the density formed by this artificial family of one-particle wave functions is that the density resulting from these wave functions must be equal to the real density $n(r)$ minimizing the F-functional.

$$n(r) = \sum_i \phi_i(r) \tag{2.14}$$

Similar to the Hartree Fock method, this approach decomposes the wave function into a Slater determinant corresponding to N one-particle wave functions.

The contribution of the kinetic energy is written:

$$T_{ni} = -\sum_i \langle \phi_i | \frac{\nabla^2}{2} | \phi_i \rangle \tag{2.15}$$

The Hartree term is expressed directly as a function of the electron density:

$$E_H = \frac{1}{2} \int \frac{n(r)n(r')}{|r - r'|} dr dr' \tag{2.16}$$

It is then possible to find the ϕ_i by imposing an orthonormality condition and using a variational method as in the Hartree-Fock approach. This approach leads to the Kohn-Sham equation:

$$[\frac{-\nabla^2}{2} + V_{KS}]\phi_i = e_i \phi_i \tag{2.17}$$

V_{KS} is the Khon-Scham potential and is composed of three contributions: the nuclei-electrons potential V_{ne}, the Hartree potential V_H and the exchange-correlation potential V_{xc}. These potentials can be read :

$$V_{ne} = \frac{\partial E_{ne}}{\partial n} \tag{2.18}$$

and

$$V_H = \frac{\partial E_H}{\partial n} = \int \frac{n(r')}{4\pi\epsilon_0 |r - r'|} dr' \tag{2.19}$$

and

$$V_{xc} = \frac{\partial E_{xc}}{\partial n} \tag{2.20}$$

The Kohn-Sham equations 2.17 can then be solved in a self-consistent manner. The resulting algorithm is shown in Figure 2.5: an initial guess $n(r)$ allows the calculation of the potentials V_{KS}, the ϕ_i are then determined by resolving 2.17 and then the density n is updated, and consequently the potential V_{KS}, and the equation 2.17 is solved again. When two densities $n(r)_n$ and $n(r)_{n+1}$ calculated during two successive steps are equal, the ground state is considered to be found and the calculation finished.

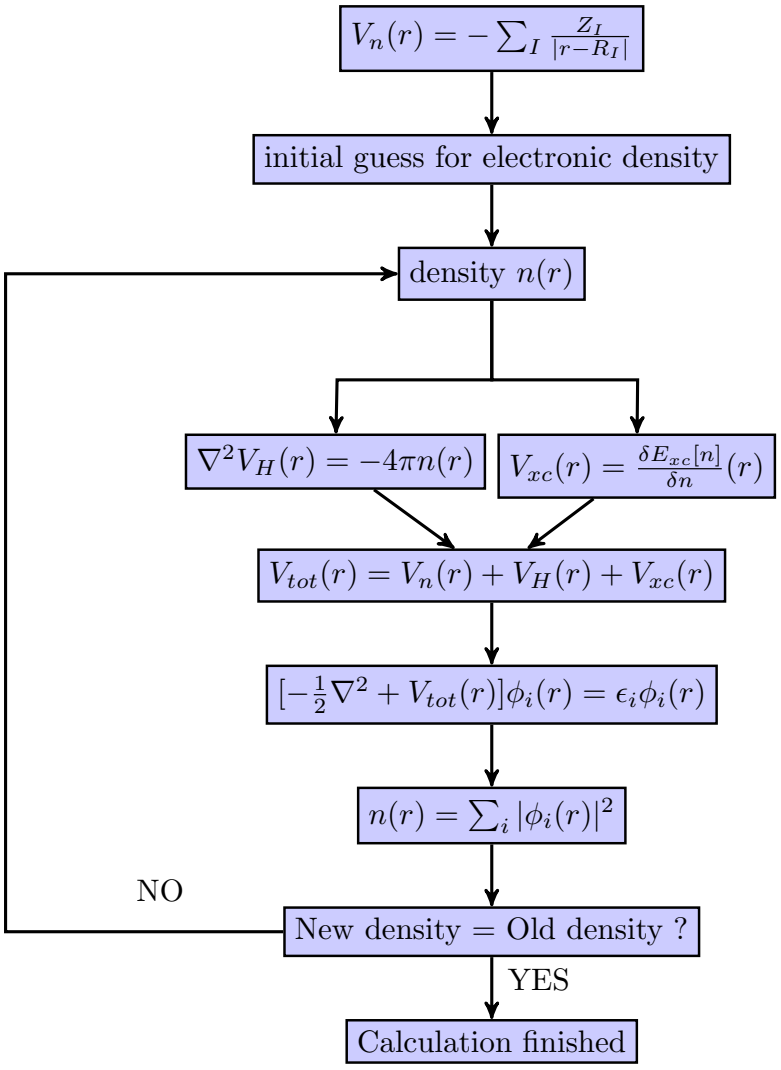

Figure 2.5: *Kohn-Sham scheme from [18].*

2.2.2 Solving with the planes-wave formalism

The code used in this thesis works on a plane waves formalism. In a crystalline material, the Khon-Sham potential is periodic. The associated wave functions are therefore represented in the following form according to Bloch's theorem:

$$\phi_i = u_{i,k} e^{ik.r} \tag{2.21}$$

$u_{i,k}(r)$ is here a periodic function and it is therefore possible to express it as a Fourier series:

$$u_{i,k}(r) = \frac{1}{\sqrt{\Omega_{cell}}} \sum_n c_{i,n}(k) e^{iG_n.r} \tag{2.22}$$

The ϕ_i wave functions can therefore be expressed in a plane wave basis whose wave vectors are the $k+G$. The Kohn-Sham equation can also be written in Fourier space. The matrix elements of the Hamiltonian are then written :

$$H_{n,m}^{KS}(k) = \frac{|k+G|}{2}\delta_{nm} + V^{KS}(G_n - G_m) \tag{2.23}$$

Its resolution gives access to the Fourier coefficients and thus allows to find the ϕ_i. The expression of 2.5 in Fourier space is simpler and it is this calculation that is solved in practice. It is a matrix diagonalization. The plane wave basis on which is expanded $u_{k,n}$ is in theory infinite. The computational time needed to find the eigenvalues in 2.23 is practically linked to the number of eigenvectors on which is expanded $u_{k,n}$. In practice a cut-off energy is defined with the aim of limiting the number of eigenvectors in the expression of $u_{k,n}$. The eigenvectors used in the expression of $u_{k,n}$ are those satisfying

$$\frac{|k+G|^2}{2} < E_{cut} \tag{2.24}$$

The ϕ_i wave functions are therefore expressed using the lowest eigenvectors. A reliable description of the sharp parts of the wave function requires however the introduction of more eigenvectors. These sharp parts of the wave function are usually located near the nuclei. In order to avoid having to use too many eigenvectors to describe the wave function, only the electrons belonging to the valence layers are handled in DFT. The effects of valence electron interactions are represented by the introduction of a pseudopotential term V_{pp} in the Kohn-Sham equation:

$$[\frac{-\nabla^2}{2} + V_{KS} + V_{pp}]\phi_i^{pp} = e_i^{pp}\phi_i^{pp} \tag{2.25}$$

Below a cut-off radius Rc, the wave functions are much smoother than the real wave functions. The pseudopotential is calibrated in such a way that for a larger radius Rc the all-electron wave functions and the wave functions calculated in DFT are similar (Figure 2.6).

As can be seen in equation 2.23, the coefficient $u_{n,k}$ found depends on k. It is not possible to compute the $u_{n,k}$ for an infinite number of points k and in practice a mesh is made to compute it only for some discrete values. The more points the mesh has, the more precise but also the longer the computation is.

It is therefore necessary to choose which parameters to select: the pseudo-potential used, the value of the energy cut-off and the k-point mesh. In practice, convergence studies are performed to fix these parameters. In this work, if not specified, the cut-off energy has been fixed at 50 Ry in calculations including oxygen and at 20 Ry for calculations including only silicon. The calculations were performed with a single k-point located in Gamma. For some types of calculations, the convergence parameters have been changed.

The DFT method of defect simulation uses supercells and periodic boundary conditions. A defect simulated in a too small box would interact with its periodic replica. The defects are therefore simulated in boxes supposed to be large enough to avoid interactions between a defect and its replicas. The size of these DFT cells varies in this thesis between 216 atoms and 1000 atoms depending on the type of simulation.

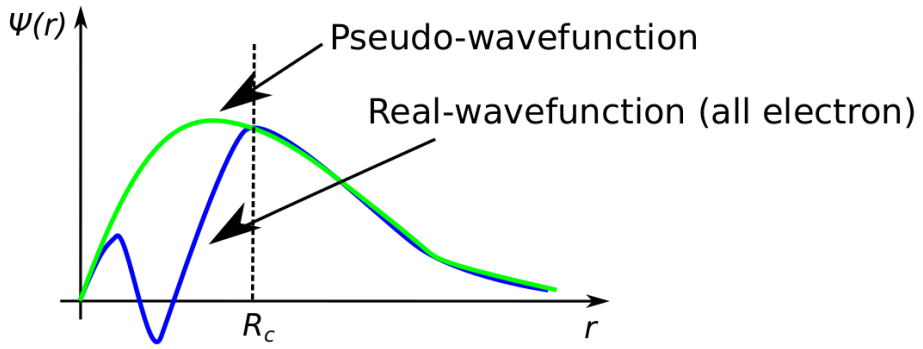

Figure 2.6: *Illustration of the pseudopotential concept from [14].*

2.2.3 Hybrid functionals and DFT bandgap problem

The theory of Hoenenberg and Kohn states that the energy of a system is a density functional but only in the case where the system is not excited. One of the limitations of this theory is that it does not allow to calculate the energy of the excited system. In order to study the effect of the addition of a charge in a system and to analyze its contribution to the dark current, it is nevertheless essential to know the excited states of a system. It could be tempting to use the Kohn-Sham equation in this case. Unfortunately, it has been shown that in the case of semiconductors the use of the Kohn-Sham equation leads to an underestimation of the band gap of the material.

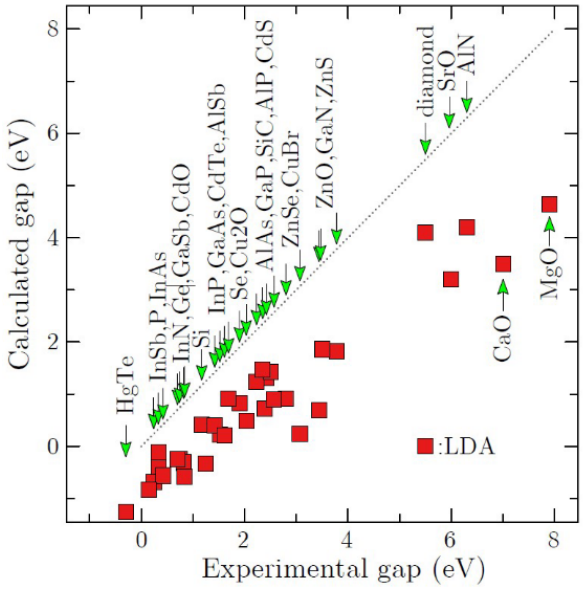

Figure 2.7: *Experimental band gap against calculated band gap using LDA, reproduced from [19].*

In order to solve this problem, several solutions exist. The solution used here is to use another type of functional that predicts a correct gap, the hybrid functionals. Hybrid functionals are a mixture of a classical functional and a contribution of the exact exchange term calculated from the Hartree-Fock equation. The hybrid functional used here is a so-called HSE (Heyd-Scuseria-Ernzerhof hybrid functional) functional. In the HSE formalism, the correlation exchange contribution is written as follows:

$$E_{xc}^{\omega PBEh} = aE_x^{HF,SR}(\omega) + (1-a)E_x^{PBE,SR}(\omega) + E_x^{PBE,SR}(\omega) + E_c^{PBE} \tag{2.26}$$

The HSE functionals have two parameters: the first one a corresponds to the fraction of the exchange parameter to be used and the second one ω corresponds to the distance of the short range interactions. HSE calculations require convergence calculations to calibrate the parameters. In particular, the parameter a chosen must allow the calculation of the correct bandgap of the silicon. In this work the parameter a satisfying this condition is 0.25. The HSE calculation also requires a refinement of the mesh of the reciprocal space that it is also necessary to calibrate. HSE calculations are more time consuming than a classical DFT calculation.

Other methods exist to obtain a correct bandgap or the right level of defect in the bandgap. GW calculations [19] or the DFT+U [20] method can be cited as alternative ways to correct the bandgap problem.

2.2.4 Exploration of potential energy surface

The first step in exploring a potential energy surface is to find the atomic positions leading to the most stable structures. A DFT calculation allows to associate an energy to a given atomic structure. In addition to this energy, it is possible to calculate the forces acting on each atom at the end of a DFT calculation using the Hellmann-Feyman theorem [21]. It is possible to change the atomic coordinates in a new calculation by following these forces in order to reduce them and then to start a new DFT calculation from these new atomic coordinates, re-calculate the forces and re-iterate the procedure. The goal of this approach is to minimize the forces at each DFT iteration and can be implemented using several algorithms. The forces converge to 0 and from a certain threshold it is possible to estimate that the atomic positions found generate quasi-zero forces and that this structure corresponds to an extremum of the potential energy surface. Since the calculation minimizes the forces, it is all the more likely that the positions found correspond to a local minimum of the potential energy surface and are in this case associated with stable structures.

To know which configurations are the most likely to be formed in a process, it is necessary to calculate their formation energies. The formation energies make it possible to compare configurations with different types of atoms as well as with different charge states. In a semiconductor, the energy of formation of a level of a charged defect evolves according to the chemical potential in the material. For a chemical potential close to the valence band, positively charged defects become more stable while negatively charged defects are more stable for a chemical potential close to the conduction band. The formation energy for a defect comprising several species is calculated as follows:

$$E_f(q) = E_d(q) - \sum_i n_i \mu_i + q(E_V + \mu_e) + \alpha_M \frac{q^2}{L\epsilon} \tag{2.27}$$

In this equation, q is the charge in the simulation, E_d represents the energy of the supercell with the defect calculated in DFT, μ_i is the chemical potential of the species i, μ_e is the Fermi level, E_v the energy level of the Valence band. The last term of the equation is implemented to take into account the electrostatic interactions between the simulation cells (the simulations having periodic boundary conditions, a charged defect interacts with its periodic repetition).

Once the stable states are found, it is interesting to find out how to go from one to the other. The most probable way to go from one stable state to the other is the one with the smallest maximum energy. The configuration that minimizes the energy barrier to cross between two stable positions corresponds mathematically to a saddle point of the PES.

In order to find these saddle points, there are several methods. Among them:

- The Nudged Elastic Band (NEB) formalism [22]. This approach allows to minimize the energy path between 2 configurations. Several configurations are initially interpolated between the starting position and the final position. Several cycles are then performed to find the minimum energy path. These cycles correspond to energy minimizations of these intermediate positions modified as follows:
  - A restoring force is added between the different configurations. This restoring force prevents the intermediate configurations from falling into energy minima
  - The intermediate configurations are relaxed only in the hyperplane perpendicular to the tangent of the path between the different configurations.

  The simulation time of a NEB calculation is very important because it consists of minimization cycles on each intermediate configuration. The larger the number of intermediate points, the more accurate the computation of the tangent at the path is and the fewer iterations are required. On the other hand, the number of points on which to perform the minimizations increases with the number of intermediate configurations. It is therefore necessary to make a compromise in the choice of the number of configurations to optimize the computation time.

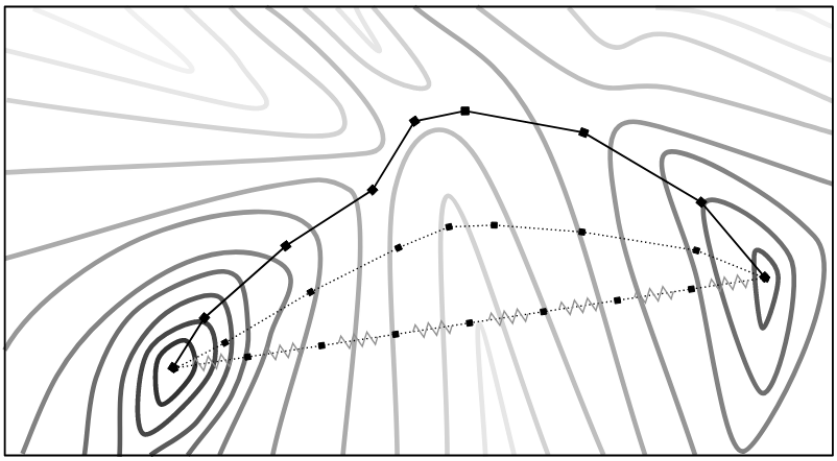

Figure 2.8: *Illustration of a calculation between two atomic configurations using NEB calculation. The lines in the background represent the isopotential surfaces of the PES. The lines connected by squares represent the intermediate configurations at different cycles of the calculation.*

- The activation-relaxation techniques [23]. These methods allow to identify saddle points without calculating a complete energy path between two configurations. The operation of the activation-relaxation technique is explained in the Figure 2.9. One of the objectives of ARTn is to explore the PES around a local minimum.
  The principle then follows three steps:
  - leave the harmonic basin
  - look for a saddle point,
  - leave this saddle point to find another local minimum of the PES

  To leave the harmonic basin, the algorithm pushes the atoms out of their equilibrium positions in a random direction. The system is then relaxed in the hyperplane perpendicular to the push direction. The eigenvalues of the Hessian matrix are then computed. If all the eigenvalues are positive, the position is still in the harmonic basin. The random push

followed by relaxation are then reiterated until a Hessian with a negative eigenvalue is found.

Once outside the harmonic basin, the configurations are no longer pushed in a random direction but according to the eigenvector associated with the lowest eigenvalue of the Hessian (negative because outside the harmonic basin). The pushes are again repeated iteratively and separated by relaxations in the hyperplane perpendicular to the push direction. The goal here is to converge on the saddle point. The weaker the forces are, the smaller the norm of the push vector is. Below a threshold of fixed forces, the algorithm considers that the saddle point is reached.
The last phase of the algorithm consists in finding the local minimums connected to the saddle point. A push is performed from the point in the direction of the initial saddle point-configuration and a push from the saddle point in the opposite direction. After the push the configurations are relaxed to fall into a local minimum.
In order to find a point connecting two configurations, it is possible to use ARTn in an alternative mode. The starting point is set as the linear interplication between the initial and the final configuration. This configuration is not, for most cases, a local minimum and is often outside a harmonic basin. In this case the algorithm starts at phase 2, pushing in the direction of the lowest eigenvalue of the Hessian matrix.

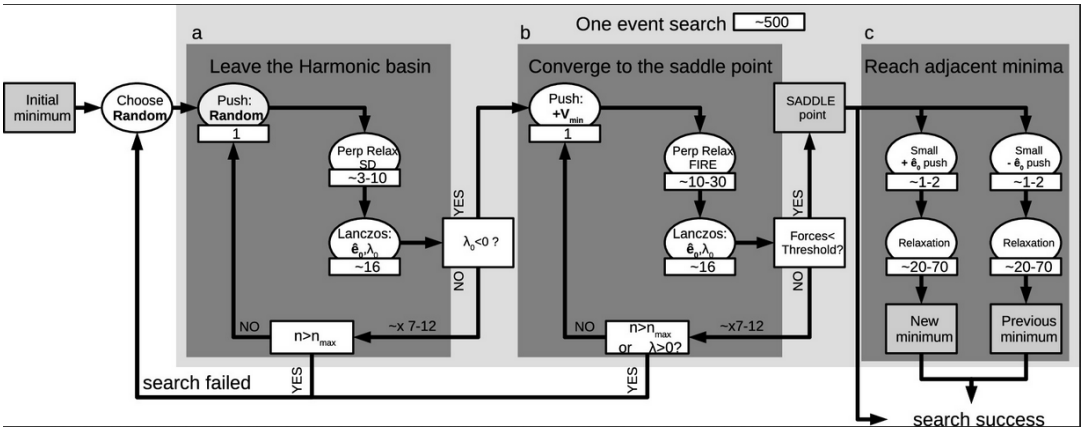

Figure 2.9: *ARTn working scheme [24] where the three main phases of the algorithm are depicted within the shaded dark gray rectangles. Phase (a) involves escaping from the harmonic basin; phase (b) focuses on converging towards the saddle point; and phase (c) centers on reaching the neighboring minima.*

2.2.5 Phonons calculations in DFT

In section 2.1.2, it was shown that in the transition state theory, the knowledge of a transition rate depends on an entropic prefactor. This prefactor could be calculated using the normal vibration frequencies in the initial and saddle point configurations. An estimation of these frequencies is possible in DFT. The kinetic and potential energies of the nuclei had been put aside in equation 2.8. The nuclei are not immobile and oscillate around their equilibrium position. These oscillations are essential to take into account when modeling atomic mechanisms because they allow jumps from one stable configuration to another. If these oscillations are not too large (much smaller than the inter-atomic distances), it is possible to study these oscillations by focusing on the displacement of the atoms relative to their equilibrium position:

$$\vec{u}(\vec{R_I}, t) = \vec{r}(\vec{R_I}, t) - \vec{R}_{I,eq} \tag{2.28}$$

Still under the assumption of small displacements, the interaction term V_{nn} can be expressed using a Taylor expansion to second order (harmonic approximation):

$$V_{nn} = V_0 + \sum_{l,\kappa,\alpha} u^{\alpha}_{l,\kappa} \frac{\partial V_{nn}}{\partial u^{\alpha}_{l,k}} + \frac{1}{2} \sum_{l,\kappa,\alpha,l',\kappa',\beta} u^{\alpha}_{l,\kappa} u^{\beta}_{l',\kappa'} \frac{\partial^2 V_{nn}}{\partial u^{\alpha}_{l,\kappa} \partial u^{\beta}_{l',\kappa'}} \tag{2.29}$$

The first term V_0 is a constant. The second term is zero if the studied position is a minimum of the potential energy surface. By omitting the constant term, the potential energy is similar to the case where the N atoms are connected by springs. It is interesting in the context of this analogy to define the stiffness constants $\Phi^{\alpha\beta}_{l\kappa l'k'}$ linking the atoms together:

$$\Phi^{\alpha\beta}_{l\kappa l'\kappa'} = \frac{\partial^2 V_{nn}}{\partial u^{\alpha}_{\kappa,l} \partial u^{\beta}_{\kappa',l'}} \tag{2.30}$$

From the point of view of classical mechanics, the oscillation of nuclei around their equilibrium positions is associated with a kinetic energy that can be written :

$$T = \frac{1}{2} \sum_{\kappa,l,\alpha} M_{\kappa,l} (\frac{\partial u^{\alpha}_{\kappa,l}}{\partial t})^2 \tag{2.31}$$

Using the Lagrangian formalism it is possible to find equations linking the second time derivative of the displacements $u^{\alpha}_{l,\kappa}$, the stiffness constants Φ from equation 2.29 and the kinetic energy 2.31:

$$\frac{\partial^2 u^{\alpha}_{l,\kappa}}{\partial t^2} = - \sum_{l',\kappa',\beta} \Phi^{\alpha\beta}_{l,\kappa,l',\kappa'} u^{\beta}_{l',\kappa'} \tag{2.32}$$

It is also possible to find equation 2.32 with a quantum treatment. It is necessary to use the Heisenberg picture (for more details the reader can refer to [25]). The difference in this case is that the u^{α}_{knl}'s are no longer coordinates in space but operators.

It is possible to solve the equation by assuming that the displacements are a sum of plane waves:

$$\vec{u}_{lk} = \frac{1}{\sqrt{M_k}} \vec{e}_{lkq} e^{\vec{q}.\vec{r}_l} e^{-iwt} \tag{2.33}$$

It is then more convenient to solve the equation 2.32 in the reciprocal space. The system to be solved can then be expressed in the form:

$$\omega^2_q e^{\alpha}_{l,\kappa}(q) = \sum_{\kappa',\beta} D^{\alpha,\beta}_{\kappa\kappa}(q) e^{\beta}_{l',\kappa'}(q) \tag{2.34}$$

The coefficients $D^{\alpha,\beta}_{\kappa\kappa}$ form here the elements of a matrix, called dynamic matrix, and are given by:

$$D^{\alpha\beta}_{\kappa\kappa'}(q) = \sum_{L} \frac{\Phi^{\alpha\beta}_{\kappa\kappa' L}}{\sqrt{M_\kappa M_{\kappa'}}} e^{i\vec{q}\vec{r}_L} \tag{2.35}$$

It is then possible to obtain the normal frequencies of vibration by calculating the eigenvalues of the dynamic matrix. The DFT calculations to find the phonon frequencies are based on a calculation of the dynamic matrix. This calculation can be done in several ways.

The first one is to move one by one the atoms from their equilibrium positions in the three directions of space and to compute the forces. Forces are the primary derivation of energy in relation to atomic positions. It is possible to find the first derivatives of the eigenvalues of a Hamiltonian as a function of a parameter α by deriving this Hamiltonian and using the eigenvectors of this Hamiltonian .

$$\frac{\partial E_\alpha}{\partial \alpha} = \langle \Phi_\alpha | \frac{\partial H_\alpha}{\partial \alpha} | \Phi_\alpha \rangle \tag{2.36}$$

It is possible to verify that the derivative of the contributions of the electron-nucleus interactions of the Hamiltonian is a function of the density, known at the end of a DFT calculation. The Φ coefficients correspond to the derivatives of the forces with respect to an atomic deformation. By calculating the forces for each displacement of atoms in the 3 directions of space it is thus possible to obtain an approximation of the derivative of the forces with respect to the displacements : This method, called frozen phonon, is in practice quite long if all the atoms of the simulation box are taken into account. The number of atoms moved in the study of a defect in a supercell is therefore often limited to the atoms close to the defect.

Another method of calculating phonons is based on the perturbation theory [26]. As mentioned above, the forces can be known at the end of a DFT calculation using the electron density. The force constants being the derivative of the forces with respect to the atomic positions, it can be shown that these constants depend on the derivative of the electronic density with respect to the atomic positions. One way to calculate this derivative is to calculate the linear response of the density with respect to the atomic displacements. This linear response can be calculated using perturbation theory applied to the wave functions found after a DFT calculation.

2.3 Continuum process modeling

The larger scale method to simulate the implantation and annealing processes are called here continuous methods. They are sometimes also named in the literature as Partial Differential Equations (PDE) methods. This name distinguishes these approaches based on a representation in the form of continuous profiles of the impurity concentrations whose evolution is governed by differential equations, from methods such as the KMC, where the defects are represented in a discrete way and whose evolution is calculated in a probabilistic way.

2.3.1 Continuum modeling on the implantation

The first goal of an implantation process simulation is to have a reliable prediction of the dopant distribution as-implanted. For this purpose, several models are available in the simulation software.

The first solution is to assume a profile shape for the implanted species. This profile can be assumed with different shape: Gaussian, Pearson, Dual-Pearson (Pearson and Dual-Pearson distributions are compared to boron implantation in Figure 2.10).

Depending on the energy and the implantation dose, the profile is adapted according to calibrated tables.

Another method uses a probabilistic method. This method is the MC implantation described in subsection 2.1.4 but without the KMC steps between each incident particles.

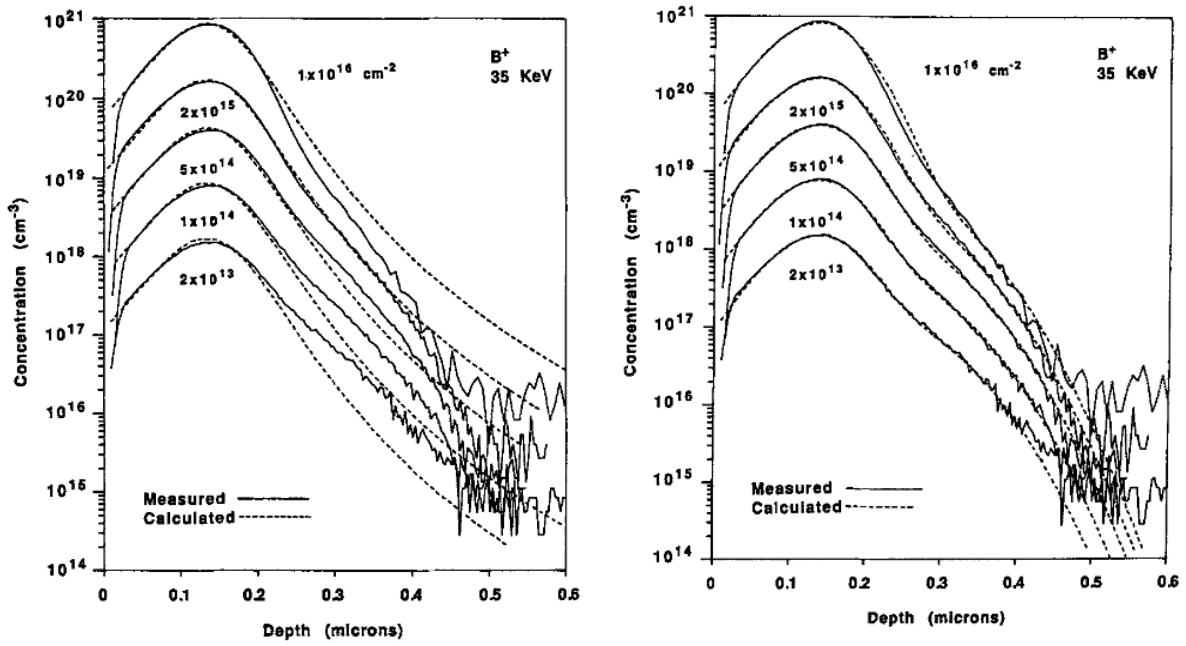

Figure 2.10: *(Left) Comparison between implanted Boron profiles and Pearson profiles (Right) Comparison between implanted Boron profiles and dual Pearson distributions.*

At the end of the implantation, it is also useful to know if an amorphous layer is created. For this purpose, a damage field is created depending on the implanted ion, its energy and its dose. This profile can be reparameterized. Above a threshold value of damage, a mesh element is considered as amorphous. This method allows an estimation of the thickness of the amorphous layer but does not guarantee the same accuracy as the KMC simulations which take into account the dynamic aspect of the evolution of the state of the material as the implantation proceeds. This number allows to simulate correctly the diffusion of dopants during annealing and the evolution of extended defects. For this purpose, the +n models are implemented where n is a function of the implanted species. The different cases of an amorphous layer or a crystalline material are presented in Chapter 1.

2.3.2 Continuous modeling of the evolution of the dopant profile during annealing

The description proposed here of the continuous model is largely inspired by [27] and the reader can refer to it for more information. During annealing, continuous simulations are used to reproduce the diffusion of dopants. This diffusion is based on the five stream model. As mentioned in Chapter 1, dopants generally diffuse more easily when they form pairs with a point defect (interstitial or vacancy). The mechanisms of dissociation or interaction of a dopant atom with these point defects or the interaction between point defects must be taken into account to model the diffusion of dopants. The different possible mechanisms for the diffusion of a given dopant A are summarized below:

$$\begin{cases} I + A \longleftrightarrow AI(Imechanism(IM)) \\ V + A \longleftrightarrow AV(Vmechanism(VM)) \\ I + AV \longleftrightarrow A(Dissolationmechanism(DM)) \\ V + AI \longleftrightarrow A(Frank - Turnbullmechanism(FT)) \end{cases} \tag{2.37}$$

In addition to reactions with dopants, interstitials and vacancies can interact with each other (formation or annihilation of a Frenkel pair).

$$I + V \longleftrightarrow 0 \tag{2.38}$$

For each type of reaction, generation-recombination rates G and R are defined and allow to monitor the evolution of the concentration of dopant-defect, dopant and point defects pairs during annealing. The creation or annihilation rates (G-R) of a defect using one of the mechanisms described in the equation 2.37 are calculated using the concentrations of the defects involved in the mechanism and the reaction coefficients K_f and K_r :

$$\begin{cases} (G-R)_{IM} = K_f^{IM} C_I C_{As} - K_r^{IM} C_{AI} \\ (G-R)_{VM} = K_f^{VM} C_V C_{As} - K_r^{VM} C_{AV} \\ (G-R)_{FT} = K_f^{FT} C_{AI} C_V - K_r^{FT} C_{A_s} \\ (G-R)_{DM} = K_f^{DM} C_{AV} C_I - K_r^{DM} C_{A_s} \\ (G-R)_{BR} = K^{BR} (C_I C_V - C_I^* C_V^*) \end{cases} \tag{2.39}$$

The notation C_X^* refers here the concentration of defects at equilibrium. Point defects can also be captured or released by defect clusters formed during the process. It is then necessary to add generation and annihilation rates for the defect clusters.

$$\begin{cases} \frac{\partial C_{As}}{\partial t} = -(G-R)_{IM} - (G-R)_{VM} + (G-R)_{DM} + (G-R)_{FT} + (G-R)_{A_s}^{clusters} \\ \frac{\partial C_{AI}}{\partial t} = \nabla D_{AI} . \nabla D_{AI^0} + (G-R)_{IM} - (G-R)_{FT} + (G-R)_{AI}^{clusters} \\ \frac{\partial C_{AV}}{\partial t} = \nabla D_{AV} . \nabla D_{AV^0} + (G-R)_{VM} - (G-R)_{DT} + (G-R)_{AV}^{clusters} \\ \frac{\partial C_I}{\partial t} = \nabla D_I . \nabla D_{I^0} + (G-R)_{IM} - (G-R)_{FT} - (G-R)_{BR} + (G-R)_I^{clusters} \\ \frac{\partial C_V}{\partial t} = \nabla D_V . \nabla D_{V^0} + (G-R)_{VM} - (G-R)_{DM} - (G-R)_{BR} + (G-R)_V^{clusters} \end{cases} \tag{2.40}$$

These five coupled equations constitute the five stream model used to predict the evolution of the doping profile during annealing processes. Several models exist to simulate the evolution of the concentration of extended defects. The term corresponding to the interstitial flows can be simulated using several different models.

In addition to being essential for a reliable simulation of dopant profiles, the interstitial term emitted by clusters can also be used to estimate the presence of extended interstitial defects. Several types of defects can emit interstitials as mentioned Chapter 1: interstitial clusters, impurity-interstitial clusters, {311} defects and dislocation loops. A first method to evaluate the number of interstitial emitted or captured by defects containing a limited number of interstitial was developed in the work of [28] and [29]. This method consists in implementing a differential equation by cluster concentration of interstitials of size n (the size refers here to the number of interstitials in the cluster). At each time step of the continuous simulation, the concentration of an interstitial cluster of size n evolves according to several mechanisms:

- Clusters of size n can evolve into clusters of size n+1 when they capture a free interstitial in the silicon.
- A cluster of size n can emit an interstitial and thus evaporate into a cluster of size n-1

- A cluster of size n can be generated by the emission of uh interstitial from a cluster of size n-1
- A cluster of size n can be generated by the capture of a free interstitial by a cluster of size n-1.

These four mechanisms can be summarized in the following equation allowing to predict the evolution during annealing of the concentration of interstitials trapped in a cluster of size n:

$$\frac{\partial C_n}{\partial t} = E_{n+1}C_{n+1} + F_{n-1}C_{n-1}C_I - E_nC_n - F_nC_nC_I \tag{2.41}$$

The evolution of the different cluster sizes during annealing depends on the emission and capture constants of each cluster size. For the capture constant a simple model allows to assume that the capture coefficient of a cluster is proportional to its size.

The interstitial emission coefficients depend on the activation energy required to emit an interstitial from a cluster.

Since the emission constant depends exponentially on these energies, their calibration is crucial. A first estimate of these activation energies has been made in [29]. In the [29] work, the energies were calibrated to reproduce the supersaturation extracted with the help of Boron marker diffusion. Boron markers were implanted deep into the wafer and then Si+ was implanted. The wafer was then annealed at different times and temperatures and the evolution of the boron marker profile for the different anneals was measured in SIMS. Because boron diffuses through a kick out mechanism using interstitials, boron diffusion was related to an interstitial supersaturation value. The activation energies chosen for interstitial emission from the different cluster sizes were the energies to reproduce the experimental supersaturation trends.

If we are only interested in the effect of these clusters on the diffusion of dopants and not on the zoology of the clusters themselves, the model can be simplified. In the work of Zechner [30], it was shown that taking into account only four cluster sizes allowed to simulate a supersaturation in agreement with the experimental trends. In the work of [30] and [29] it is also shown that it is necessary to introduce a cluster with an energy for interstitial emission in order to reproduce the experimental results. Historically [29] had placed maximum activation energies on clusters of sizes 4 and 8 to be in agreement with ab initio calculations on interstitial clusters. The issue of calibration of the activation energy for interstitial emission from clusters will be discussed in more detail in Chapter 4.

For defects with a large number of interstitials like DLs and {311} defects, another model is used [31]. It is based on a two moment approach. In this formalism the distribution of {311} defects or DLs of different sizes are grouped into two distribution, C311 and Cloops. These distributions are the first moment of the the different size distributions and contain the average concentration of interstitials trapped in the {311} defects and in the loops. The second moments of these distributions D311 and Dloops are also calculated and represent the average interstitial concentration per defect.

2.4 Conclusion

Several simulation methods have been described here. The next two chapters in this thesis consists in using them, and in particular the KMC methodology. This method has the advantage

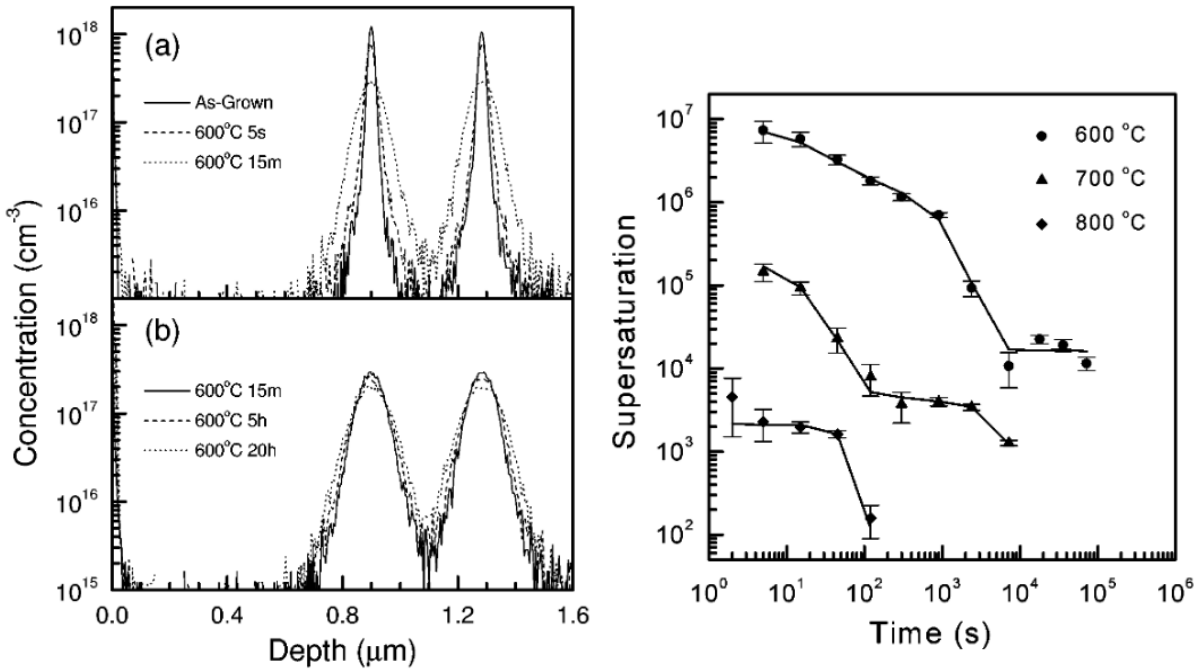

Figure 2.11: *(Left) Boron marker scattering after Si+ implantation as a function of annealing time [29] (Right) Extraction of supersaturation using Boron marker diffusion as a function of temperature and annealing time.*

of being able to link DFT simulations at the atomic scale to continuous simulations at the device scale. The calibration of this KMC for a new element based on DFT calculations is presented in Chapter 3. The link between continuous simulations and KMC will be further developed in Chapter 4 where a combination of both methods will be used to simulate heated implementations followed by annealing.

References

[1] Sentaurus Process User Guide, R-2020.09, Synopsys Inc.

[2] M. Michaillat, D. Rideau, F. Aniel, C. Tavernier, and H. Jaouen, "Monte carlo-based analytical models for electron and hole electrical parameters in strained sigec alloys", in 2009 international conference on simulation of semiconductor processes and devices (IEEE, 2009), pp. 1–4.

[3] W. Krauth, *Statistical mechanics: algorithms and computations*, Vol. 13 (OUP Oxford, 2006).

[4] N. Metropolis, A. Rosenbluth, M. Rosenbluth, A. Teller, and E. Teller, "Introduction of the metropolis algorithm for molecular-dynamics simulation", J. Chem. Phys **21**, 1987 (1953).

[5] A. B. Bortz, M. H. Kalos, and J. L. Lebowitz, "A new algorithm for monte carlo simulation of ising spin systems", Journal of Computational Physics **17**, 10–18 (1975).

[6] H. Eyring, "The activated complex in chemical reactions", The Journal of Chemical Physics **3**, 107–115 (1935).

[7] G. H. Vineyard, "Frequency factors and isotope effects in solid state rate processes", Journal of Physics and Chemistry of Solids **3**, 121–127 (1957).

[8] M. T. Robinson and I. M. Torrens, "Computer simulation of atomic-displacement cascades in solids in the binary-collision approximation", Physical Review B **9**, 5008 (1974).

[9] G. Calogero, D. Raciti, P. Acosta-Alba, F. Cristiano, I. Deretzis, G. Fisicaro, K. Huet, S. Kerdilès, A. Sciuto, and A. La Magna, "Multiscale modeling of ultrafast melting phenomena", npj Computational Materials **8**, 36 (2022).

[10] B. Sklénard, "Physical modeling of junction processing in fdsoi devices for 20 nm node and below", PhD thesis (Université de Grenoble, 2014).

[11] M. Gunde, "Development of ira: a shape matching algorithm, its implementation, and utility in a general off-lattice kmc kernel", PhD thesis (Université Paul Sabatier-Toulouse III, 2021).

[12] M. Gunde, N. Salles, A. Hémeryck, and L. Martin-Samos, "Ira: a shape matching approach for recognition and comparison of generic atomic patterns", Journal of Chemical Information and Modeling **61**, 5446–5457 (2021).

[13] F. El-Mellouhi, N. Mousseau, and L. J. Lewis, "Kinetic activation-relaxation technique: an off-lattice self-learning kinetic monte carlo algorithm", Physical Review B **78**, 153202 (2008).

[14] T. Jarrin, "Modélisation des effets de déplacements atomiques induits par irradiation dans les matériaux pour la microélectronique", PhD thesis (Toulouse 3, 2021).

[15] C. Cohen-Tannoudji, B. Diu, and F. Laloë, *Quantum mechanics, volume 3: fermions, bosons, photons, correlations, and entanglement* (John Wiley & Sons, 2019).

[16] J. C. Slater, "A simplification of the hartree-fock method", Physical review **81**, 385 (1951).

[17] P. Hohenberg and W. Kohn, "Inhomogeneous electron gas phys. rev. 136", B864 (1964).

[18] L. J. Sham and W. Kohn, "One-particle properties of an inhomogeneous interacting electron gas", Physical Review **145**, 561 (1966).

[19] M. van Schilfgaarde, T. Kotani, and S. Faleev, "Quasiparticle self-consistent g w theory", Physical review letters **96**, 226402 (2006).

[20] V. Anisimov and O. Gunnarsson, "Density-functional calculation of effective coulomb interactions in metals", Physical Review B **43**, 7570 (1991).

[21] R. P. Feynman, "Forces in molecules", Physical review **56**, 340 (1939).

[22] H. Jónsson, G. Mills, and K. W. Jacobsen, "Nudged elastic band method for finding minimum energy paths of transitions", in *Classical and quantum dynamics in condensed phase simulations* (World Scientific, 1998), pp. 385–404.

[23] G. Barkema and N. Mousseau, "Event-based relaxation of continuous disordered systems", Physical review letters **77**, 4358 (1996).

[24] A. Jay, C. Huet, N. Salles, M. Gunde, L. Martin-Samos, N. Richard, G. Landa, V. Goiffon, S. De Gironcoli, A. Hémeryck, et al., "Finding reaction pathways and transition states: r-artn and d-artn as an efficient and versatile alternative to string approaches", Journal of Chemical Theory and Computation **16**, 6726–6734 (2020).

[25] C. Cohen-Tannoudji, B. Diu, and F. Laloe, "Quantum mechanics, volume 2", Quantum Mechanics **2**, 626 (1986).

[26] S. Baroni, S. De Gironcoli, A. Dal Corso, and P. Giannozzi, "Phonons and related crystal properties from density-functional perturbation theory", Reviews of modern Physics **73**, 515 (2001).

[27] E. M. Bazizi, "Modélisation physique et simulation de défauts étendus et diffusion des dopants dans le si, soi, sige pour les mos avancés", PhD thesis (2010).

[28] C. J. Ortiz, P. Pichler, T. Fühner, F. Cristiano, B. Colombeau, N. E. Cowern, and A. Claverie, "A physically based model for the spatial and temporal evolution of self-interstitial agglomerates in ion-implanted silicon", Journal of applied physics **96**, 4866–4877 (2004).

[29] N. Cowern, G. Mannino, P. Stolk, F. Roozeboom, H. Huizing, J. Van Berkum, F. Cristiano, A. Claverie, and M. Jaraiz, "Energetics of self-interstitial clusters in si", Physical Review Letters **82**, 4460 (1999).

[30] C. Zechner, N. Zographos, D. Matveev, and A. Erlebach, "Accurate and efficient tcad model for the formation and dissolution of small interstitial clusters and {3 1 1} defects in silicon", Materials Science and Engineering: B **124**, 401–403 (2005).

[31] N. Zographos, C. Zechner, and I. Avci, "Efficient tcad model for the evolution of interstitial clusters,{311} defects, and dislocation loops in silicon", MRS Online Proceedings Library (OPL) **994**, 0994–F10 (2007).

Calibration of the BO_2 cluster in KMC: complexity of the oxygen implementation

3

Contents

Introduction

We are interested in understanding the mechanisms of formation of BO_2 impurity clusters with the ultimate goal of implementing them in commercial process simulation software, in particular sProcess from Sentaurus [1]. To simulate the formation of BO_2 clusters in a KMC code, it is necessary to have implemented the migration and evolution mechanisms of the different species constituting the complex BO_2. In the process simulation code that we use in this work, namely sProcess from Sentaurus, the mechanisms relating to the boron species have already been calibrated and implemented in the KMC [2]. However, we note the lack of oxygen treatment in this KMC software. We then begin this chapter with a theoretical study using ab initio calculations to characterize the atomic migration events likely to be involved in the formation of the BO_2 cluster. Our work here focuses on the mechanisms related to O_i and O_{2i} and their interactions with boron. In a first part of the chapter, the stable structures of O_i, O_{2i} and BO_{2i} are studied. The second part of the chapter is dedicated to the implementation of such atomistic events in the KMC. It describes both the simulations allowing to obtain the input data necessary for the implementation of O_i and O_{2i} in the object KMC [1] and how it has been implemented. The third part of the chapter proposes a more detailed ab initio study of the kinetics and interactions of O_i, highlighting the complex diffusion phenomena of such a specie. The last part of the chapter is devoted to the implementation of the previous mechanisms related to oxygen in an off-lattice KMC and how to relate it to the object KMC of [1]. The process simulations on the formation of BO_2 were not deepened, the ab initio results not confirming their impact on the imagers devices.

3.1 From O_i to BO_{2i} : atomic configurations and electronic activities

3.1.1 O_i structures

Stress analysis in X-ray measurements showed that oxygen naturally tends to occupy an interstitial position in Si [3]. Infrared (IR) measurements also lead to the conclusion that the position of the oxygen O_i is between two neighboring Si-atoms in a position called the bond-center [4]. The bond center position for O_i is considered in this work as the natural starting point for our ab initio simulations.

Considering O_i specie, the first step of our DFT calculations is to find the stable configurations in which the specie can exist using relaxation. Previous work [5] have shown the existence of several configurations very close in energy. These configurations correspond to an oxygen between two neighbouring Si atoms and are distinguished from each other by their symmetry.
In our work, we also studied several configurations. The tested configurations have D_{3d}, C_{1h} and C_1 symmetries (shown in Figure 3.1). In the D_{3d} configuration, O_i is located on the axis passing through the two Si with which it is linked. In the C_{1h} configuration, O_i is in the (101) plane passing through its two neighbouring Si atoms but deviates from the axis passing through the two Si atoms. In the C_1 configuration, there are no more symmetries and O_i is slightly outside the (101) plane.

The differences between the calculated formation energies of the three configurations are very small, both in PBE and in HSE (see Table 3.1). However, the configurations C_1 and C_{1h} have lower formation energies than the configuration D_{3d} configuration. The energy difference between the two configurations C_1 and C_{1h} is lower than the DFT accuracy (which is around 0.01 eV according to our convergence study). The study of the transition between these two

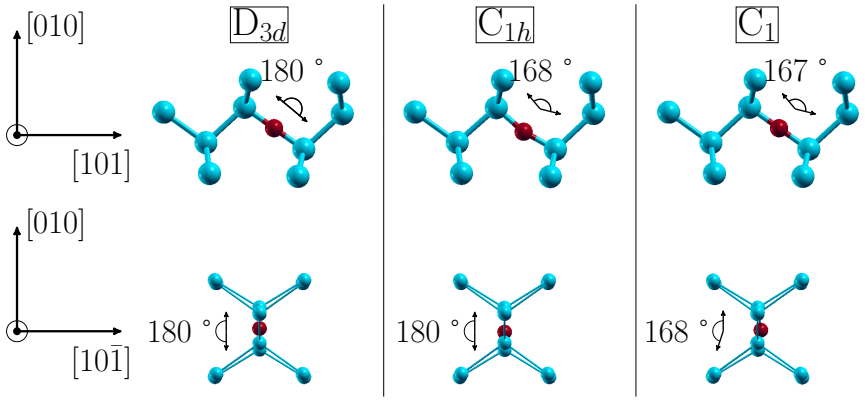

Figure 3.1: *Different O_i configurations relaxed with ab initio calculations, from left to right: D_{3d}, C_{1h} and C_1. The configurations are represented in a (101) plane (top) and in its orthogonal plane (10$\bar{1}$) (bottom).*

configurations shows that the energy barrier to go from one to the other is also very low, also lower than the DFT accuracy. The position of the oxygen in the C_{1h} configuration differs slightly from those found by [5]. The distance between the O_i atom and the Si atoms is the same but the angle formed by the Si-O-Si bond is higher in our work than in [5]. The relaxation of the C_{1h} with a smaller Si-O-Si angle have been tested but leads to the same final structure. The distance and angle can also be compared to more recent ab initio studies. The distance and angle found for our C_{1h} are in fair agreement with the one calculated by [6]. In their work, the O_i in the (101) plane has an angle of 165 ° and a distance Si-O of 1.62 . In the work of [7] the angle is 162 ° and Si-O bond 1.63 which is between our results and the one of [5]. The comparison with the experimental data is not obvious due to the different conclusions found in the literature and the very small energy differences of the configuration. The positions out of the Si-Si axis for the oxygen have been studied using IR measurements. In the work of [8], it is believed that the O_i forms an angle of 164 ° with the $< 111 >$ direction. However, the IR measurements coupled to peaks of the theoretical models are more consistent with an O_i in an effective position D_{3d} [9][10]. In these works, the energy barriers are of the meV, so that the O_i is considered as tunneling from the position out of the Si-O-Si axis with a maximum probability in the D_{3d} position.

In order to determine whether these configurations change their stability when a charge is associated with the oxygen, additional calculations have been performed with charges in the DFT supercell. The positions of the three structures were relaxed with a negative charge as well as with a positive charge. Once relaxed, the energy of these structures was also calculated using the HSE formalism. The formation energy as a function of the charge state of the structures is shown in Figure 3.2. It is observed that the most stable charge state is the neutral charge state, independently of the Fermi level.

3.1.2 O_{2i} structures

A similar study has been conducted on the O_{2i} dimer, consisting of a pair of oxygen atoms. The configurations tested are the configurations called squared and staggered in the literature [11]. In these two configurations, the two oxygen atoms are in a (101) plane. Several studies do not agree on the most stable configuration of O_{2i}. The work of [11] showed that at a Fermi

Table 3.1: *Comparison of O_i formation energies, distances and angles between our work (both in PBE and HSE) and other DFT calculations of Coutinho [5], Binder [6] and Timerkaeva [7].*

	Relative energy (meV)		
	C_1	C_{1h}	D_{3d}
Our work PBE	0	0.00	2.25
Our work HSE	0	0	45.67
Coutinho	8	0	12
	Distance Si-O ( )		
Our work PBE	1.63	1.63	1.63
Coutinho	1.62	1.62	1.61
	Angle Si-O-Si (°)		
Coutinho	166	157	180
Binder	-	165	-
Timerkaeva	-	161	-

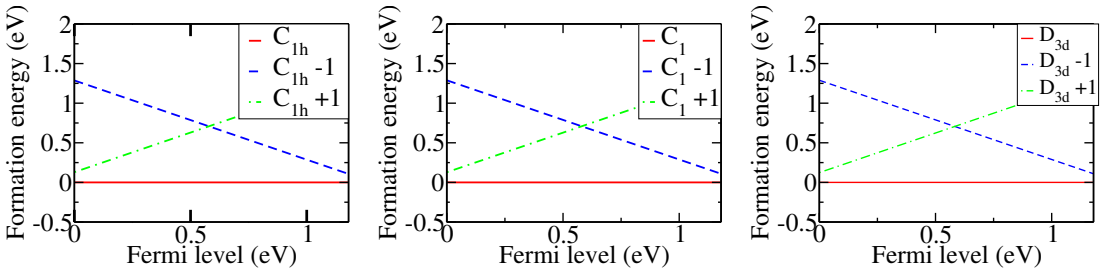

Figure 3.2: *O_i formation energies in C_1, C_{1h} and D_{3d} configurations in charge state -1, 0 and +1 calculated with HSE.*

level lower than 0.9 eV, the most stable configuration was a squared O_{2i} (with two positives charges). Conversely, the calculations of [12] show that the stable O_{2i} configuration is the staggered configuration for any Fermi level.

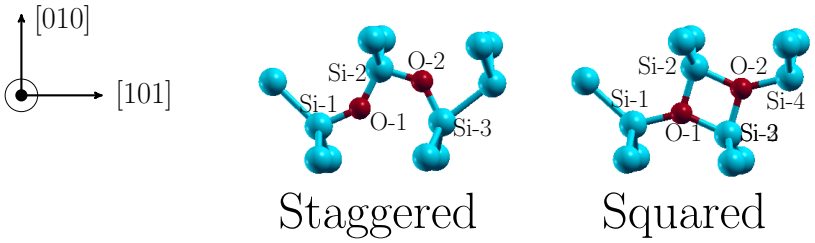

Figure 3.3: *O_{2i} configurations: staggered (left) and squared (right) in a (101) plane from ab initio simulations.*

We relaxed the two structures with a PBE functional for neutral charge states, with one positive charge and two positive charges. In order to compare the charge states, the energies of these structures were also calculated with the HSE formalism. The formation energies of squared and staggered structures with different charge states as a function of the Fermi level are presented in Figure 3.4. We note that for any Fermi level, the most stable structure is the staggered configuration in a neutral charge state. The results of our calculations are thus in agreement with those of [12]. The difference with the results of [11] can be explained by the different level of theory (use of HSE functional) and also by the method used for the formation energy calculation. For the latter, as mentioned in Chapter 2, in our calculations a term is added to correct the effect

Table 3.2: *Distances (in Å) and angles (in °) between atoms for O_{2i} staggered structure from our work comparing data available in the literature [5][13].*

	O1-Si1	O1-Si2	O2-Si2	O2-Si3	—	Si-O1-Si	Si-O2-Si
Our work PBE	1.66	1.64	1.64	1.68	—	140.2	133
Coutinho	1.66	1.64	1.63	1.67	—	130	127
Timerkaeva	1.63	1.61	1.62	1.64	—	143	145

of periodic conditions in the presence of an electrical charge. Indeed, the charge of a cell can interact with the periodic replication of the cell. Unlike the work of [12], this interaction is not taken into account in [11]. For sake of clarity, if we do not add this term in the calculation of our formation energy, we obtain a good agreement with the work of [11]: the O_{2i}-squared 2+ becomes stable at a Fermi level below 0.2 eV.

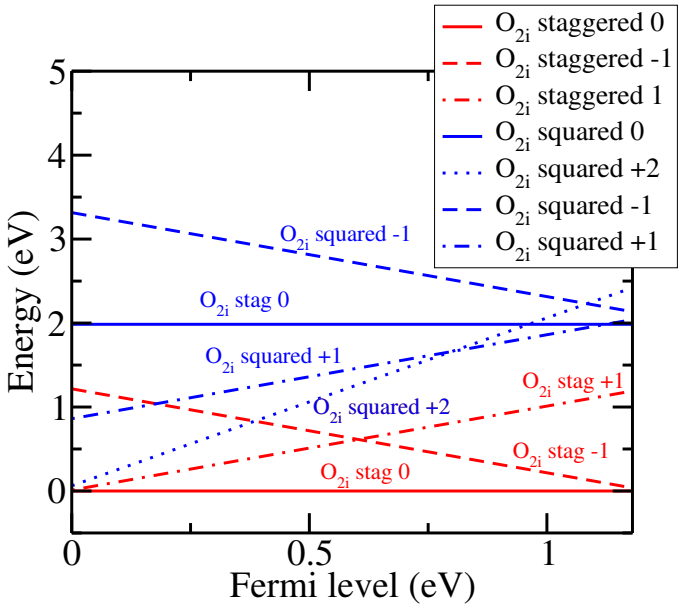

Figure 3.4: *O_{2i} formation energies calculated using HSE formalism in neutral,+1 and +2 charge states for squared configuration and in neutral,-1 and +1 charge states in staggered configurations.*

A detailed analyse of the structural properties of O_{2i} in staggered and squared configurations can be made and compared with the literature ([7] and [5]). The distance between Si atoms and O atoms are shown in Table 3.2 and are consistent with other works for the O_{2i} staggered structure. The angles of the O_{2i} show a divergence with the other DFT works. The angles calculated are higher than the one calculated in the work of [5] but smaller than those calculated in the work of [7]. An interesting point is that is our calculation, the difference between the two angles is higher than in [5] and [7]. The two O_i are not symmetrical for all the calculations but this trend is more visible in our work. The comparison was also made for the squared structure with the work of [7]. In our case, the angles are symmetrical, whereas in [7], a difference in the angles exists.

3.1.3 B_sO_{2i} structures

One of the structural hypotheses for the BO_2 defect at the origin of the dark current is a boron atom in substitutional position associated with an O_{2i} dimer. In this hypothesis, different configurations can be tested depending on the configuration in which O_{2i} is located and its position relative to the boron atom. The different configurations calculated in [12] have been tested in our DFT study. The different configurations are shown in Figure 3.5. As in the case of O_i and O_{2i}, these configurations were relaxed in DFT first without charge state and then by adding a positive or negative charge. The formation energies were then calculated with the HSE method. The calculated formation energies of the different configurations in the different charge states as a function of the chemical potential are shown in Figure 3.6. The most stable configuration for B_sO_{2i} changes as a function of the chemical potential, and thus the doping, of silicon. For a chemical potential close to the valence energy, the most stable configuration of B_sO_{2i} is the +1 charged X form. When the chemical potential is in the middle of the gap or close to the conduction energy, the stable configuration is the negatively charged A configuration. The change between the X and A configurations occurs at a chemical potential of 0.24 eV. These results is in agreement with the work of [12] in which a transition between these configurations is found at 0.22 eV. In boron-doped wafers, the Fermi level is closer to the valence band than to the conduction band.

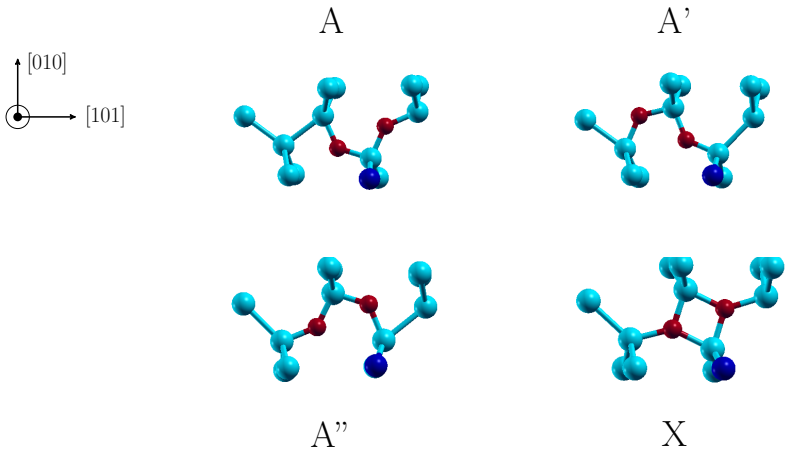

Figure 3.5: *BO_{2i} configurations A, A', A" and X represented in the same (101) plane.*

According to the SRH theory [14], the dark current generated by a defect of energy level E_i in the bandgap decreases exponentially when this level moves away from the middle of the bandgap. To know if these defects introduce an energy level in the bandgap, a density of states (DOS) calculation has also been performed. The DOS have been calculated with HSE in the configurations A, A', A" and X and for neutral, -1 and +1 charge states and are shown in Figure 3.7 for each configuration at neutral charge state. None of them has a deep acceptor or donor level close the mid-gap. The defect with the deepest level is the X configuration with a donor level at $E_c - 17\ eV$. The DOS of the charged configurations are not provided, but none of them has a deeper donor level than that found for the X neutral configuration. Therefore, none of the defects with studied introduce deep levels as observed in [15]. The dark current generated by these defects is therefore not maximum according to the SRH theory.

3.1.4 B_iO_{2i} structures

The other candidates for the degradation of the optoelectronic properties observed in the presence of oxygen and boron is when the boron atom occupies an interstitial site nearby a O_{2i} dimer. In our work, we have studied the most stable configurations as obtained in [16] and

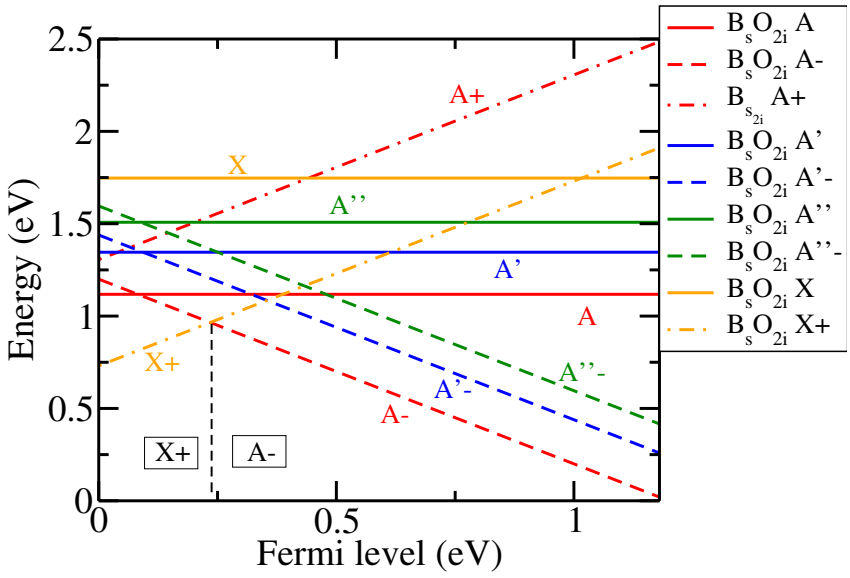

Figure 3.6: *B_sO_i formation energies for the different configurations (A,A',A" and X) calculated using HSE formalism.*

presented in Figure 3.8. The study is conducted as described in the previous sections. This structure will be named C in this thesis. When looking at the plot of the formation energy as a function of the Fermi level, the defect C is mainly in a +1 charge state. A transition between -1 and neutral charge state is observed for a Fermi level close to the bandgap (Figure 3.8). The formation energies calculated afterwards in HSE are Figure 3.8 and compared to that of B_sO_{2i}. The formation energies of B_iO_{2i} are higher than those of B_sO_{2i}. The difference between B_iO_{2i} and B_sO_{2i} is smaller for a Fermi level close to the Valence band and broad after the transition of B_sO_{2i} into A- charge state. This result is explained by the position of the boron atom in interstitial site, which is more energetic than in substitutional position. Without an interstitial generation process, it is therefore easier to form B_sO_{2i} than B_iO_{2i}.

The density of state of the C configuration in several charge states has also been calculated. It can be observed in Figure 3.9 that the -1 charge state introduces a deeper charge state than the X B_sO_{2i} configuration. However, we can notice that the energy level close to the conduction band is also shifted to higher energy. The deep level could correspond to a mathematical anti-crossing error where two close eigenvalues repeal each other. To test this hypothesis, another calculation was performed in a larger cell containing 512 atoms. In this calculation, no deep levels is observed in the bandgap. The energy level is much closer to the conduction band. This result is in contradiction with the work of [16] where a deep donor state is associated with the configuration. This discrepancy can be explained by the method used in [16] to calculate level into the bandgap. The method used in [16] to reproduce the real bandgap of Si with DFT is the one proposed in [17] and called the marker method. This approach is different from the HSE calculation used in our work.

3.1.5 Discussions on O_{2i} and BO_2 on LID phenomena

The stable structures presented in this section for O_i, O_{2i} and BO_{2i} already allow us to make several remarks about the type of defect responsible for the decrease in performance observed in photovoltaic cells after illumination. In previous investigations [18][19], it was assumed that

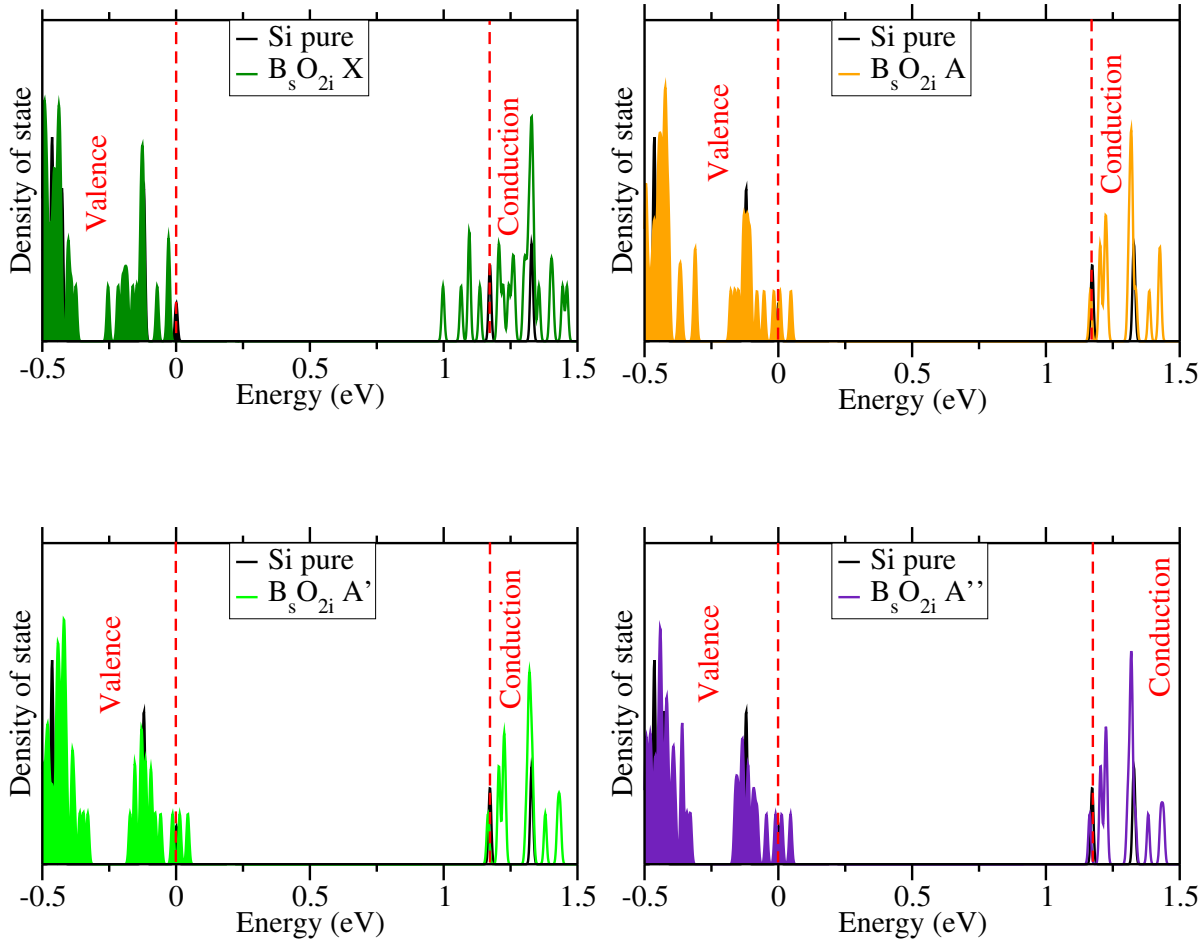

Figure 3.7: *DOS of the different configurations A, A', A" and X for neutral charge state calculated with HSE.*

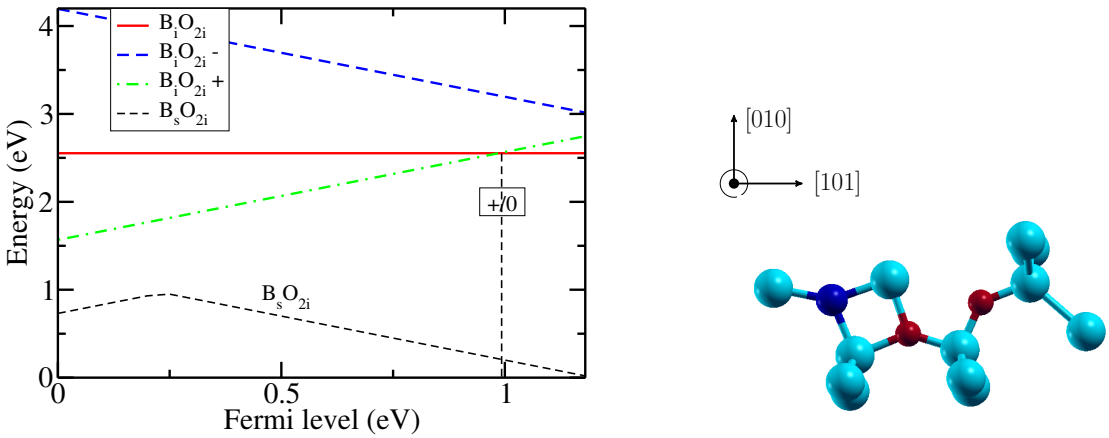

Figure 3.8: *$B_i O_{2i}$ formation energy compared to $B_s O_{2i}$ formation energy calculated with HSE.*

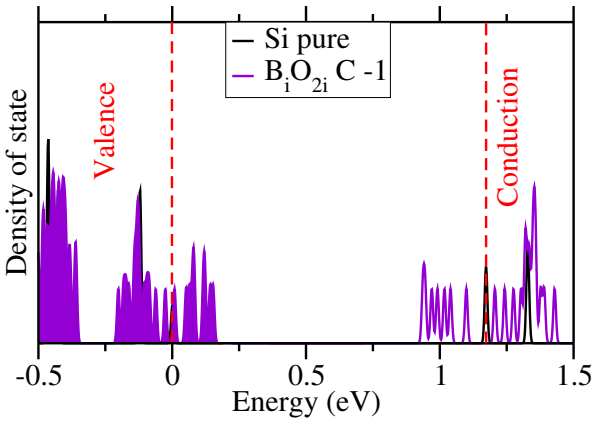

Figure 3.9: *DOS of B_iO_{2i} C configuration calculated with HSE.*

the carrier decay process originated from the decrease in O_{2i} migration energy caused by the change in chemical potential upon illumination. This assumption was based on an O_{2i} in the squared configuration. As we have calculated, the presence of squared O_{2i} is not energetically favorable at any chemical potential. It is therefore unlikely that the phenomenon of charge carrier drop is associated with accelerated O_{2i} migration upon wafer illumination. Another possible discussion following these calculations is the nature of the defect responsible for the degradation between B_iO_{2i} and B_sO_{2i} structures. None of the structures studied has a deep level in the bandgap. As indicated, without interstitial generation, the B_iO_{2i} defect is much less likely to be formed compared to B_sO_{2i}. In [20], they attempted to introduce interstitials into the wafers and measure the effect on the optoelectronic degradation. The result of this study shows that the injection of interstitials is not correlated with an increase in the BO_2 formed. However, the process to generate these interstitials requires annealing, which could also contribute to dissolve the impurity complexes present. The study of the kinetics of formation and dissociation of the defects is therefore essential to better understand them. The physical phenomenon at the origin of the LID is still under discussion and following our calculations the most likely effect would be the one proposed by [21][12].

3.2 Implementation in the KMC

Beyond the knowledge of the relevant atomic structures encountered in the structure of a material, the second most important ingredient in a kinetic Monte Carlo simulation is the kinetics of events, that is to say the energy barriers of atomic diffusions.

In the following, we study and characterize the migration of the oxygen species both in O_i and O_{2i} configurations. The activation energy for the dissociation mechanism of O_{2i} into two O_i is also determined. Once the migration and dissociation energies of O_i and O_{2i} are implemented, these two species will be likely to interact with the boron atoms, kept as immobile in the KMC, and to form the B_sO_{2i} complex whose evolution we will follow. Once formed, this complex must also be able to dissociate by emitting either an O_i or an O_{2i}. The emission of a boron atom out of the complex is not envisaged, such mechanism being very unfavorable. Cluster migration is also not considered since the boron atom in a substitutional site is indeed an obstacle to the migration.

Table 3.3: *O_i migration energies in our work and in the literature*

This work	PBE-216	PBE-512	HSE-216
$E_m(O_i)$ (eV)	2.25	2.30	2.80
Other work	PBE 216 [7]	PBE 512 [6]	HSE 216 [6]
$E_m(O_i)$ (eV)	2.41	2.27	2.7
Experiments			
$E_m(O_i)$ (eV)	2.44 [22]	2.53 [23]	2.55 [24]

3.2.1 O_i migration

In order to implement the O_i specie in the KMC, it is necessary to know the activation energies of its migration (called migration energy in the rest of the thesis) and the associated prefactors. The migration energy can be calculated by DFT with several methods. Both results obtained with NEB and ARTn-DFT methods are discussed here. For migration from O_i to a nearby site, no intermediate minimum was found along the migration path. The obtained migration energy is given in Table 3.3 and the configuration at the saddle point is shown in Figure 3.10. Once the saddle point was found, the energy of the saddle point was also calculated with an HSE functional. The calculated energy in HSE is higher of 0.6 eV than the one calculated with PBE. The migration path is shown in Figure 3.10.

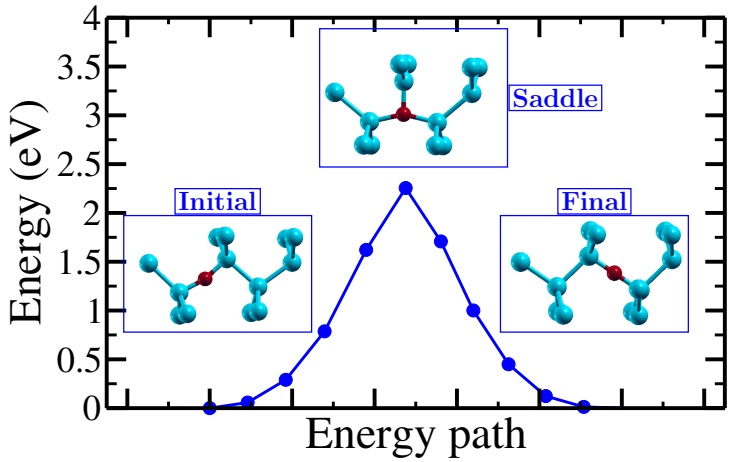

Figure 3.10: *O_i migration path calculated with NEB method. Initial, final and saddle configurations are represented on the Figure.*

Further analysis of the saddle point is necessary to understand this difference in energy between the use of PBE and of HSE functional, that can be explained by the energy levels introduced in the bandgap at this saddle point, whose values are shifted depending on the level of theory used. In the stable O_i structures, the oxygen atom shares its bonds with two silicon atoms. In the structures at the saddle points of the O_i migration, the oxygen atom shares bonds with three silicon atoms. Furthermore, in the configuration found at the saddle point, not all silicon atoms have their four bonds. These changes in the bonding of the different atoms have consequences for the energy states in the gap. By plotting the DOS at the saddle point, energy levels in the gap are observed (Fig.3.11). The HSE formalism is used in this case, as the classical functional underestimate the silicon bandgap. The bandgap energy is expanded with the HSE functionals and therefore the bandgap energies are higher in HSE calculation than with a PBE functional.

Since the total energy of the system can be approximated by the sum of the energies of the wave functions, if the energy of the states in the bandgap change, the total energy of the system will also change.

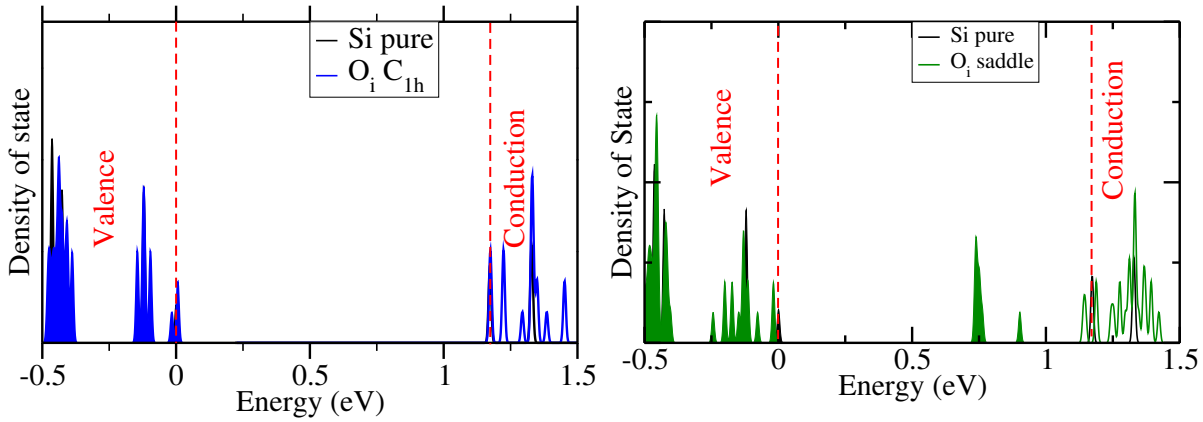

Figure 3.11: *DOS of O_i migration stable and saddle structure calculated using HSE formalism.*

In the work of [6], the saddle point is not the same as the one we found. In the work of [6], the migration of O_i was calculated with an O_i staying in the (101) plane and using NEB methods. The biggest difference in our work is that the saddle point is asymmetrical in the calculations. The so-called Y-lid configuration [5] that corresponds to our saddle point was also calculated and found to have a slightly higher energy for calculations in a 64, 216 and 512 atoms cell. However, the two configurations are very closed in energy. In our work, starting from Y-Lid configuration, the system relaxed to initial and final configurations. However, this may be due to a too strong push at the beginning of the relaxation. The NEB calculation does not show an asymmetrical saddle point even if the number of points is increased. It is also observed in [7] where the saddle point for the O_i migration is the same as in our work.

Others migration paths have also been explored for the O_i migration. In Fig.3.12 migration path for an O_i to its second neighbor is described. The aim of these calculations is to check whether the migration from bond-center site to the first neighbor bond center is the mechanism with the lowest activation energy. Two different paths have thus been explored for the migration of an O_i on a second neighbor. Two trends are observed: - in the first situation (in blue on Figure 3.12), the O_i must migrate on the neared bond center site to migrate on the second neighbors, - in the second situation (in red on Figure 3.12), two energy barriers have to be overcome but we can observe that these barriers are higher than that of the migration of direct O_i migration (3.1 eV compared to 2.25 eV for the direct migration presented in Figure 3.10).

In the case of the O_i migration, many experimental values are available, all in good agreement. The migration energy of O_i from a bonded center site to its first bond center neighbors can be directly estimated with symmetry arguments. In the work of [24], stress is applied on heated Si wafers containing oxygen. An oxygen atom is bonded to 2 silicon atoms, each of which is bonded to 3 other silicon atoms. This results, without stress, in 6 equivalent migration positions for O_i. Because of the stress, the six migration sites for O_i jump are not longer equivalent depending on the stress orientation. This phenomena is supposed to dump the mechanical vibration into the crystal. By comparing the relaxation time after an exposition to acoustic wave, it is therefore

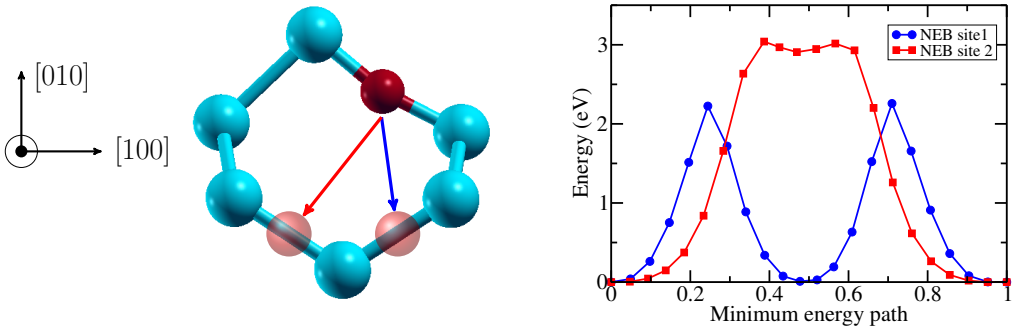

Figure 3.12: *Other O_i migration paths.*

possible to estimate O_i migration energy.

The activation energy of oxygen diffusivity at high temperature is also used to compare the migration energy of O_i. It can be assumed that at high temperature, O_i is the dominant specie in Si and the values extracted at high temperature for diffusivity activation energy are close to those calculated using the method of [24]. This diffusivity can be obtain using SIMS profile in experiment of in-diffusion [25] and out-diffusion of oxygen in Si wafers [23]. In the case of out-diffusion, an oxygen-rich silicon wafer is heated. The concentration of oxygen at the surface is fixed and the total concentration therefore varies in the bulk. SIMS measures the oxygen content as a function of distance from the surface and by fitting the oxygen concentration with Fick's law solution. Then the diffusivity value for the annealing temperature can be obtained. In the case of in-diffusion experiment, the principle is very similar, except that this time oxygen is introduced in the wafer. The surface concentration is thus equal to the oxygen solubility in silicon and oxygen diffuses into the bulk. The different experimental values are reviewed in [26] and in [27].
The values calculated in our work are in-between experimental values. Using PBE functional, the activation energy is underestimated by 0.25 eV. It can be seen than increasing the simulation cell to a 512 atoms cells improve the value slightly and gives an activation energy closer to experimental value. Our results also compare well with other DFT works [7][5]. In the case of the HSE, the activation energy is larger than the experimental one. This result is also observed in other DFT simulation work of [6].

3.2.2 O_{2i} migration

The migration path of O_{2i} is not direct and has an intermediate minimum as can be seen in Figure 3.13.
One of the migration steps corresponds to the change in orientation of O_{2i} from the staggered configuration (left part of the Figure 3.13). This step has a very low activation energy of 0.14 eV, it does not break any bonds between atoms. The saddle point (S1 in Figure 3.13) is strongly constrained by the reorientation. The other step observed during this migration requires the two oxygen atoms to change their bonds to bind to neighboring silicon atoms. The saddle point S2 is shown in Figure 3.13 and is very close to the stable O_{2i}-squared structure. The energy of the obtained saddle point is 1.4 eV, which corresponds to the activation barrier of this diffusion. Using an HSE functional applied to a single point calculation on the saddle point of Figures 3.13, the activation energy is large of 2.0 eV (not plotted). The comparison between our simulations and other ab initio investigation is quite relevant [7] as can be seen in Table 3.4.

Table 3.4: *O_{2i} migration energies in our work and in the literature.*

This work	PBE-216	PBE-512	HSE-216
$E_m(O_{2i})$ (eV)	1.39	1.4	1.96
Ohter work	PBE 216	PBE 512	HSE 216
$E_m(O_{2i})$ (eV)			
Experiments			
$E_m(O_i)$ (eV)	2.0 [32]		

In the work of [28], an intermediate minimum is found along the migration path. This structure is closed to the saddle point one. This intermediate structure is not found in our ARTn calculations where the O_{2i} relaxed to the initial and final state starting from the saddle. As in the case of the O_i this may be caused by a too high push at the beginning. In our NEB calculation this intermediate structure is not observed. The migration in this case is flatter than in the case of the O_i migration and structures have close energies at the middle of the path (Fig.3.14).

We can note that in the work of [28], an intermediate minimum is found along the same studied migration path, as the S1 of Figure 3.13. This intermediate structure is similar to the saddle point structure. In our NEB calculations, this intermediate structure is not observed, certainly due to the number of images we used. The migration in our case is flatter than in the O_i case and the structures have close energies in the middle of the path (Fig.3.14).
The experimental values for the activation energy of the O_{2i} migration are more spread out than that of O_i. The O_i is considered as the predominant specie at high temperature and its migration energy is assimilated with the diffusivity of oxygen at high temperature in Si, which follows an Arrhenius law. This is not the case for O_{2i} and therefore there are only indirect methods to calculate its migration energy. Among the indirect experimental evidence for O_{2i}, we can cite the works based on stress locking experiments [29][30][31]. The overestimation of the migration barrier for O2i in HSE is exluded in a similar way to the case of Oi: Figure 3.15 shows energy levels in the bandgap for the saddle point S2.

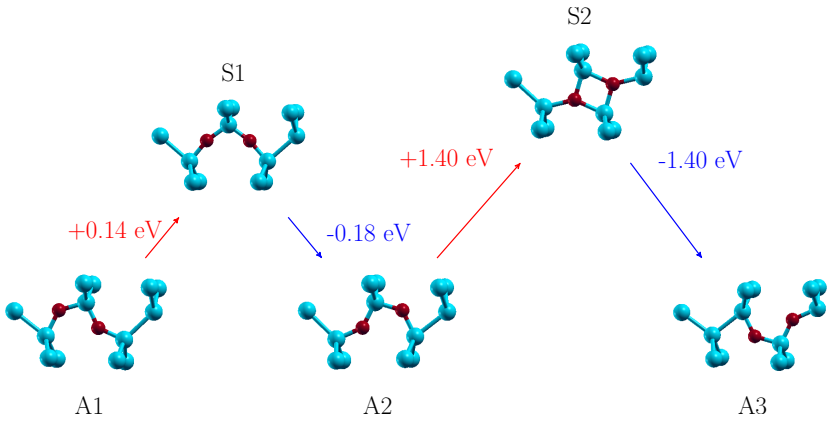

Figure 3.13: *O_{2i} migration path between two staggered configurations. Activation barriers are given in eV obtained for PBE calculations.*

3.2.3 O_{2i} and B_sO_{2i} Dissociation energies

In order to implement a dissociation-type mechanism, it is necessary to characterize its activation energy. In the KMC used, only a mobile particle can be emitted from a cluster. The activation

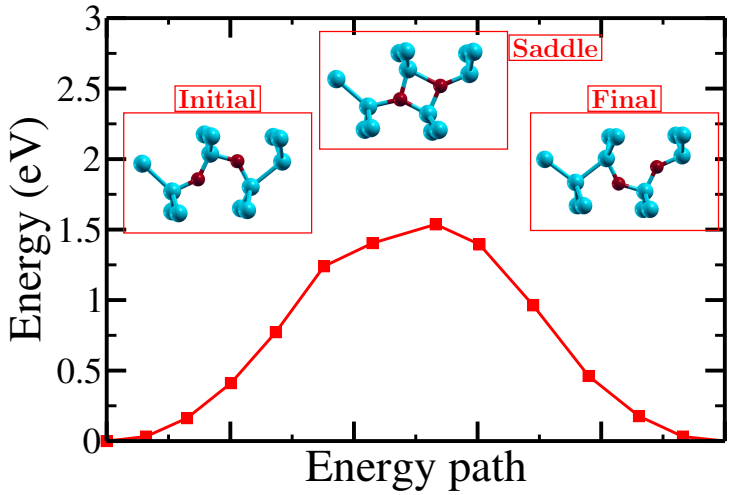

Figure 3.14: *O_{2i} migration path determined with NEB method for PBE calculations.*

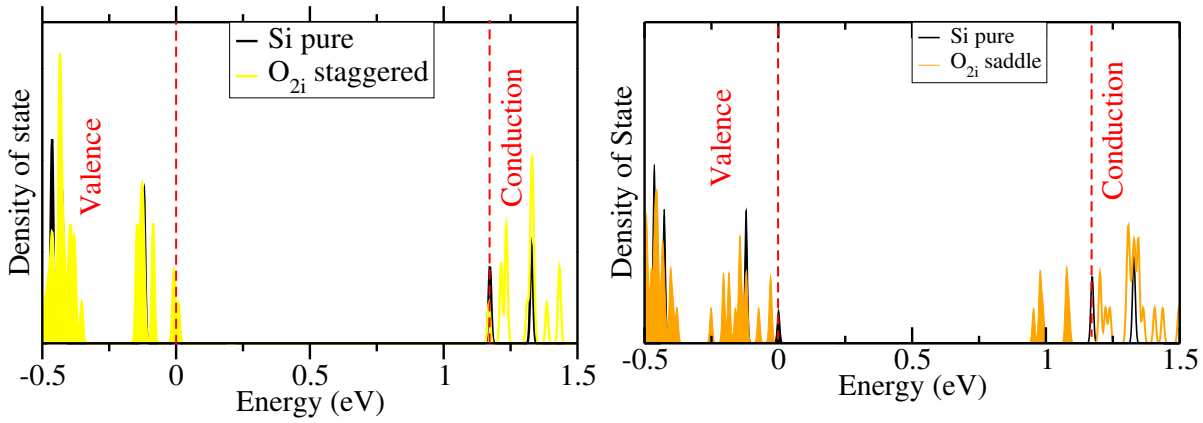

Figure 3.15: *DOS for O_{2i} stable structure and migration saddle point structure.*

energy for the dissociation of a cluster AX into a particle A and a particle X is then estimated according to the following formula:

$$E_{dis}(AX) = E_m(X) + E_f(AX) - E_f(X) - E_f(A) \tag{3.1}$$

The physical meaning of this estimate is illustrated in Figure 3.16. The particle moving away from the cluster jumps from metastable site to metastable site until there are no more interactions between the A and X particles.

Far from each other, the emitted particle and the remaining cluster have an energy $E_b(O_{2i})$. The energy required for the emission of a particle is thus assimilated to the sum between the migration energy of the emitted particle and the energy difference between the cluster and the two separated particles. This approach is the one used in the calibration of many pairs doping-defects and clusters in the KMC used [2]. For O_{2i} the energy needed for dissociation is first calculated as $E_m(O_i)$+$E_b(O_{2i})$. In general, as said above, only one mobile particle can be emitted from a cluster in the framework of the KMC [1]. For the B_sO_{2i} cluster, several particles

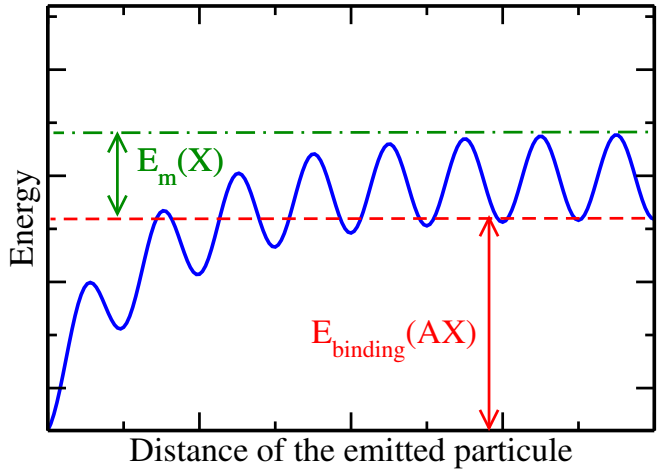

Figure 3.16: *Dissociation energy scheme of a cluster.*

Table 3.5: *Dissociation energies (in eV) for O_{2i} and B_sO_{2i}.*

O_{2i}	B_sO_{2i}
0.25	1.09

can be emitted: one O_i or one O_{2i} (the boron atom being immobile as already mentioned). To calculate the emission energy of an O_i from the B_sO_{2i} cluster, we must also calculate the formation energy of BO_i. The latter can then emit an O_i. The table 3.5 summarizes the different activation energies for the dissociation of O_{2i} and B_sO_{2i}.

The implementation of O_i and O_{2i} also raises the question of the form in which these particles should be implemented in the KMC. The dopants implemented in the KMC are stable in substitutional positions but can form a dopant-defect pair when they interact with an interstitial or a vacancy. In this case the dopant-defect pair can diffuse in a kick-out mechanism. The interstitial will return to the substitutional position by pushing the dopant out of the substitutional site, which in turn will push a silicon atom out of the crystalline lattice site, which can then start the cycle again by moving to the interstitial site. To model this mechanism, KMC [1] considers that the interstitial and the dopant atom form a dopant-defect pair, which can migrate until the pair dissociates. A dopant atom in an interstitial site is thus considered to be the association of the dopant atom and of an interstitial and can migrate. On the contrary, a dopant in a substitutional site is not allowed to migrate. In the case of oxygen, the situation is different. The most stable position of oxygen is the interstitial site as described in section 3.1. The structure of the oxygen that would replace a crystalline silicon atom is known and is often referred to in the literature as O-V [5]. Our ab initio calculation shows that a configuration with a O-V and an interstitial out of its substitutional site has a formation energy superior of 2.04 eV compared to the O_i formation energy [5].

Oxygen atoms can therefore be implemented in two ways : - as a particle and considering that the O object refers to an interstitial oxygen or - as an O-I pair with a negative formation energy of -2.04 eV. This results in most oxygens being in an O_i configuration when introduced into the simulation box. Both methods have been tested and give the same results. In the framework of the method where the interstitial oxygen is represented by an of O-I pair approach, the

dissociation event of the O-I pair is also possible and can be integrated. The O_{2i} dimer is also represented by the interaction of two O_i and thus by an O_2I_2 complex. In this case, dissociations of O_2I_2 into O_2I and then into O_i can also be implemented but has not been studied in this work. The representation of the interstitial oxygen O_i in O-I pair allows a better coherence with the impurities already implemented. In the framework of the complexes, which are also stable, this approach was chosen by the KMC developers.

3.2.4 Calibration of the prefactor in an KMC

Once the activation energies for the O_i and O_{2i} migrations as well as the O_{2i} separation have been calculated, it is then necessary to determine the entropic prefactors of these events. To do so, a first approach has been tested by calibrating the prefactors to fit the experimental data. We can note that the mobile species (dopant-defect pair) considered in the used TCAD KMC also use calibration to implement the prefactors and part of the activation energies [2]. The first step in this calibration strategy is to determine on which experimental data to base it. For the calibration of the other mobile species, diffusivity is used as a calibration criterion. For charged dopant-defect pairs, the diffusivity versus chemical potential is used to distinguish prefactors from charged or neutral pairs. In our case, we need to find an experimental data to discern the mobility of O_i and O_{2i}. The diffusivity of oxygen is known to have two distinct regimes [27]. At temperatures above 700 °C, the diffusivity decreases exponentially as a function of the inverse of the temperature and follows an Arrhenius's law. It is therefore possible to extract an energy responsible for the diffusivity at high temperature. This energy is associated in the literature with the migration of O_i, being the species naturally present in silicon. At temperatures below 700 °C, the diffusivity changes trend and the exponential decay is attenuated. This property is known in the literature as enhanced diffusion [33] and has been observed several times in SIMS experiments [34] and IR measurements [35]. However, the intensity of this phenomenon varies between studies. Several hypotheses have been put forward: the phenomenon has been linked to the presence of hydrogen investigated in out-diffusion experiments [36][37] and in molecular dynamics (MD) [38] or DFT calculations [39]. O-V was also used to explain the phenomena using kinetic experiments [32] and MD simulations [40]. Ab initio calculations [28] have reported small migration energies for oxygen chains which are another candidate to explain the enhanced diffusion phenomena. In our work, we hypothesize that the enhanced diffusion is caused by the formation and migration of O_{2i} pairs when the temperature is below 700 °C and that these pairs dissociate faster than they diffuse at high temperatures. Oxygen diffusivity is thus the experimental data on which our calibration is based, with calibrated prefactors expected to report for a change in the slope of diffusivity under 700 °C.

The second step of the calibration is to simulate the diffusivity with the KMC and to choose the parameters that recover the experimental trends. Oxygen diffusivity depends on O_i migrations, O_{2i} migrations, their dissociation and formation frequency. The method used to extract a diffusivity value at a given temperature is to simulate the diffusion of a thin oxygen-rich buried layer in a large volume of silicon. If the number of migration par oxygen atom is greater than 1, the oxygen distribution obtained after oxygen diffusion at a given temperature and after a certain time follows a Gaussian profile [41]:

$$C_{oxygen} = \frac{N_{oxygen}}{\sqrt{\pi.D.t}} \exp\left\{-\left(\frac{x^2}{4.D.t}\right)\right\} \tag{3.2}$$

This distribution thus allows to obtain the value of the diffusivity. By simulating the diffusion of a buried layer and then fitting the oxygen concentration with a Gaussian profile, it is possible to extract the diffusivity for one given temperature (Fig.3.17).

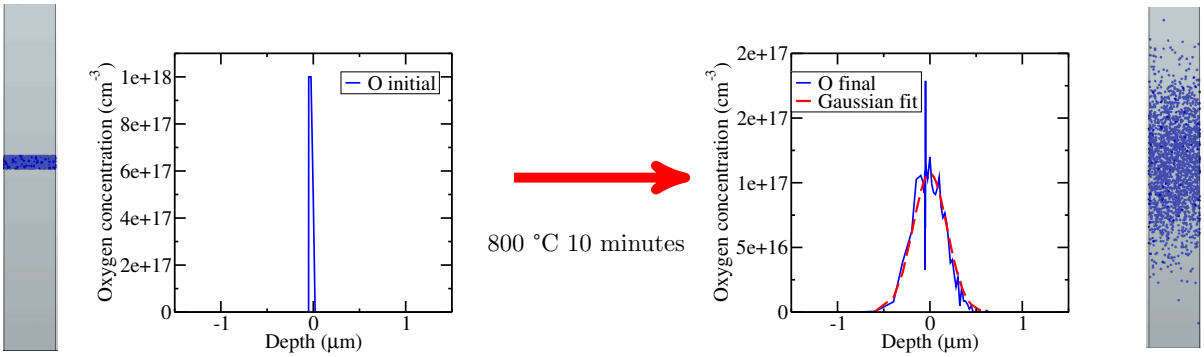

Figure 3.17: *Methodology to extract the diffusivity from KMC simulations.*

Once the diffusivity has been extracted for a given temperature, it is necessary to repeat the method for a set temperatures in order to plot the diffusivity as a function of the temperature and to compare it to the experimental diffusivity. The number of migration steps is dependant on the temperature. The simulation time must thus be adjusted for all temperatures to be in the regime in which the average number of migration step par atom is greater than 1 [41]. Too few migration steps lead to non-Gaussian profile [41] for the oxygen concentration while too long annealing time increases computational time and could lead to diffusion of oxygen outside the KMC simulation box. The procedure can be repeated with several sets of prefactors until a diffusivity curve in agreement with the experimentally measured curves is simulated. In our case, we had calculated activation energies using a PBE functional, but we obtained different activation energy results by refining the saddle points with an HSE functional. We therefore calibrated different prefactors corresponding to values obtained for activation energies in PBE and in HSE. Experimental data on the change in slope obtained at temperatures below 700 °C vary greatly from one experiment to another [34][30]. The criteria chosen to estimate whether the simulation reproduces the experimental trend are:

- The change in slope of the diffusivity at 700° C
- The simulation of the diffusivity at high temperature (the diffusivity at high temperature does not vary much from experiment to experiment).

The obtained diffusivities are compared to the experimental values in Figure 3.18. The prefactors used to reproduce these diffusivity values are shown in Table 3.6. The diffusivity values of O_i are compared with those obtained experimentally and in other DFT works.

Table 3.6: *Comparison of the calculated migration energy barriers E_m and binding energy E_b (eV) and the experimental ones. Best match is obtained with an average of PBE and HSE in the KMC. The prefactor D (s^{-1}) is adjusted empirically to fit experimental data from [35][42].*

	DFT-PBE	DFT-HSE
$D_m(O_i)$	3.10^{15}	1.10^{15}
$D_m(O_{2i})$	7.10^{15}	3.10^{15}
$D_b(O_{2i})$	7.10^{16}	7.10^{16}

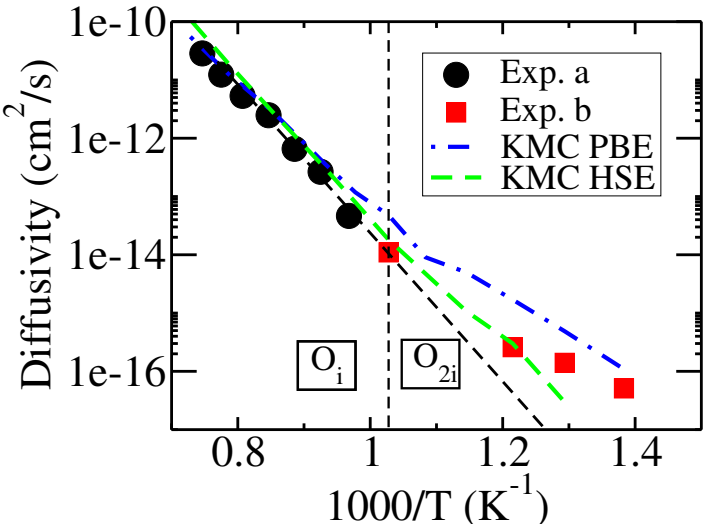

Figure 3.18: *Diffusivity of oxygen obtained with KMC using the activation energies calculated with ab initio calculations using PBE and HSE functionals.*

3.2.5 Conclusions

DFT calculations have been for the calibration of the migration of oxygen to simulate the experimental trend of regime change at 700 °C. This calibration also allows the extraction of prefactors for O_i, O_{2i} migration and O_{2i} dissociation. However, this calibration method has several limitations :

- The first limitation is that the share of diffusion provided by O_{2i} depends on the ratio between the migration of O_{2i} and the dissociation of O_{2i}. The calibration performed allows to fix the $\frac{\nu_{migration}}{\nu_{dissociation}}$ ratio but not to calculate a unique prefactor value for the two events. It is possible to reproduce the same diffusivity by keeping the ratio constant and varying $\nu_{migration}$ and $\nu_{dissociation}$ (Figure 3.19). It is therefore necessary to find a method to fix this last degree of freedom.

- The second limitation concerns the assumption about the activation energy of O_{2i} dissociation. The estimated energy allows to account for a change in the diffusivity trend at low temperature. This would not be the case if the ratio of the O_i migration energy on the sum of O_{2i} migration and binding energies was less than value 1. However, the differences between the experimental values do not support the hypothesis. Any other dissociation energy value higher than satisfy the condition $E_m(O_{2i}) + E_b(O_{2i}) < E_m(O_i)$ could indeed lead to a change of slope at low temperature. An thorough study of the dissociation mechanism is therefore required to better calibrate this factor.

Another problem with the implementation of the oxygen in the KMC is that an isotropy of the oxygen diffusion is supposed in the formalism of the model, in the sense that a single value is assigned for the diffusion in the three directions of space. In the next section, we will demonstrate that oxygen diffusion is, in fact, significantly more intricate.

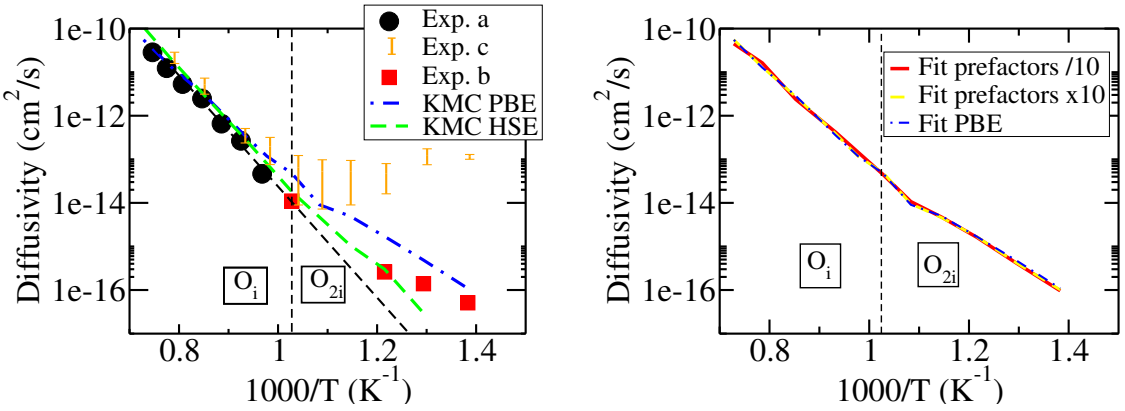

Figure 3.19: *(Left) O_{2i} diffusion calibrated and compared to other experimental data [42] and [34] (Right) Predict oxygen diffusion in KMC using a same ratio with different values for $\nu_{dis}(O_{2i})$ and $\nu_m(O_{2i})$.*

3.3 Beyond Object KMC: events library for an Off-Lattice KMC

Three issues need to be resolved in the case of the oxygen diffusion: the anisotropy, the ratio between $\nu_m(O_{2i})$ and $\nu_{dis}(O_{2i})$ and the validation of the hypothesis for the O_{2i} dissociation energy. These issues can be addressed with the use of a Kinetic Monte Carlo methodology, where the atomistic description of the events is highly detailed. For this, we use the Off-Lattice Kinetic Monte Carlo as developed in the team in LAAS-CNRS (see Chapter 2). This type of KMC requires a more detailed catalogue of events and and a more thorough ab initio study to both access the atomic configurations and the activation barriers. For this demonstration, a complete catalogue of events would necessitate to consider different charge state and using an HSE functional, but these require too much computational time. In the following, the ab initio calculations have been performed using a PBE functional and assume a neutral charge state for all the configurations.

3.3.1 Determining the activation energies involved in the dissociation of O_{2i}

The ab initio simulations should describe the detailed mechanisms for the dissociation of the O_{2i}. In such objective, studying O_{2i} dissociation (or association) and more generally the O diffusion raises the following questions:

- Is the dissociation mechanism different depending on the direction the O_i takes?
- What are the activation barriers for each direction?
- At what distance can two O_i be considered as two independent O_i?
- Is it possible that oxygen atoms have to overcome several energy barriers before behaving as an O_i?

In this calculation, one O_i of the staggered structure migrates away from the other. It is assumed that the possible metastable states for the migration oxygen are always an interstitial position between two Si. The evolution of the dissociation between the two O_i can be described by the

minimum number of Si-Si bonds separating the two O_i. For the possible migration site away from the other oxygen, different directions are possible. For ease of notation, we will adopt the following conventions:

- A configuration of two O_i will be defined by a number and by a list of letters. The name started with the minimum number of Si atoms that separate the two O_i (starting from 1 in the staggered position).

As there are several configurations possible for a same number, the letters will defined the mechanisms that allow to obtain the actual configuration starting from an O_{2i} staggered structure.

- The letter P represents a migration of the O_i away from the (110) plane of the initial O_{2i} configuration.
- The letter O represents a migration in a direction opposite to from the initial (110) plane.
- The letter B represents a migration with the final configuration in a plane (110), parallel but different than the initial plane, with a migration in the $(1\bar{1}0)$ direction, bringing closer the two O_i in absolute distance.
- The letter F represents a migration whose final configuration is in a plane (110), parallel but different than the initial one, with a migration far from the other O_i.
- An atom with three Si atoms that has migrated in the (110) plane, then out of the plane and again out of the plane will the named 3-POO. With this approach, the same configuration can be defined by different letters. This allows to differentiate all the configurations explored in the following.

In the staggered configuration, only one Si atom separates the two O_i, so this number is 1. The first possible dissociation step is therefore to place the migration O_i in a position separated with one Si-Si bond from the other. From a given interstitial position of the O_i, four neighboring interstitial sites are available. In these four sites, one brings the two O_i closer and the other one can be symmetric. Two different configurations are possibles. The first one is called 2-P in Fig.3.20. The two O_i stayed in the same (101) plane described by themselves and their common neighbor in the staggered structure. The second one have a symmetric image and is a migration of the O_i outside the (101) plane. This configuration is the 2-O configuration in Fig.3.20. The energies of the 2-O and of the 2-P configurations are already very different (Table 3.7). The binding energy of O_{2i} is positive and equal to 0.3 eV. The increase of energy (positive value) means that far away for each other the O_i have an higher energy that in the O_{2i} configuration. In the case of the 2-P configuration, the increase in energy is higher than the binding energy of O_{2i}, which means that as we move away from 2-P, the energy decreases. On the other hand, as dissociation continues, the energy is expected to continue to increase in the 2-O case, until reaching a difference of 0.3 eV with the O_{2i} energy, where the two O atoms are considered as isolated. The activation barriers are also different in the two cases. The 2-O have an higher activation energy, closer to the single O_i migration energy. The activation energy to go from O_{2i} to the 2-P configuration is 0.4 eV lower.

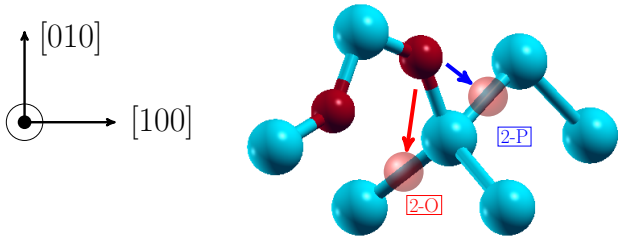

	E_{act} (eV)	ΔE (eV)
2-O	2.12	0.14
2-P	1.82	0.61

Table 3.7: *Activation energies for O_{2i} dissociation into 2-O and 2-P configurations.*

Figure 3.20: *Dissociation from O_{2i} to 2-O and 2-P configurations.*

The dissociation paths of the O_{2i} of two to three (2-X to 3-X) Si atoms between the O_i must be distinguished according to whether they start from the 2-P direction or the 2-O direction. From the 2-O configuration, three non-equivalent positions can be reached in a single jump. They are called 3-OO, 3-OF and 3-OB in the Fig. 3.21. The energies of these configurations are different. For the 3-OO and the 3-OF the energies continue to increase while it decreases for the 3-OB configuration (Table 3.8). In term of activation energies, the mechanism to go away from the 2-O has activation energies higher than 2.0 eV. These energies are also close to the single O_i migration energy.

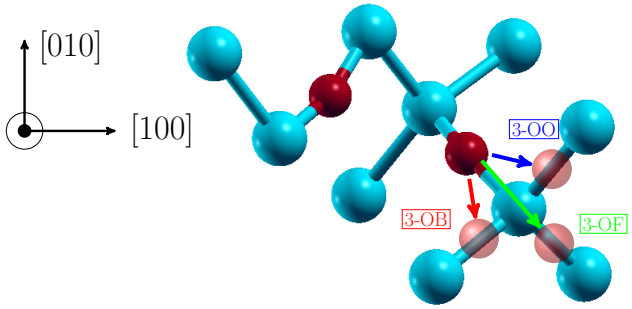

	E_{act} (eV)	ΔE (eV)
3-OO	2.24	0.17
3-OF	2.29	0.07
3-OB	2.42	0.10

Table 3.8: *Activation energies for dissociation of O_{2i} from 2-O configuration into 3-OO, 3-OF and 3-OB configurations.*

Figure 3.21: *Dissociation scheme of O_{2i} from 2-O to 3-OO, 3-OF and 3-OB configurations.*

Starting from the 2-P configuration, two different paths enable to dissociate the two O_i. The first one remains on the initial plane and is called 3-PP. The second one is on the Si atoms outside the plane and is called 3-PO. Once again, the activation energies are different depending on whether the final configuration is on the plane or not (Table 3.9).

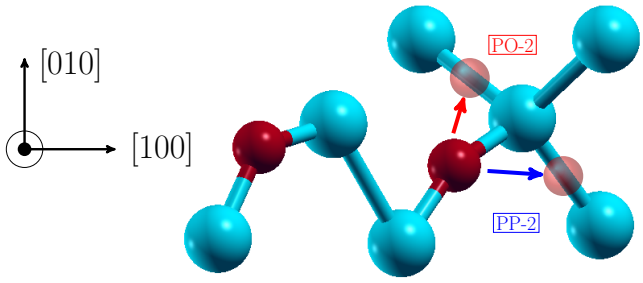

	E_{act} (eV)	ΔE (eV)
3-PO	1.67	-0.37
3-PP	1.36	-0.14

Table 3.9: *Activation energies for dissociation of O_{2i} from 2-P configuration into 3-PP 3-PO configurations.*

Figure 3.22: *Scheme of O_{2i} dissociation from configuration 2-P to configurations 3-PO and 3-PP*

It is now time to compare the energy barriers depending on the path. It seems that by staying in the (110) plane the activation barriers are smaller. The O_i will tend to do move more in the (110) plane than out of the plane. The first step of the dissociation can also act as a migration mechanism. Starting from an O_{2i} configuration, if the O_i go in a 2-P position, the most probable event is that the two O_i join to reform an O_{2i}. If the migrating atom goes back, the situation is the same as the initial state but if it is the other O_i which joins the O_i which first migrate first, a diffusion step is performed. This is not the dominant mechanism because first energy for this mechanism is 0.4 eV higher than the simple O_{2i} migration but it must be considered. It is also interesting to look at which neighbor the O_i can be considered as independent. The two O_i can be considered as independent at two conditions :

- The formation energy of the DFT box containing to the two O_i is equal to twice the formation energy of a single O_i. If this conditions is met, the difference between the energy of the simulation box containing the two O_i and the simulation box containing O_{2i} is equal to the binding energy of O_{2i}.
- The migration to the next interstitial site for the oxygen is equal to the O_i migration energy.

The situation is not the same for all dissociation paths. Figure 3.23 shows several paths from O_{2i} to O_i in fifth neighbors. It can be seen that for most dissociation paths, the two O_i of the simulation box can be considered isolated. However, it can be seen that it is not the case for the path staying in the (101) plane. In order to study the dissociation path for this direction more precisely, another cell is needed: the 216-atoms cell and the 512-atoms cell are not large enough to go beyond the 5^{th} neighbors. Simulations in a 1000 atoms box are very expensive. The activation barrier along the (101) have been calculated using a 600 atoms cell elongated in the (101) direction (Figure 3.24). The z-direction of the box has no importance as the O_i are considered as independent considering a replica of the cell in this direction. The results show that at the 8^{th} neighbor, the behavior is close to the one on the single O_i migration step.

3.3.2 O_{2i} dissociation anisotropy

Further simulations are exposed here to explain the anisotropy of O_{2i} dissociation and in particular the long-range interactions on the (101) plane. Three trends need to be explained :

- The range of interactions extending to the 8^{th} neighbors in the (110) direction.

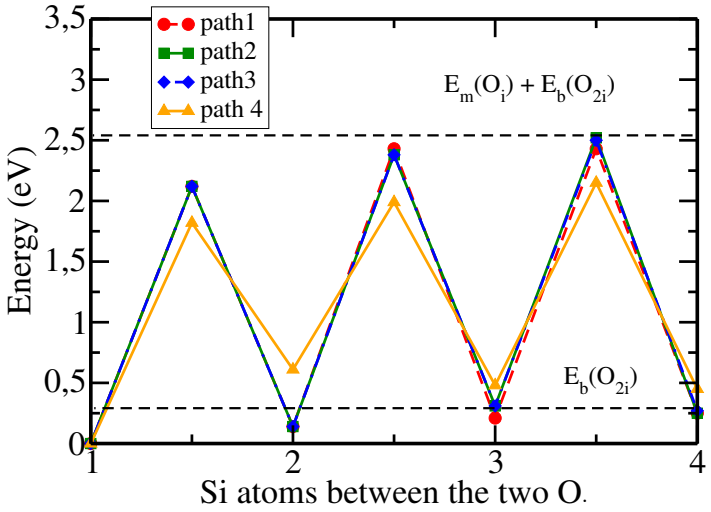

Figure 3.23: *O_{2i} dissociation energies for saddle structures and intermediate stable structures calculated with ARTn. Path 1, 2, 3 start with the $O_{2i} \rightarrow 2O$. Path 4 is $2P \rightarrow 3PP \rightarrow 4PPP$.*

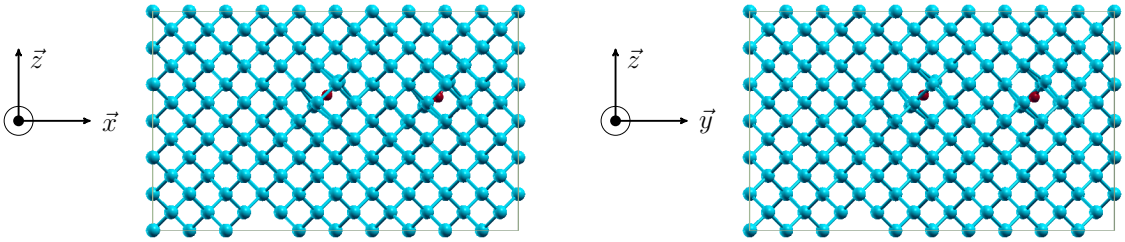

Figure 3.24: *(Left) 600 atoms silicon cell used for the calculation (Right) Saddle and intermediate structures obtained with ARTn for the O_{2i} dissociation in the (101) direction.*

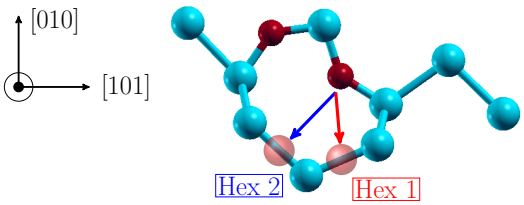

Figure 3.25: *Dissociation of O_{2i} .*

- The metastable positions along the dissociation path of O_{2i} which are in the (101) plane are higher in energies that the positions outside the plane.
- The activation energies barriers are higher for the dissociation outside the plane.

Here we will attempt to explain the first two trends. First, the individual O_i is studied in more details to understand at what distance the O_i interact with the Si atoms and whether this

Figures/Dissociation_O2i.pdf

interaction reveals anisotropy. Oxygen atoms have six valence electrons: two electrons $2s$ and four $2p$ electrons. These electrons are distributed as shown in Figure 3.26. Two of them form bonds with the first two neighboring silicon atoms. The other four are in two even lones around the oxygen. A Bader charge analysis was tested in an attempt to observe whether an anisotropy appeared in the charge distribution on the out-of-plane (110) and in-plane (110) atoms. This study was unsuccessful because there is no charge density minimum in the Si-O bond and the Bader volumes created from the charge density iso-surfaces do not take this bond into account. The analysis of the charge density iso-surface reveals no significant difference in the distribution of the electrons on the out-of-plane atoms and in the (110) plane (if we exclude the two atoms of Si forming the bonds with O).

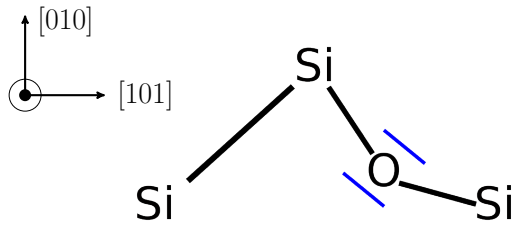

Figure 3.26: *Diagram of the valence electrons of oxygen O_i. Two of them participate to Si-O bond and two other electrons are in non-bonding doublet.*

Another possible physical quantity to analyze is the effect of O_i on the displacements of Si atoms with respect to their positions in the perfect Si lattice. This quantity has been extracted thanks to the IRA software [43]. This software allows an accurate comparison of the displacements by taking into account a small global displacements of all atoms in the simulation box. The displacements are represented in the plane (101) of the O_i and in the orthogonal plane in Figure 3.27. The largest displacements are located on the first neighbors of Si. The two Si atoms closest to O_i are on the (101) plane and this is no surprise that these atoms are the most displaced. When comparing the third neighbors inside and outside the plane, no clear difference in displacement is observed. The displacements of the Si atoms further than the third neighbors are also calculated. Atoms until the fourth positions experienced displacements. No anisotropy is observed for these atoms outside and inside the plane. The displacements appear to depend more on the number of Si bonds separating the Si and O_i atoms than on any direction in space. The displacements up to the fourth neighbors are consistent with the interactions up to eight neighbors for the dissociation of O_{2i}.

The structures of 2-O and 2-P have been investigated to understand the anisotropy. The angles between oxygen atoms and their two nearest Si neighbors are reported in Table 3.10 as well as the angles formed by a single O_i and its nearest neighbors in Si. 2-P and 2-O structures are shown on Figure 3.28 to enumerate the angles. The Table 3.10 shows that in the 2-P case, the angles are different from those observed in the single O_i case. The angles are smaller for both $Si_1\widehat{O_1}Si_2$ and $Si_1\widehat{O_1}Si_2$. In the case of the 2-O structures, the angles are closer to the angle of the single O_i. This difference in angles in the 2-P case could explain the different distributions in charges and thus the higher energy of 2-P. In the 2-O case, the angles are closer to the single O_i, even if they are also 5° smaller. The angles close to the O_i in the 2-O configuration lead to the hypothesis that the behavior of the two oxygens in this configuration is closer to the behavior of two isolated O_i atoms. This hypothesis is verified in the energy difference between 2-O

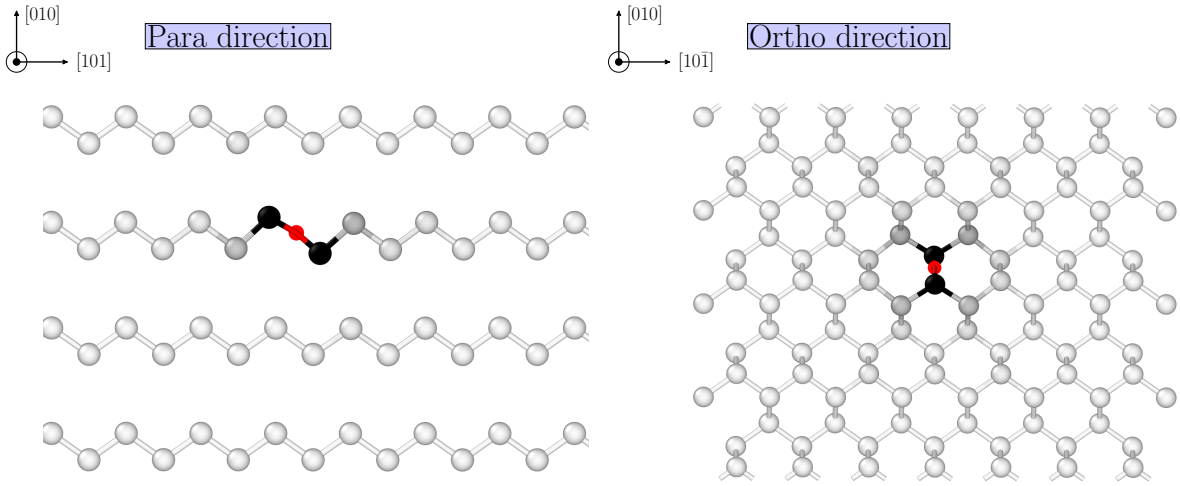

Figure 3.27: *Displacements of Si atoms in a O_i supercell compared to their positions in a pure Si cell calculated using IRA [43].*

Table 3.10: *Angles (in °) between O_i an their nearest Si neighbors.*

	O_i	2-P	2-O	3-PP	3-OP	3-OB	3-OF
$Si_1\widehat{O_1Si_2}$	167.6	149.0	161.5	153.1	159.6	157.1	157.4
$Si_3\widehat{O_2Si_4}$	-	149.3	162.1	153.4	164.2	157.0	156.6

configuration and O_{2i} which is closer to the binding energy of O_{2i} (0.16 eV) than the difference between the 2-P energy and the energy of O_{2i} (0.30 eV). The activation energy for the migration of O_i far from the other is also close to the migration energy of single O_i.

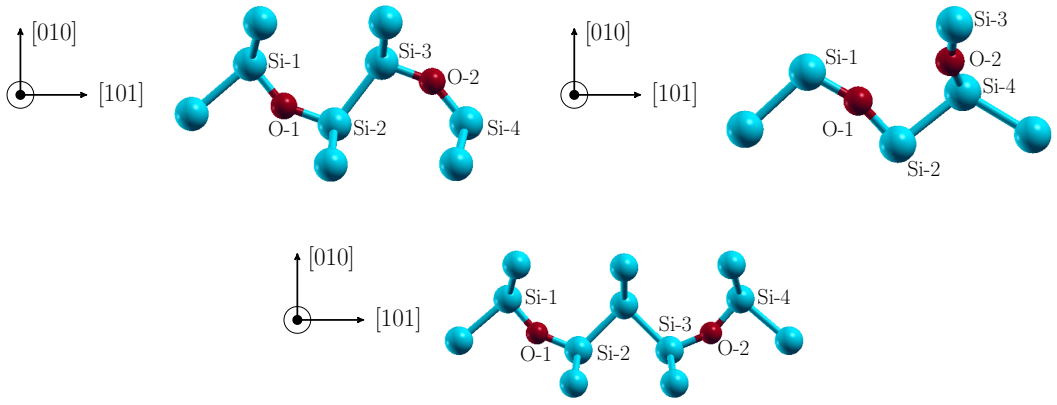

Figure 3.28: *Atomic configurations for 2-O and 2-P structures in a (101) plane and in the orthogonal plane.*

The difference in angles in the P-2 case can be explained by the direction of displacements caused by the two O_i. In the study of a single O_i, one can notice than the O_i tends to repeal the nearby Si atoms. In the 2-P structure, the Si atoms between the two O_i are subject to two opposite forces: one coming from the O1 which tends to push the Si in the forward on the (101) direction and one from O2 which tends to push in the opposite direction. Positions of these two atoms induce a change in the angles and in the charge density.

It is a possible to continue the investigation for the configurations in neighboring 3. In this case, the energy of the 3-PP structure is also higher than that of the other 3 directions. The difference between 3-PP and O_{2i} energies is still higher than the binding energy of the O_{2i} (0.48 eV). In the 3-OO, 3-OP and 3-OF structures, the energy is close to the binding energy. The angles of the 3-PP configuration are still smaller than the angles of O_i with its nearest neighbors. However, the difference is smaller than in the case of 2-P. This could explain why 3-P have still an higher energy than the binding energy of Si.
The effects of the angles on the charge density, and thus on the energy calculated in DFT, are visible Figure 3.29. In the case of O_i, the charge density is slightly asymmetric with respect to the axis formed by the two first Si neighbors of the oxygen. The slight asymmetry is also observed in the charge density corresponding to the 2-O configuration. On the other hand, in the 2-P configuration, the asymmetry of the charge density is much more pronounced. The charge density is thus similar in the O_i and 2-O cases, which is consistent with the energy of the 2-O configuration (close to the energy of 2 separated O_i). In the 2-P configuration, the charge density changes compared to that observed on O_i may explain the higher energy obtained for this configuration.

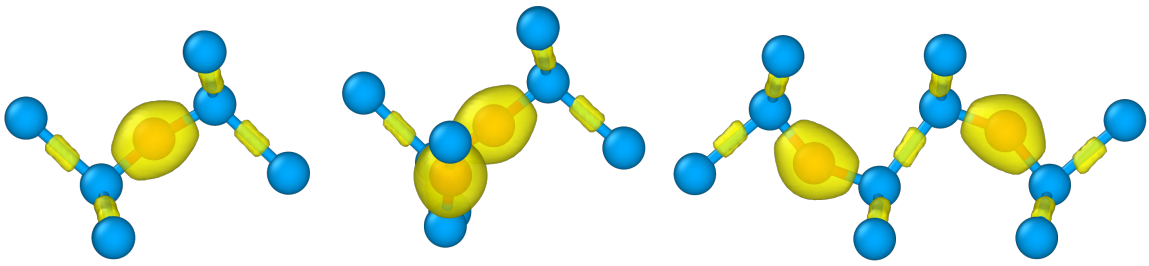

Figure 3.29: *Iso-surface of the O_i charge density (Left), 2-O charge density (Middle) and 2-P charge density (Right). All views are in the (101) plane.*

3.3.3 O_{2i} reorientation

After understanding the mechanism of dissociation of the O_{2i}, it is interesting to understand the mechanism of O_{2i} reorientation in space. It has been shown that O_{2i} in staggered configuration are found in the (101) planes. From here, there are six possible orientations. From a staggered structure, it is possible for the O_{2i} to re-orient itself in two other (101) with a single jump of one the O_i atoms out the plane keeping a common neighbors with the other, and in two others (101) planes by the single jump of the second O_i out of the plane. The reorientation of the O_{2i} in a plane perpendicular the one of the starting point requires more than a single jump of O_i.

In this work, two types of reorientation are investigated. In the first one, the common Si atoms between the two O_i remain the same after the reorientation. In the other, the O_{2i} change their central atom after the reorientation. These two mechanisms take into account the four different plane reorientations as the mechanism are symmetric. The result of ARTn calculations demonstrates that the two different pathways do not lead to the same activation energy. The reorientation of the O_{2i} keeping the same central Si atom requires an activation energy of 2.5 eV. This energy is larger than the activation energy of the O_i and O_{2i} migration. We can notice that this energy is higher than the one of the dissociation of the O_{2i} into 3-O. In this case, the mechanism of dissociation into 3-O requires less energy.

On the other hand, the mechanism in which the O_{2i} changes its central Si atoms requires less energy, its activation barrier being 1.99 eV. This value is lower than the O_i migration energy

Table 3.11: *Prefactor for O_{2i} migration*

	Our work	Frozen phonons [7]
$D_m(O_{2i})$ (s^{-1})	2.92×10^{14}	4.64×10^{14}

Table 3.12: *Prefactor for O_{2i} dissociation*

	$O_{2i} \rightarrow$ 2-P	2-P $\rightarrow O_{2i}$	$O_{2i} \rightarrow$ 2-O	2-O $\rightarrow O_{2i}$
D_{act} (s^{-1})	1.94×10^{14}	3.90×10^{13}	9.98×10^{14}	9.61×10^{14}

and than the $O_{2I} \rightarrow$ 3-O dissociation.

These values can be compared with previous ab initio results and experimental investigations. In their work, [28] found a reorientation activation energy of about 2.1 eV. This is 0.1 eV higher than our second mechanism.

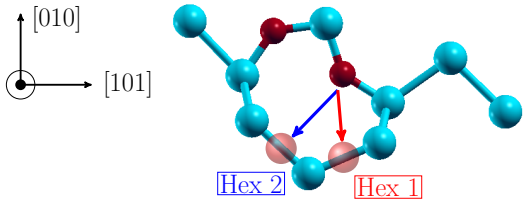

Figure 3.30: *O_{2i} reorientation alternative paths.*

3.3.4 Entropic prefactor calculations for O_{2i} events

The prefactors have not been accurately calibrated with the KMC and thus require further study. There are different methods to calculate prefactor using DFT simulations, as mentioned in Chapter 2. The phonons for the O_{2i} migration and for the first dissociation steps have been calculated using DFPT (Density Functional Perturbation Theory) methods [44]. The calculation of the different frequencies was then used to find the prefactors for the migration and dissociation of O_{2i}. For the O_{2i} configuration, it is possible to compare the obtained prefactors with those found in other theoretical works. The comparisons are shown in Table 3.11.

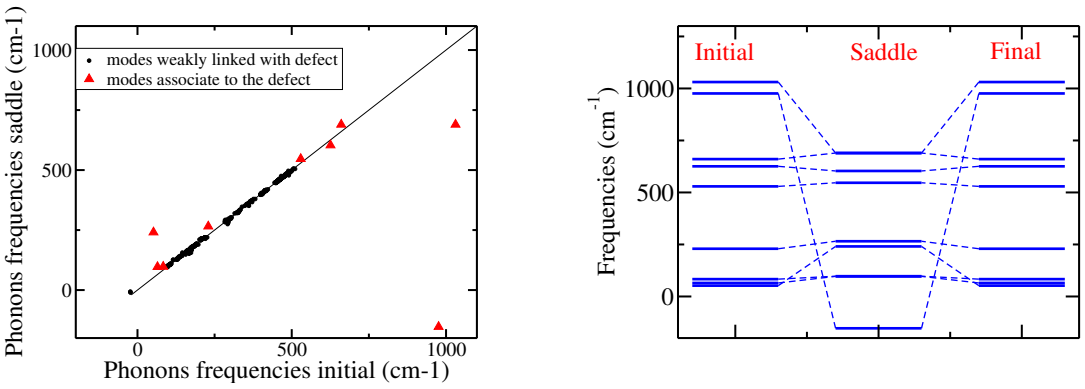

Figure 3.31: *Phonons frequencies in the O_{2i} staggered and in the O_{2i} migration saddle points.*

After calculating the phonons, it is possible to see for each mode of vibration if it is associated with a movement of oxygen atoms. In the Figure 3.31 are represented in red the contribution of oxygen in each mode of vibration of the saddle point of the O_{2i} migration. It is also possible to project the vibration modes at the saddle point onto those of O_{2i}. This projection consists in performing the scalar product of the normal modes. The modes associated with crystalline silicon are not supposed to be different at the saddle point and at O_{2i}. This assumption is verified on the Figure 3.31 where the silicon modes are represented in black and appear to be aligned with the line y=x. On the other hand, the frequencies of the modes associated with oxygen change between the saddle point and O_{2i}. The evolution of the frequencies between O_{2i} and the saddle point of the O_{2i} migration are also represented on the left of the Figure 3.31.

The calculation of the O_{2i} migration prefactor is normally sufficient to fix the O_{2i} dissociation migration prefactor (the ratio between the two can be determined using an experimental fit on oxygen diffusion). It is still possible to calculate the migration prefactor of the first steps of O_{2i} dissociation. These calculations are for example useful to be able to implement oxygen in the off-lattice KMC presented later. The phonons were therefore calculated for the 2-O and 2-P configurations as well as for the saddle points to switch from O_{2i} to these two configurations. The contribution of the phonons related to oxygen in the cases of the O_{2i} dissociation to 2-P and 2-O are shown in Figures 3.32 and 3.33.

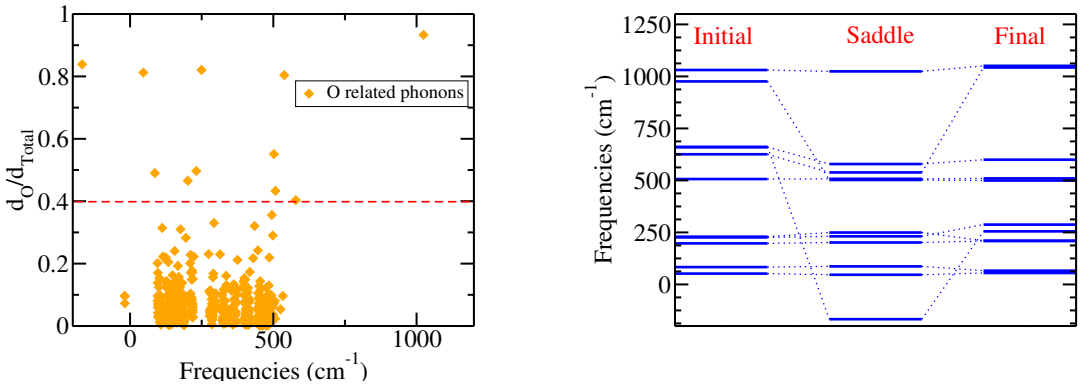

Figure 3.32: *(Left) Part of oxygen displacement in the phonons of O_{2i} to 2-P saddle point. (Right) Projection of the phonons related to oxygen (upon the doted red line in the left figure) on the phonons of O_{2i} and 2-P.*

For O_i, the calculation of phonons is more complicated to perform using the DFPT method. Indeed as mentioned in section 3.1, O_i has several configurations very close in energy (C_{1h}, C_1 and D_{3d}). The potential energy surface around O_i is therefore almost flat. The derivative of the Hamiltonian with respect to the potential energy surface is therefore almost zero, which leads to convergence problems for the phonon calculation. For such stable C_{1h} configuration, phonons calculations provide also imaginary frequencies.
The impossibility of calculating the migration prefactor of O_i is not limiting in the calibration of KMC. Indeed, contrary to O_{2i}, the diffusion of oxygen at high temperature depends only on the migration of O_i. The calculated prefactor in section 3.2.4 is therefore a good approximation of the prefactor. It is still possible to estimate the O_i migration prefactor from ab initio calculations subject to assumptions and simplification. One idea is to consider that apart from the imaginary frequency of the saddle point, the other phonon frequencies do not change drastically between the local minimum and the saddle point. The result of the product of phonons frequencies of the minimum configuration over phonons frequencies of the saddle point would then simplify to a single term corresponding to a single frequency. The mode of vibration associated with this

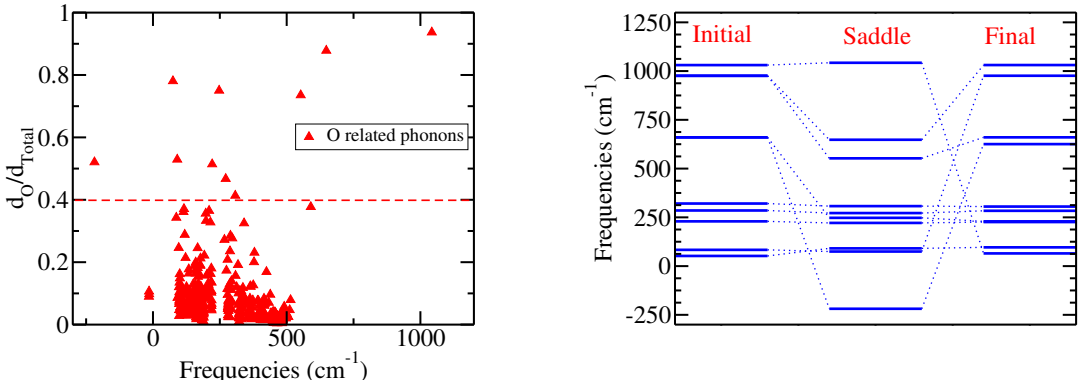

Figure 3.33: *(Left) Part of oxygen displacement in the phonons of O_{2i} to 2-O saddle point. (Right) Projection of the phonons related to oxygen (upon the doted red line in the left figure) on the phonons of O_{2i} and 2-O.*

frequency would then be the mode allowing to leave the minimum to reach the saddle point. To obtain this mode, a NEB calculation with many points is performed on the O_i migration (Figure 3.34). This assumption is drastic and can be seen as a strong simplification because we observe several frequencies change between the saddle point and the local minimum (Figure 3.31). The prefactor found using this approximation is still of the same order of magnitude.

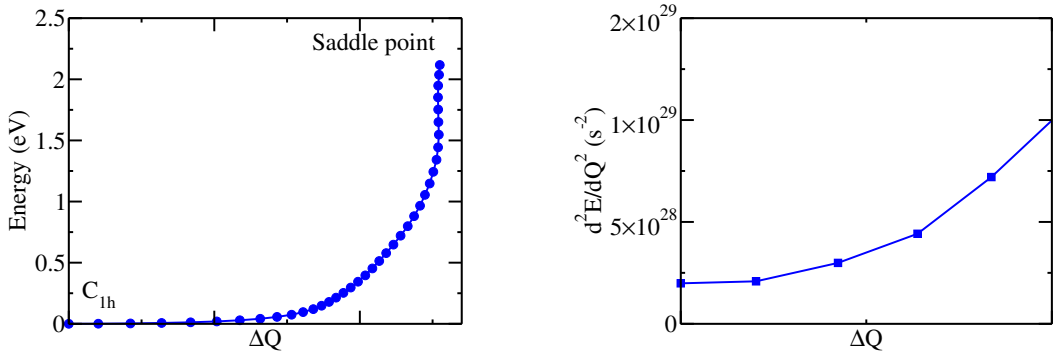

Figure 3.34: *(Left) Energy along the dissociation path as function of the displacement vector Q .(Right) Second derivative of the energy along the dissociation path against the displacement vector Q.*

3.3.5 B_sO_{2i} dissociation events

In this work, the first events for the dissociation of the B_sO_{2i} are investigated. It is difficult in the case of B_sO_{2i} to develop an exhaustive study of all dissociation mechanisms as the number of possible mechanisms increases considerably. Ab initio calculations must focus on the most probable mechanisms. The starting configuration chosen for B_sO_{2i} is here the A of 3.5. The particle emitted from the BsO_{2i} must also be discussed. In the KMC, the only particles that can be emitted from a clusters are those which can migrate. In B_sO_{2i}, two particles are mobile and can be emitted: the O_i and O_{2i}. The migration of the emitted O_{2i} has been calculated in the (110) plane as shown in Fig. 3.35. This plane was shown in Figure 3.14 as the direction in which the O_{2i} migration takes place. It is thus also believed to be the preferred direction of dissociation. The dissociation along this path corresponds to the change of the A configuration

into the structure A' and A" described in 3.5.

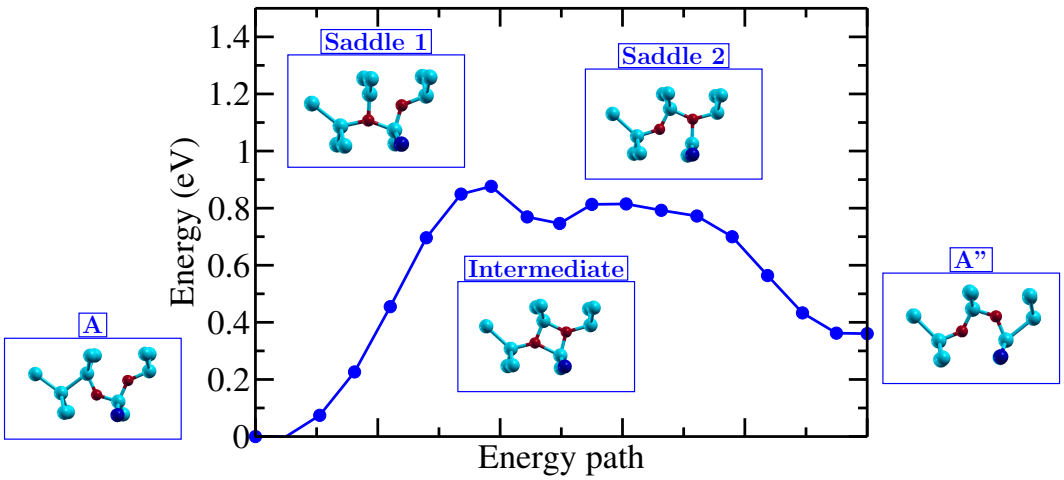

Figure 3.35: *NEB calculations of B_sO_{2i} dissociation with O_{2i} going away from B atom.*

The migration of an O_i away from the B_sO_{2i} cluster has also been calculated in the (101) plane (Figure 3.35) and are greater than the B_sO_{2i} dissociation with an O_{2i} emission.

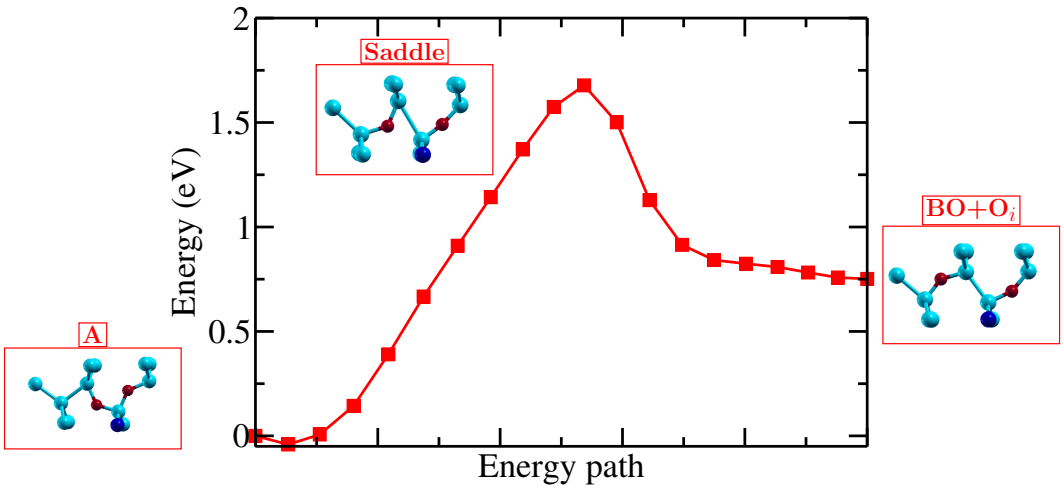

Figure 3.36: *NEB calculations of B_sO_{2i} dissociation with O_i going away from BO_i complex.*

3.4 Off-Lattice KMC simulations

3.4.1 Input parameters

The off-lattice KMC needs more information to work than the KMC [1]. The useful information are stored in three different files [45] :

- inputkmc.in
- buildlist.in
- catalogueinput.in

The inputkmc.in file contains the parameters necessary to run the KMC simulations. It provides the type of algorithm to use (onlattice KMC, off lattice KMC), the spatial and temporal domain of the simulation, the temperature and allows the coupling with the LAMMPS software to relax the structures.

The aim of the buildlist.in file is to provide the different types of events desired to create the event catalog. For each event, the initial and the final structures are provided. The number of atoms to be included in the events and the central atom used to analyze the system topology are also provided for each event. The activation energies and entropic prefactors are also required to write each event defined in the buildlist.in file.

The cataloginput.in is used to specify some parameters for building the event catalog. It specifies the number of different atoms types to be used in the construction of the graph. For each type, it indicates the distance at which two atoms are connected in the topology graph. It also specifies whether the graph should be constructed depending on the distance between atoms or with the number of atom connected. Two identical structures can also have a small numerical error in their positions. In practice, a distance is calculated to compare the topology of two structures. The parameters is used to define a threshold for which two distances should lead to the same topology.

3.4.2 Displacement issues

One of the issue of the off-lattice KMC is the propagation or the accumulation of small lattice distortion when an event is applied. It has been shown in 3.27 that O_i produces distortions on the Si lattice until the 4^{th} neighbor. When an event is applied, it is interesting to observe that the atoms of the initial positions are not the same as the atoms in the final positions. The atoms which are in the initial positions and not in the final positions keep their structure in the initial position after that the event is applied. This position is slightly deformed compared to the perfect crystalline position. The accumulation of these small distortion can create a topology where the event is not recognized anymore.

To solve this issue in the case of oxygen in Si, two methods were used:

- The simplest one is to modify the events implemented in the KMC. In our case, it is possible to manually placed O_i atoms bond-centered in a perfect Si crystal. This implementation has completely removed the distortion created by the O_i. The structures implemented in the catalogue are physically incorrect as they neglect the distortion, but this does not change the accuracy of the KMC. The distortion were taken into account in the DFT calculations and thus their effects are present in the implemented activation energies barriers.

  There is, however, a problem in this implementation: it does not take into account the possible angles for the O_i position around the <111> axis. In the case of the O_{2i}, there is no difference with the O_{2i} at the end of the migration path in the Figure 3.13. It have been shown in section 2 that in order to move from one configuration to the other, an activation barrier of 0.14 eV must be crossed. This events is thus forgotten in our simulations. The events have a much lower activation energy than the other mechanism which makes this approximation not too drastic. This small energy will lead to a system trapped between the two different forms of O_{2i} and is well known in the literature as the basin issue. The simulations will require an huge number of steps to leave the basin and the computational time required will explode. To solve this issues several methods exist with different level of accuracy. These methods are not implemented yet in the KMC used and the event to

pass from to has to be neglected. The other limitation of this method is that it is not suitable in the development of the KMC into a self-learning machine.

- Another method is to relax the structure between KMC steps to avoid the distortion in the simulation box. The relaxation can be performed by plugin a molecular dynamics software to the KMC. An issue of this solution is that the structure using MD are the same as obtained using DFT calculations. The relaxed LAMMPS structures are therefore not recognized if the events are implemented with structures obtained with DFT. The events structure must be relaxed in the events related files to avoid mismatch issues. As in the case of O_i on perfect Si lattice, the DFT precision is not lost by using MD relaxed structures because the DFT is take into account in the activation barriers energies implemented for the events. By minimizing the system energy between each step, the simulations no longer have distortion problems. The drawback of this method is that the MD takes more computation time than the KMC step. The simulation time is thus increased when using the MD relaxation.

In our simulations, we use the option of counting the bonds between atoms to define their connection. The catalogue of implemented events was set to take into account all the topologies where oxygens have less than 5 Si between then.

3.4.3 Dissociation energy

As mentioned previously, one of issue of the calibration of section 3.2.4 is that it does not calibrate a prefactor for the migration of O_{2i} and its dissociation, but the ratio of the two prefactors. Another limitation was the representation of O_{2i} dissociation in a single step. In order to solve these problems, a simulation of the O_{2i} lifetime was performed. The simulation of the time required for the dissociation of O_{2i} at higher temperatures allows to check if this dissociation follows an Arrhenius law or if the introduction of several events to perform the dissociation introduces several different regimes as a function of temperature. If the representation of this life time in logarithmic scale as a function of the inverse of the temperature is linear, then the dissociation follows an Arrhenius law and it is then possible to extract an activation energy and a prefactor. This activation energy can then be compared with the one implemented in the KMC. The migration prefactor can then also be implemented and allows to lift the degeneracy on the prefactors of O_{2i} migration and dissociation.

Initially the barriers calculated up to the fourth neighbor were implemented in the off-lattice KMC. The prefactors for the O_{2i} migration and O_{2i} dissociation events in 3-O and 2-P were fixed with the calculated values in DFT. The dissociation time is here averaged over 20 off-lattice KMC simulations for each temperature.

We observe that the dissociation time follows an Arhenius law on Figure 3.37. The associated parameters are an activation energy of 2.33 eV for the dissociation with a prefactor of 1.77×10^{15} s^{-1}. The activation energy found is less than the sum of the binding energy and the migration energy of the oxygen. The activation energy found actually corresponds to the energy maximum on the dissociation path of O_{2i} to 3-PP. However, a major problem of these simulations is that as shown in Figure 3.30, in fourth neighbor position the oxygens still interact with each other. Therefore, it is normal that the activation energy is lower than the estimate in Section 2. In order to evaluate the impact of the intermediate events, the interactions must be implemented up to the eighth neighbor. This implementation is difficult because the number of events to be implemented increases exponentially with the number of atoms in the events. The use of KMC on the fly is in this situation a possibility to take into account all these different events in the dissociation of O_{2i}.

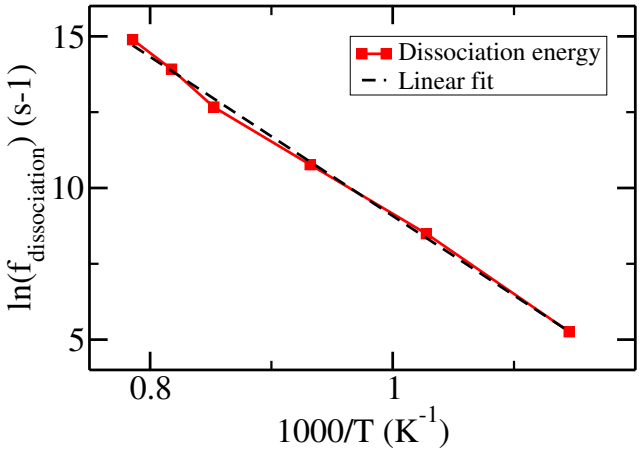

Figure 3.37: *Logarithm of the dissociation frequency in the Off-Lattice KMC depending on the temperature with the barriers implemented until the 4th neighbors (averaged on 20 simulations).*

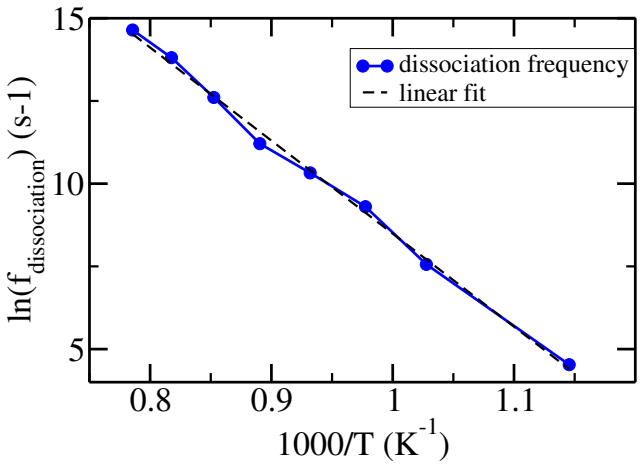

Figure 3.38: *Logarithm of the dissociation frequency in the off-lattice KMC depending on the temperature using an intermediate points in the O_{2i} dissociation path (averaged on 20 simulations).*

In a second approximation it was tested to observe only one intermediate event in the dissociation of O_{2i} in each direction. The 2-P and 2-O configurations are thus considered here. The dissociation events from 2-O and 2-P in the third neighbor are implemented with the prefactor and the migration activation energy allowing to overcome the $E_m(O_i) + E_b(O_{2i})$ barrier. The frequency evolution is shown in Figure 3.38. The dissociation energy found is then 2.51 eV and the entropic prefactor is 7.93×10^{15} s^{-1}. This approach shows that the approximation for the activation energy remains correct when an intermediate point is implemented in the dissociation path. The prefactor found represents a first approximation to a prefactor based entirely on DFT calculations. It can be seen that this prefactor is superior to the O_{2i} migration prefactor calculated using phonons and this trend is similar to that observed in the fit in section 2. Since the diffusivity simulation depends on the ration of the two prefactors, it should be possible to simulate the oxygen diffusivity reliably using the prefactors calculated in DFT and with the

off-lattice KMC for the migration and dissociation of O_{2i}, respectively.

3.4.4 Diffusion simulations with off-lattice KMC: perspectives

In order to simulate the diffusion of oxygen, two O_i are randomly placed into the simulation box. Then, a number N_{sim} of simulations is run in the KMC for a fix temperature and a fix number of steps. At then end of the simulation, the difference between the final positions of the two O_i and their initial position is computed. The physical time is also extracted. The diffusivity D can then be averaged by the formula:

$$D = \frac{\sigma_{traveled}}{2t} \tag{3.3}$$

With $\sigma_{traveled}$ being the distance between final and initial oxygens positions and t the time simulated.

There are several problems with this method. The first is that the simulation box used is too small compared to the maximum path traveled by the oxygen. The number of events simulated must to be greater than the number of migration to meet and rejoin. It must also be high enough to enable the O_{2i} to dissolve. At each migration jump, the O_i is displaced by 1.5 in the simulation box. With a number of 10000 simulated events, the simulation box should be larger than 1 micron. This is not possible in practice. The simulation box is thus limited to smaller size. The cell has periodic boundary conditions. The position along all the simulation is store in a .xyz file. At the end of the simulation, oxygen positions at each KMC step are analyzed to determine if the atoms overcome the cell box an to take into account this effect in the final distance.

The second issue is that the number of oxygen particles is limited to two. This caused because the event catalogue is generated with DFT data containing only two atoms. If more particles are introduced there is a probability that the 3 O_i be close to each other. In this situation the topology of the system will not be recognized and the KMC will stop.

A third limitation is the concentration of O_i in the simulation box. This concentration is tunable by changing the size of the box (the oxygen C_{oxygen} concentration will be obtained by $C_{oxygen} = \frac{2}{V_{box}}$). If we use a volume limited to 100000 atoms, the oxygen concentration will be limited to 5 x 10^{17} which is a high concentration of oxygen.

Simulations have been performed to simulate the diffusion of oxygen and in particular the phenomenon of enhanced diffusion at 700°C. When the two O_i form an O_{2i} dimer, they can either diffuse as a dimer or dissociate. As shown in the previous section, the activation energy of the transition rate for an O_{2i} separation event is approximated by 2.51 eV. The transition rate of the dimer migration for temperatures below 1000 °C is much lower than that for its dissociation. Thus, the event chosen at each iteration will be much more often an emigration event than a sequence of events corresponding to the dissociation of the dimer. The average number of migration events before achieving dimer dissociation is arround 10^6 for a temperature of 800°C. This number of steps is possible in the KMC object [1] but this number of steps is more difficult to simulate in the off-lattice KMC. The version used in this thesis is not yet fully optimized making the calculation of the diffusion coefficient very computationally expensive.

3.5 Conclusions

In this chapter, we have studied the BO_2 defect with the objective to understand its effect on the performance degradation of optoelectronic devices. We show that this defect is not sufficient to explain the degradation. In order to simulate in a predictive way the formation of this type of defect, we have shown the current limitations of commercial simulation codes, in particular the lack of description of some species. The implementation of a new species, here oxygen, has been a major work of this thesis. We have shown how to calibrate a new element in this kind of KMC using ab initio calculations. We highlight that commercial KMC codes use simplifications, necessary for a fast code execution, but which do not account for the true complexity that exists in the diffusion of atoms, anisotropy and long range interactions that can however be determinant in the arrangement of atoms.

Nevertheless, the DFT allows to calculate the different energies of the stable positions of the different oxygen and boron-oxygen complexes and this for several charge states. The ab initio calculations also give access to the activation energy values for the migration of O_i and O_{2i} species. An estimate of the activation energy for the dissociation of O_{2i} can also be made with the formation and migration energy values calculated in ab initio. Once the energies were calibrated, the prefactors could be calibrated to experimental values by simulating oxygen diffusion and these two regimes (high temperature and low temperature) in the KMC. This calibration is incomplete and complementary DFT calculations have been performed to study in more detail the dissociation of O_{2i} as well as to access the theoretical values of the prefactors. These complementary calculations allowed to use an off-lattice KMC and to extract a prefactor and an activation energy for the dissociation of O_{2i} which takes into account an intermediate point in the dissociation event.

References

[1] Sentaurus Process User Guide, R-2020.09, Synopsys Inc.

[2] I. Martin-Bragado, P. Castrillo, M. Jaraiz, R. Pinacho, J. Rubio, and J. Barbolla, "Physical atomistic kinetic monte carlo modeling of fermi-level effects of species diffusing in silicon", Physical Review B **72**, 035202 (2005).

[3] W. Bond and W. Kaiser, "Interstitial versus substitutional oxygen in silicon", Journal of Physics and Chemistry of Solids **16**, 44–45 (1960).

[4] W. Kaiser, P. H. Keck, and C. Lange, "Infrared absorption and oxygen content in silicon and germanium", Physical Review **101**, 1264 (1956).

[5] J. Coutinho, R. Jones, P. Briddon, and S. Öberg, "Oxygen and dioxygen centers in si and ge: density-functional calculations", Physical Review B **62**, 10824 (2000).

[6] J. F. Binder and A. Pasquarello, "Minimum energy path and atomistic mechanism of the elementary step in oxygen diffusion in silicon: a density-functional study", Physical Review B **89**, 245306 (2014).

[7] D. Timerkaeva, D. Caliste, T. Deutsch, and P. Pochet, "Oxygen in silicon: switch in the diffusion-mediated mechanism", Physical Review B **96**, 195306 (2017).

[8] D. Bosomworth, W. Hayes, and A. Spray, "Rl, and watkins, gd: proc", in Royal soc. london, series a, Vol. 317 (1970), p. 133.

[9] H. Yamada-Kaneta, C. Kaneta, and T. Ogawa, "Theory of local-phonon-coupled low-energy anharmonic excitation of the interstitial oxygen in silicon", Physical Review B **42**, 9650 (1990).

[10] H. Yamada-Kaneta, "Far-infrared absorption by interstitial oxygen impurities in silicon crystals", Physical Review B **58**, 7002 (1998).

[11] M.-H. Du, H. M. Branz, R. S. Crandall, and S. Zhang, "Bistability-mediated carrier recombination at light-induced boron-oxygen complexes in silicon", Physical review letters **97**, 256602 (2006).

[12] M. Vaqueiro-Contreras, V. P. Markevich, J. Coutinho, P. Santos, I. F. Crowe, M. P. Halsall, I. Hawkins, S. B. Lastovskii, L. I. Murin, and A. R. Peaker, "Identification of the mechanism responsible for the boron oxygen light induced degradation in silicon photovoltaic cells", Journal of Applied Physics **125**, 185704 (2019).

[13] D. Timerkaeva, D. Caliste, and P. Pochet, "Deciphering mechanisms of enhanced-retarded oxygen diffusion in doped si", Applied Physics Letters **103**, 251909 (2013).

[14] W. Shockley and W. Read Jr, "Statistics of the recombinations of holes and electrons", Physical review **87**, 835 (1952).

[15] T. Mchedlidze and J. Weber, "Direct detection of carrier traps in si solar cells after light-induced degradation", physica status solidi (RRL)–Rapid Research Letters **9**, 108–110 (2015).

[16] X. Chen, X. Yu, X. Zhu, P. Chen, and D. Yang, "First-principles study of interstitial boron and oxygen dimer complex in silicon", Applied Physics Express **6**, 041301 (2013).

[17] A. Resende, R. Jones, S. Öberg, and P. Briddon, "Calculations of electrical levels of deep centers: application to au-h and ag-h defects in silicon", Physical review letters **82**, 2111 (1999).

[18] J. Schmidt and K. Bothe, "Structure and transformation of the metastable boron-and oxygen-related defect center in crystalline silicon", Physical review B **69**, 024107 (2004).

[19] J. Adey, R. Jones, D. Palmer, P. Briddon, and S. Öberg, "Degradation of boron-doped czochralski-grown silicon solar cells", Physical review letters **93**, 055504 (2004).

[20] D. Macdonald, P. N. Deenapanray, A. Cuevas, S. Diez, and S. W. Glunz, "The role of silicon interstitials in the formation of boron-oxygen defects in crystalline silicon", in Solid state phenomena, Vol. 108 (Trans Tech Publ, 2005), pp. 497–502.

[21] V. P. Markevich, M. Vaqueiro-Contreras, J. T. De Guzman, J. Coutinho, P. Santos, I. F. Crowe, M. P. Halsall, I. Hawkins, S. B. Lastovskii, L. I. Murin, et al., "Boron–oxygen complex responsible for light-induced degradation in silicon photovoltaic cells: a new insight into the problem", physica status solidi (a) **216**, 1900315 (2019).

[22] J. Mikkelsen Jr, "Diffusivity of oxygen in silicon during steam oxidation", Applied Physics Letters **40**, 336–337 (1982).

[23] S.-T. Lee and D. Nichols, "Outdiffusion and diffusion mechanism of oxygen in silicon", Applied physics letters **47**, 1001–1003 (1985).

[24] P. Southgate, "Internal friction of single crystal silicon from 25° c to 1100° c", Proceedings of the Physical Society. Section B **70**, 804 (1957).

[25] J. Mikkelsen Jr, "Excess solubility of oxygen in silicon during steam oxidation", Applied Physics Letters **41**, 871–873 (1982).

[26] J. Mikkelsen, "The diffusivity and solubility of oxygen in silicon", MRS Online Proceedings Library (OPL) **59** (1985).

[27] R. Newman, "Oxygen diffusion and precipitation in czochralski silicon", Journal of Physics: Condensed Matter **12**, R335 (2000).

[28] Y. J. Lee, J. Von Boehm, M. Pesola, and R. M. Nieminen, "First-principles study of migration, restructuring, and dissociation energies of oxygen complexes in silicon", Physical Review B **65**, 085205 (2002).

[29] S. Senkader, P. Wilshaw, and R. Falster, "Oxygen-dislocation interactions in silicon at temperatures below 700° c: dislocation locking and oxygen diffusion", Journal of Applied Physics **89**, 4803–4808 (2001).

[30] J. Murphy, S. Senkader, R. Falster, and P. Wilshaw, "Oxygen transport in czochralski silicon investigated by dislocation locking experiments", Materials Science and Engineering: B **134**, 176–184 (2006).

[31] A. Giannattasio, J. Murphy, S. Senkader, R. Falster, and P. Wilshaw, "Oxygen and nitrogen transport in silicon investigated by dislocation locking experiments", Journal of The Electrochemical Society **152**, G460 (2005).

[32] V. Quemener, B. Raeissi, F. Herklotz, L. Murin, E. Monakhov, and B. Svensson, "Kinetics study of the evolution of oxygen-related defects in mono-crystalline silicon subjected to electron-irradiation and thermal treatment", Journal of Applied Physics **118**, 135703 (2015).

[33] P. Pichler, *Intrinsic point defects, impurities, and their diffusion in silicon* (Springer Science & Business Media, 2012).

[34] S.-T. Lee, P. Fellinger, and S. Chen, "Enhanced and wafer-dependent oxygen diffusion in cz-si at 500–700 c", Journal of applied physics **63**, 1924–1927 (1988).

[35] F. Livingston, S. Messoloras, R. Newman, B. Pike, R. Stewart, M. Binns, W. Brown, and J. Wilkes, "An infrared and neutron scattering analysis of the precipitation of oxygen in dislocation-free silicon", Journal of Physics C: Solid State Physics **17**, 6253 (1984).

[36] A. Brown, R. Murray, R. Newman, and J. Tucker, "Measurements of enhanced oxygen diffusion in silicon during thermal donor formation: new evidence for possible mechanisms", MRS Online Proceedings Library (OPL) **163** (1989).

[37] L. Zhong and F. Shimura, "Hydrogen enhanced out-diffusion of oxygen in czochralski silicon", Journal of applied physics **73**, 707–710 (1993).

[38] R. Capaz, L. Assali, L. Kimerling, K. Cho, and J. Joannopoulos, "Mechanism for hydrogen-enhanced oxygen diffusion in silicon", Physical Review B **59**, 4898 (1999).

[39] M. Ramamoorthy and S. Pantelides, "Enhanced modes of oxygen diffusion in silicon", Solid state communications **106**, 243–248 (1998).

[40] P. Grönberg, J. v. Boehm, and R. Nieminen, "Molecular dynamics study of oxygen defects in silicon", in *Early stages of oxygen precipitation in silicon* (Springer, 1996), pp. 441–446.

[41] N. Cowern, K. Janssen, G. Van de Walle, and D. Gravesteijn, "Impurity diffusion via an intermediate species: the b-si system", Physical review letters **65**, 2434 (1990).

[42] Z. Zeng, J. Murphy, R. Falster, X. Ma, D. Yang, and P. Wilshaw, "The effect of impurity-induced lattice strain and fermi level position on low temperature oxygen diffusion in silicon", Journal of Applied Physics **109**, 063532 (2011).

[43] M. Gunde, N. Salles, A. Hémeryck, and L. Martin-Samos, "Ira: a shape matching approach for recognition and comparison of generic atomic patterns", Journal of Chemical Information and Modeling **61**, 5446–5457 (2021).

[44] S. Baroni, S. De Gironcoli, A. Dal Corso, and P. Giannozzi, "Phonons and related crystal properties from density-functional perturbation theory", Reviews of modern Physics **73**, 515 (2001).

[45] M. Gunde, "Development of ira: a shape matching algorithm, its implementation, and utility in a general off-lattice kmc kernel", PhD thesis (Université Paul Sabatier-Toulouse III, 2021).

Calibration of a process effect: heated implantations

4

Contents

Introduction

This chapter discusses the defects generated by the use of a heated implantation during the elaboration process. To study the heated implantation process, we investigated several implantation cases with respect to the experimental data that were available for the study. Three cases are then studied both by experimental characterizations and by modeling and simulation.

- In a first part, the heating produced by the implantation process itself, so called self-heating, is studied in the case of the carbon implantation. A model taking into account the heating of the wafer during the implantation in the KMC simulations has been implemented. The reliability of the model was then tested by comparing the KMC predictions of amorphous layers thickness with amorphous layers observed in TEM on wafers where the self-heating had been intentionally modified.
- The second and third sections discuss the effect of wafer heating during implantation on defect formation and the nature of these defects at the end of the process. Two different implants are studied both experimentally using TEM and Photoluminescence characterizations and with modeling:
  - In the second section, we detail defects obtained after phosphorus heated implantations.
  - in the third section, we detail defects obtained after phosphorus heated implantations. For the specific case of arsenic heated implant, we also develop and propose an improvement of the defect calibration and the use of TCAD models in the case of heated implantations. Such calibration can be done regarding data available in the literature or with the objective to fit experimental trends. Another strategy using ab initio calculations is also discussed.

4.1 The self-heating during implantation: study of the of carbon implantation

4.1.1 Implantation machines

The implant tool used in this study is an industrial Viista HCS implanter by Applied Materials, specifically designed for low energy implants. The end-station of the Viista HCS is represented in Fig. 4.1. Ions are implanted using a fixed ribbon beam placed in front of the wafer, which moves back and forth in front of it. The full implant dose is achieved by N_{passes} (back or forth) of the wafer. Ions are accelerated and hit the wafer with an energy E_{ions}. The flux of ions hitting the wafer is given by the intensity I_{beam}. The cooling system consists of a N_2 gas in contact with the wafer. The gas itself is cooled down by an internal water system. Velocity of the wafer, width of the ribbon beam and number of steps N_{passes} are not the same from one process to another. These parameters are optimized by the implanter for each implant depending on the requested ion energy and dose.

4.1.2 Model for the self-induced heating during implants

The temperature evolution of one unit area at the center of the wafer is calculated in our model. This area is alternatively heated and cooled down, depending on whether it is exposed to the beam or not. The first step for the estimation of the temperature profile of such unit area is then to calculate the time during which the beam is above the area and the time interval between two consecutive beam exposures. The velocity of the moving wafer is measured by the implanter

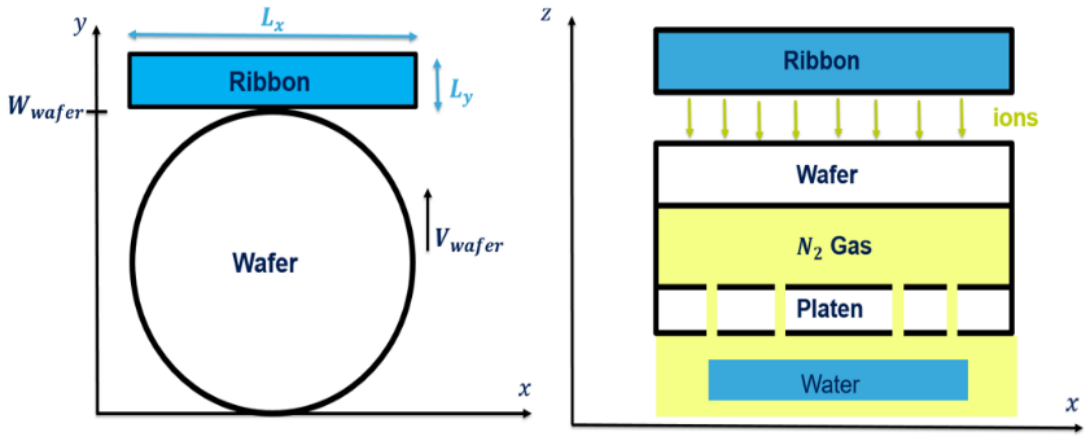

Figure 4.1: *Schematics of the implanter end-station used in this work (left) and of its cooling system (right).*

sensor. The diameter of the wafer, W_{wafer}, being known, it is therefore possible to calculate the beam exposure time, $t_{exposed}$, and the time between two consecutive exposures, $t_{cooling}$:

$$t_{exposed} = \frac{L_y}{V_{wafer}} \tag{4.1}$$

$$t_{cooling} = \frac{W - L_y}{V_{wafer}} \tag{4.2}$$

The temperature profile is then calculated using the one-dimensional heat equation:

$$d_w \rho c_p \frac{dT}{dt} = -\alpha p_{cooling}(T - T_f) + P_{beam}(t) \tag{4.3}$$

This equation assumes that the wafer is thin enough (d_w being the wafer thickness) to be heated uniformly throughout its depth while exposed to the beam. It also assumes that the heat dissipation along the x and y axes can be neglected compared to the heat exchanges with the surface in contact with the cooling system. The power of the beam per unit area $P_{beam}(t)$ is equal to $\frac{E_{ions} I_{beam}}{qA}$ for a heating phase and is null for a cooling phase. The remaining parameters are defined as follows: ρ and c_p are the silicon mass density and thermal capacitance, T_f is the water temperature (cf. Fig. 4.1), $p_{cooling}$ is the cooling gas pressure and α ($m.s^{-1}.K^{-1}$) is a constant. The temperature evolution calculated according to eq. (3) by our homemade code is expected to exhibit a saw-tooth like increase. An example is shown in Fig. 4.2 (details will be discussed in next section). In a second step, our code generates a KMC input file containing the information about the temperature time evolution, which is transferred to the Sentaurus Process KMC software [1] for the simulation of the ion implant step. The implantation process is divided in N_{passes} and each implantation step is simulated at a temperature determined at the end of the previous one.

Atomic diffusion steps are included between successive implant steps in the KMC input file to simulate the defect evolution in the wafer when the area is not irradiated by the ribbon ion

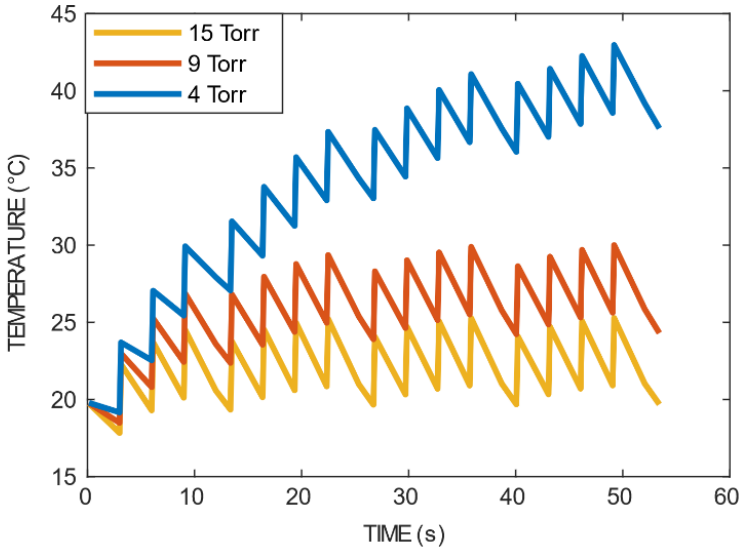

Figure 4.2: *Simulation of temperature evolution during a 60 keV carbon implant with a dose of* 1.5×10^{14} cm^{-2} *for three different cooling pressures (4, 9 and 15 Torr).*

beam. Finally, the dose rate is also implemented in the KMC input file, it is defined as the ion dose received per unit time by a given area during the time interval at which the area is exposed to the ribbon beam.

4.1.3 Experiments to validate the model

The validation of our self-heating model has been achieved by comparison with experimental results. The parameter used for the comparison is the thickness of the continuous amorphous layer created by a carbon implant. Indeed, amorphous pockets are too small to be reliably observed and measured while a continuous amorphous layer can be simply measured by TEM due to the different contrast of the amorphous and crystalline phases in TEM images. Moreover, the amorphization kinetics is not the same for heavy and light ion implants. For a light ion implant, an amorphous layer is created by the accumulation and growth of small amorphous pockets whereas a single heavy ion can directly create a stable amorphous area around its collision cascade. Amorphization by light ions is therefore more sensitive to a modification of the implant temperature, which justifies the choice of carbon for our model validation.

In order to study only the impact of wafer temperature on amorphization and to isolate it from other experimental parameters, a fixed implant energy and dose were used for the experiment, while the backside cooling pressure was changed. Indeed, the implanter fixes the ribbon beam dimension, the number of implantation steps and the velocity of the wafer depending on the selected implant dose and energy. The temperature modification of the wafer therefore occurs at fixed heating and cooling time intervals, with differences in temperature levels due only to the different cooling pressures used.

For this experiment, the ion energy was fixed at 60 keV, while the ion dose was set at 1.5×10^{15} cm^{-2}, which is close to the threshold value for amorphization in the case of a room temperature implant. Indeed, near this threshold, light mass ions exhibit a super-linear behavior in the damage accumulation as a function of temperature. Implantation of a light ion such as carbon in this super-linear regime therefore makes the system very sensitive to temperature changes, which are expected to result in easily observable changes in damage formation.

Fig. 4.2 reports the simulated temperature profiles for a carbon implant performed at 60 keV and to a dose of 1.5×10^{15} cm^{-2}, using a cooling pressure of 4, 9 and 15 Torr, respectively. The results clearly indicate that the lowest cooling pressure leads to the higher wafer temperatures.

4.1.4 Experimental and simulation results

Figure 4.3 (right, A, B and C) reports the TEM cross section images taken from silicon samples implanted with 60 keV C+ to a dose of 1.5×10^{15} cm^{-2} for three different cooling pressures (15, 9 and 4 Torr, respectively). The TEM images clearly show that an amorphous layer is formed in the three samples, as indicated by the uniform light contrast regions visible in all images below the surface. However, its thickness varies depending on the backside cooling pressure used for the implant: it decreases when the cooling pressure decreases, i.e. when the wafer temperature increases (cf. Fig. 4.2). This result already provides a qualitative explanation about the impact of the self-induced heating on damage generation. Indeed, the increased temperature favors the point defect recombination and hence slows down the amorphization process.

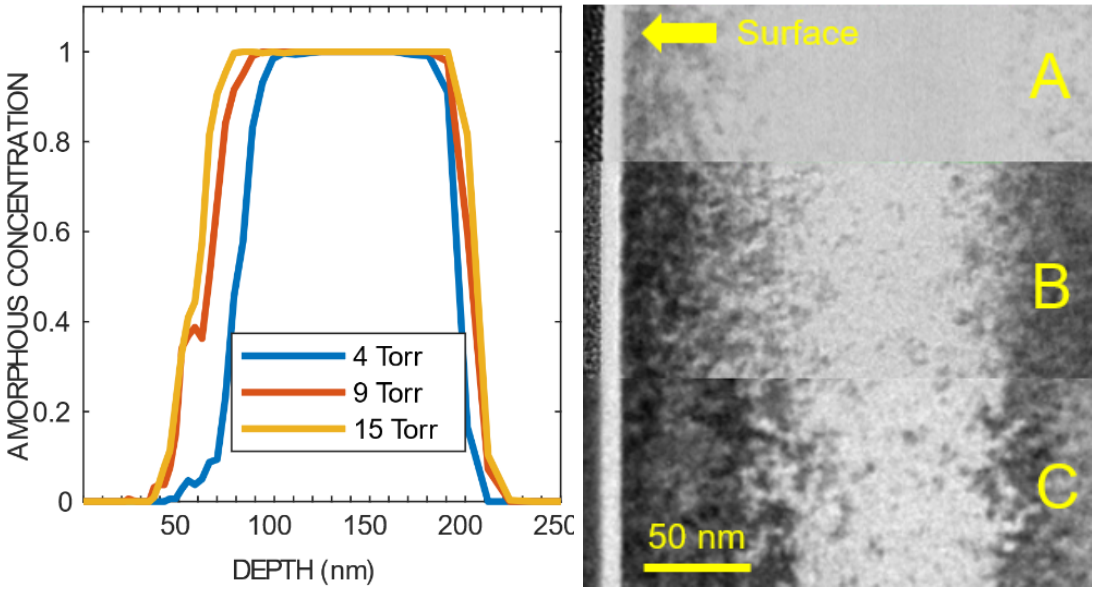

Figure 4.3: *(Left) Simulation of amorphous concentration as function of the depth for a 60 keV carbon implantation with a dose of* 1.5×10^{15} *cm*$^{-2}$ *and for cooling pressures of 15, 9 and 4 Torr. (Right) A, B and C are the TEM images of 60 keV carbon implanted wafers with a dose of* 1.5×10^{15} *cm*$^{-2}$ *and a cooling pressure of 15, 9 and 4 Torr respectively.*

To enable the quantitative comparison between the experimental observations and the model predictions, the experimental values of the amorphous layer thickness have been determined by plotting the depth profile of the image contrast from each TEM micrograph. The contrast level at a given depth is obtained by laterally integrating the signal over the entire image. At a given depth on the sample the silicon is considered as amorphous where the brightness is above 85 % of the brightest point in the TEM image. The extracted values are reported in Table 4.1 and compared with those obtained with the KMC simulation code, which enables to plot average 1-D depth profiles of the point defects generated during the implant. The threshold value for amorphization is set at a point defect concentration of 1.5×10^{22} cm^{-3}. This enables amorphization 1-D profiles along the depth of the wafer, which are presented in Fig. 4.3 (left) for the three different values of the gas cooling pressure. The simulated curves indicate the same trend as for the experimental results, i.e. the amorphous thickness increases proportionally to the backside cooling pressure. The amorphous layer thickness reaches 120 nm

Table 4.1: *Comparison between simulation and experimental data for amorphous layer thickness (in nm).*

Wafer	KMC	experimental
Carbon 60 keV 1.5×10^{15} cm^{-2} 4 Torr	80	80
Carbon 60 keV 1.5×10^{15} cm^{-2} 9 Torr	103	100
Carbon 60 keV 1.5×10^{15} cm^{-2} 15 Torr	120	110

with a backside cooling pressure of 15 Torr, whereas an amorphous layer of 80 nm is obtained for a backside cooling pressure of 4 Torr. The simulated values are in very good agreement with the measured ones, as shown in Table 4.1, therefore demonstrating the reliability of the physical model developed for their calculation.

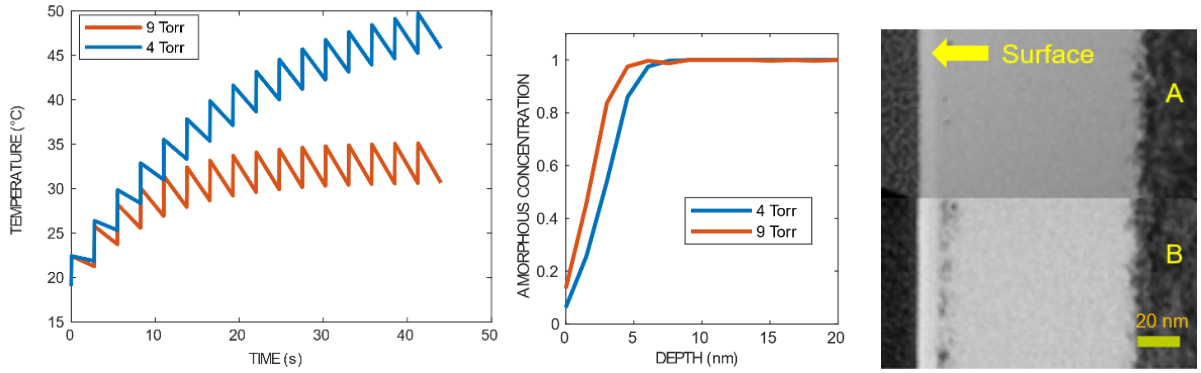

Figure 4.4: *(Left) Simulation of temperature evolution during a 30 keV carbon implant with a dose of* 2×10^{15} *cm*$^{-2}$ *for three different cooling pressures (4, 9 and 15 Torr). (Center) Simulation of amorphous concentration as function of the depth for a 30 keV carbon implantation with a dose of* 2×10^{15} *cm*$^{-2}$ *and for cooling pressures of 9 and 4 Torr. (Right) A and B are the TEM images of 30 keV carbon implanted wafers with a dose of* 2×10^{15} *cm*$^{-2}$ *and a cooling pressure of 9 and 4 Torr respectively.*

The effect of the cooling pressure on amorphization was also simulated for a reduced carbon implantation energy (30 keV) compared to the previous case, while the implant dose was increased up to 2×10^{15} cm^{-2}. The difference in temperature for the two implantation conditions can be observed in Fig. 4.4 (left). The effect of the pressure is the same as for the 60 keV implantation: a smaller cooling pressure induces higher temperature during implantation. Amorphization profiles for these two conditions are simulated in Fig. 4.4 (center). They follow the same trend as in the 60 keV implant case, i.e. the higher the cooling pressure, the thicker the amorphous layer. However, the difference between the amorphous thicknesses calculated with the two gas pressures is much smaller compared to the previous case. Still, the TEM images allow to confirm the reliability of the calculations by showing more crystalline areas near the surface (and hence a thinner amorphous layer) for the high-pressure case (Fig. 4.4, right, image B).

Finally, we tested the simulation model in the high dose regime (4×10^{15} cm^{-2}), *i.e.* well beyond the amorphization threshold, where the wafer temperature is expected to have an even weaker impact on the amrophisation kinetics. The simulation results are shown in Fig. 4.5 for an implant energy of 30 keV and cooling pressures of 4, 9 and 15 Torr. A difference in wafer temperature is still observed (cf. Fig. 4.5 left), which is even larger than in the previous lower dose implants. However, the KMC simulations do not predict any significant difference in the amorphous thickness, in perfect agreement with the TEM images (Fig. 4.5 right).

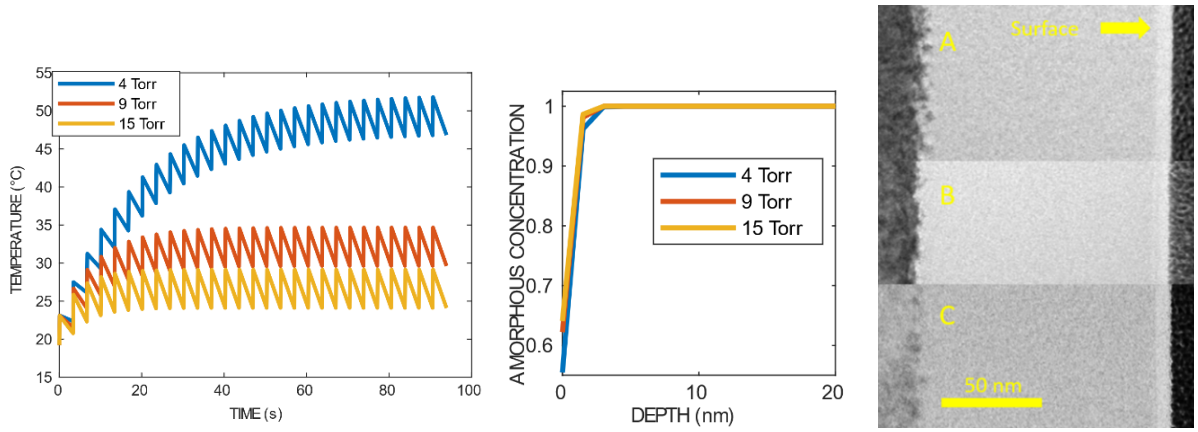

Figure 4.5: *(Left) Simulation of temperature evolution during a 30 keV carbon implant with a dose of* 4×10^{15} cm^{-2} *for two different cooling pressures (4, 9 Torr).(Center) Simulation of amorphous concentration as function of the depth for a 30 keV carbon implantation with a dose of* 4×10^{15} cm^{-2} *and for cooling pressures of 4, 9 and 15 Torr. (Right) A, B and C are the TEM images of 30 keV carbon implanted wafers with a dose of* 4×10^{15} cm^{-2} *and a cooling pressure of 15, 9 and 4 Torr respectively.*

In summary, this work shows that the amorphous thickness can be finely tuned from dozens of nm to less than 5 nm by changing a specific machine-related parameter (i.e. the backside pressure cooling) on a standard industrial implanter. Moreover, the combination of a "homemade" model (for the prediction of the wafer temperature as a function of this specific machine-related parameter) with the KMC simulation code Sentaurus Process (for the evolution of implant-induced damage and amorphous pockets kinetics) results in a perfect prediction of the observed amorphization kinetics in a wide range of implant conditions, including those corresponding to the super-linear regime (close to the amorphization threshold) as well as the high-dose implants (full amorphization).

4.2 Characterization of phosphorus heated implantations

4.2.1 Experimental results

4.2.1.1 Experimental details

Phosphorus implantations are studied. The implantations are followed by annealing to activate the dopants. An implantation with the dose of the classical recipe was implanted at RT and another one at 150°C. Another wafer was implanted with phosphorus but this time with a lower dose. A fourth wafer was implanted with the same dose and energy as in the original recipe but with a different annealing. The conditions of implantation and annealing are indicated in the Table 4.2.

Table 4.2: *Energies, dose of phosphorus implantations and temperature and time of annealing.*

Sample name	Energy (keV)	Dose (cm^{-2})	$T_{implant}$	Annealing
Ph 2	1.39 MeV	6×10^{13}	RT	3 min 950°C in N2/O
Ph 3	1.39 MeV	6×10^{13}	150°C	3 min 950°C in N2/O2
Ph 12	1.39 MeV	2×10^{13}	RT	3 min 950°C N2/O2
Ph 18	1.39 MeV	6×10^{13}	RT	3 min 875°C in N2

4.2.1.2 Photoluminescence imaging

The implanted samples were also analyzed by photoluminescence (PL) imaging, a non-destructive optical characterization technique available at STMicroelectronics [2], specifically developed to be compatible with industrial manufacturing environment. In particular, PL imaging allows detecting defect-related PL emission peaks at room temperature, which is extremely difficult with conventional PL spectroscopy, due to thermal broadening. In contrast, all the wavelengths contained in the selected range are integrated to enhance the signal to noise ratio, so that the specific information on the energy levels associated to the emitting defects is lost. In addition, the spatial resolution is limited by the minimum size of the detecting pixels (0.145 μm x 0.175 μm). Still, for sufficiently large defects, this technique enables an estimation of the density of emitting defects and of their size. Moreover, depending on the intensity of the emitted signal, it is possible to qualitatively separate defects of different nature. This technique has already been shown to successfully detect PL signals from DLs formed by high-energy phosphorus implantation and anneal [2].

The photoluminescence imaging method was applied to the four investigated samples (cf. Table 4.2) and typical PL maps are shown in Figure 4.6. Defects appear as clear spots or lines (with different levels of grey contrast) on a dark background. Elongated defects (lines) are systematically parallel to either <100> or <110> directions, and are therefore tentatively related to the dislocations observed in cross-section TEM. Additional defects appear in the form of spots and might be related to shorter (unresolved) dislocations or to defects of a different nature. The impact of the implant temperature can be estimated by comparing the maps reported in the top row of Figure 4.6 (RT implant on the left, 150°C implant on the right). A decrease of the elongated defects density is clearly visible when the implant temperature is raised to 150°C, which is in perfect agreement with the expected reduction of residual damage in high-temperature implants. Moreover, when the implant dose for a RT implant is decreased from 6×10^{13} cm^{-2} (Figure 4.6 top left) to 2×10^{13} cm^{-2} (bottom left), no PL signal is detected. This suggests that the implant damage induced by the low dose implant is fully recovered during the anneal, or that the density of the extended defects is below the detection limit of the technique. Finally, the PL image from the sample implanted at RT with a dose of 6×10^{13} cm^{-2} and annealed in pure nitrogen (Figure 4.6 bottom right) exhibits a higher density of smaller defects compared to the sample implanted in N_2/O_2 (top left). Indeed, during annealing in a N_2/O_2 ambient, it is expected that the interstitial atoms injected due to oxidation strongly contribute to the growth of the extended defects.

4.2.1.3 Photoluminescence spectroscopy

A more detailed optical investigation of the defects formed in the P implanted samples was finally achieved by photoluminescence spectroscopy, which allows assigning a specific "signature" to each type of defect (energy level, peak width). Photoluminescence spectroscopy is a complementary technique to TEM, especially in the case of extremely small defect clusters composed of few atoms, which cannot be directly observed by TEM. The photoluminescence experiments were performed with an Oxxius laser diode with a wavelength of 488 nm. This wavelength enables to probe a ~500 nm-thick layer below the surface. The excited area on the wafer has a diameter of 1.2 μm. The power used is 20 mW. Photoluminescence spectra are normalized with respect to the acquisition time. Spectra were acquired at temperatures ranging from 300 K down to 8 K.

Figure 4.7 shows the PL spectra recorded at 8 K for the four samples implanted with phosphorus (cf. Table 4.2). It can be clearly seen that the two samples implanted with a dose of 6×10^{13} cm^{-2} and annealed in N_2/O_2 (black and red curves) exhibit a very similar spectrum, with two

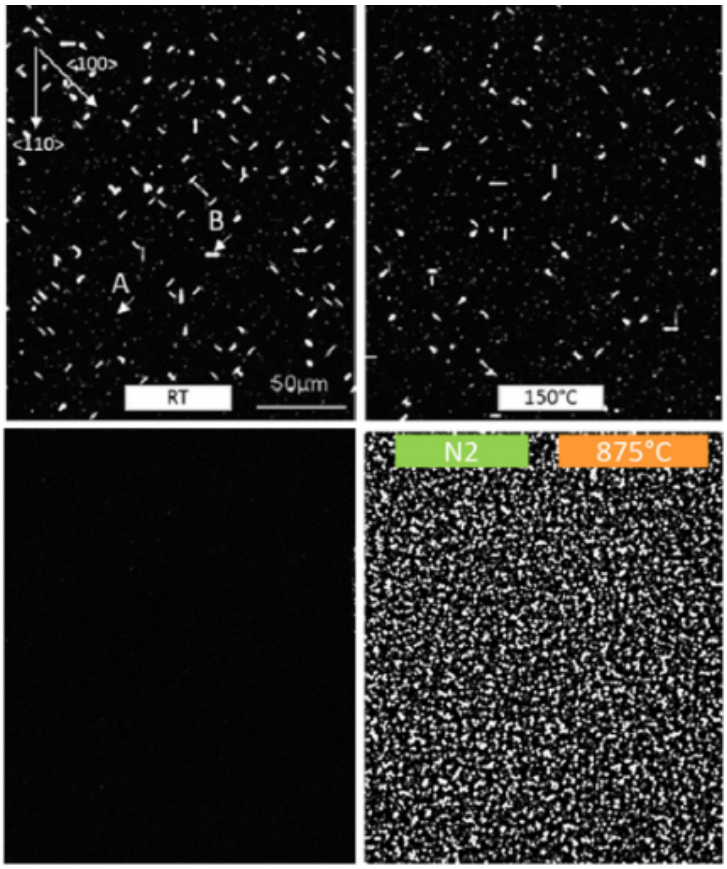

Figure 4.6: *Photoluminescence imaging maps taken from samples implanted with high-energy P ions with different conditions (cf. Table 4.2). Top left: Sample Ph 2. Top right: Sample Ph 3. Bottom left: Sample Ph 12. Bottom right: Sample Ph 18.*

broad peaks centered at ∼1390 nm and ∼1490 nm. The main difference consists in a lower peak intensity for the sample implanted at 150°C (Ph3, red curve) compared to the sample implanted at RT (Ph2, black curve). Assuming that the observed peaks are related to the dislocations observed in TEM as well as to the elongated defects seen in PL imaging maps, this result is in perfect agreement with the reduced implant damage expected when the implant temperature is increased to 150°C. Moreover, the PL spectrum from sample Ph12 implanted with a dose of 2×10^{13} cm^{-2} exhibits the highest band-to-band signal with no other emission peaks throughout the spectrum (blue curve in Figure 4.7), indicating the absence of defects, in agreement with the PL imaging results (cf. Figure 4.6 bottom left). Finally, sample Ph18 implanted with a dose of 6×10^{13} cm^{-2} and annealed in N_2 (green curve in Figure 4.7) shows several low intensity peaks in the 1150-1250 nm range, and a more intense peak centered at 1530 nm.

Deconvolution analysis was applied in order to determine the main optical emission peaks from all the investigated samples, which are labeled P1/P2 (sample Ph 2), P3/P4 (sample Ph3) and P5 (sample Ph 18) in Figure 4.7. The corresponding wavelength positions are summarised in Table 4.3.

We now focus on the samples Ph2 and Ph3, processed under the same conditions except for the implant temperature. The PL spectra acquired at different temperatures from these two samples are reported in Figure 4.8. In all cases, the intensity of the emission peaks P1-P4 is

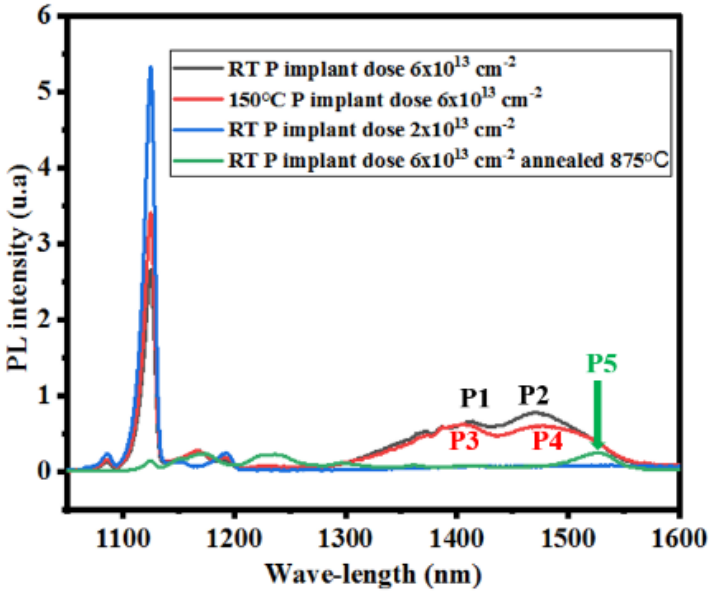

Figure 4.7: *PL spectra taken at a temperature of 8K from samples implanted with P under different conditions (Table 4.2.*

Table 4.3: *Peak wavelength positions determined by deconvolution from the samples implanted at RT and 150°C.*

	Ph 2 - RT implant N_2/O_2 anneal		**Ph 3 - 150°C implant N_2/O_2 anneal**		**Ph 18 - RT implant N_2 anneal**
Peak label	P1	P2	P3	P4	P5
Wavelength (nm)	1390	1482	1397	1493	1530

found to decrease when increasing the acquisition temperature, which is expected due to thermal broadening. In addition, all the observed peaks are shifted towards higher wavelength at higher acquisition temperatures. Such a common behavior for the four identified peaks suggests that they all originate from defect type. In previous section, the optical behavior of dislocations was briefly discussed. In particular, it was mentioned that they are generally observed by pairs D1/D2 and D3/D4 [3], while the presence of contaminants and/or precipitates located in the vicinity of the dislocations have been shown to play an important role in enhancing or reducing their intensity [3]. In our case, the peak pairs observed in each sample (P1/P2 in sample Ph 2 and P3/P4 in sample Ph3) are located at slightly lower wavelengths (∼35 nm) than the D1/D2 lines. This wavelength shift is very close to the one found in previous section for As implants (∼38 nm between the observed A1/A2-A3/A4 pairs and the reference S1/S2 lines). This shift might be due to a setup problem that is currently under investigation. However, the wavelength separation between the peaks observed in each sample (P1/P2 in sample Ph 2 and P3/P4 in sample Ph 3) is ∼95 nm, which perfectly corresponds to the one reported for the D1/D2 pair (91 nm in [3], 106 nm in [4]). Moreover, the peak evolution as a function of the acquisition temperature (cf. Figure 4.8) is also consistent with that of the D1/D2 peaks, including the progressive shift towards higher wavelength when the acquisition temperature increases [5]. Considering that, in these samples, dislocations were observed by TEM and elongated defects were imaged in PL maps, it can therefore be concluded that, P1-P4 peaks observed in this work correspond to the D1/D2 lines originating from the dislocations. It is interesting to note that samples Ph2 and Ph3 were annealed in an oxygen-reach annealing ambient, which is known to enhance the optical emission from D-lines [4]. In contrast, sample Ph18, annealed in pure nitrogen did not exhibit

any peak in the D1/D2 region, the main peak (P5 in Table 4.7) being located at 1530 nm. This result is in agreement with work of Giri et al [6]. who investigated the impact of the annealing ambient on the optical properties of silicon samples implanted with different species, including Al, P and Si ions [7] at doses of 2×10^{14} cm^{-2}. Indeed, the authors found that D1/D2 lines were observed in Al and P implanted samples followed by annealing in pure oxygen ambient, whereas, in the case of a pure nitrogen ambient, no D1/D2 lines were observed and a peak was instead observed at ∼1600 nm that the authors attributed to impurity-related precipitates. Due to the lower implant doses investigated in our study (6×10^{13} cm^{-2}), it is unlikely that the P5 peak observed at 1530 nm is related to P precipitates. Further analyses are therefore needed to identify its origin.

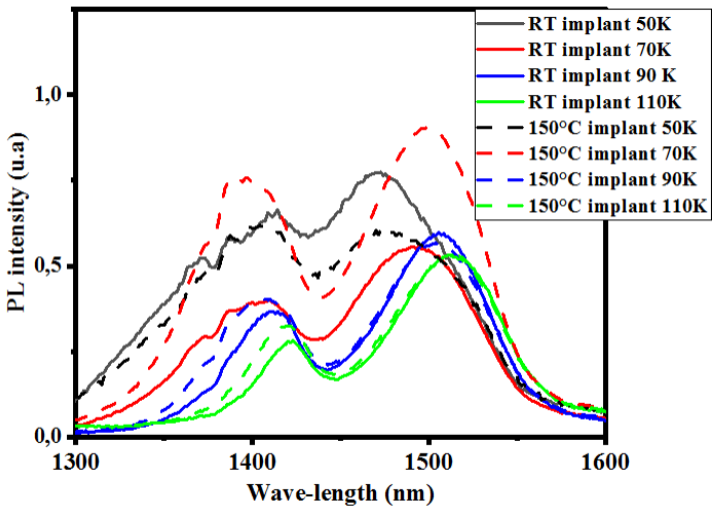

Figure 4.8: *PL spectra acquired at different temperatures from samples Ph2 and Ph3 (cf. Table 4.2) implanted with P at different temperatures (RT and 150°C respectively).*

4.2.2 Modeling: phosphorus KMC simulations

The phosphorus implantations have also been simulated with KMC. The impact of the oxygen in the annealing is not simulated here. Oxygen is believed to affect the evolution of DLs during annealing [8][9] but this effect is not implemented in the KMC. A simulation cell area of 150 nm^2 is needed to reproduce DLs in RT and 150 °C cases.

It can be observed that the formed DLs are far from the surface (Figure 4.9). The process simulation using a dose of 2×10^{13} cm^{-2} does not lead to the appearance of DLs. In these cases, the KMC simulation is therefore qualitatively consistent with the PL images.

The density of DLs predicted in the simulations is strongly related to the size of the simulation cell and the area used in the simulation and therefore cannot be compared to the PL images in Figure 4.6. Indeed, the size of the defects in the Figure 4.6 is larger than the size of the KMC simulation box Figure 4.9. Moreover, from a certain size, the DLs in the KMC simulation exchange interstitials with themselves because of the periodic boundary conditions. In reality, a DL does not exchange interstitials with itself but with a neighboring DL of a different size. The Ostwald ripening mechanism favors in this situation the growth of the larger of the two DLs to the benefit of the other.

The study of the defects generated by these phosphorus implantations was then not deepened. Their density and size observed in PL do not make them the best candidates to study with the KMC.

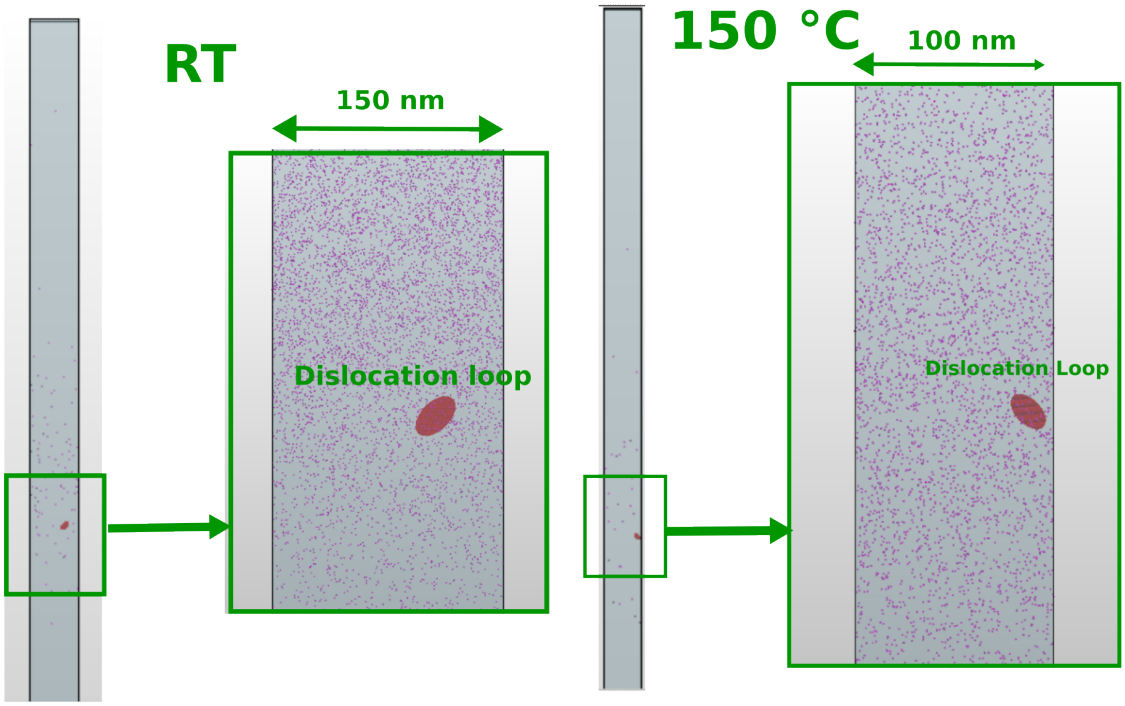

Figure 4.9: *KMC simulations of phosphorus implantation at RT and 150°C with a dose of* 6×10^{13} cm^{-2} *and followed by annealing described Table 4.2. The red circles represent the DLs.*

4.3 Characterization of arsenic heated implantations and their annealing sequence

4.3.1 Experimental results

4.3.1.1 Experimental details

The heated As implantations investigated are high energy and medium dose implantations. The details of these implantations are shown in Table 4.4. A total of three wafers were implanted under the same dose and energy conditions, but at different temperatures: One wafer was implanted at RT while for the two other wafers, the chuck was heated during the two other implantations to 150°C and 500°C respectively. These implantations were characterized as-implanted by TEM. An industrial annealing sequence was then applied to these wafers following the conditions given in Table 4.5. The annealing sequence is quite complex but is adapted to the technological constraints of the studied process. The purpose of heating the wafer during implantation was in this case to reduce the concentration of defects appearing at the end of annealing in the original recipe.

Table 4.4: *Arsenic implantation doses, energies and temperatures used during implantation*

$T_{implant}$	energy (keV)	Dose (cm^{-2})
RT (20 °C)	180 + 100	$10^{14} + 8 \times 10^{13}$
150 °C	180 + 100	$10^{14} + 8 \times 10^{13}$
500 °C	180 + 100	$10^{14} + 8 \times 10^{13}$

Table 4.5: *Annealing process performed after As implantation.*

Annealing steps	Temperature (°C)	Time
1	625	2h
2	750	1h
3	700	3h30
4	625	52 mn
5	800	30 mn
6	750	1 h

4.3.1.2 TEM characterization

Figure 4.10 presents the cross-section TEM images taken from samples implanted at different implant temperatures and prior to the annealing step. It is evident that the residual damage remaining after the implant strongly depends on the implant temperature.

- At room temperature (Figure 4.10 left), a continuous buried amorphous layer is formed, as indicated by the uniform light contrast region located below the surface and indicated by the green vertical lines in the figure. Its thickness is of ∼140 nm.
- When the implant temperature is increased up to 150°C (Figure 4.10, center), no continuous amorphous layer is formed, however a highly damaged buried layer is observed within an otherwise crystalline material, which extends from a depth of ∼40 nm down to ∼150 nm. This clearly indicates that, thanks to the higher implant temperature, an enhanced point defect annihilation occurs during the implant (compared to the RT case), which prevents the formation of a continuous amorphous layer, while still leaving a considerable level of damage.
- Finally, the crystalline quality of the sample implanted at 500°C (Figure 4.10, right) is almost perfect, with no evidence of amorphous or highly damaged regions. If any defects clusters or amorphous pockets are still formed in this case, their size is therefore below the detection limit of the TEM analysis.

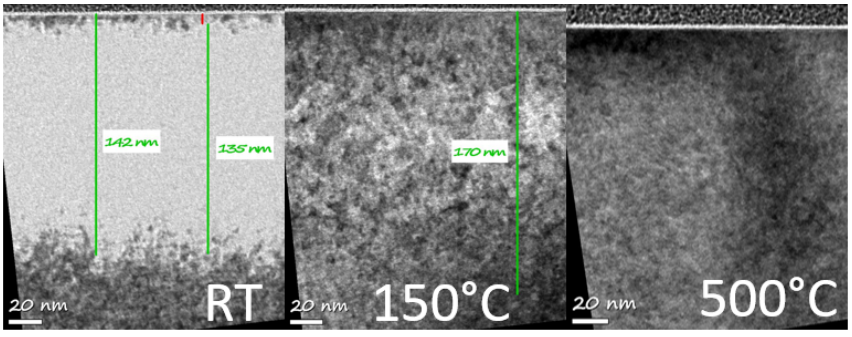

Figure 4.10: *Cross section TEM micrographs taken from samples implanted with As (cf. Table 4.4 for implant details) at different implant temperatures: room temperature (left), 150°C (center) and 500°C (right).*

The differences in the nature and spatial extension of the residual damage observed in the as-implanted samples is expected to have a strong impact on the extended defects formed during the annealing step. After annealing (carried out according to the recipe described in Table 4.4),

the three samples were observed again in both cross-section (Figure 4.11) and plan-view (Figure 4.12) configuration.

- In the cross section image of the sample implanted at room temperature (cf. Figure 4.11 left), a double layer of extended defects (loop-like contrast) is clearly observed. Such double layer is consistent with the formation of a buried amorphous layer after the implant containing two a/c interfaces [10]: the lower defect layer corresponds to the end-of-range defects formed below the deeper a/c interface, while the upper one is probably related to the defects formed when the two advancing a/c interfaces meet during regrowth (type IV defects in [10]). The end-of-range defects formed below the deeper a/c interface are due to the excess Si interstitial atoms remaining on the crystalline side of the interface [11] and are clearly identified thanks to plane-view TEM analysis (Figure 4.12 left). In this particular sample, they mainly consist of faulted DLs lying on {111} planes.
- The cross-section and plane-view TEM images relative to the sample implanted at 150°C are shown in Figures 4.11 (center) and Figure 4.12 (center), respectively. In this case, a single layer of DLs is observed after the anneal, extending from a depth of ∼70 nm down to ∼150 nm. Indeed, in the case of a subamorphizing implant, a single layer of defects is expected to form in the vicinity of the ion mean projected range, *i.e.* at a depth where the highest level of damage is produced (Type I defects [10]). This is confirmed by SIMS depth profile of the as-implanted sample (not shown), showing that the As concentration peak is located at a depth of 75 nm.
- Finally, Figure 4.11 (right) and Figure 4.12 (right) report the TEM images relative to the sample implanted at 500°C. Despite the apparent absence of residual damage after the implant (cf. Figure 4.10 (right)), extended defects are observed after the anneal. Their density is low compared to the samples implanted at RT or 150°C (only two defects visible in the cross section image of Figure 4.11 right), which makes it difficult to determine a reliable "average" location of the defect layer. However, considering that no amorphization occurred in this sample (*i.e.* similarly to the sample implanted at 150°C), the observed defects are to be associated to the peak of the implant induced damage, located near the ion mean projected range. Moreover, the much lower level of residual damage of the sample implanted at 500°C seems to have a strong impact on the crystallographic nature of the extended defects formed during the anneal. Indeed, in this case, the defects consist of extremely long (several hundreds of nm) {311} rod-like defects, while no circular DLs were observed (cf. Figure 4.12 (right)).

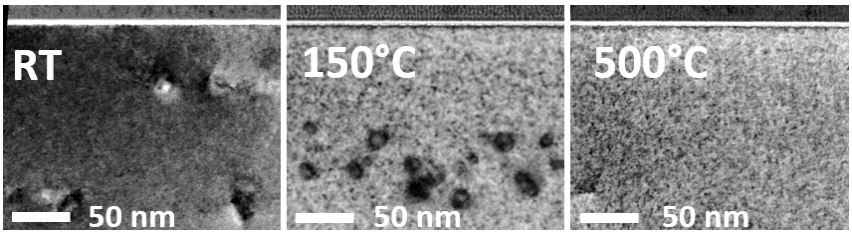

Figure 4.11: *Cross section TEM micrographs taken from samples implanted with As (cf. Table 4.4 for implant details) and annealed according to Table 4.5. The As implants were carried out at different temperatures: room temperature (left), 150°C (center) and 500°C (right).*

It is possible to count the interstitials in the extended defects in TEM images. Depending on the diffraction vector (g-vector) and of the kind of defect observed a of defects can be observed. From this analysis, it is possible to calculate a density of interstitials trapped into extended

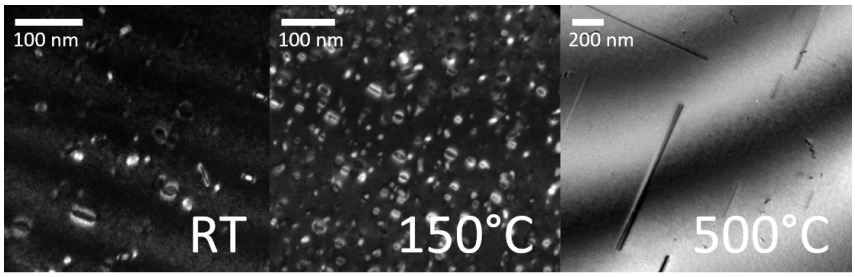

Figure 4.12: *Plan view TEM micrographs taken from samples implanted with As (cf. Table 4.4 for implant details) and annealed according to Table 4.5. The As implants were carried out at different temperatures: room temperature (left), 150°C (center) and 500°C (right).*

defects observed in the TEM planar view in the three cases. Theses interstitial densities are summarized in Table 4.6.

Table 4.6: *Interstitial density of interstitials in extended defects from the TEM count.*

	FDLs	PDLs	{311}	Total
RT	1.06×10^{14}	4.39×10^{13}	-	1.49×10^{14}
150°C	1.69×10^{14}	-	-	1.69×10^{14}
500°C	-	-	5.61×10^{12}	5.61×10^{12}

4.3.1.3 Photoluminescence imaging

The three samples implanted at different temperatures were also analyzed by photoluminescence imaging as described in previous section. Typical PL maps from the three As-implanted wafers are shown in Figure 4.13. Defects appear as clear spots (with different levels of grey contrast) on a dark background. The analysis of these maps suggests that the apparent density of emitting defects is highest in the sample implanted at room temperature and decreases when increasing the implant temperature, which is in qualitative agreement with the reduction of residual damage in samples implanted at high temperature. Moreover, the intensity of the emitted signal is clearly highest in the sample implanted at 500°C (Figure 4.13, right), whereas the defects contained in the samples implanted at RT and 150°C exhibit a very similar signal intensity. Again, this result is in qualitative agreement with the TEM observations, which showed that both samples implanted at RT or 150°C exhibited circular DLs, while {311} rod-like defects only were observed in the sample implanted at 500°C.

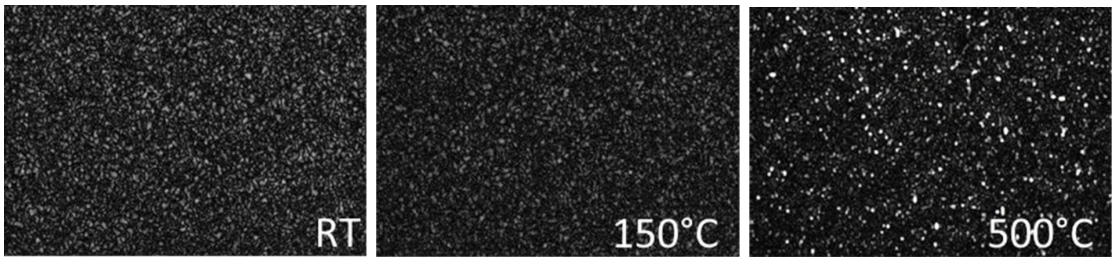

Figure 4.13: *PL imaging maps (120x175 µm area) taken from samples implanted with As (cf. Table 4.4 for implant details) and annealed according to Table 4.5. The As implants were carried out at different temperatures: room temperature (left), 150°C (center) and 500°C (right).*

4.3.1.4 Photoluminescence spectroscopy

Photoluminescence spectroscopy measurements were carried out using the same setup described in previous section. Figure 4.14 shows the PL spectra recorded at 8 K for the samples implanted at three different temperatures. It can be clearly seen that the samples implanted at RT (black curve in Figure 4.14) and 150°C (red) exhibit a similar behavior. Indeed, they both exhibit a broad peak in the 1300 nm wavelength region (labelled A1 and A3 for the samples implanted at RT and 150°C, respectively), followed by a "shoulder" extending up to ∼1400 nm (labelled A2 and A4 for the samples implanted at RT and 150°C, respectively). In contrast, none of these peaks are observed in the sample implanted at 500°C (blue curve in Figure 4.14), which instead exhibits two peaks in the 1150-1200 nm region. Similarly to the Photoluminescence imaging results showed in previous section, the PL spectroscopy results are again consistent with the TEM observations, which showed that both samples implanted at RT or 150°C exhibited circular DLs, while {311}rod-like defects only were observed in the sample implanted at 500°C.

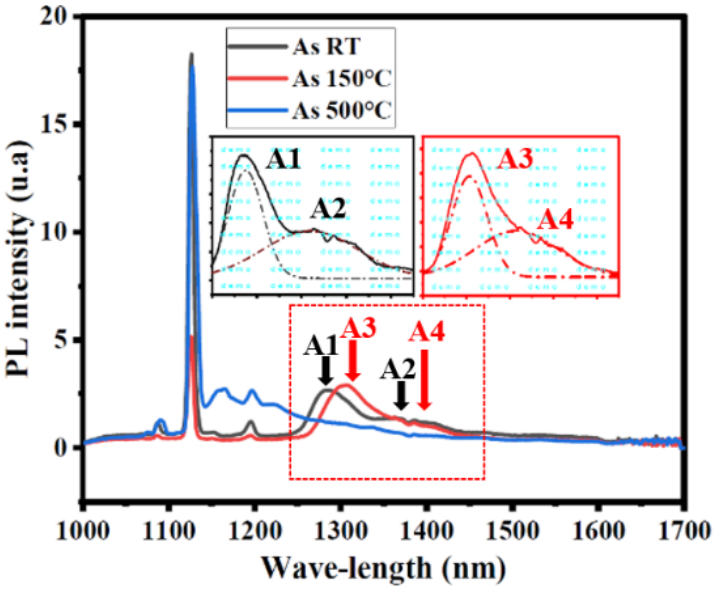

Figure 4.14: *PL spectra taken at a temperature of 8K from samples implanted with As (cf. Table 4.4 for implant details) and annealed according to Table 4.5. The As implants were carried out at different temperatures: room temperature, 150°C and 500°C.*

We first discuss the PL spectra recorded from samples implanted at RT and 150°C. Deconvolution analysis was applied in order to determine the main optical emission peaks, which are shown in the insets of Figure 4.14. In both cases, the deconvolution of the 8K PL spectra indicates two broad peaks in the same range of wavelength range which are summarized in Table 4.7.

Table 4.7: *Peak wavelength positions determined by deconvolution from the samples implanted at RT and 150°C.*

	RT implant		**150 °C implant**	
Peak label	A1	A2	A3	A4
Wavelength (nm)	1287	1358	1303	1357
FWHM (nm)	40	115	41	95

The PL spectra acquired at different temperatures from the three implanted samples are reported in Figure 4.15 (RT and 150°C implants on the left plot, 500°C on the right plot). In all cases, the intensity of the emission peaks is found to decrease when increasing the acquisition temperature,

which is expected due to thermal broadening. More importantly, the intensity of the PL spectra of the samples implanted at RT and 150°C (Figure 4.15 left) decreases in a very similar way, suggesting that the four peaks identified in these samples (A1-A4) have the same origin, *i.e.* they originate from the same defect type.

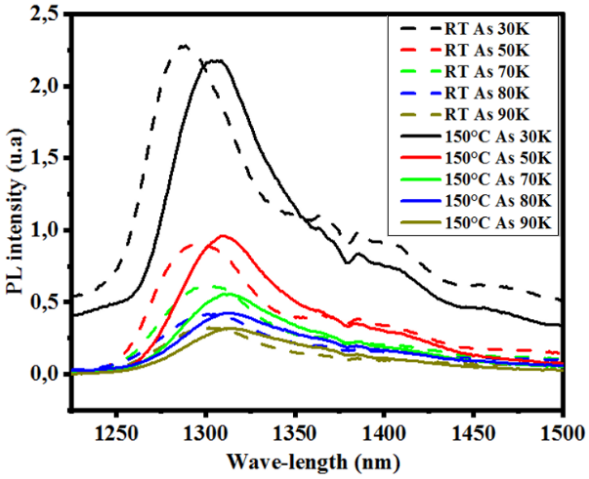

Figure 4.15: *PL spectra acquired at different temperatures from samples implanted with As (cf. Table 4.4 for implant details) and annealed according to Table 4.5. The As implants were carried out at different temperatures: room temperature (left), 150°C (left) and 500°C (right).*

TEM analysis from the samples implanted at RT and 150°C showed that both samples exhibited circular DLs (cf. Figure 4.12), however none of the observed PL peaks in these samples (A1-A4) correspond to the emission lines typically associated to dislocations in the literature [3]. These are known as D-lines and are generally observed by pairs called D1/D2 and D3/D4 in [3]. In our case, although peaks A1 and A3 are close in wavelength to the D3 line, no peaks are observed near the "coupled" D4 wavelength. In addition, the observed peaks are much broader than the typical D-lines peaks. In fact, D-lines were first observed in samples containing dislocations generated by plastic deformation ([3] and references therein), which is a different process compared to ion implantation and annealing. Moreover, the presence of contaminants and/or precipitates located in the vicinity of the dislocations has been shown to play an important role in enhancing or reducing their intensity [3][12]. In the case of dislocations induced by ion implantation and annealing, D-lines were observed in the extreme case of a high dose As implant at 1×10^{16} cm^{-2} [13] (i.e. ∼50 times higher than the dose investigated in this work) and annealing at temperatures not lower than 900°C (*i.e.* 100°C higher than the temperature investigated here). In such conditions, both the high density and size of the formed dislocations might explain the appearance of the D-lines in the PL spectra. In contrast, for lower implant doses, many examples exist in which no D-lines were observed by PL in the presence of DLs [7][14], in agreement with our results. Several other works have investigated the photoluminescence spectra in silicon samples containing implant-induced defects, especially in the case of Si^+ ion implants [6][15][16]. In this case, the formation and evolution of the defects, from small clusters to {311} rod-like defects up to DLs is well known [11], and a better correlation with the PL peak evolution is therefore possible. An example is given in Figure 4.16, taken from ref. [15], which shows the PL spectra obtained from silicon implanted with Si + ions (300 keV, 3×10^{14} cm^{-2}) and annealed for 30 minutes at different temperatures. At 300°C, the PL spectrum shows sharp X and W peaks at 1193 nm and at 1219 nm (with W phonon replica at 1244 nm), which are associated to small "compact" interstitial clusters (*i.e.* I_2, I_4,) [6]. At 600°C, the broad S1 and S2 peaks are observed at 1325 nm and 1398 nm. They are likely to be associated with <110>-oriented chains of I-clusters clusters corresponding to the precursors of the {311} rod-like defects. The latter are

finally associated to the R-line peak observed at 1372 nm after a 700°C anneal. The observed A1 and A2 peaks are close to the S1 and S2 peaks in the literature. However, simulations (not shown) indicate that the amount of interstitial clusters is too small to be observed in PL. Further characterization is needed to identify these A1 and A2 peaks.

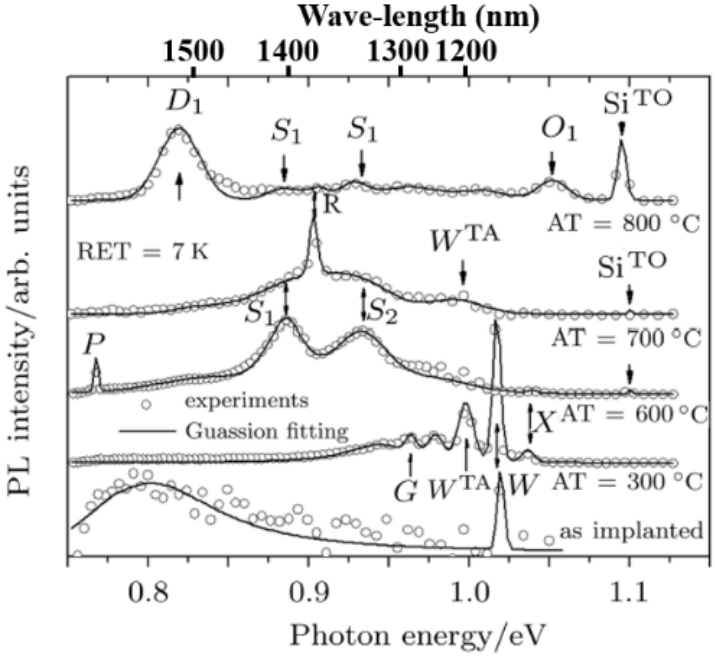

Figure 4.16: *Photoluminescence spectrum of interstitial cluster evolution during different annealings after Si+ implantation in silicon wafers.*

4.3.1.5 Complementary TEM and photoluminescence analysis

To help to identify and discriminate the observed peaks, an additional annealing was performed on the samples of the three wafers: they were annealed for 30 minutes at 700°C, 800°C, 900°C and 1000°C (resulting in 15 samples, including the reference sample without additional annealing). The purpose of these annealings is to follow the evolution of the photoluminescence spectra as a function of the temperature of the additional annealings applied, in particular the peaks that appear/disappear. The photoluminescence spectra of wafers implanted at 150°C and 500°C are shown in Figure 4.17.

For the sample implanted at 150°C, additional annealing at 700°C and 800°C does not drastically change the photoluminescence peaks and the A1 and A2 peaks observed in Figure are still visible. However, after additional annealing at 900°C, the peaks in the photoluminescence spectrum are different. The annealing at 900°C is therefore associated with an evolution of the defects responsible for the A1 and A2 peaks.
Assuming that the A1 and A2 peaks are caused by the DLs observed in the TEM images, the defect change observed in the photoluminescence at 900°C should also be visible in the TEM images. Therefore, TEM analysis was performed on the wafer implanted at 150°C that were annealed at 800°C and 900°C. The in plane-view TEM images of the samples without additional annealing, with annealing at 800°C and with annealing at 900°C are shown in Figure 4.17. For the three samples, DLs are observed in the TEM images (see Figure 4.18). The density and size of the DLs are different depending on the additional annealing performed. For the 800°C annealing, the number of DLs visible in TEM is high and comparable to that found in the reference sample. For the sample annealed at 900°C, the number of DLs observed in the TEM image is much lower. The average size of the DLs appears to be larger in the case

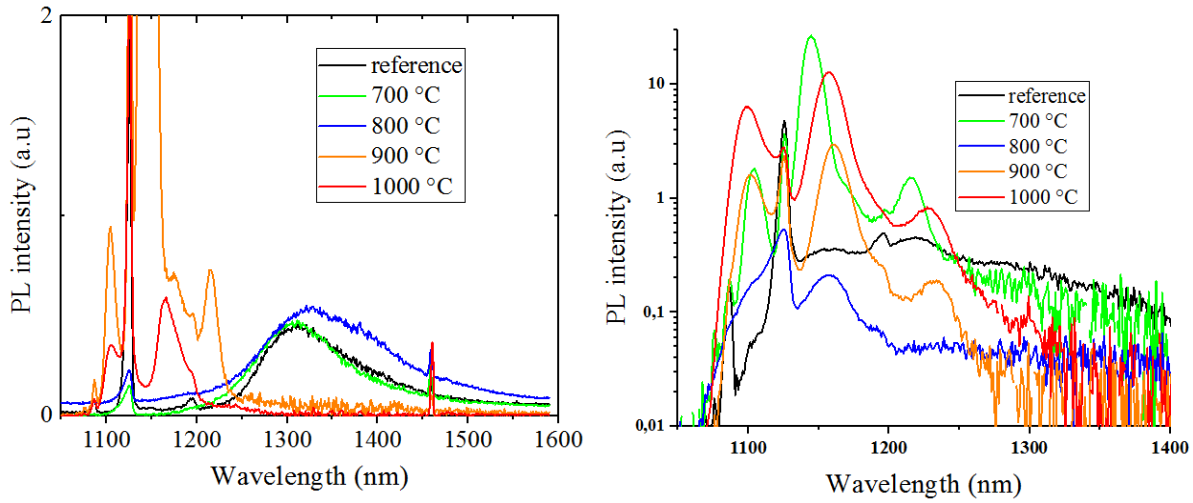

Figure 4.17: *Photoluminescence spectra after additional annealing for the wafer initially implanted at 150°C (Left) and 500°C (Right).*

of the additional annealing at 900°C than in the reference case and the annealing at 800°C. The annealing at 900°C causes a change in the DLs observed in TEM. The TEM images are therefore consistent with the hypothesis of a link between the A1 and A2 peaks observed in photoluminescence and the presence of DLs.

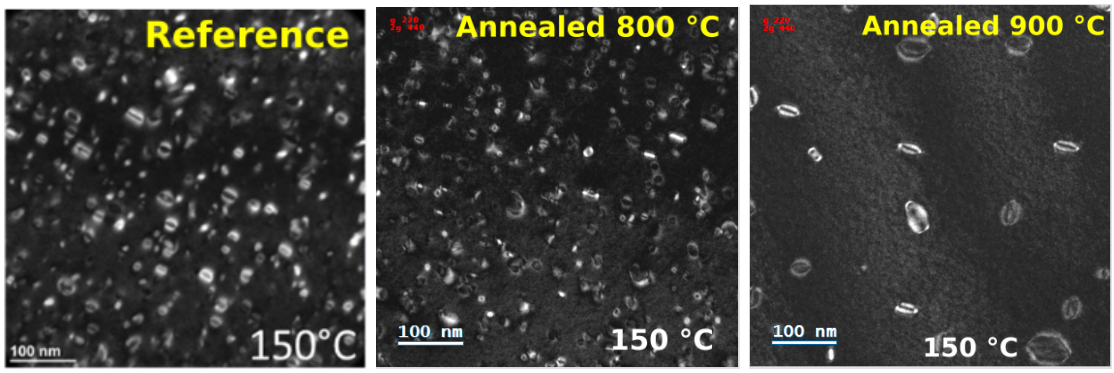

Figure 4.18: *TEM cross section images of as implanted wafers.*

4.3.2 Simulations of As heated implantations

4.3.2.1 Arsenic continuum simulations

The fastest solution to simulate the defects evolution after heated implantations and annealing process is to use the continuum model. The continuum model has been calibrated to take into the implantation temperature in [17]. However the implantations used for the calibration in [17] have lower energies that the ones investigated in this work. In order to provide correct predictions for the defects after the implantation and the annealing, the continuum model have to predict a correct description of the damage as-implanted. The damage predicted as-implanted in the RT and 150 °C cases are shown in Figure 4.19. The amorphous regions after continuum simulations are based on the damage profile. Above a fixed threshold of damage the silicon is considered as amorphous in the simulation. This threshold is generally set to 1.5×10^{22} cm^{-3} [18]. It can be seen that in using this threshold value of amorphous threshold results in an amorphous layer formation both in the RT and in the 150 °C cases. This prediction is thus not

consistent with the TEM images of Figure 4.12 where no amorphous layers have been observed after the 150 °C implantation.

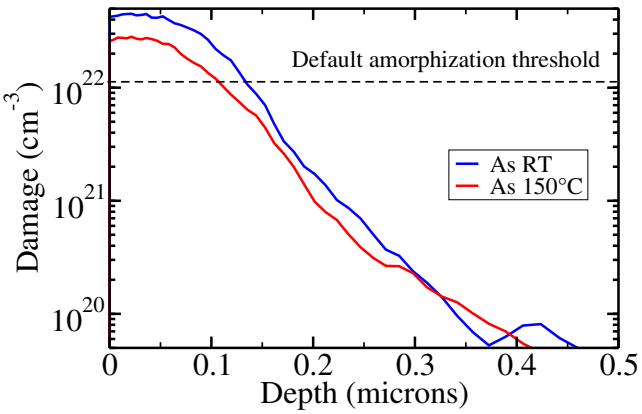

Figure 4.19: *Damage predicted in continuum simulations after As implantations at RT and 150°C.*

The prediction of the simulation for the defect evolution after the annealing all demonstrate the formation of DLs. This result is not qualitatively consistent with the TEM observations after annealing where {311}defects are observed in the 500 ° case.

Continuum simulations predictions can also be examined for the location of the defects (Figure 4.20). The maximum defect concentration is found in the RT case at the end of the a/c interface formed as-implanted. In the 150 °implantation the defect formed after the annealing have a maximum concentration at the predicted a/c interface as-implanted. This behavior is consistent with the prediction of the continuum implantation simulation but not with the TEM observations. A larger difference between the defects depth in the RT and 150 °C implantations is observed in TEM cross-section provided Figure 4.10. This difference is explained by the formation of defects near the R_p in the 150 °C case because the implantation is not amorphizing. The interstitial density trapped into the DLs is well simulated in the RT case and 150 °C case. The failures of the continuum prediction for these implantations is a reason to use a more precise simulation model, namely the KMC.

4.3.2.2 Arsenic KMC simulations

In the KMC, the implantation temperature is considered in the model as well as the dose rate. The dose rate is a critical parameter for estimating the as-implanted damage caused by implantation. As mentioned in Chapter 1, the formation of the amorphous layer formation strongly depends on the competition between I-V recombination between two collision cascade and thus on the competition between the dose rate and the implantation temperature. The dose rate has been estimated in the implantation to be 2×10^{13} cm^{-2}s^{-1} based on the extracted time in implant machine.

The KMC prediction for the as-implanted damage are shown in Figure 4.21. The damage shown is the concentration of point defects, I and V. As with the continuum simulation, a region is considered amorphous if the damage, here the points defects, overcomes a threshold concentration. The KMC simulation therefore predicts the formation of an amorphous layer after RT implantation. According to KMC, the damage prediction in the 150 °C and the 500 °C implantations does not result in the formation of an amorphous layer even though more damage

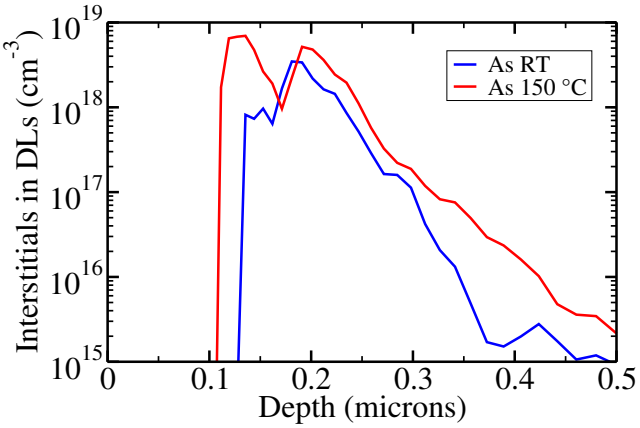

Figure 4.20: *Continuum prediction for interstitials concentration in DLs after the annealing sequence following the RT and 150 °C implantations.*

is predicted for the 150 °C implantation. The as-implanted KMC predictions are therefore in a fair agreement with the TEM as implanted cross section and more accurate than the continuum simulations which predict an amorphous layer after the 150 °C implantation.

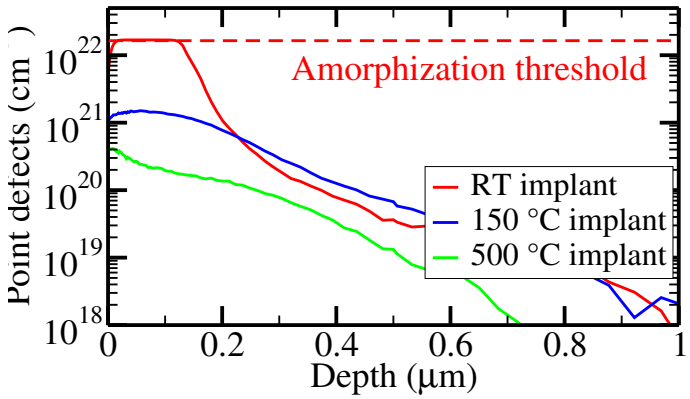

Figure 4.21: *KMC prediction for the concentration of points defects as-implanted in the RT, 150 °C and 500 °C cases.*

The KMC can also be used to simulate the defects after the annealing process.Since defects observed in TEM can measure several hundred nm, it is important to have a large simulation domain to be able to predict the formation of these extended defects. Note that the size of the surface used in the simulation is set to 150×150 nm^2.

The DLs are predicted by the KMC after the annealing in the three cases. The result is consistent with the TEM observation in the RT and 150 °C cases but not in the 500 °C case where {311} have been observed in TEM. The accuracy of the KMC can also be examined quantitatively by looking at the interstitial density trapped into the predicted defects (see Table 4.8). The interstitial density of the RT is close to the TEM count. For the 150 °C implantation, the interstitials trapped in the DLs are slightly larger in the KMC than in the TEM count. The KMC prediction for the annealing following the 500°C is once more not in fair agreement with the TEM observation. The interstitials in the DLs predicted in this case are overestimated by a factor 30 in the KMC simulation. This disagreement depends on the type of defects formed

and the overestimation of interstitial trapped in the defects in the 500°C case could be partially explained by the inaccuracy in the defect type prediction.

Table 4.8: *Comparison of interstitials density trapped in extended defects between TEM observations and KMC with by default parameters.*

	RT (DLs)	150 °C (DLs)	500°C ({311})
TEM	1.5×10^{14}	1.7×10^{14}	5.6×10^{12}
KMC	1.4×10^{14}	2.4×10^{14}	1.9×10^{14}

The depths at which defects are predicted in the KMC can also be analyzed. The location of the predicted defects in the KMC can be compared with TEM observations. However, there are few extended defects in the KMC simulation boxes, so the comparison is therefore based on weak statistics. The DLs observed in the simulation of the RT case are localized close to the a/c interface predicted as implanted (150 nm), which corresponds to end-of-range defects observed in TEM. The DLs predicted in the 150 °C case are more spread over the depth of the simulation box than in the RT case. This behavior is similar to the one found in the TEM images. The DLs also appear closer to the surface in the KMC prediction of the 150 °C case than in the RT case which is consistent with TEM. The DLs simulated in the 500 °C case are also spread over the depth.

On drawback of the KMC is that the results on this kind of surface predict a small and finite number of extended defects. It is difficult to extract an accurate distribution of extended defects along the depth from these results. Another limitation of the KMC is the computational time. The use of large surface enables to predict extended defects but increases the simulation time. The computational time reaches hours to simulate the DLs observed in Figure 4.22 versus a few minutes with the continuum model. Finally, the KMC even if it takes more physical effects into account is not accurate for the 500 °C case.

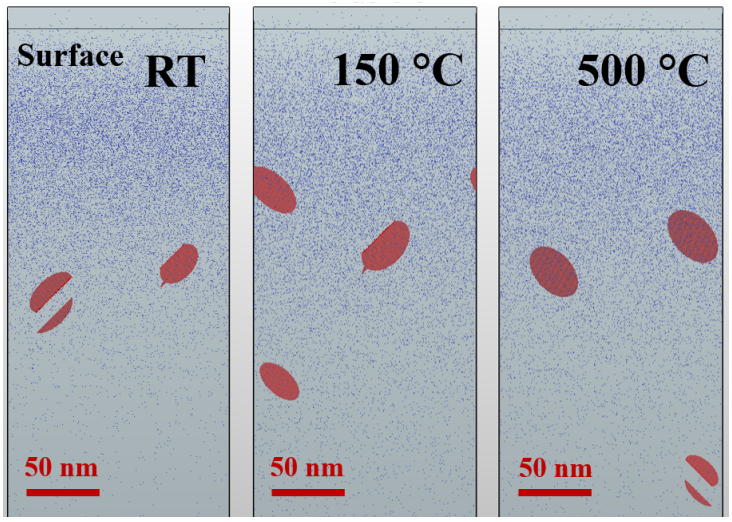

Figure 4.22: *Simulation of the 3 implantations followed by annealing (left RT, middle 150°C and right 500°C) using the default KMC model. The red loops correspond to the dislocation loops.*

4.3.2.3 An hybrid KMC-continuum approach

In order to solve the computational time issue previously mentioned without loosing the accuracy of the KMC for the implantation step, an hybrid method has been explored, which consists as follows: The KMC is used for the simulation of the implantation, atomistic data are then deatomize and convert into continuous field to perform the annealing step using continuum model. This approach enables also to obtain a distribution of the extended defects concentration along the depth at end of the simulation compared to a full-KMC simulation. The annealing computational time being more important than the one of the implantation part in KMC, this hybrid approach can be expected to drastically reduce the computational time.

The deatomization of at the end of the KMC implantation simulation have been performed using the integrated command of the process simulation solver [1]. Using the command called UnsetAtomistic, the transfer of interstitials present in the discrete defects of the KMC into continuous interstitial fields is done as follows:

- The various defects present in the KMC box and containing interstitials are parsed. These defects can be SMICs, APs (amorphous pockets), impurity-interstitial clusters.
- For each defect, the excess interstitials are extracted.
- In an AP I_nV_m, the number of excess interstitials is equal to the difference between the number of interstitials n and and the number of vacancy m if the $n > m$ (and is equal to 0 in the opposite case $m < n$). For other types of defects, the excess interstitials are equal to the number of interstitials in the defect.
- Once extracted, the excess interstitials are converted into a continuous field of interstitial concentration. The spatial distribution of this continuous field is realized using the internal mesh of the KMC. A number n_I of excess interstitials in a mesh element n_e increment the continuous field of a concentration $\frac{n_I}{V_e}$ (where V_e is the volume of the mesh element n_e) at the position of the mesh element.

The UnsetAtomistic procedure also converts the dopant atoms in the KMC box into doping profiles, so that electrical simulations can then be performed, but this part will not be detailed here. The UnsetAtomistic command takes the interstitial in excess and put them in interstitial cluster field called Icluster. In this work, we transfer the Icluster continuous field interstitials into the I_2 continuous field and activate the model developed in [19] to simulate the annealing. It have been shown in some previous work that initializing the interstitials in a continuous field of free interstitials does not change drastically the results [20]. The results exhibit a qualitatively correct trends when its compare to the TEM images defect type for the RT and 150 °C case. The profile of the concentration interstitials trapped into DLs along the depth is also consistent with TEM observation. A sharp peak of interstitials are trapped in the RT case close to the a/c interface predicted as implanted which correspond to the EOR defects. The interstitial in DLs in the 150 °C case is more spread than in the RT case and have non negligible values close to the surface. This prediction is in fair agreement with the +1 model for interstitial after non-amorphizing implantation explained in Chapter 1.
However the methodology is not quantitatively consistent with the TEM count. The interstitial concentration profiles can be integrated along the depth to calculate the interstitial density trapped into the DLs. When comparing the results with the TEM count of interstitial density it can be seen that the simulation overestimate this density by a factor 10 both for the RT and 150 °C cases.

I in loops (cm^{-2})	TEM	KMC	Hybrid-test
RT	1.4 10^{14}	1.2 10^{14}	2.1 10^{15}
150°C	1.6 10^{14}	2.3 10^{14}	3.2 10^{14}

Table 4.9: *Interstitial densities trapped in dislocation loops using the methodology described the methodology described in subsection 4.3.2.3.*

The hybrid approach used in section 4.3.2.3 has been shown to overestimate the interstitial density in DLs. The problem with this model is that the vacancies are not accounted in the annealing simulation. However, the vacancies are essential to reproduce the interstitial-vacancies recombination during the annealing and to avoid the overestimation of interstitial during the annealing. The method of transferring atomistic data of KMC simulations to continuum data to start the annealing simulations with continuum model needs to be improved. The excess vacancies in the amorphous pockets has to be stored into a continuum data field related to vacancies. The simulation of interstitials and vacancies recombination have also to be take into account in the continuum model used for the annealing.

4.4 Improvement and calibration of TCAD tools for As heated implantation

4.4.1 RT and 150 °C cases: an hybrid approach coupling KMC and continuous model

Therefore, the proposed solution is to better account for interstitial-vacancy recombination during annealing. A first step is to simulate the annealing ramps using the KMC. This step increases the computational time, but also the number of I-V recombinations. The prediction of I-V recombinations using KMC simulation is believed to be more accurateconsidered more accurate and leads to a better estimate of the excess interstitial and vacancies field to start the annealing the continuum simulation.

It is then essential to account for the interstitial-vacancy recombinations during the rest of the annealing. The excess vacancies in the KMC box must be transferred into a continuous field modeling the evolution of the vacancy concentration during the annealing. This step can be done by improving the UnsetAtomistic procedure presented in subsection 4.3.2.3. The excess vacancies can be parsed into the KMC box and increment continuous fields. For APs, the procedure is similar to that of excess interstitials, if $m > n$ in an AP I_nV_m, then there are $m-n$ excess vacancies transferred into a continuous field. Several models exist and can be used then to predict vacancies clusters evolution and the I-V recombinations using a continuum model (a model base on a first moment approach [1] and a model based on vacancies clusters investigated in [21]. The model used is the simplest, as it uses the one moment approach to determine the vacancy evolution.

The evolution of the interstitials during the simulations and the profile of interstitial concentration are shown in the Figure 4.24. Qualitatively, the simulations match well. The {311}progressively dissolve to form DLs. The depth of the DLs is also consistent with TEM images. Quantitatively, the results demonstrate an improvement compared to the first hybrid approach. The interstitial density trapped in DLs are closer to the experimental count in RT case, but still overestimated by a factor 2 in the 150 °C case. This is better than the factor 10 overestimation of the first approach. The computation time was divided by 8 compared to a KMC simulation. The accuracy of the two methods is comparable but the hybrid approach is faster and provides an more accurate distribution of the concentration of interstitials trapped

I in loops (cm^{-2})	TEM	KMC	Hybrid-test
RT	$1.4\ 10^{14}$	$1.2\ 10^{14}$	$9.4\ 10^{13}$
150°C	$1.6\ 10^{14}$	$2.3\ 10^{14}$	$3.9\ 10^{14}$

Table 4.10: *Interstitial densities trapped in dislocation loops using the methodology described the improved methodology described in subsection 4.4.1.*

in extended defects.

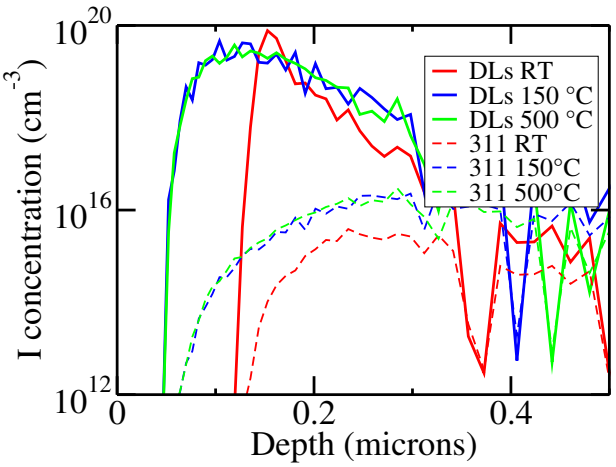

Figure 4.23: *Interstitial concentration in DLs and in {311}in KMC-continuum.*

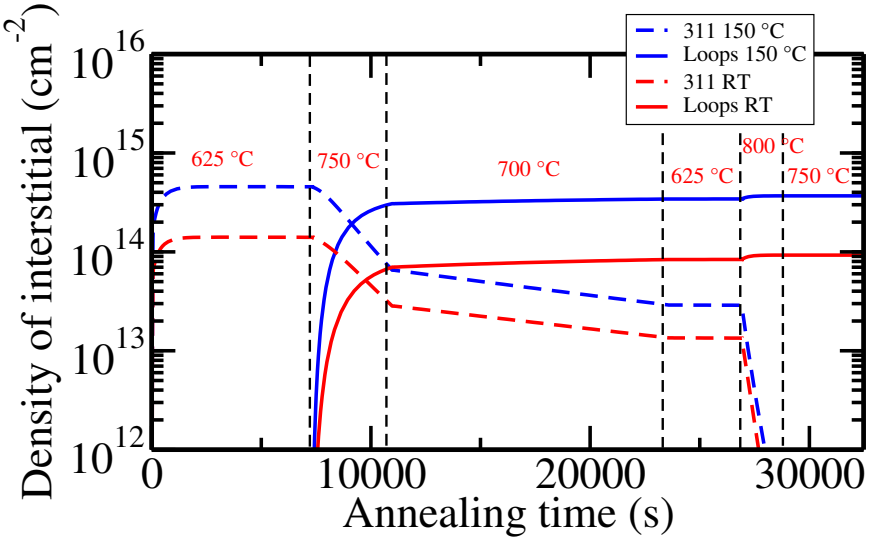

Figure 4.24: *Number of I trapped in DLs and {311} defects using the hybrid approach combining KMC and continuum model after implantation at RT (red) and at 150 °C (blue).*

4.4.2 500 °C implantation case: calibration from Molecular Dynamics data

In the case of 500 °C, the KMC simulations do not predict the {311} defects observed in the TEM images.

A calibration of the KMC must therefore be performed. The first step is to determine which parameter should be calibrated.

In the experiments, the same annealing sequence was applied after all three implantations. This means that the observed difference comes from the condition of the sample at the end of the implantation, as-implanted state of the material, between the RT, 150 °C and 500 °C implantations. As a reminder about the as-impanted material: RT and 500 °C exhibits a clear difference as-implanted because an amorphous layer is formed in RT case. The 150 °C and 500 °C both do not show an amorphous layer but the formed defects can be compared.

A first quantity to compare is the number of excess interstitials than can be expected after I-V recombinations. The difference between interstitials and vacancies as-implanted is shown in Figure 4.25. Although the profiles are noisy, no drastic difference is visible between RT and 150 °C implantations. It is also possible to integrate the profiles to obtain an estimate of the density of excess interstitials. The integrated profile also shows a difference, in contrast to the observations after the annealing sequence for the interstitial density trapped in the extended defects. The difference between the 150 °C and 500 °C implantations is thus not in the amount of excess interstitials as-implanted but in the type of defects formed.

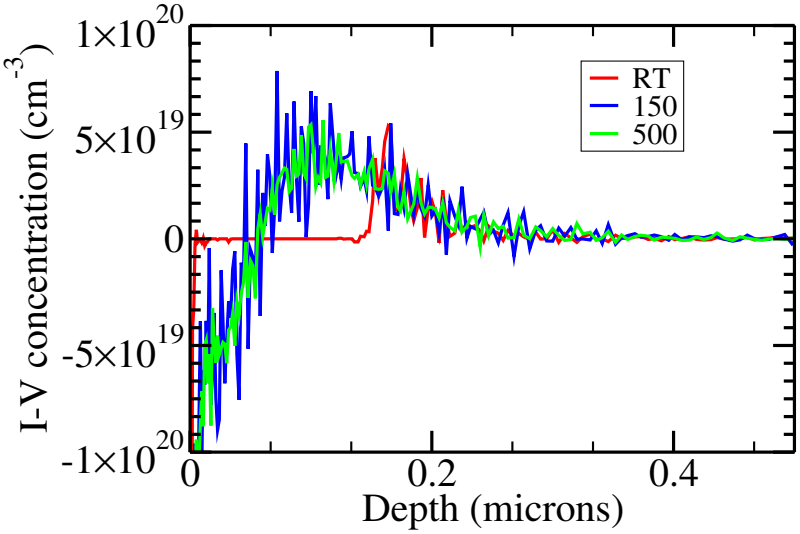

Figure 4.25: *Difference between interstitials and vacancies as-implanted in RT, 150 °C and 500 °C.*

4.4.2.1 Default KMC values

After implantation at 150 °C, most interstitials are found in interstitial-only defects (SMICs or larger defects with more than 20 interstitials), although there are still large APs in the 150 °C case. After implantation at 500 °C, interstitials are also found in interstitial-only clusters, but smaller in size, and there are no APs. In order to monitor and identify the type of defects formed during the implantation, the implantation of a single As ion was been simulated with KMC at

150 °C and 500 °C. The same dose rate was used than in the case of the full-implantation. This method enables to compare the KMC predictions for clusters types formed between two collisions cascades at 150°C and 500°C. The histogram of the clusters I-V for the three implantations is shown in Figure 4.26. In the 150 °C, most of the interstitials are in SMICs. In the RT case, interstitials are found in APs containing both interstitials and vacancies. It can be seen that large APs are formed and do not dissolve between two cascades at 150 °C. On the contrary, at 500 °C, all interstitials are in SMICs with a size < 10. In RT and 150°C, the large APs can interact with defects produced by the further cascades to form larger clusters types. In the 500 °C, the interstitials are less likely to form large interstitial clusters and will tend to evolve in the most stable form of SMICs.

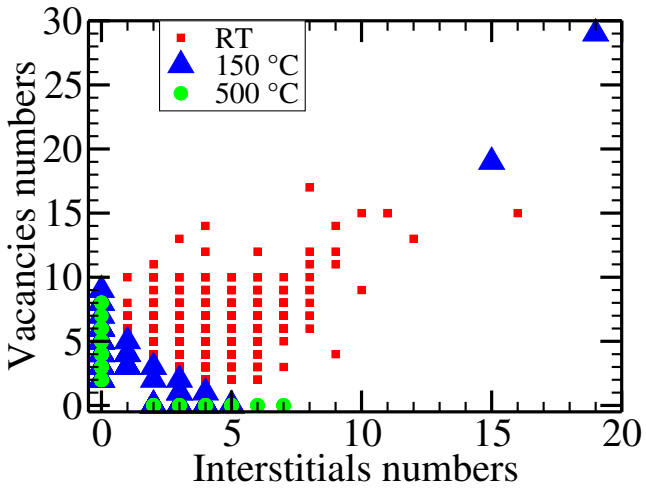

Figure 4.26: *Histogram of I and V clusters for implantation at RT and heated implantation at 150 °C and 500 °C.*

In the literature, the interstitials cluster structures have been investigated using atomistic simulations such as MD or DFT [22][23][24]. In both MD [22] and DFT [23], two different types of clusters exist for a SMIC of a given size.

- A first type of structure has configuration very similar to those found for the I_4 in [24]. These structures are compact. For I_4 and I_8, all the Si atoms of the structures have their four bonds. MD and DFT simulations show that, in the case of compact clusters, the evolution of the formation energy of I_n as a function of the number of interstitials n in the cluster exhibits strong minima for clusters of type I_{4n}.

- The other type of structures is composed of chains of interstitial along the (110) directions. For chain-like clusters, the evolution of the formation energy per interstitials decreases monotonically with the number of interstitials in the cluster. At small size, the compact type seems to have lower energies, whereas for larger size chain-like have lower formation energies.

In the case of 500°C implantation, the clusters formed by a single As atom are smaller than I_8 and are much likely to evolve into the compact form during the implantation. It is thus tempting to calibrate the KMC with energies of the compact like structures.

The activation energy for an emission of an interstitial from a SMIC I_n can be calculated as followed:

$$E_{emission}(I_n) = E_f(I_{n-1}) - E_f(I_n) + E_f(I) + E_m(I) \tag{4.4}$$

The $E_f(I_n)$ is the formation energy of a SMIC of size n and $E_m(I)$ the interstitial migration energy.

- Using the values of the formation energies of compact SMICs given in [22], it is therefore possible to estimate the emission energies.
- Different values of interstitial migration energy and of interstitial formation energy can be found in the literature [22][25].

In our work, the sum of $E_m(I)$ and $E_f(I)$ was assumed to be 4.52 eV [25] to allow a comparison between the emission energies implemented in KMC and extracted from formula eq. 4.4.

The comparison between the emission energies obtained with formula eq. 4.4 for compact-like SMICs and the one implemented by default in the KMC is shown on Figure 4.27. In both cases, the I_{4n} clusters have larger emission energies, but this difference is much larger if the values of [22] are used (green in Figure 4.27). The emission energies implemented by default in the KMC are based on the experience of [25] that was calibrated with the implantation at RT with retroengineering (the method is detailed in Chapter 2). The energies currently implemented in the KMC (blue in Figure 4.27) have been shown to be effective in simulating defects after RT implantation processes and annealing sequences [26]. However, in [25], it is also mentioned that several sets of emission energies can be used to reproduce experimental trends. The only mandatory criterion to reproduce the supersaturation in [25], is to have two minima in the evolution of SMICs emission energies depending on their size. Moreover the calibration of SMICs for heated implantation has not yet been shown to be robust.

4.4.2.2 Our calibration set

The exact values of emission energies are not easy to implement because the I_2 and I_3 are considered as non-migrating species in the KMC, such assumption is different from what is observed in MD. The emission energies also depend of the values chosen for $E_f(I)$ and $E_m(I)$ which change between KMC calibration, DFT and MD. It is possible to observe the trends of very high emission energies for I_{4n} found when using MD values for the calibration of the KMC in the 500 °C case. Increasing the difference between I_{4n} emission energies and other clusters size seems to slow down the growth of extended defects in the KMC prediction. The total number of interstitials in the simulation domain also decreases, which is consistent with TEM conclusions. Using the activation energies, shown in red in Figure 4.27, it is possible to predict the {311}defects after the annealing sequence for the 500 °C case (Fig. 4.27 (Right)). The energy differences are close to the one calculated with MD for compact type SMICs [22].
It is then possible to estimate a density of interstitial trapped in the extended defect using the size of the {311}defect formed by dividing the number of interstitial atoms in the {311}defect by the simulation area. This gives a density of trapped interstitials of 5.1×10^{12} cm^{-2}. The result agrees well with the density found in TEM images count which is equal to 5.6×10^{12} cm^{-2} (Table 4.6. This result is very statistical because it is based one a single predicted defect in the simulation.

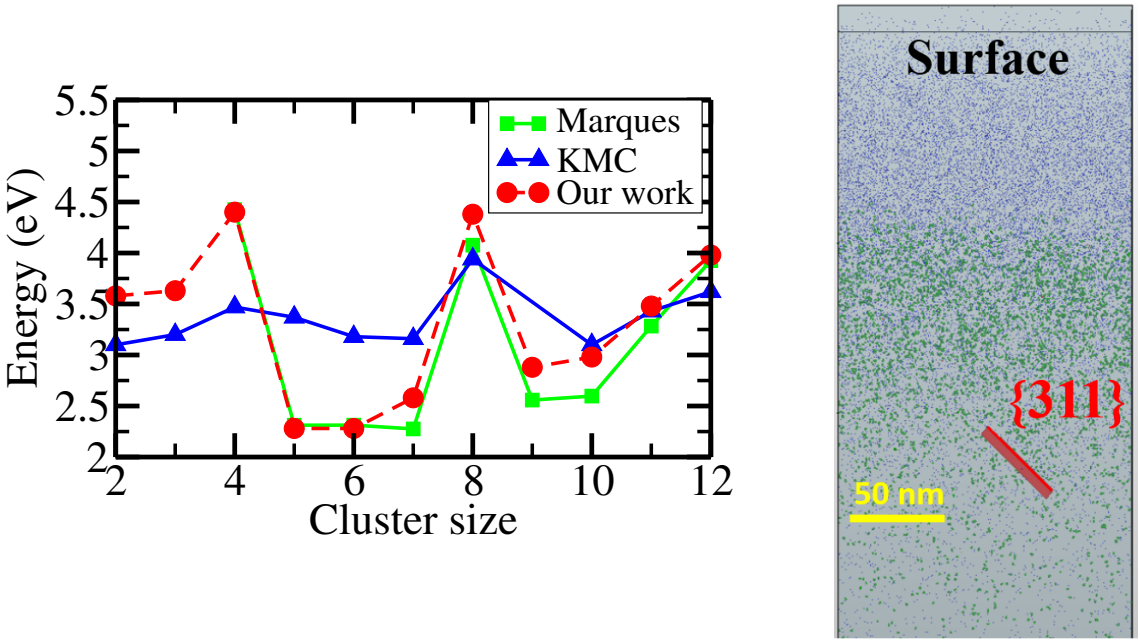

Figure 4.27: *(Left) Activation energies for interstitial emission depending on the SMICs size (Right) Predicted {311} in KMC using the calibration presented on the left.*

The ideal situation would be to use a single set of energies for all the implantation temperatures. It is not the case of the energies calibrated in Figure 4.27. If the compact-type calibrated energies are used for KMC simulations of the RT and 150 °C implantations, no DLs are predicted for the RT case, the simulation still predicts DLs in the 150 °C case.

Table 4.11: *Comparison of interstitials density trapped in extended defects between TEM observations and KMC predictions after calibration.*

	RT (DLs)	150 °C (DLs)	500°C ({311})
TEM	1.5×10^{14}	1.7×10^{14}	5.6×10^{12}
KMC	8.0×10^{13}	1.5×10^{14}	6.0×10^{12}

4.4.2.3 Second calibration set

An additional KMC calibration with a different set of energies was performed to better predict DLs in RT and 150 °C cases and {311}defects in 500 °C case. In order to match the experimental results, the amorphization threshold was set to 1.5×10^{22} cm^{-3} and the minimum size to form DLs to 8500 interstitials. The values of the SMICs emission energies that reproduce {311}defects in 500 °C case and DLs for others implantation temperatures are shown in Figure 4.28. It can be seen that the differences between I_{4n} and other SMICs sizes are even more important in this calibration. Table 4.11 shows the results for the interstitial density trapped in extended defects for the three cases. It can be seen that the KMC predictions are of the same order of magnitude than the TEM count. On the other hand, the DLs size is not consistent with the TEM measurements. The mismatch can be explained by the value of the minima size to form DLs. On the contrary, the {311}defect size predicted in KMC in the 500 °C implantation is smaller than that measured in TEM. An increase of the {311} size in the simulation would lead to an overestimation of the interstitial density trapped in the defect. Enlarging the simulation box would be a more accurate approach, but computational constraints hinder this solution.

The calibration performed can also be compared to the photoluminescence results. If the A1

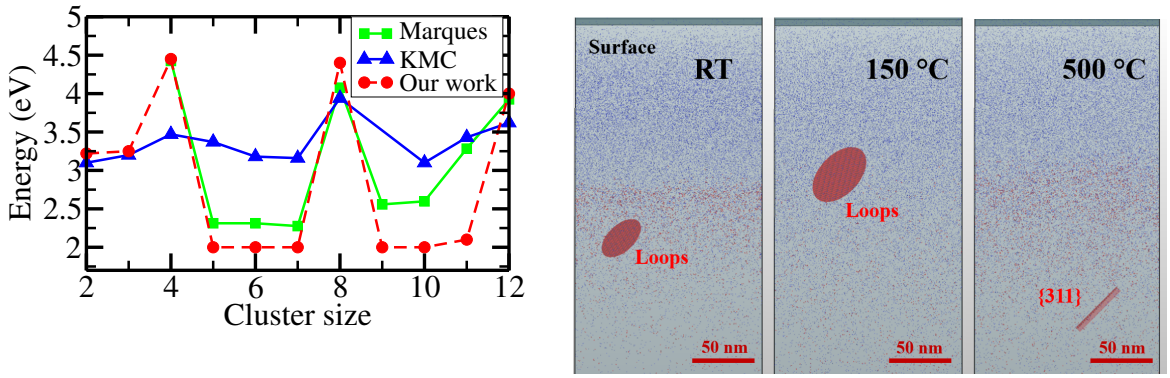

Figure 4.28: *(Left) Activation energies for interstitial emission depending on the SMICs size (Right) Resulting defects formed after the annealing in the 3 cases (implantations at RT, 150°C and 500°C).*

and A2 peaks mentioned in the subsection 4.3.1.4 are caused by DLs, the comparison between simulations and photoluminescence is similar to that between simulations and TEM: the KMC reproduces dislocation loops well. For the sample implanted at 500°C, the peaks observed in photoluminescence do not correspond to the R peak co-released with 311 defect formation in [15]. The observed peaks have lengths closer to the X and W peaks of [6]. These peaks are generally associated with SMICs, between I_2 and I_4. The continuous simulations performed in section 3 do not predict SMICs of this size after the annealing sequence, but these simulations were performed with parameters calibrated for RT implantations. If more stable SMICs are formed during implantation at 500°C, these can potentially be retained longer during annealing. The calibrated KMC simulations also show the existence of I_4 after annealing in the simulation box. It would then be tempting to explain the peaks observed on the sample at 500°C by I_4 and I_8 SMICs.

4.4.2.4 Limitation of the calibration approach

There are several limitations to this calibration. The first is that it is highly dependent on the surface area used. The same calibrated values do not produce extended defects in a surface simulation domain of 100×100 nm^2. A better approach would be to examine at the convergence of the calibration and observe whether an increase of the surface leads to the same structures. At some point the density and type of defects should not change. The growth of SMICs of compact type prevents the formation of extended defects in the annealing following the 500 °C implantation. This is explained by the low emission energies of the compact SMICs, except for the size I_{4n}. To evolve into large and extended defects, some clusters of big size must act as nucleation site. The simulation depends strongly on the initial clusters formed and is very sensitive. Small changes in the parameters or seed changes can impact the final defect type formed, which is not ideal for repeatability of the simulations.

Another issue is the reliability of the calibration compared to other experiments. The newly calibrated energies were tested against the experiments used for the KMC which was calibrated in the KMC by default [25]. The simulation consists of Si implantation followed by different types of annealing with different temperatures and durations. The supersaturation was extracted experimentally for these different annealing conditions and can be compared to that predicted by the KMC. The default implemented energies reproduce the trends of supersaturation for

all temperatures. The simulations using the energies are not accurate for temperatures higher than 700 °C where for such simulations above 700 °C the supersaturation decreases too rapidly compared to experimental data. Therefore, the values of activation energies in Figure 4.28 should not then be used in a general case. The supersaturation is related to the dopant diffusion and overestimation of supersaturation leads to an error in dopants doping profile.

The values for SMICs emission energies of Arai-type [24] are thus not suitable for RT implantations. One hypothesis would be that both types of clusters exist at room temperature, namely compact and chain clusters. This hypothesis could explain that minima are needed to simulate supersaturation, as compact clusters slow down the growth, but that interstitial clusters can still growth following an Ostwald ripening mechanism because of the presence of chain-like clusters. In 500 °C implantation, the chain-like clusters could be in lower concentration because the interstitial clusters does not originate from the annealing of large APs but from the SMICs formed during the implantation.

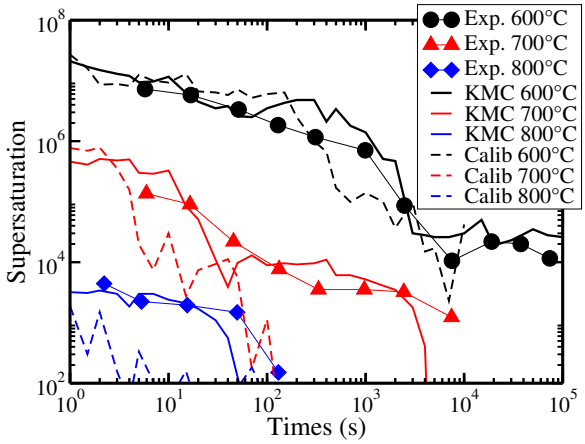

Figure 4.29: *Comparison of supersaturation extracted from [25] experiments (exp in the legend) and predicted by the KMC using the default implementation (KMC in the legend) and the calibrated energies on the As implementations (calib in the legend).*

4.4.3 Calibration using ab initio calculations of small interstitial clusters

In this section, we study the possibility of refining the atomistic events implemented in the KMC, through an ab initio study. We demonstrate the contribution of this methodology for a truer calibration, but also, as in the previous chapter, the complexity of entering into a fine description of the atomic structure, far from the industrial KMC techniques and prerequisites.

4.4.3.1 SMICs configurations

An ab initio study was also conducted to acquire our own database for the formation energies of SMICs according to their sizes. In this work, the structures of the two families of clusters, compact and chain-like, were relaxed in molecular dynamics, using the structure of [23] as a reference. The configurations were then optimized in DFT in a cell of 1000 atoms. For chain-like clusters, the extremity of the chains varies according to the size and of the method used. Using MD simulations, there are two types of patterns for the ends of the chain, respectively P1 and P2 in the Figure 4.30. For chains with an even number of interstitials, the two types of patterns, P1 and P2, are distributed at both ends of the chain. For SMICs with an odd number of interstitials, the situation is different: one of the patterns is repeated twice, at the beginning

and at the end of the chain. It is therefore necessary to find which of the two is the most stable. In molecular dynamics, the P1 pattern has a lower energy than the P2 pattern.

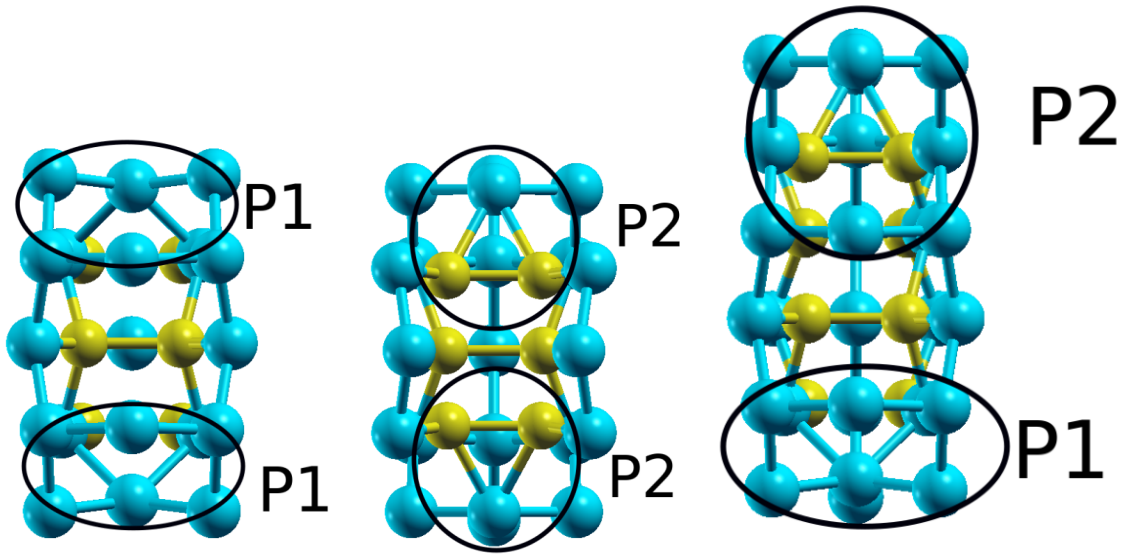

Figure 4.30: *The different possibilities to form I_3 chain-like clusters after MD relaxations. (Left) I_3 with a P1 extremity (Middle) I_3 with a P2 extremity (Right) I_4 with a P1 and P2 extremity.*

In DFT, the results are different. For small sizes of chain-like clusters with an odd number, an asymmetry appears after the DFT relaxation. The asymmetry disappears as the number of interstitials increases in the chain-like SMICs. The most likely hypothesis is that this asymmetry is caused by the interaction between the chain ends in our simulation cell.

4.4.3.2 Formation energies of SMICs

The formation energies calculated in DFT in our work are compared here to the formation energies calculated in [22] and [23]. For SMICs of compact type, all simulations predict local minima for clusters I_{4n}. We can also note that for a small number of interstitials, the DFT predicts the compact like SMICs have the lowest formation energies. This observation is consistent with the formation of compact-like SMICs during implantation at 500°C. Since the structures of the compact clusters were extracted from [23], it was expected to find similar formation energies. The formation energies calculated in our work are slightly smaller than those of [23] (∼0.1 eV), but this discrepancy can be explained by the different DFT parameters used. It is also important to note that the structures of compact I_3 are not the same in the [23] and [22] works.

Using the formation energy values calculated in DFT, it is also possible to estimate the emission energy of an interstitial of a SMICs using the formula eq. 4.4. The differences in emission energies of the I_{4n} SMICs and the others are less pronounced than in the case where MD energies were used. The differences in activation energies between I_4 and I_5 (3.3 eV and 2.2 eV) and between I_8 and I_9 (3.5 eV and 2.4 eV) are still larger than in the KMC implementation, and may thus slow down the growth of interstitial clusters.

4.4.3.3 Emission of interstitial atom from SMICs

The estimate used for the activation energies of an interstitial emission from a SMICs in formula eq. 4.4 can be discussed. There may be an or multiple additional barriers, as in the case of O_{2i} dissociation discussed in Chapter 3, and might be not simply associated to a single value.

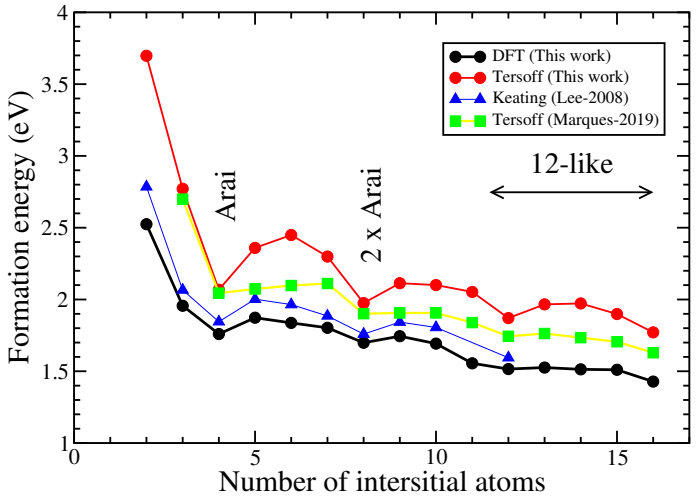

Figure 4.31: *Comparison of the interstitial formation energies of SMICs from [22] and [23] works and the energies calculated in this thesis using the coupled MD - DFT strategy.*

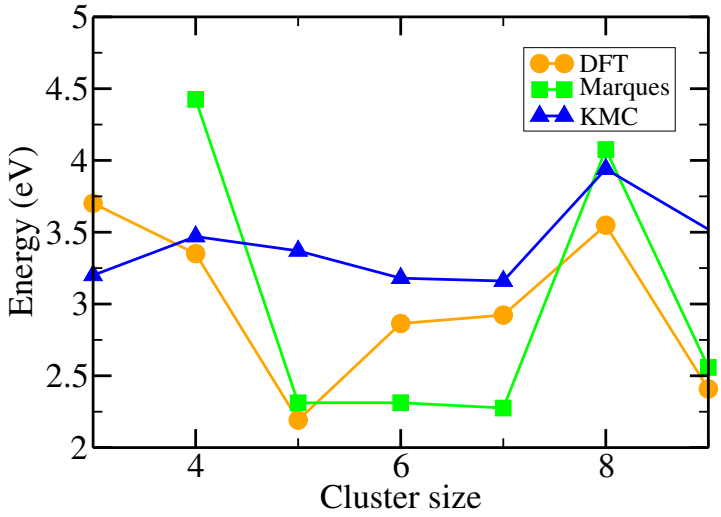

Figure 4.32: *Comparison of the activation energies for the emission of an interstitial from a SMICs between the values implemented in the KMC, the values extracted using the formula 4.4 with the formation energies of [22] and those calculated in DFT.*

For instance,

- in the I_4 configuration, the interstitial atoms are all bonded four times. The four bonds of the Si atoms are very favorable energetically and the emission of an interstitial from the cluster must break one of these bonds. The minimum energy path for the emission of an interstitial from the cluster is therefore not necessarily direct and probably passes through high energy configurations and additional barriers.

- while the SMIC I_5 can be described as an I_4 with an additional interstitial atom attached. The emission of this interstitial therefore has little influence on the other bonds in the I_4 cluster and few additional barriers are expected.

In the following, we illustrate the emission of interstitial from two SMIC compact-like I_4 and I_5 and the activation barriers of the interstitial emission from these SMICs have been calculated. For these two examples, all these barriers encountered during these emissions have been calculated using ARTn or NEB to obtain a global activation energy, for a better estimate of the calibration (see Figure 4.33).

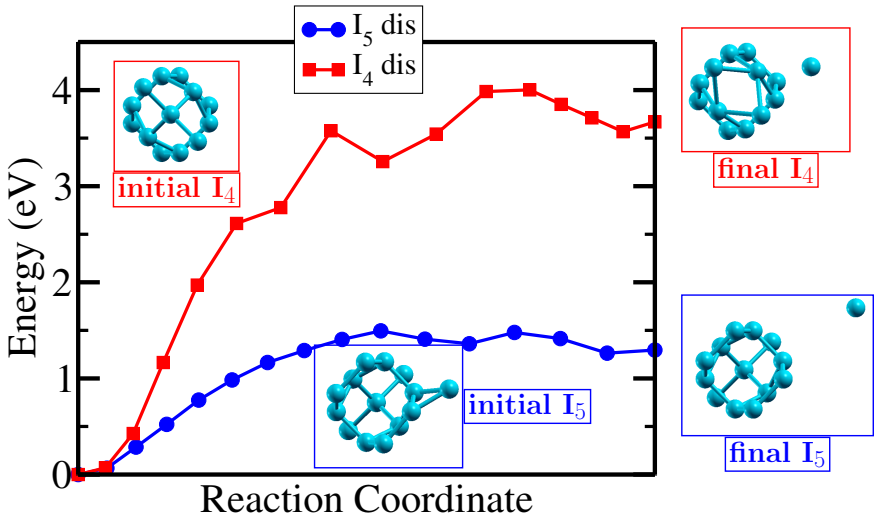

Figure 4.33: *Emission paths to emit one I from I_4 (red curve) and I_5 (blue curve) of compact type into respectively I_3 and I_4.*

I emission from an I_5 SMIC - To characterize the emission of an interstitial from an I_5 SMIC, we determine the activation barriers for dissociating an I_1 atom from the I_5 cluster until we obtain isolated behavior of both the I_4 and the resulting I_1. For such compact-I_5, we can guess the path of an interstitial emission moving away from the interstitial cluster. I_5 is composed of an interstitial bound to an I_4 compact cluster. The dissociation (emission) path is therefore assumed to be the migration of this additional interstitial away from the I_4 cluster. A NEB calculation was used to calculate the minimum energy path. As can be observed in Figure 4.33, the activation barrier is of 1.5 eV. This value is lower than those used in the KMC (3.3 eV). The dissociation path consists of several intermediate stable states and the migration of the interstitial between these intermediate states. It can be seen that at some point, the barrier between the intermediate states does not change anymore, around 0.2 eV. This value is close to that of a single interstitial migration calculated in DFT [23] *I emission from an I_4 SMIC* - In the case of I_4 cluster, the dissociation path is more difficult to guess. The compact I_3 used in this calculation is close to the structure found in [22] and is not the ground state of the I_3 configuration as mentioned in [23]. It is similar to the compact I_4 structure with a atom missing. The first assumption used is to take away the missing atom of the I_3 in the I_4 structure. The energy path to take away this atom is shown here in Figure 4.33 - red curve. As in the case of the I_5, intermediate stated can be observed in the dissociation path. The distance at which the migration of the interstitial from one site to the other is equal to a single interstitial migration barrier is farther away than in the I_5 dissociation. The activation barrier in this case is high (4.5 eV).

Critical discussion on these results - In such calculations, NEB calculation has two major drawbacks. First of all the resulting configuration of I_3 shown in the Figure 4.33 is not the ground state. The emission of an interstitial from I_4 does not necessarily pass through this local minimum of I_3 to form the ground state I_3. And this is difficult then to guess what is the correct structure. Second, this is not the only dissociation path that exists for the interstitial emission. In the paper by [27], an alternative path is found: the activation barrier to form a chain I_4 to a compact I_4 has been calculated as well as the activation barrier for an interstitial emission from an I_4 chain-like cluster to form the I_3 ground state. If these two paths are combined, an alternative path for an interstitial emission from a compact I_4 cluster is obtained. The maximum energy barrier taken from the data of [27] appears to be lower than that calculated obtained in our first NEB calculation (2.9 eV). This proposed path in the literature should then be studied with our own DFT parameters.

The last option to investigate dissociation path of the compact I_4 is to use different methods. A self-learning KMC can be used to investigate the different possible paths that exist, such as kART [28] that uses interatomic potentials to explore the potential energy surface. The energy barriers should be then refined at the ab initio level.

4.5 Conclusions

In this chapter we studied the relevance of the KMC in the simulation of a new technological process, namely the heated implantations.

First, it was demonstrate that the KMC could easily integrate the machine parameters into the simulation of implant processes, which can modify the temperature of the wafer. The KMC is able to model the effect of the wafer heating caused by the collisions of the ions with the silicon. The mechanics of the implantation tool, the cooling system, the dose rate are parameters that can change from one equipment or recipe to another and can be properly integrated in the KMC simulations. This point has been studied by comparing the KMC simulations to TEM analyses of amorphizing C implantations.

In a second step, the defects resulting from deliberately heated implantations have been characterized. The presence or absence of an amorphous layer in the wafers following implantation as a function of temperature and the resulting defects following an annealing sequence were analyzed in TEM. It was shown that heating the wafer during implantation could change the type of defects formed at the end of the process, after a complex annealing sequence. For As implantations at RT and 150°C DLs were observed while for an As implantation temperature of 500°C {311}defects are seen after annealing. These results were confirmed by a photoluminescence characterization. The wafers implanted at RT and at 150°C have indeed similar peaks while the sample implanted at 500°C has a different spectrum. Photoluminescence represents a complementary means of characterization to TEM. This method allows the analysis of defects that would be too small to be visible in TEM. The link between the observed peaks and the type of defect present is however difficult and requires a good knowledge of the peaks already characterized, as well as some additional analysis cases. The I1 and I2 peaks seen in photoluminescence could be associated with the presence of dislocations with the help of additional annealing performed on the samples and TEM analysis. Samples implanted with phosphorus have also been characterized. Photoluminescence revealed the presence of DLs in two cases. In P implantation, we notice that the implanted dose has a greater impact than the implantation temperature on the defects formed after annealing.

The previous implantations and their annealing sequence were then simulated in KMC for both

P and As. For As, the presence of an amorphous layer is well modeled by KMC as well as the absence of amorphous layer for the 150°C and 500°C implantations. This is an advantage compared to the continuous simulations which do not predict a correct amoprhization profile by default. The predictions of the KMC simulations for the RT and 150°C implantations are consistent with the experimental results: DLs are predicted in KMC with interstitial densities close to those measured on the TEM analyses. The predictions of defects at the end of annealing for the 500°C implantation are not in agreement with the experimental observations. The KMC simulations predict DLs while {311}defects are observed in TEM.
In the cases of P implantations the KMC also predicts DLs for RT and 150°C implantations, in agreement with the experimental findings. The size and density of the DLs in the simulations do not match the experimentally measured size. This difference is explained by the size of the simulation boxes used which are limited due to the simulation time. It is also interesting to note that the predictions of the DLs depend on the size of the box used (no DLs observed in the RT implementation for a box of 100 nm x 100 nm).

To improve the KMC simulations in the case of the As implantation at 500°C, the formation energies of the SMICs have been studied in detail using atomistic data available in the literature and from a dedicated ab initio study performed in the framework of this thesis. It is indeed in the form of SMICs that the excess as-implanted interstitials are stored and this seems to have an influence. By using the formation energies of the most stable type of SMICs calculated in ab initio, it is possible to predict the formation of {311}defects after the annealing following the implantation at 500°C. Tests were also conducted to be able to use the same energy for RT, 150°C and 500°C implantations. It is then possible to simulate the correct type of defect, as well as the correct density of pieced interstitials in these defects, for all implantation temperatures. However, this calibration is not adapted to other experiments, it does not reproduce the interstitial oversaturation of the Cowern experiments. One hypothesis is that depending on the implantation temperature the type of clusters formed is different. For implantations at RT and 150°C chain-like clusters are formed and allow an evolution following the Ostwald maturation. For high temperatures the as-implanted SMICs are mostly of compact type and slow down the growth of defects. A more detailed study of the different types of clusters has been carried out in DFT, in particular to try to refine the calculation of the activation energy necessary for the emission of an interstitial from a SMIC.

References

[1] Sentaurus Process User Guide, R-2020.09, Synopsys Inc.

[2] R. Duru, D. Le-Cunff, M. Cannac, N. Laurent, L. Dudas, Z. Kiss, D. Cseh, I. Lajtos, F. Jay, and G. Nadudvari, "Photoluminescence for in-line buried defects detection in silicon devices", in 2017 28th annual semi advanced semiconductor manufacturing conference (asmc) (IEEE, 2017), pp. 262–266.

[3] T. Arguirov, W. Seifert, M. Kittler, and J. Reif, "Temperature behaviour of photoluminescence and electron-beam-induced current recombination behaviour of extended defects in solar grade silicon", Journal of Physics: Condensed Matter **14**, 13169 (2002).

[4] E. Steinman and H. Grimmeiss, "Dislocation-related luminescence properties of silicon", Semiconductor science and technology **13**, 124 (1998).

[5] M. Tajima, H. Takeno, and T. Abe, "Characterization of point defects in si crystals by highly spatially resolved photoluminescence", in Materials science forum, Vol. 83 (Trans Tech Publ, 1992), pp. 1327–1332.

[6] P. Giri, "Photoluminescence signature of silicon interstitial cluster evolution from compact to extended structures in ion-implanted silicon", Semiconductor science and technology **20**, 638 (2005).

[7] P. Giri, S. Coffa, V. Raineri, V. Privitera, G. Galvagno, A. La Ferla, and E. Rimini, "Photoluminescence and structural studies on extended defect evolution during high-temperature processing of ion-implanted epitaxial silicon", Journal of Applied Physics **89**, 4310–4317 (2001).

[8] S. Hu, "Dislocation pinning effect of oxygen atoms in silicon", Applied Physics Letters **31**, 53–55 (1977).

[9] S. Senkader, P. Wilshaw, and R. Falster, "Oxygen-dislocation interactions in silicon at temperatures below 700° c: dislocation locking and oxygen diffusion", Journal of Applied Physics **89**, 4803–4808 (2001).

[10] K. S. Jones, S. Prussin, and E. Weber, "A systematic analysis of defects in ion-implanted silicon", Applied Physics A **45**, 1–34 (1988).

[11] A. Claverie, B. Colombeau, B. De Mauduit, C. Bonafos, X. Hebras, G. Ben Assayag, and F. Cristiano, "Extended defects in shallow implants", Applied Physics A **76**, 1025–1033 (2003).

[12] S. Pizzini, M. Guzzi, E. Grilli, and G. Borionetti, "The photoluminescence emission in the 0.7-0.9 ev range from oxygen precipitates, thermal donors and dislocations in silicon", Journal of Physics: Condensed Matter **12**, 10131 (2000).

[13] S. Kumar, G. Chaussemy, P. Roura, and A. Laugier, "Spectroscopic investigation of arsenic-induced surface defects in high-dose as+ implanted rapid thermal annealed silicon", MRS Online Proceedings Library **138**, 215–220 (1988).

[14] W. L. Ng, M. Lourenco, R. Gwilliam, S. Ledain, G. Shao, and K. Homewood, "An efficient room-temperature silicon-based light-emitting diode", Nature **410**, 192–194 (2001).

[15] Y. Yu, W. Chong, Y. Rui-Dong, L. Liang, X. Fei, and B. Ji-Ming, "Photoluminescence evolution in self-ion-implanted and annealed silicon", Chinese Physics B **18**, 4906 (2009).

[16] S. Coffa, S. Libertino, and C. Spinella, "Transition from small interstitial clusters to extended {311} defects in ion-implanted si", Applied Physics Letters **76**, 321–323 (2000).

[17] A. Schmidt, I. Jang, T. Kim, K.-H. Lee, Y.-K. Park, M.-H. Yoo, and C.-H. Chung, "Compact process model of temperature dependent amorphization induced by ion implantation", in 2010 international conference on simulation of semiconductor processes and devices (IEEE, 2010), pp. 197–200.

[18] L. Pelaz, L. A. Marqués, and J. Barbolla, "Ion-beam-induced amorphization and recrystallization in silicon", Journal of applied physics **96**, 5947–5976 (2004).

[19] N. Zographos, C. Zechner, and I. Avci, "Efficient tcad model for the evolution of interstitial clusters,{311} defects, and dislocation loops in silicon", MRS Online Proceedings Library (OPL) **994**, 0994–F10 (2007).

[20] C. J. Ortiz, P. Pichler, T. Fühner, F. Cristiano, B. Colombeau, N. E. Cowern, and A. Claverie, "A physically based model for the spatial and temporal evolution of self-interstitial agglomerates in ion-implanted silicon", Journal of applied physics **96**, 4866–4877 (2004).

[21] M. Prasad and T. Sinno, "Internally consistent approach for modeling solid-state aggregation. i. atomistic calculations of vacancy clustering in silicon", Physical Review B **68**, 045206 (2003).

[22] L. A. Marques, M. Aboy, M. Ruiz, I. Santos, P. López, and L. Pelaz, "{001} loops in silicon unraveled", Acta Materialia **166**, 192–201 (2019).

[23] S. Lee and G. S. Hwang, "Growth and shape transition of small silicon self-interstitial clusters", Physical Review B **78**, 045204 (2008).

[24] N. Arai, S. Takeda, and M. Kohyama, "Self-interstitial clustering in crystalline silicon", Physical review letters **78**, 4265 (1997).

[25] N. Cowern, G. Mannino, P. Stolk, F. Roozeboom, H. Huizing, J. Van Berkum, F. Cristiano, A. Claverie, and M. Jaraiz, "Energetics of self-interstitial clusters in si", Physical Review Letters **82**, 4460 (1999).

[26] I. Martin-Bragado, I. Avci, N. Zographos, M. Jaraiz, and P. Castrillo, "From point defects to dislocation loops: a comprehensive modelling framework for self-interstitial defects in silicon", Solid-state electronics **52**, 1430–1436 (2008).

[27] Y. Du, R. Hennig, T. Lenosky, and J. Wilkins, "From compact point defects to extended structures in silicon", The European Physical Journal B **57**, 229–234 (2007).

[28] F. El-Mellouhi, N. Mousseau, and L. J. Lewis, "Kinetic activation-relaxation technique: an off-lattice self-learning kinetic monte carlo algorithm", Physical Review B **78**, 153202 (2008).

General conclusions and perspectives

5

Contents

In this manuscript, we have seen how the kinetic Monte Carlo (KMC) methodology, a strategic modeling tool for simulating manufacturing processes and supporting technologies, is used to simulate defect formation that can have detrimental effect on the operation of a microelectronic device, with the help of atomic scale understanding of the atomic dynamics in the material.

To go further, we have shown how when this kinetic Monte Carlo methodology is used in an integration scheme of applied modeling techniques according to a multilevel strategy, that it can be further improved to match the new constraints or new needs of microelectronics technologies. We demonstrate how each level of this multi-level approach contributes to the improvement of these commercial process simulation codes and in particular how a dialogue between the methodologies must be established so that each one feeds the other one in order to improve it in terms of prediction and accuracy.

- In particular, thanks to an exhaustive study of the diffusion mechanisms of a chemical species at the atomic scale, it is possible to implement new species. Above all, we demonstrate the complexity of atomic diffusions in the material. This complexity is currently not exhaustively described in commercial software due to the limit of the formalism of the equations implemented in these simulation software
- We show how, still with the help of these atomic resolution calculations, it is possible to improve these tools with a better knowledge of the dynamics of the atoms, which then gives access to a precise calibration of the structures and the activation barriers of the atomistic mechanisms without introducing empirical parameters
- We also show how kinetic Monte Carlo is placed upstream of continuous codes to offer input data to these continuous codes to guide towards a simulation closer to reality, where the dynamics of atoms dominate at the early stages of technological processes

In this concluding chapter, we come back to the two studies addressed in this thesis, *i.e.* the formation of BO_2 type defects through the calibration of the O species and the heated implantation, by discussing the results obtained, identifying the limits and opening up perspectives.

5.1 Implementation of new impurity in KMC

5.1.1 Calibration of impurities in KMC

KMC is a suitable method to simulate the diffusion and evolution of an impurity in different cluster shapes. While continuous methods require solving a differential equation per different type of cluster, the KMC mechanism is more efficient in dealing with different types of impurity clusters.
The calibration of a new impurity, the oxygen specie, in the KMC was performed. In the case of oxygen two types of particles were implemented, O_i and O_{2i} because O_{2i} was supposed to be mobile in silicon. For O_i, sole a migration event was implemented while the implementation of O_{2i} required both the implementation of a dissociation event and a migration event. The implementation of an event requires the calibration of a prefactor and an activation energy. The activation energies are characterized by ab initio calculations, using an approximation for the dissociation event in order to fit with the formalism of the KMC. Several calibration methods have been proposed for the calibration of the prefactors: an approach based on the experimental fit, an approach based on the DFT calculation of phonons and the use of a KMC off-lattice.
Based on events at the atomic scale (migration of a particle to a neighboring site) the KMC can reproduce trends at larger scales. The diffusion of an oxygen profile during annealing is

simulated. The simulation is able to reproduce the experimental trend of faster diffusion for temperatures below 700°C.
The KMC has the advantage of a calibration with a physical sense. The activation energies correspond to real atomistic mechanisms describing the ability of an atom to move in the material and are then not adjustable factors from one experiment to another. For a detailed atomistic simulation, the calibration is then longer and requires more exploration of the events than for a continuous model. In the long run, however, the simulations have a better chance of capturing the experimental trends of a larger number of experiments.

5.1.2 Limits of the model and of the calibrations

Several limitations have been observed in the implementation of oxygen in KMC.

Limitations of the on-lattice KMC model - The first limitations are those of the KMC model itself. The events calculated in DFT reveal a complex diffusion mechanism, characterized in particular by anisotropy in the diffusion direction and dissociation mechanisms of O_{2i}. This anisotropy cannot be taken into account in the lattice KMC. The diffusion of an oxygen profile in depth would change depending on the orientation of the silicon substrate used.

Oxygen diffusion is also characterized by its complexity when it interacts with another oxygen, as is the case for O_2 dissociation (or association). Thus another limitation of KMC is the implementation of simple barriers in the evolution mechanisms of species while we show by DFT calculations a quite different complexity: Upon dissociation of an O_{2i}, the oxygen atom that moves away from the other must be separated by a certain distance from the other oxygen to recover the behavior of an isolated O_i, with activation barriers that are modified as a function of this distance, which cannot be implemented in the current formalism of TCAD codes.

Limitations of the calibration from experiments - The calibration method based on the experimental fit also has some disadvantages. The first drawback concerns the validity of the assumptions used for the fit. If the hypothesis of a high temperature diffusion using O_i migration seems to be solid, the hypothesis of an accelerated diffusion only due to O_{2i} migration is more debatable. Several hypotheses have been formulated to explain the enhanced diffusion of oxygen in silicon and the migration of O_{2i} is only one of them. DFT calculations have also shown that an oxygen dimer O_{2i} has a lower migration energy than O_i. It was also calculated that the largest O_i clusters has a lower migration energy than O_i. The enhanced diffusion phenomenon could therefore be an accumulation of these different contributions, or even be sensitive to impurities depending on the experiment considered.

Another difficulty in the experimental calibration is the variation of the enhanced diffusion phenomenon observed according to the experiments carried out. The slope associated with the diffusion below 700°C is more or less marked depending on the type of experiment performed. Experiments using a model based on DL-induced stress show an activation energy of 1.6 eV for the phenomenon. Whereas experiments based on out-diffusion or in-diffusion of oxygen measured by SIMS find lower values of activation energy.

A final limitation of the experimental calibrations is that they do not allow to distinguish two contributions in a measured phenomenon. In the case of oxygen, the enhanced diffusion depends on both the O_{2i} dissociation event and the O_{2i} migration event.

Limitations of the calibration from DFT - From a DFT calibration point of view, there are also several limitations. The first one is the modeling of the atomic configurations of defects that induce one or several energy levels located in the silicon bandgap. The classical functionals underestimate in this case the energy of these configurations. This problem arises in particular when calculating the energy at the saddle point for O_i and O_{2i} migrations. HSE functionals can be used to try to address this problem, but they also have their limitations. By taking the high-temperature oxygen diffusion activation energy value as a reference for the migration energy of O_i, the HSE functional used appears to overestimate the saddle point energy. Such differences could also come from the ideal model system considered in DFT.

An effect of the size of the simulation cell is also observed in our calculations. The migration energy of O_i increases with the size of the box (2.25 eV to 2.29 eV for a box with 216 silicon atoms and one with 512 silicon atoms) and testifies to the necessity of simulating large systems to obtain converged systems.

The calculation of phonons to obtain entropic prefactors can also be difficult. The calculation of phonons is very time consuming and requires a lot of computational resources. Moreover, if the potential energy surface around the studied configuration is flat, the phonon calculation may not converge in some cases, as it is the case for the O_i C1h position.

The different possibilities of geometry for a defect can also be considered as a limitation when using DFT calibration. In this work, configurations previously found in the literature have been tested and an exploration of the PES has been performed using the ARTn tool. However, nothing allows us to state with certainty that it is impossible to find more stable configurations than those exposed in this thesis. For defects containing a small number of atoms the possibilities of configurations are limited and it is likely to find the most energetically favorable ones with the help of physical consideration or the ARTn tool. The more atoms the defect contains, the larger the number of possible geometries. The O_i, O_{2i} and BO_{2i} configurations studied here are quite simple and the calibration work would certainly be more complicated for clusters containing more atoms.

Another problem is the management of intermediate configurations separated by small energy barriers. This is the case for example in the O_{2i} migration. This configuration has been ignored for the moment. Taking it into account, for example in a KMC off-lattice formalism, would lead to slow down the simulations considerably. The small activation barriers would be almost systematically chosen because they have a very high transition rate, and the system would oscillate between two configurations with a very low time increment.

The off-lattice KMC tool was found to be useful, but it also has room for improvement. The simulation boxes used overestimate the oxygen concentration compared to the concentration in industrial wafers. The simulated annealing time is also too short to correctly simulate the enhanced diffusion phenomenon, as the annealing times used in in-diffusion experiments can reach several days. The study of defects with a larger number of atoms is also more difficult with the off-lattice kmc. The O_{2i} case was rather simple but could already pose a problem. The number of configuration and topology to take into account depends on the number of atoms to take into account in the events. Two atoms of sixth neighboring oxygens interacted together, so it was necessary to take into account all configurations where the oxygens were sixth neighbors, at the risk of obtaining a configuration with a topology not recognized by the solver. The catalog of events increases exponentially with the number of atoms to be taken into account in the events.

5.1.3 Perspectives

One idea for future work would be to implement other common oxygen-based defects. Among these, the oxygen-vacancy complex OV is already well studied and could be the next target. First calculations on this complex were performed at the end of the thesis, as well as on the O2V and OV_2 complexes that were reported to introduce an energy level in the silicon bandgap. The interstitial oxygen clusters would also be interesting as they could introduce dark current, and also BO cluster.

For defects with a higher number of atoms, the use of empirical potentials could be useful in the calculation of the different possible defect configurations. The most stable structures found with the help of empirical potential could be used as a starting point for a DFT study.

For the problem of energy levels in the bandgap, other formalisms can be considered. The GW method can for example be a way to obtain more accurate energies for the saddle point of O_i migration (even if this method has also some drawbacks).

Regarding the new off-lattice KMC methodology, several improvements are currently being explored towards a self-learning KMC. A recent update has sped up the simulation time, that could model both oxygen diffusion regimes, using larger boxes and longer annealing times. The complexity of catalog generation, especially when studying larger defects, can be solved using KMC on-the-fly methods. This technique may be rather cumbersome but could prove to be promising, especially with the development of increasingly accurate empirical potential. Advances in empirical potentials developed in machine learning could be used to refine off-lattice kmc simulations. A basin algorithm is also being implemented in order to deal smartly the problem of low energy intermediate configurations.

5.2 KMC for new process simulations

5.2.1 Calibration of parameters for new process

The KMC methodology was demonstrated to be suitable for simulating heated or cold implantations. The mechanisms all take into account the effect of temperature through events that follow an Arrhenius law. KMC simulations are particularly useful under amorphizing implantation conditions. In Chapter 4, the KMC was shown to be accurate in simulating the depth of amorphization for implantation at RT, as well as in simulating the absence of an amorphous layer following implantation at 150 °C. The KMC was also used to simulate the correct depth of amoprhization for cold implantations. Continuous simulations, depending on the model, are less efficient to simulate the amorphization depth and depend on parameters to be calibrated.
The KMC without additional calibration was unable to simulate the correct type of defects at the end of the annealing sequence. A calibration using molecular dynamics data was performed. As with the oxygen calibration, the extended defects could be simulated using a physical explanation. The energy values obtained at the ab initio level could be easily implemented in the KMC and allowed to obtain the correct type of defects at the end of the annealing sequence.
Another strong point of the KMC is that it can be adapted to the different machines used by the industry. The different parameters extracted from the implantation machines can be translated into the KMC by command lines. This is the case, for example, for self-heating or the ribbon passage time during an implantation.
The ability of KMC to couple with continuous simulation methods has also been demonstrated and improved in this thesis. This capacity could make it possible to consider its use only for specific steps of the manufacturing process.
Photoluminescence or TEM experiments remain essential in the calibration of KMC. It is the

TEM cross-section views that have allowed the validation of the KMC model using the machine parameters. The photoluminescence analyses can also be complementary with the simulations. Continuous simulations could be used to exclude the SMICs hypothesis for the S1 and S2 peaks observed in photoluminescence. The evolution of the peaks as a function of the additional annealing performed could also be correlated with the evolution of the defects.

5.2.2 Limits of the model

Interstitial migrations -One of the major limitations of using KMC to simulate extended defects is the simulation time. Large simulation box sizes were used, which resulted in significant simulation times. The simulation time can take several days, especially after calibration. This simulation time is very important if it is necessary to vary many parameters in order to optimize the implantation and annealing recipes. This point has been partly improved with the procedure mixing KMC for implantation and continuous simulations for annealing. During annealing, most of the simulation time is devoted to the migration of interstitials to neighboring sites. Among the simulated events, more than 99 % are interstitial migrations. Procedures already exist to try to solve this problem, like the double hope event.
It was observed that the type of defects formed depends on the size of the simulation box. This observation is problematic because it is not necessarily possible to guess in advance what size of box is needed to simulate the occurrence of extended defects.

Defect implementation -Another limitation concerns the implementation of defects in the KMC. For the emission of an interstitial from a cluster, only one activation energy is informed. This method is reliable if there is one type of cluster formed that is much more stable than the others, regardless of the temperature of the processes used. The problem with this formulation is that if two types of clusters coexist, one more stable than the other depending on the process conditions, then the KMC is unable to model the phenomena related to these clusters. This can be the case for interstitial clusters.
As observed in the oxygen case in the other study of interest of the thesis, the complexity of the potential energy surface around the SMICs is a limit in the calibration. We note also here that the size of the boxes used in ab initio matters, as shown when comparing similar structures characterized in different simulation cells.
Another limitation of the calibration is that it is not possible to adjust the entropic prefactor of the interstitial emission event as a function of the size of the SMICs considered.
Experimental calibration -We also face the limitations regarding the calibration based on experimental methods. The first is the availability of equipments. TEM images have limited resolution and do not allow observation of SMICs. High resolution TEM methods can be used to observe smaller defects but it is necessary to know where these defects are located in the sample. Photoluminescence allows to observe smaller defects, provided that they emit a sufficient signal (this condition depends partly on their concentration in the sample). The major drawback of this method is the identification of the observed peaks. Several peaks associated with different defects may be close in location, or it is also possible to find peaks not observed in the literature. The identification of peaks requires comparing them to peaks already observed in the literature and trying to use the process conditions used to determine which known peaks are most likely to be observed.

5.2.3 Perspectives

KMC computational time reduction -Several leads could be explored to improve the use and calibration of KMC in heated implantations. To reduce the simulation time, the method of using the KMC for implantation and the continuous method for annealing is promising. It could

be improved by placing the excess interstitials after the implantation and the first annealing ramp in more appropriate continuous fields. For now, all excess interstitials are placed in the continuous field corresponding to the I2 clusters. In the future, the procedure used can be modified to be able to place the larger SMICs in other continuum fields such as the I3, I4 fields or in the 311 defect field for the larger interstitial clusters.
Another idea to improve the computation time would be to reduce the time spent on interstitial migrations. One idea would be to directly choose the next defect with which the interstitial interacts after being emitted from a cluster. (The surface would then also be considered as a possible interaction location). This mechanism would save time, specifically in the situation where some extended defects are very spaced in space and far from the surface. This situation corresponds in particular to the case where large simulation boxes are used to simulate annealing following a high energy and medium/high dose implantation. A shortcoming of this method is that it does not take into account the mechanism where two interstitials migrate at the same time in the simulation box and interact together to form an I2 cluster. Another limitation is that it is difficult to implement in the software.
Calibrations based on ab initio tools can also be a way of progress. In order to calculate an interstitial emission energy from the compact I4 cluster, a method based on a self-learning KMC is under study. The objective of these simulations would be to calculate several dissociation paths with self-learning KMC and using empirical potentials. The saddle points of the different dissociation paths would then be refined using DFT calculations.
Experimental -For the experimental part of the calibration, work is still in progress. The best hypothesis at the moment to explain the S1 and S2 photoluminescence peaks is to associate them to the strain-field induced by the DLs. An idea of work to be done would be to verify this hypothesis with theoretical calculations, in particular in DFT which would allow us to estimate the energy levels produced by the strain (using a GW or HSE type method). It would also be interesting to simulate in KMC, in continuous method and with the hybrid method the evolution of defects during an additional annealing. These simulations could confirm the reliability of the hybrid method. TEM images of the implanted sample at 500°C are provided. These images would allow to better understand the link between the defects observed on the photoluminescence spectrum and the 311 defects observed on the first TEM images. The hypothesis of very stable SMICs formed during implantation could be clarified using these TEM images. In a longer term perspective, it would also be interesting to study heated phosphorus implants with implantation conditions similar to those of Arsenic implants and the same annealing sequence. Implanting phosphorus could allow to refute the hypothesis of interstitial arsenic impurity clusters.

5.3 KMC use in a TCAD workflow

5.3.1 Link with devices simulations for SRH

One of the goals of using KMC was to be able to determine the defects formed after the process and identify those that could generate SRH. This objective raises two issues:

- Can we simulate the defects that cause SRH using KMC simulation?
- How to quantify the impact of a simulated defect in KMC on SRH?

Electrical measurements show that on a silicon wafer, only a percentage of pixels have a high dark current. To be industrialized, a wafer must contain a percentage of pixels exceeding an SRH limit below a certain threshold. Either the dark current in these pixels comes from a single defect in the pixel, or the effect of defects in the pixel is cumulative and above a threshold, a dark current is observed. In the case where a small number of defects in the pixel is responsible

for the dark current, the KMC does not seem to be suitable for predicting the dark current. Indeed, the pixel dimensions can be in the micron range. If we want to simulate a single defect on a surface of 1 μ^2 the KMC is not powerful enough to simulate a whole manufacturing process on such a large area. If the defects responsible for the dark current are in high concentration in a pixel, it is possible to simulate only a part of the pixel. At the end of the KMC, it is then possible to study the different remaining clusters and to study one by one their electrical properties in KMC. This approach has been tried with known processes to generate SRH in the company but did not identify a specific defect a precise defect. To be effective, it is necessary to consider the hypothesis that all defects that could introduce dark current are correctly modeled in the KMC. In accordance with the initial objective of the KMC development, a number of clusters have been calibrated to correctly reproduce the dopant diffusion. The calibration of the KMC does not seem to be adapted to the study of faults that are a source of dark current. An exact calibration of the different geometry types for a given defect stoichiometry is not obvious as it has been shown in this thesis. This method also assumes that it is possible to link a defect to its impact on the electrical current, which is the second challenge mentioned.

It is possible to simulate the impact of a defect in the sdevice simulator of [1]. To do so, it is necessary to calibrate its energy level in the bandgap as well as its cross-section. If a defect is small enough, it is possible to estimate these parameters using DFT simulations. The calculation of energy levels in the bandgap induced by a defect has been developed in this thesis. They require at least the use of hybrid functionals or GW calculations. The calculation of the cross-section is a bit more tricky. An attempt has been made in [2].

In the case of extended defects such as DLs, DFT is not suitable to find the electronic levels in the bandgap generated by these defects. There are experimental works that could link DLTS peaks to extended defects. One must also consider the cases of "decorated" DLs where impurities are included in the DL. These impurities trapped in the DLs could modify the electronic levels induced in the gap.

5.3.2 KMC simulations for accurate doping profiles

Another possibility to use the KMC is to simulate correct doping profiles. One of the strengths of the KMC is that it can accurately simulate the amorphization during the implantation process. KMC simulations can take into account machine parameters, such as implant tool speed or dose rate, as well as new processes such as heated implants. An accurate description of amorphization is necessary to reliably model the channeling phenomenon. This phenomenon can change the as-implanted doping profile , and consequently the spiking profile at the end of the process, in a non-negligible way. Moreover, amorphization has an impact on the location of interstitial defects formed during annealing and on the number of excess interstitials at the beginning of annealing (after the SPER phenomenon in the case of amorphizing implantation). The location and nature of the defects formed during annealing also has an effect on the doping profile. This is an indirect effect of the amorphization that must be properly modeled. The KMC is therefore necessary for implantations with amorphizing conditions or close to amorphization (where it is possible to observe the beginning of a channeling effect). For non-amorphizing ion implantations, the KMC and continuum models are in agreement and simulate the dopant profiles rather well. In this type of implementation without an amorphous layer, continuous simulations are to be preferred because they require less computing time. The question is therefore to know when an amorphization generates or is close to generating an amorphous layer. The creation of an amorphous layer depends on several parameters: the implanted dose, the implantation energy, the type of implanted ion, the dose rate, the tilt, the self-heating of the wafer. In order to draw up an abacus to answer the question when an implantation is likely to create an amorphous layer, some of the previous parameters can be simplified or ignored. The temperature rise,

while having an effect, can be initially considered negligible or related to the dose, energy and machine used. The dose rate also depends on the dose and energy implanted. The mechanics of the implantation beam can also be neglected in the case of this question. A goal would be to create an amorphization abacus according to the dose, energy, ion implanted.

5.3.3 Simulations for variability and discrete effects

Device simulation currently uses continuous doping profile fields to simulate device performance. This approach is correct because when used to simulate devices much larger than the dimension between two dopant atoms. As the size of the devices is reduced, the discrete effects of implantation will become more pronounced. The variability for the same manufacturing process between two devices is already studied and will be made an increasingly important criterion. The KMC can already be used to simulate small devices entirely. In the context of variability, the KMC could be useful because it represents a finite number of dopants per device. The variability between two devices could therefore be studied using several simulations of KMC processes by changing the random seed between each simulation. The KMC does not depend on mesh size, which is expected to be increasingly refined as the device size is reduced. Therefore, the performance of the KMC improves when the device size decreases.

However, this use of the KMC has its limitations. Indeed, some defects may require a large surface to be simulated, even though the defect itself can be contained in the simulation box. A specific example could be the appearance of a dislocation loop. As mentioned in Chapter 1, the more interstitials a DL contains, the more stable it is. It is then interesting to study the statistical effect of a DL of size N1 in a small simulation box with periodic boundary conditions compared to several DLs, whose average size is equal to N1, distributed in a larger simulation box. All interstitials are assumed to be pieced into the DLs. The interstitial density is the same in both situations. The evolution of the defects will be different in the two cases. In the one-loop case in the small box with periodic conditions, the maximum loop size is the initial size. The emitted from the DLs will either recombine at the surface or be re-captured by the loop itself (especially with these periodic repetitions). In the multi-DL case, the DLs will follow an Ostwald ripening phenomenon. The smallest DLs will disappear in favor of the largest ones. The size of the largest DL will potentially be larger at the end of the annealing than at the beginning of the annealing. This DLs will then be larger and more stable than the DL of the first case. Complete dissolution of the DL will then require a longer anneal or at a higher temperature. Smaller devices require shallow implants whose energies are less likely to generate DLs (although these ¡18 keV implants can still generate DLs after annealing). However, the problem remains the same for smaller defects. One idea could be to simulate several devices in the same simulation box (if their size allows it). It would then be necessary to find the right size of simulation box, large enough to take into account statistical effects and small enough to be adapted to KMC simulation times. Another approach would be to first test the statistical phenomena on a large simulation box, potentially with a hybrid method, and then to check the effect of a discrete distribution of dopants on the variability using several KMC simulations containing a single device.

References

[1] Sentaurus Device User Guide, R-2020.09, Synopsys Inc.

[2] A. Jay, A. Hémeryck, F. Cristiano, D. Rideau, P.-L. Julliard, V. Goiffon, A. LeRoch, N. Richard, L. M. Samos, and S. De Gironcoli, “Clusters of defects as a possible origin of random telegraph signal in imager devices: a dft based study”, in 2021 international

conference on simulation of semiconductor processes and devices (sispad) (IEEE, 2021), pp. 128–132.